UNIVERSIDAD DE GRANADA

PROGRAMA DE DOCTORADO EN FARMACIA (B15.56.1)

ESTUDIO FOTOFÍSICO DE NUEVAS SONDAS FLUORESCENTES Y SU APLICACIÓN EN SISTEMAS BIOLÓGICOS DE INTERÉS BIOMÉDICO

PHOTOPHYSICAL STUDY OF NEW FLUORESCENT PROBES AND THEIR APPLICATION IN BIOLOGICAL SYSTEMS OF BIOMEDICAL INTEREST

PhD Thesis

Autor/a: Laura Mª Espinar Barranco

Directores: Luis Crovetto González / José Manuel Paredes Martínez

Granada, 2022

Editor: Universidad de Granada. Tesis Doctorales
Autor: Laura Espinar Barranco
ISBN: 978-84-1117-369-8
URI: http://hdl.handle.net/10481/75456

TABLE OF CONTENTS

SUMMARY

El principal tema de investigación de esta Tesis es el estudio de nuevas y diferentes sondas y su aplicación en procesos biológicos a través de la innovadora técnica de microscopía de fluorescencia como es la microscopía de imagen de tiempo de vida de fluorescencia (FLIM). Las técnicas de fluorescencia, y en particular la microscopía, representan un método no invasivo caracterizado por su baja toxicidad, proporcionando un gran número de ventajas entre las que se incluyen un alto nivel de sensibilidad, especificidad y un amplio rango de concentración. Este trabajo puede dividirse en el estudio de dos tipos diferentes de fluoróforos, las sondas sensibles al medio ambiente, incluyendo los colorantes solvatocrómicos y fluorogénicos, y las sondas de larga duración, como los biosensores basados en lantánidos, con sus aplicaciones biomédicas.

En el primer grupo, hemos incluido dos sondas diferentes; una es un derivado de xanteno modificado con silicio (2-4-TM), que presenta unas fuertes propiedades solvatocrómicas capaces de detectar cambios en la polaridad de su entorno. Durante el estudio de sus propiedades solvatocrómicas descubrimos una unión de adsorción natural de este derivado de xanteno modificado con silicio a macroestructuras. La combinación de estas propiedades nos permitió detectar en tiempo real los cambios en la polaridad del entorno alrededor del colorante durante las etapas iniciales del proceso de agregación del β-amiloide (Aβ), utilizando la espectroscopia de fluorescencia en estado estacionario y resuelta en el tiempo y técnicas avanzadas de obtención de imágenes de fluorescencia como FLIM. Mediante el uso de FLIM como un excelente enfoque para el estudio de la agregación amiloidogénica como método de detección no invasivo, pudimos establecer una escala de polaridad para distinguir la hidrofobicidad de los agregados y diferenciar entre los diferentes tipos de agregados Aβ-42 preamiloides. Las primeras etapas del proceso de agregación del péptido β-amiloide (Aβ) son de especial interés para comprender el origen de múltiples trastornos neurodegenerativos, como la enfermedad de Alzheimer, un importante problema de salud pública que afecta a millones de personas en todo el mundo y que sigue aumentando de forma espectacular.

El segundo fluoróforo incluido en las sondas sensibles al medio consiste en la sonda basada en emisión inducida por agregación (AIE, por sus siglas en inglés), denominada PEMC. Tras estudiar sus propiedades solvatocrómicas, descubrimos que presentaba preferencias por medios no polares, exhibiendo AIE en condiciones específicas por inmovilización. Esto nos permitió estudiar su tasa de incorporación espontánea en las células mediante imágenes de tiempo de vida de fluorescencia y observar su patrón intracelular producido por la AIE. Curiosamente, las fuertes diferencias en la intensidad y el tiempo de vida de fluorescencia de los diferentes compartimentos intracelulares facilitaron un aislamiento selectivo para el estudio detallado de orgánulos específicos, como el citoplasma, las mitocondrias y las estructuras periféricas de F-actina en la membrana plasmática. Dado que los orgánulos de las células eucariotas desempeñan un papel fundamental en la función celular, la importancia de visualizar y controlar la morfología y los cambios de actividad de determinados orgánulos proporciona información muy útil a nivel subcelular y molecular en el diagnóstico y la terapéutica de enfermedades.

En lo que respecta a las sondas de larga duración, hemos realizado el estudio de un biosensor basado en lantánidos, que consiste en una pequeña molécula que se comporta como un aceptor de Michael reactivo no fluorescente, que al reaccionar con tioles se vuelve fluorescente, y una antena eficiente de Eu^{3+}, que tras autoensamblarse con este catión en agua representa un logro muy innovador y químicamente interesante en la detección de biotioles, y específicamente de glutatión (GSH). El comportamiento de nuestro biosensor altamente selectivo de GSH mostró un alto potencial para estudios en células murinas y humanas del sistema inmune (células T $CD4^{+}$, T $CD8^{+}$ y B) por citometría de flujo, siendo capaz de capturar las diferencias basales en sus niveles de GSH intracelular. Nuestro biosensor también fue capaz de monitorizar con éxito los cambios intracelulares de GSH asociados a las variaciones metabólicas que rigen la inducción de las células T naïve $CD4^{+}$ en células T reguladoras (Treg).

Summary

The main research topic of this Thesis is the study of new different probes and their application in biological processes through the innovative fluorescence microscopy technique as fluorescence lifetime imaging microscopy (FLIM). Fluorescence techniques, and particularly microscopy, represent a non-invasive method characterized by their low toxicity, providing a number of advantages including a high level of sensitivity, specificity and wide concentration range. This work can be divided into the study of two different types of fluorophores, environment-sensitive probes, including solvatochromic and fluorogenic dyes, and long-lifetime probes, such as lanthanide-based biosensors, with their biomedical applications.

In the first group, we have included two different probes; one is a silicon-modified xanthene derivative (2-4-TM), that present a strong solvatochromic properties able to detect changes in the environment polarity. We studied the solvatochromic properties and discover a natural adsorption binding of this silicon-modified xanthene derivative to macrostructures. The combination of these properties allowed us to detect in real time changes in the environment polarity around the dye during the initial stages of the β-amyloid (Aβ) aggregation process, using

steady-state, time resolved fluorescence spectroscopy and advanced fluorescence imaging techniques such as FLIM. By using FLIM as an excellent approach to study amyloidogenic aggregation as non-invasive detection method, we were able to establish a polarity scale to distinguish the hydrophobicity of the aggregates and differentiate between different types of pre-amyloid Aβ-42 aggregates. The early stages of the β-amyloid (Aβ) peptide aggregation process are of particular interest in understanding the origin of multiple neurodegenerative disorders, such as Alzheimer's disease, an important public health problem affecting millions of people worldwide, and one that continues to increase dramatically.

The second fluorophore included in the environment-sensitive probes is the aggregation-induced emission (AIE)-based probe, named PEMC. After study its solvatochromic properties, we found that presents preferences for nonpolar media, exhibiting AIE under specific conditions by immobilization. This allowed us to study the rate of its spontaneous incorporation into cells by fluorescence lifetime imaging and to observe its intracellular pattern produced by the AIE. Interestingly, the strong differences in fluorescence intensity and fluorescence lifetime of the different intracellular compartments facilitated selective isolation for detailed study of specific organelles, such as cytoplasm, mitochondria and peripheral F-actin structures in the plasma membrane. Since organelles in eukaryotic cells play a key role in cellular function, the importance of visualizing and monitoring the morphology and activity changes of specific organelles provide very useful information at the subcellular and molecular level that opens up opportunities for use in disease diagnosis and therapy.

Respecting long-lifetime probes, we have studied and lanthanide based biothiol sensor, consisting of a small molecule that behaves as a reactive non-fluorescent Michael acceptor, which upon reaction with thiols becomes fluorescent, and an efficient Eu^{3+} antenna, after self-assembling with this cation in water represents a very innovative and chemically interesting achievement to detect biothiols, and specifically glutathione (GSH). The behaviour of our highly GSH-selective biosensor showed a high potential for studies in murine and human cells of the immune system (CD4+ T, CD8+ T, and B cells) by flow cytometry, being able to capture their baseline differences in intracellular GSH levels. Our biosensor was also successfully monitored intracellular changes in GSH associated with the metabolic variations governing the induction of $CD4^+$ naïve T cells into regulatory T cells (Treg).

BACKGROUND

In the recent years, the synthesis of xanthenic fluorescein derivatives has played a central role in our research group. The ability to monitor changes in the concentrations of anions released in important biological processes became especially attractive through the development of sensors based on anion- which induces changes in their fluorescent properties allowing non-invasive methods of detection. In that way, it was carried out the synthesis and study of different biosensors based on an excited-state proton-transfer (ESPT) reaction characteristic of fluorescein derivatives with an important application in real-time detection of intracellular phosphate levels through FLIM technique[1]. The presence of the pair $H_2PO_4^-$ / HPO_4^{2-} as a suitable proton donor/acceptor, does promote an intermolecular proton transfer to the prototropic species of xanthene dyes altering its fluorescence emission parameters[2] as it occurs in the fluorescein, interconverting the mono- and dianion forms in which exits in aqueous solution and physiological pH[1]. Our group showed that in the presence of a high concentrations of phosphate buffer and neutral pH, the fluorescence decays of these excited prototropic forms become coupled by ESPT and their decay times varies depending on both the phosphate and pH concentrations[3,4,5]. This dependence of lifetime not exclusive for one experimental parameter and the biexponential fluorescence decays of the fluorescein limit its use in FLIM[1] and raised the interest to find fluorescent derivatives as a suitable phosphate-mediated ESPT reaction with a monoexponential decay time, such as the xanthenic derivatives of the Tokyo Green dye family[6]. The design of this new family of fluorescein derivative has taken into account the structure proposed for the fluorescein a few years ago, in which the molecule could be interpreted as a directly linked donor-acceptor system, divided into two mutually orthogonal moieties which modulate their fluorescence properties by intramolecular photoinduced electron transfer (PET) from the benzoic acid moiety donor (d-PET) to the xanthene ring as the acceptor fluorophore (acceptor-excited PET; a-PET) in which PET could determine the fluorescence quantum efficiency (φ_F)[5,7].

Despite the suitable properties of these derivatives as phosphate-mediated ESPT reaction, their fluorescence emission in the same region of the cell autofluorescence focused the aim in the development of near-infrared (NIR) probes. Based on the historical synthesis of the fluorescein derivative Tokyo Magenta 7-hydroxy-5,5- dimethyl-10-(o-tolyl)dibenzo[b,e]silin-3(5H)-one (**2-Me TM**) by Egawa et al.[8] in which the O atom was replaced with a Si atom at position 10’ of the xanthene chromophore, we designed and developed the analog 7-hydroxy-10(4-methoxy-2-methylphenyl)-5,5-dimethyldibenzo[b,e]silin-3(5H)-one(**2-Me-4OMe-TM)** dye. One of the most exciting characteristics of these fluorophores is the deprotonation that their hydroxyl group suffers resulting in a very interesting redshift. As occurs in the Si-containing pyronine molecule[9], the red emission is due to σ* - π* conjugation and its strength could be different between their neutral and anion species (Scheme B.1.1)[8].

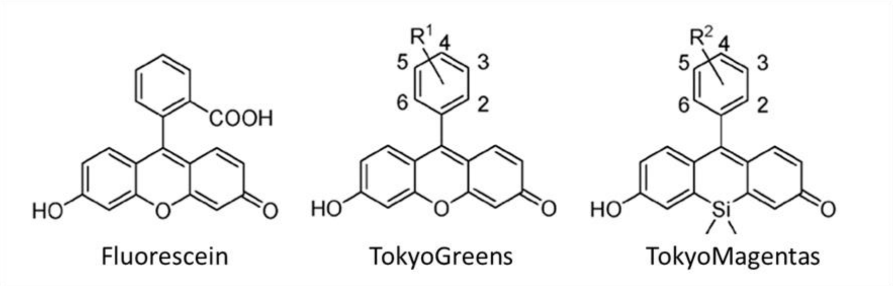

Figure B1.1. Chemical structures of fluorescein, Tokyo Green and Tokyo Magenta derivatives. R^1 = 2-Me: 2-Me TG. R^2 = 2-Me: 2-Me TM[8].

Although 2-Me-4OMe-TM was used as a multiplexed intracellular detector of both biothiols and phosphate ions[2], its behaviour in intracellular FLIM imaging was less sensitive to phosphate ions than the predicted by buffer-mediated ESPT reaction. We then hypothesize that the dynamics of the excited state of the dye might be influenced by a combination of effects when is in the complex matrix of cytoplasm. Thus, we have found that dye-macromolecule interactions and changes in the polarity of the microenvironment surrounding the dye, lead to changes in its photophysical properties due to solvatochromic effects.

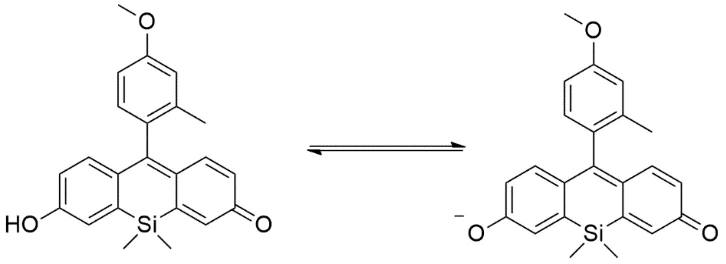

Scheme B1.1. Chemical structure between the prototropic neutral (left) and anionic (right) species of 2-Me-4-OMe-TM.

Our group's experience with β-amyloid oligomerization[10,11,12,13,14] sparked us the idea of testing our solvatochromic dye in the monitorization of the amyloidogenic aggregation by changes in the polarity of its environment. We carried out this hypothesis on the basis of two assumptions, the first was the dependence of the emission properties and fluorescence lifetime of 2-Me-4OMe-TM on polarity of the medium. And the second was that, as with any protein, the process of amyloid aggregation produces an increasingly non-polar environment. Therefore, we monitored the initial stages of Aβ peptide aggregation by the non-invasive technique FLIM *in vitro*.

In addition to this solvatochromic dye, the collaboration with Ramon Rios's laboratory (School of Chemistry, University of Southampton), allowed us the study of their compound 2-((4-((E)-2-((E)-3-((E)-3-(4-cyano-5-(dicyanomethylene)-2-phenyl-2-(trifluoromethyl) -2,5 dihydrofuran-3-yl) allylidene)-5,5-dimethylcyclohex-1-en-1-yl) vinyl) phenyl) (ethyl)amino) ethyl methacrylate, which we called PEMC. Due to the solvatochromic and aggregation-induced emission (AIE) characteristics of this molecule, we were able to study its behaviour in live cells by FLIM. In this regard, we isolated and mapped different intracellular regions through the strong differences in fluorescence intensity and lifetime of PEMC[15].

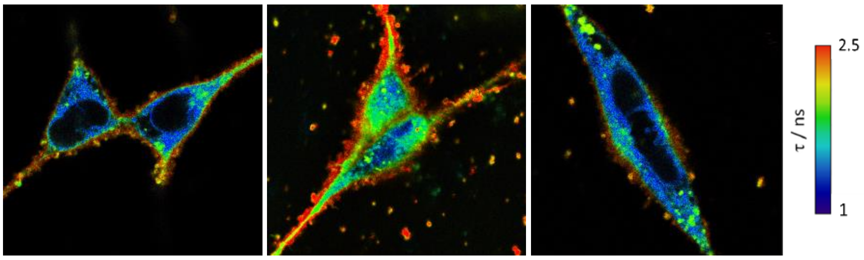

Figure B1.2. FLIM images of PEMC in HEK cells in which the different intracellular regions can be identified through their different fluorescence lifetimes. These range from 1 ns in the cytoplasm to 2.5 ns in the peripheral F-actin structures in the plasma membrane.

Finally, the incorporation of Dr. Juan Antonio González Vera to the Photochemistry and Photobiology group and his previous work with Dr. Francisco José Fueyo González allowed us the study of a **dihydrocyclopenta[de]quinolin-2-one** derivative that they synthesized. The introduction of a carboxylic acid in position 3 of the molecule made it highly reactive against thiols in a Michael addition reaction, capable of sensitizing Eu^{3+} emission. Considering its application as a thiol sensor, it was studied in the detection of biothiols (cysteine, homocysteine, glutathione and hydrogen sulphide), and could be the first lanthanide antenna of this type to be an off-on sensor of biothiols. The design and development of this biosensor, was a very innovative and chemically interesting achievement. The antenna's ability to capture biothiol changes in living cells through the increase in its fluorescence intensity and therefore, the lanthanide ion intensity, allowed us to establish the differences in biothiol levels that exist in cells of the immune system[16] in Miguel Fribourg's laboratory at the Icahn School of Medicine at Mount Sinai, where I also carried out a research stay thanks to the award of the Boehringer Ingelheim Fonds Travel Grant 2021.

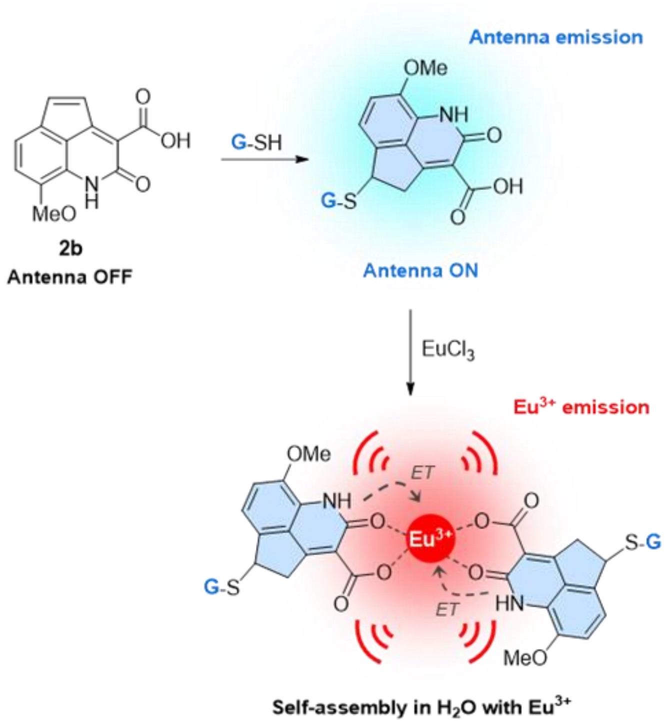

Figure B1.3. Schematic representation of biothiol sensor strategy. After the addition of GSH to Michael acceptor biosensor, the resulting antenna will increase its fluorescence. Moreover, if lanthanide ions are present, the antenna will self-assemble and intramolecularly transfer its energy (ET) to the metal, resulting in a significant increase in the red long- lived luminescence emission of Eu^{3+}.

BIBLIOGRAPHY

1 Paredes, J. M.; Giron, M. D.; Ruedas-Rama, M. J.; Orte, A.; Crovetto, L.; Talavera, E. M.; Salto, R.; Alvarez-Pez, J. M. Real-Time Phosphate Sensing in Living Cells Using Fluorescence Lifetime Imaging Microscopy (FLIM). *J. Phys. Chem. B* **2013**, *117* (27), 8143–8149.

2 Herrero-Foncubierta, P.; Paredes, J. M.; Giron, M. D.; Salto, R.; Cuerva, J. M.; Miguel, D.; Orte, A. A Red-Emitting, Multidimensional Sensor for the Simultaneous Cellular Imaging of Biothiols and Phosphate Ions. *Sensors (Switzerland)* **2018**, *18* (1).

3 Alvarez-Pez, J. M.; Ballesteros, L.; Talavera, E.; Yguerabide, J. Fluorescein Excited-State Proton Exchange Reactions: Nanosecond Emission Kinetics and Correlation with Steady-State Fluorescence Intensity. *J. Phys. Chem. A* **2001**, *105* (26), 6320–6332.

4 Boens, N.; Basarić, N.; Novikov, E.; Crovetto, L.; Orte, A.; Talavera, E. M.; Alvarez-Pez, J. M. Identifiability of the Model of the Intermolecular Excited-State Proton Exchange Reaction in the Presence of PH Buffer. *J. Phys. Chem. A* **2004**, *108* (40), 8180–8189.

5 Martínez-Peragón, A.; Miguel, D.; Orte, A.; Mota, A. J.; Ruedas-Rama, M. J.; Justicia, J.; Alvarez-Pez, J. M.; Cuerva, J. M.; Crovetto, L. Rational Design of a New Fluorescent “ON/OFF” Xanthene Dye for Phosphate Detection in Live Cells. *Org. Biomol. Chem.* **2014**, *12* (33), 6432–6439.

6 Urano, Y.; Kamiya, M.; Kanda, K.; Ueno, T.; Hirose, K.; Nagano, T. Evolution of Fluorescein as a Platform for Finely Tunable Fluorescence Probes. *J. Am. Chem. Soc.* **2005**, *127* (13), 4888–4894.

7 Ueno, T.; Urano, Y.; Setsukinai, K. I.; Takakusa, H.; Kojima, H.; Kikuchi, K.; Ohkubo, K.; Fukuzumi, S.; Nagano, T. Rational Principles for Modulating Fluorescence Properties of Fluorescein. *J. Am. Chem. Soc.* **2004**, *126* (43), 14079–14085.

8 Egawa, T.; Koide, Y.; Hanaoka, K.; Komatsu, T.; CooTeraiper, T.; Nagano, T. Development of a Fluorescein Analogue, TokyoMagenta, as a Novel Scaffold for Fluorescence Probes in Red Region. *Chem. Commun.* **2011**, *47* (14), 4162–4164.

9 Nie, H.; Qiao, L.; Yang, W.; Guo, B.; Xin, F.; Jing, J.; Zhang, X. UV-Assisted Synthesis of Long-Wavelength Si-Pyronine Fluorescent Dyes for Real-Time and Dynamic Imaging of Glutathione Fluctuation in Living Cells. *J. Mater. Chem. B* **2016**, *4* (28), 4826–4831.

10 Paredes, J. M.; Casares, S.; Ruedas-Rama, M. J.; Fernandez, E.; Castello, F.; Varela, L.; Orte, A. Early Amyloidogenic Oligomerization Studied through Fluorescence Lifetime Correlation Spectroscopy. *Int. J. Mol. Sci.* **2012**, *13* (8), 9400–9418.

11 Castello, F.; Casares, S.; Ruedas-Rama, M. J.; Orte, A. The First Step of Amyloidogenic Aggregation. *J. Phys. Chem. B* **2015**, *119* (26), 8260–8267.

12 Ruiz-Arias, Á.; Paredes, J. M.; Di Biase, C.; Cuerva, J. M.; Giron, M. D.; Salto, R.; González-Vera, J. A.; Orte, A. Seeding and Growth of β-Amyloid Aggregates upon Interaction with Neuronal Cell Membranes. *Int. J. Mol. Sci.* **2020**, *21* (14), 1–19.

13 Fueyo-González, F.; González-Vera, J. A.; Alkorta, I.; Infantes, L.; Jimeno, M. L.; Aranda, P.; Acuña-Castroviejo, D.; Ruiz-Arias, A.; Orte, A.; Herranz, R. Environment-Sensitive Probes for Illuminating Amyloid Aggregation in Vitro and in Zebrafish. *ACS Sensors*.

2020, pp 2792–2799.

14 Ruiz-Arias, Á.; Jurado, R.; Fueyo-González, F.; Herranz, R.; Gálvez, N.; González-Vera, J. A.; Orte, A. Selecting FRET Pairs for Visualizing Amyloid Aggregation. *Results Chem.* **2021**, 100275.

15 Espinar-Barranco, L.; Meazza, M.; Linares-Perez, A.; Rios, R.; Paredes, J. M.; Crovetto, L. Synthesis, Photophysics, and Solvatochromic Studies of an Aggregated-Induced-Emission Luminogen Useful in Bioimaging. *Sensors (Switzerland)* **2019**, *19* (22), 1–12.

16 Fueyo-González, F.; Espinar-Barranco, L.; Herranz, R.; Alkorta, I.; Crovetto, L.; Fribourg, M.; Paredes, J. M.; Orte, A.; González-Vera, J. A. Self-Assembled Lanthanide Antenna Glutathione Sensor for the Study of Immune Cells. *ACS Sensors* **2022**.

INTRODUCTION

Health maintenance is one of the most laudable technological goals challenging science and technology. In this sense, an important support to improvement society health maintenance is the biomedical diagnostics. These detection tools are essential requirements for effective disease treatment and prevention. In this respect, biosensors are a key element in disease detection and monitoring[1,2].

Sensor, from the Latin *sentio* = to sense, refers to an analytical device capable of converting a biological response that origin a physical or chemical signal into a measurable signal[3] that can then be processed to detect biomolecules or to obtain the concentration of an analyte[4]. Biosensors have multiple applications, some of them include the detection of biomarkers, drug targets, multiple analytes or even cellular environments, among others. Since the publication of the first example of an enzymatic electrochemical biosensor for glucose detection by Professor Leland C. Clark in the 1960s, great progress has been made in this field of research[2,5]. Today, a classification can be made according to the method of signal transduction: optical, electrochemical, thermometric, piezoelectric or magnetic, where optical biosensors are the most diverse and best known class[6].

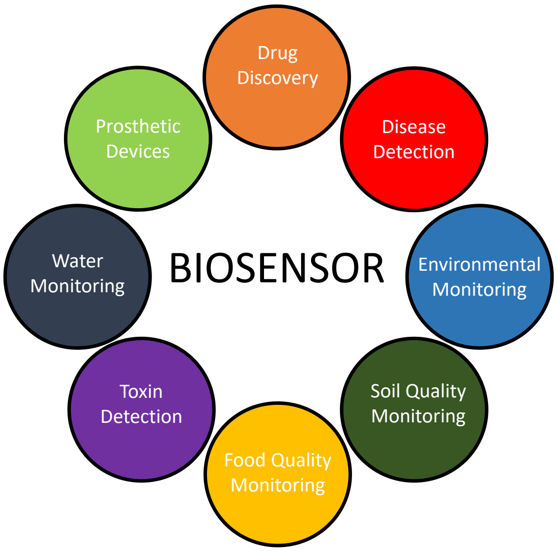

Figure 1.1. Main application areas of biosensors.

Optical detection is performed by exploiting the interaction of the electromagnetic field with a biorecognition element, which at the same time, can be divided into two general types: in the presence or absence of an external label. In the first strategy, detection involves the use of a label and the optical signal is then generated by a colorimetric, or luminescent method[6]. These methods allow the detection of analytes on the basis of absorption, fluorescence or light scattering, and the possible simultaneously detection of multiple analytes using different monitoring wavelengths. Furthermore, the use of optical fibres in these methods allow *in vivo* application. It exists different types of spectroscopies such as absorption, fluorescence, phosphorescence, Raman, SERS, refraction and scattering spectrometry. Among the wide variety of biosensors currently available, fluorescence spectroscopy is one the most common optical methods. A fluorescence-based device allows individual molecules to be repeatedly excited and detected to produce a bright signal that is easily measured even at the single-cell level[1].

1.1 FLUORESCENT BIOSENSORS

Fluorescent tools have released biological research into a new domain of understanding cellular processes and dynamics at the single-cell level[7]. Among the existing biosensing and bioimaging techniques, fluorescence is one of the most popular as it allows direct investigation of biological samples and provides extensive information at the biomolecular level with high spatial and temporal resolution[8]. It allows us to characterise the heterogeneity of biological systems that cannot be adequately reflected by techniques based on large-scale analysis of cell populations. Fluorescent sensors increasingly provide information on what might once have been called "dark matter" in the cellular environment: small molecules, secondary metabolites, metals and ions. They enable us to probe global changes in cellular state that are not well captured by any single molecular indicator, such as membrane potential and cell division. They can also be used to probe gene expression, protein localisation and conformation in fields such as signal transduction, transcription, cell cycle and apoptosis[9]. They can be used to target numerous diseases such as inflammatory, cardiovascular and neurodegenerative diseases, arthritis, viral infections, cancer and metastasis[7]. Since biological objects fluoresce poorly, current fluorescence techniques are largely based on the use of extrinsic fluorescent dyes, proteins and nanoparticles. The first of these being particularly important because of their small size, precise tuning of their physical, chemical and photophysical properties and chemical modification. When dyes are specially designed as tools in biodetection or bioimaging, they are called fluorescent molecular probes and can specifically target biomolecules, cell organelles, or allow detection and imaging of metal ions, pH, etc[8]. For example, monitoring the 5(6)-carboxy-fluorescein fluorescence has been extensively for virus quantification in real-time polymerase chain reaction (PCR) testing. Due to its high sensitivity, PCR tests have been considered the reference technique in SARS-CoV-2 diagnosis[10].

Fluorescent biosensors, therefore, are unmasking agents that base their action on this phenomenon, produced when electromagnetic radiation is absorbed by a fluorophore or a fluorescently labelled molecule and that energy is converted into fluorescence emission. They typically include an excitation light source (LEDs (light emitting diodes), lasers), a receptor attached to one or more fluorescent probes (enzymatic, chemical or genetic) and a photodetector. The receptor identifies a specific analyte or target and transduces a fluorescent signal that can be easily detected and measured. Typically, this signal is biorecognised using the following techniques (Figure 1.2): FRET (Förster resonance energy transfer), FLIM (fluorescence lifetime imaging microscopy), FCS (fluorescence correlation spectroscopy) or IF (fluorescence intensity changes). Today, breakthroughs in these techniques have revolutionised biology by increasing the resolution of optical microscopy capable of providing non-invasive observation methods[7,11]. Due to the multi-parameter nature of fluorescence, any aspect can be explored, such as fluorescence intensity, anisotropy, fluorescence lifetime, energy transfer (radiative or non-radiative) and/or quantum yield[12].

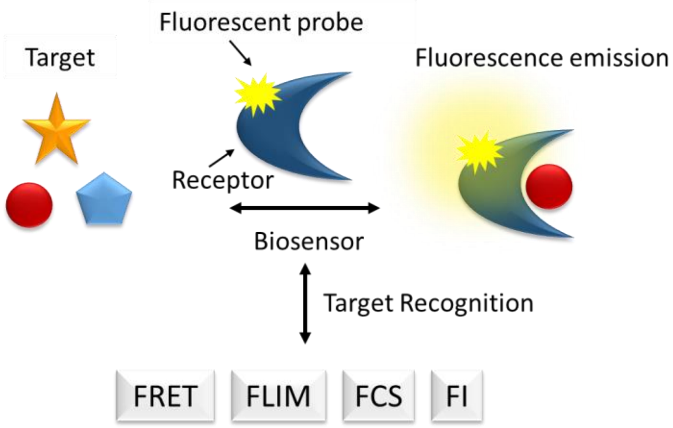

Figure 1.2. Schematic of a fluorescence-based biosensor.

The fluorescent probe attached to the target receptor can be either a fluorophore (small molecules, proteins, quantum dots) or a labelled molecule (nucleic acids, lipids)[11]. In a general way, fluorophores can be divided into intrinsic or endogenous and extrinsic. The first are those that are present naturally, such as the indole group of the dominant tryptophan in proteins with absorption near 280 nm and emission at 340 nm[13,14]. They can operate by different strategies such as "on/off" or an increase in emission upon reaction/interaction with their target, the latter being known as fluorogenic sensors[3,15]. Table 1.1 represents the main intrinsic or endogenous fluorophores and their corresponding excitation and emission wavelengths.

Representative Endogenous Fluorophores

fluorophore	excitation (nm)	emission (nm)	lifetime (ns)
NAD(P)H	310 – 370	410 – 510	0.3
flavine	380 – 500	500 – 600	5.2
collagen	270 – 370	305 – 450	5.3
elastin	300 – 370	420 – 460	2.0
lipofuscin	410 – 470	500 – 695	1.3
tryptophan	280 – 340	300 – 400	2.6
tyrosine	273 (max)	303 (max)	3.6
phenylalanine	258 (max)	280 (max)	7.5
melanin	340 – 400	440, 520, 570	0.1/1.9/8.0

Table 1.1. Main endogenous (intrinsic) fluorophores[14].

On the other hand, extrinsic fluorophores are those that are added to a sample that does not exhibit the desired spectral properties[13]. In addition, detection be carried out by (i) direct or (ii) indirect interaction of the fluorophore with the analyte. In indirect detection the sensors are conjugates in which the fluorophore(s) is/are attached to the molecule that specifically binds to the target biomolecule, without direct involvement of the fluorophore in the binding process. They are usually the most common because most biomolecules are not fluorescent, such as nucleic acids or lipids, and their design allows a high degree of flexibility[3]. Within these indirect detection sensors, we can distinguish between those based on genetically encoded proteins and extrinsic fluorophores.

1.2 LUMINESCENT PROBES

Luminescence, from the Latin *lumen* = light[16], refers to the phenomenon of light production after excitation that does not lead to an increase in temperature, by any method. Luminescence phenomena are very diverse and can be observed in both natural and artificial materials[17,18] establishing their classification according to the mode of excitation. We can differentiate among photoluminescence (light absorption - photons), cathodoluminescence (cathode rays - electron beam), radioluminescence (ionising radiation - X, α, β, γ-rays) and the phenomenon of thermoluminescence (heating by pre-stored energy - radioactive irradiation)[16]. However, we can also find other forms of luminescence when the mode of excitation is not ionising radiation. These include chemiluminescence (chemical process), electroluminescence (electrical energy), triboluminescence (frictional and electrostatic forces), sonoluminescence (ultrasound) and bioluminescence (biochemical process)[16,17].

Luminescent probes used in biomedicine are based on photoluminescent processes, in which a molecule absorbs a photon by exciting one of its electrons to a higher electronic state, and irradiates it upon returning to a lower energy state[19]. The main difference between these photoluminescent phenomena lies in their emission time or fluorescence lifetime (τ), the average time it takes for a fluorophore to return to its ground state from the excited[13]. This is an intrinsic property of each fluorophore and therefore independent of the measurement method. It could be considered as a state function because it also does not depend on the initial perturbation conditions, the excitation wavelength, the exposure time to the light source, mono- or multiphoton excitation, and is not affected by photobleaching. Moreover, it is independent of fluorescence intensity and fluorophore concentration. Being related to an energetically unstable state, it is sensitive to a wide variety of internal factors defined by the fluorophore structure, and to external factors such as temperature, polarity and the presence of quenchers or fluorescence deactivators. The combination of environmental sensitivity and parametric independence makes this property an ideal complement to molecular imaging.

The ability to monitor changes in the fluorescence lifetime of a probe provides an enormous advantage for imaging dynamic cellular events. It allows us to monitor functional changes that may be caused by environmental factors, as well as to eliminate background fluorescence and improve image contrast[20,21]. The fluorescence lifetime range is different among the most common fluorescent compounds, of natural and synthetic origin, used in lifetime imaging. In general, fluorophores with shorter lifetimes are characteristic of weak emitters and those with longer lifetimes tend to have a low photon turnover rate. These are generally less attractive for lifetime imaging because they have limited sensitivity and require longer exposure and acquisition time. Fluorescent compounds with shorter lifetimes include endogenous fluorophores, organic molecules, fullerenes and fluorescent proteins. Nanotubes, quantum dots and pyrenes have considerably long lifetimes between 10 - 100 ns, while organometallic complexes and luminescent lanthanides are the fluorophores with the longest lifetime (µs - ms)[21].

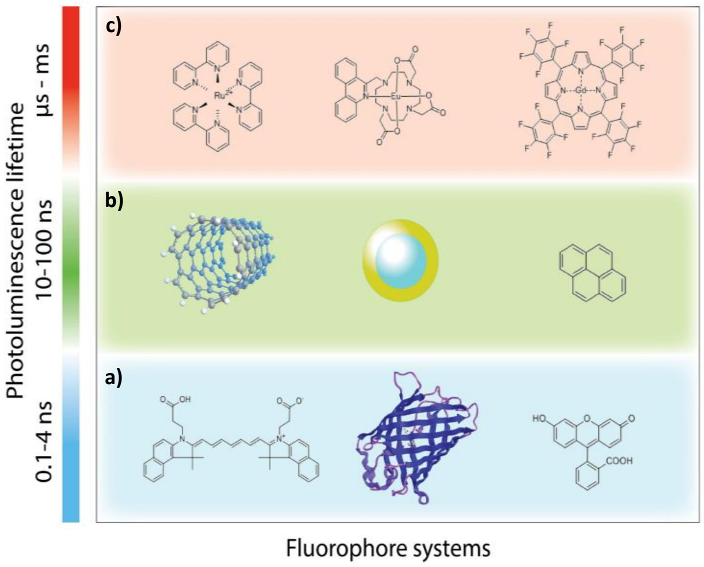

Figure 1.3. Fluorophore systems commonly used for lifetime imaging and the range of their photoluminescence lifetimes. (a) Indocyanine green, GFP and Fluorescein. (b) Nanotube structures, quantum dots and the organic molecule pyrene. (c) Organometallic (ruthenium) and lanthanide (europium) complexes[22].

In order to increase the quality of the lifetime images, interference from autofluorescence in the sample must be kept to a minimum. This requires that probes used have sufficiently long fluorescence lifetimes compared to the autofluorescence generated by the biological samples. At times, the detection of a specific analyte at low concentration or a less common event by standard fluorescence microscopy and analysis techniques, may be hampered by the presence of naturally occurring fluorescent substances. In this case, the use of time gate luminescence (TGL) technique offers a very effective approach. The probe, which should have relatively long luminescence times, is excited by a pulsed light source. The detector, in turn, will remain in the off-state until short duration signals (<1µs) disappear and only long duration events can enter the signal collection window. These signals are therefore distinguished from unwanted short-duration noise in the time domain, although their intensity is weak, allowing a considerable increase in detection accuracy and sensitivity[14,23].

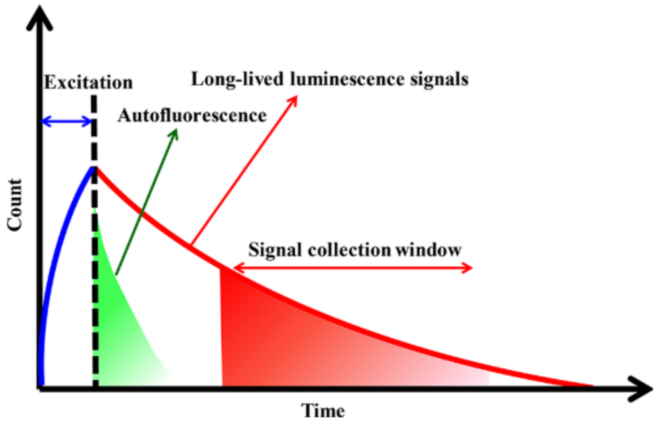

Figure 1.4. Principle of the time-gate luminescence (TGL) technique to suppress autofluorescence.

Luminescence techniques have converted the study of biological systems, enabling visualization of molecular events with extraordinary sensitivity and selectivity[24]. Long luminescence times offer a huge advantage, therefore, for time gate detection of biological samples (as in time-resolved luminescence microscopy) where short-lived autofluorescence and light scattering are suppressed, drastically improving the signal-to-noise ratio and greatly increasing the overall sensitivity of the probe. In this regard, lanthanides and transition metal complexes are known for their long times due to the forbidden spin nature of their luminescence[25,14]. Table 1.2 lists the lifetime intervals of the main groups of long-lived luminophores[14].

Long-lifetime luminophores

Luminophores	Lifetimes
Lanthanide chelates	µs – ms
Lanthanide-doped nanocrystals	µs – ms
Transition-metal complexes	hundreds ns – µs
2,3-diazabicyclo[2.2.2]oct-2-ene	Up to 1 µs
Aza/oxa triangulenium compounds	20 ns
Organic compounds with delayed fluorescence	hundreds ns – µs
QDs doped with Mn or In	µs
Thiol-capped metal nanoclusters	µs
Nanodiamonds	> 10 ns
Silicion nanoparticles	> 10 ns
Persistent phosphors	> 1 s

Table 1.2. Main groups of long-lifetime luminophores and their luminescence lifetime.

1.2.1 LANTHANIDE-BASED LUMINESCENT PROBES

Since the appearance of the first responsive luminescent, lanthanides based-probes have emerged as powerful chemical tools for cellular imaging revolutionizing the field of chemical biology[26]. Lanthanides luminophores have been released as biological probes thanks to technological developments and innovations in probe design, instrumentation and imaging modalities have increased interest in these rare-earth metals[27]. Furthermore, the considerable interest of these bioprobes in clinical diagnosis and life sciences[14] as emissive species in luminescent sensors is due to their unique photophysical qualities and coordination chemistry[26] that include millisecond scale luminescence lifetimes, large Stokes shifts of several hundred nanometers, and the ability to undergo resonance energy transfer or photon up conversion[27]. The long-lived luminescence of lanthanides enables eliminating interferences from scattered light and autofluorescence, and the quantitative determination of the intracellular concentration of an analyte through specific filtering time gates. Their narrow emission bands which span both the visible and NIR ranges do not overlap, enabling the simultaneous use of different lanthanide probes without crossinterference to quantitatively detect several analytes[24,26,28]. This feature is potentially useful in multiplex experiments that require simultaneous monitoring of more than one spectroscopic signal that along with imaging depth lead to these probes to obtain information of biological systems in a new way[24,27]. The first approach of this bio-applications started in the mid-1970s when Eu^{3+}, Sm^{3+}, Tb^{3+} and Dy^{3+} polyaminocarboxylates and β-diketonates were proposed as luminescent sensors for time-resolved luminescent (TRL) immunoassays[28,29]. Currently, the more sensitive enzyme amplified lanthanide luminescence assay (EALL) can compete with the established enzyme-linked immunosorbent assay (ELISA) widely used, and they have also found commercial use in DNA assays[26]. Lanthanide-based probes have been also applied to the detection of reactive oxygen species (ROS), pH, intracellular analytes, such as ATP[30].

Lanthanides comprise the fourteen elements from cerium to lutetium and present strong chemical similarities, as the +3-oxidation state is the most stable for all lanthanide cations in aqueous solution[31] (with the exception of Ce^{4+} and Eu^{2+})[32], a clear predilection for hard donor ligands (preferentially oxygen), and high coordination numbers (usually higher than six) with little stereochemical preferences[24]. The luminescence emission of lanthanides covers from UV (Gd^{3+}) to visible (Tb^{3+}, Dy^{3+}, Sm^{3+}, Eu^{3+}) and near-infrared (Yb^{3+}, Dy^{3+}, Pr^{3+}, Sm^{3+}, Ho^{3+}, Er^{3+}, Tm^{3+}, Nd^{3+}) regions. Among visible lanthanide ions, the most popular metals along with the order of brightness for lanthanide luminescence are $Eu^{3+} > Tb^{3+} > Sm^{3+} > Dy^{3+}$. Their intrinsic luminescence arises from f-f electron transitions in the 4fn shell of the [Xe]$5s^25p^6$ configuration. Due to the excited 4f states are shielded by the filled $5s^2$ and $5p^6$ orbitals of Ln^{3+} and do not participate in chemical bonding, the electrons involved in the transitions are protected from the environment (solvent molecules, ligands, anions) and thus minimally perturbed by the ligand field[42,46,40]. As a result, lanthanide ions exhibit very sharp absorption and emission bands, usually in the orders of tens of nm (in comparison with the wide emission bands of transition metal complexes or organic fluorophores that often extend over 100 nm)[29] and their narrow bandwidths are easily distinguishable. The line-like emissions in the visible range of Tb^{3+} at 490, 540, and 580 nm and Eu^{3+} at 590, 610, and 720 nm make them very useful as imaging probes[33]. Moreover, the forbidden nature of the 4f – 4f transitions by the spin and Laporte rules results in the slow decay of lanthanide excited states which translates into long-excited lifetimes, in the millisecond range for Tb^{3+} and Eu^{3+} (0.5 to 2.5 ms, respectively) and the microseconds for Sm^{3+} and Dy^{3+}, while the lifetimes of most organic dyes are in the order of nanoseconds[24,25].

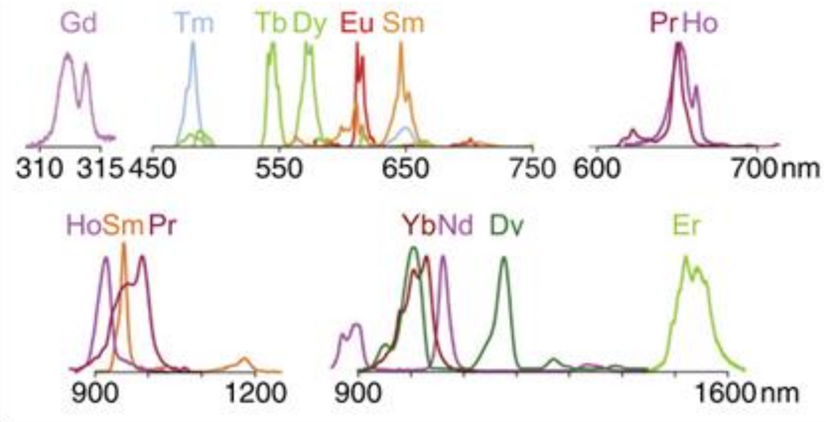

Figure 1.5. Emission spectra of different trivalent lanthanide ions[42].

A second consequence of the disallowed f–f electronic transitions is the weak absorption of the Ln^{3+} with extinction coefficients several orders of magnitude lower than those of commonly used fluorophores (1 – 5 M^{-1} cm^{-1} versus 10,000 to 100,000 M^{-1} cm^{-1}) which make the direct excitation of these cations impractical cause requires light intensities that are destructive to biological samples[24,25,27,31]. However, this drawback can be overcome via the advantage of Förster resonance energy transfer[34] through an indirect excitation mechanism called “sensitization” or “antenna effect” between nearby organic fluorophores and the lanthanide ion. It was Weissman in 1942 who observed that the photoluminescence of Eu^{3+} could be greatly increased in the presence of some organic aromatic ligands concluding that the excitation was a multistep process with absorption of the ligands and energy transfer to Eu followed by its emission. This mechanism in which heteroaromatic ligands are designed to coordinate to the lanthanide cations emitters is highly sensitive to changes in the immediate surroundings of the metal ion or the antenna and establishes the basis of most applications of lanthanide luminescence in sensing strategies[24,31].

Europium, terbium and samarium are commonly used in time-resolved luminescence assays since they can be excited by energy transfer using a variety of organic chromophores and emit efficiently in the visible. The antenna chromophores absorb energy from UV-visible radiation (300 to 400 nm) and transfer it to the lanthanide ion[27] in a sensitization process highly complex that involves different energy levels from both the donor fluorophore and the accepting metal ion. The lowest triplet state of the antenna is achieved by intersystem crossing (ISC) after the initial S_1 state upon its excitation and the coupling between the donor and the acceptor is followed by various mechanisms, as through-bond energy transfer (Dexter mechanism)[35] and intramolecular energy transfer (Förster mechanism)[36] between the dipole moment of the T_1 state of the antenna and the 4f orbitals in the acceptor lanthanides[24,26]. Then, the latter emits light in the visible range: 545 nm in the case of Tb and 611 to 618 nm for Eu.

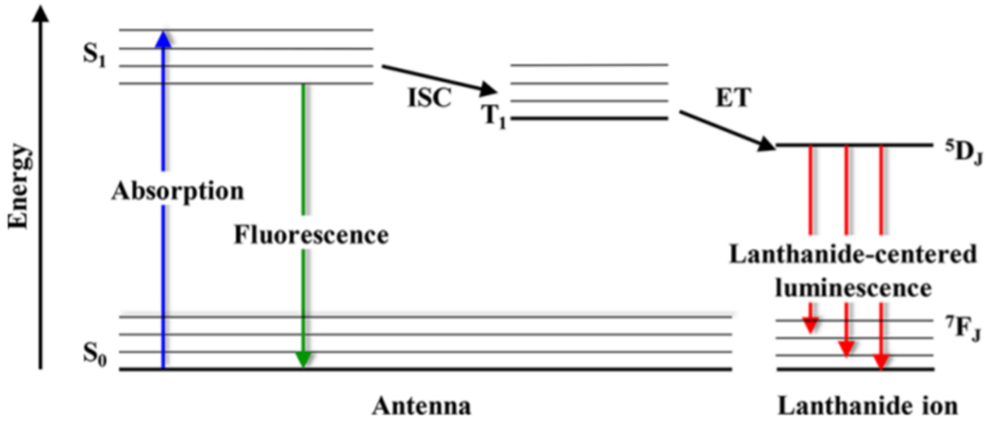

Figure 1.6. Jablonski diagram sensitization[26].

The quantum yield of sensitized lanthanide luminescence is reliant of four summary parameters as can be seen from the Jablonski diagram (Figure 1.6):

I. The efficiency to populate the triplet excited state of the antenna.

II. The energy between the T_1 state of the antenna needs to be higher with respect to the ^5D excited state of the lanthanide ion for the intramolecular energy transfer to occur. Considering that similar energy in both states can produce back energy transfer (BET) from the lanthanide to the antenna decreasing the lanthanide emission.

III. The efficacy of Förster energy transfer which follows an r^6 dependence on the distance between the antenna and lanthanide ion.

IV. The number of coordinated water molecules in the coordination sphere of the lanthanide to avoid the quenching of luminescence induced by the H_2O reducing its quantum yield[26].

As the endpoint indicates, the excited states of lanthanide cations are very sensitive to quenching by water molecules[37] and this luminescence extinction effect could be avoided by the formation of chelates, in order to reduce the number of water molecules coordinated to the lanthanide ion center, q, which strongly influences its emission. This parameter is quantified by the luminescence lifetimes in H_2O and D_2O and the intrinsic properties (A and B) of the Ln^{3+}:

$$q = A\,(1 / \tau_{H2O} \; - 1 / \tau_{D2O} - B)$$

Through coordinate saturation or steric crowding of the metal center, chelates attenuate solvent quenching and increment its quantum yield. Moreover, this strategy is typically used for biological imaging to minimize the toxicity of free lanthanide ions. In consideration of the hard acid character of the Ln^{3+} hard bases are commonly used as chelating ligands, such as carboxylic acids, amides, and pyridines, being EDTA (ethylenediaminetetraacetic acid) and NTA (nitrilotriacetate) one of the first discovered chelates in avoid aqueous quenching[42,40]. Since then, the most widely ligands utilized for luminescent applications include linear polyaminocarboxylates such as DTPA (diethylenetriaminepentaacetic acid) derivatives and azacrown macrocycles with one or more carboxamide pendant arms to insert the antenna probe. These last could be cyclen as DO3A (1,4,7,10- tetraazacyclododecane-1,4,7-triacetic acid) and DOTA (1,4,7,10-tetraazacyclododecane-1,4,7,10-tetraacetic acid) or cyclam derivatives as TETA (1,4,8,11-tetraazacyclotetradecane-1,4,8,11-tetraacetic acid) chelators[24,30]. The complexes chelated are stable and kinetically inert providing an important property for their *in vivo* use[31,38]. This is evidenced by Gd(DTPA), used as an NMR contrast imaging agent, which is 50 times less toxic than $GdCl_3$ on a molar basis[32].

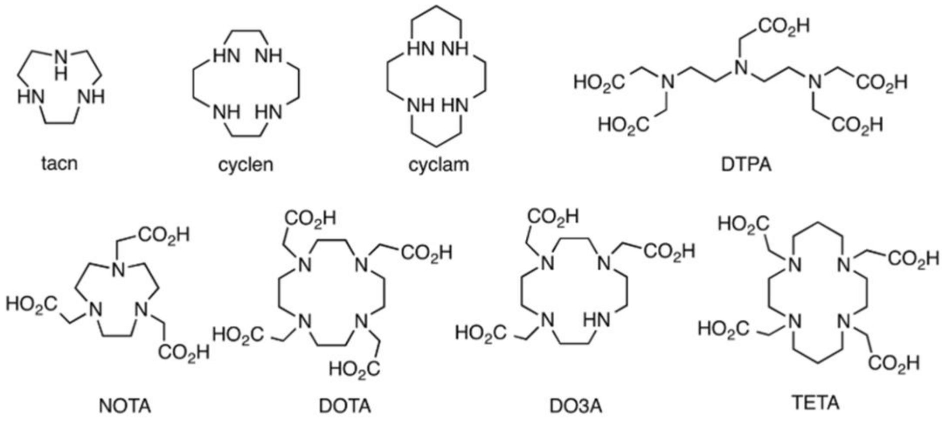

Figure 1.7. Structures of common lanthanide chelators[24].

Therefore, the most common luminescent lanthanide probes covalently link to a chelating group through a linker or spacer, referred as a pendant antenna, which sensitize through Förster resonance energy transfer the Ln^{3+}. Pendant antenna usually consists in derivatives of existing organic probes, such as azaxanthone, phenanthridine, and tetracycline which are among the main sensitizers of Eu^{3+} and Tb^{3+} used in time-resolved luminescent bioassays and cellular imaging. The efficiency of the sensitization (as bright emission) requires optimization of the distance between the antenna and the trivalent lanthanide ion and, and in that sense, the process can be improved by increasing the number of pendant antennas linked to a single chelate, or by decreasing the length of the[25]. In that sense, an alternative approach involves the use of chromophores acting simultaneously as sensitizers and protective chelates, named chelating antennas or cryptates[33]. In this case, the sensitization of the lanthanide ion is produced by both the Förster and Dexter mechanism. Some of the reported lanthanide complexes with chelating antenna developed for biological applications are based on the IAM (2-hydroxyisophthalamide) and 1,2-HOPO (1-hydroxy-pyridine-2-one) as a binding unit to sensitize Tb^{3+} and Eu^{3+}, respectively[39].

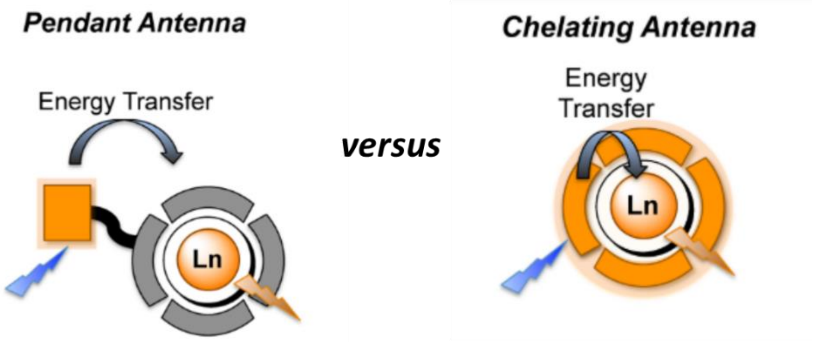

Figure 1.8. Strategy of pendant antenna in contrast with chelating antenna.

The usefulness of antenna/lanthanide systems as biosensors is determined by the ability of the analytes to modulate their luminescence, which will be produced through different strategies. a) Modulating luminescence by modifying the antenna/lanthanide distance by inducing conformational changes in the spacer between the antenna and the lanthanide or by affecting their binding. b) Modulating luminescence by modifying the number of H_2O molecules in the coordination sphere through their displacement. c) The analyte can act directly as an antenna and coordinate the lanthanide. d) Modulating luminescence by inducing chemical changes in the antenna, which modify its photophysical properties and thus its behaviour as sensitizer. e) Modulating luminescence by the presence of groups capable of modifying the energy transfer of the antenna by photoinduced electron transfer (PET) due to the presence or absence of an analyte[26].

BIBLIOGRAPHY

1 Bachas-Daunert, S.; Dikici, E.; Deo, S. Biosensors: Design and Applications. *Encycl. Agric. Food, Biol. Eng. Second Ed.* **2010**, 1–11.

2 Bhalla, N.; Jolly, P.; Formisano, N.; Estrela, P. Introduction to Biosensors. *Essays Biochem.* **2016**, 60–61.

3 Pazos, E.; Vázquez, O.; Mascareñas, J. L.; Vázquez, M. E. Peptide-Based Fluorescent Biosensors. *Chem. Soc. Rev.* **2009**, *38*, 3348–3359.

4 Chen, C.; Wang, J. Optical Biosensors: An Exhaustive and Comprehensive Review. *Crit. Rev. Cite this Anal.* **2020**, *145*, 1605.

5 Bolella, P.; Katz, E. Biosensors — Recent Advances and Future Challenges. *Sensors* **2020**, *20* (22), 6645.

6 Damborský, P.; Svitel, J.; Katrlík, J. Optical Biosensors. *Essays Biochem.* **2016**, *60*, 91–100.

7 Mehrotra, P. Biosensors and Their Applications - A Review. *J. Oral Biol. Craniofacial Res.* **2016**, *6* (2), 153–159.

8 Klymchenko, A. S. Solvatochromic and Fluorogenic Dyes as Environment-Sensitive Probes: Design and Biological Applications. *Acc. Chem. Res.* **2017**, *50* (2), 366–375.

9 Specht, E. A.; Braselmann, E.; Palmer, A. E. A Critical and Comparative Review of Fluorescent Tools for Live-Cell Imaging. *Annu. Rev. Physiol* **2017**, *79*, 93–117.

10 a) Wang, J.; Zhang, L.; Li, Z. Aggregation-Induced Emission Luminogens with Photoresponsive Behaviors for Biomedical Applications. *Advanced Healthcare Materials*. 2021. b) Perng, C.; Jian, M.; Chang, C.; Lin, J.; Yeh, K.; Chen, C.; Chiu, S.; Chung, H.; Wang, Y.; Liao, S.; et al. Novel Rapid Identi Fi Cation of Severe Acute Respiratory Syndrome Coronavirus 2 (SARS-CoV-2) by Real-Time RT-PCR Using BD Max Open System in Taiwan. *PeerJ* **2020**, *2*, 1–12.

11 Chen, Y. T.; Lee, Y. C.; Lai, Y. H.; Lim, J. C.; Huang, N. T.; Lin, C. T.; Huang, J. J. Review of Integrated Optical Biosensors for Point-Of-Care Applications. *Biosensors* **2020**, *10* (12), 1–22.

12 Sharma, A.; Khan, R.; Catanante, G.; Sherazi, T. A.; Bhand, S.; Hayat, A.; Marty, J. L. Designed Strategies for Fluorescence-Based Biosensors for the Detection of Mycotoxins. *Toxins (Basel).* **2018**, *10* (197).

13 Lakowicz, J. R. *Principles of Fluorescence Spectroscopy*, Springer.; New York, 2006.

14 Zhang, K. Y.; Yu, Q.; Wei, H.; Liu, S.; Zhao, Q.; Huang, W. Long-Lived Emissive Probes for Time-Resolved Photoluminescence Bioimaging and Biosensing. *Chem. Rev.* **2018**, *118* (4), 1770–1839.

15 Li, C.; Tebo, A. G.; Gautier, A. Fluorogenic Labeling Strategies for Biological Imaging. *Int. J. Mol. Sci.* **2017**, *18* (7), 1473.

16 Valeur, B. *Molecular Fluorescence. Principles and Applications*, Wiley-VCH.; Weinheim, 2002.

17 Girigoswami, K.; Akhtar, N. Nanobiosensors and Fluorescence Based Biosensors: An Overview. *Int. J. Nano Dimens.* **2019**, *10* (1), 1–17.

18 Shinde, K. N.; Dhoble, S. J.; Swart, H. C.; Park, K. *Phosphate Phosphors for Solid-State Lighting*, Springer-V.; Berlin, Heidelberg, 2012.

19 Munson, C. A.; Gottfried, J. L.; De Lucia, F. C.; McNesby, K. L.; Miziolek, A. W. Laser-Based Detection Methods of Explosives; Elsevier B.V., **2007**, pp 279–321.

20 Chen, Y.; Periasamy, A. Characterization of Two-Photon Excitation Fluorescence Lifetime Imaging Microscopy for Protein Localization. *Microsc. Res. Tech.* **2004**, *63* (1), 72–80.

21 Berezin, M. Y.; Achilefu, S. Fluorescence Lifetime Measurements and Biological Imaging. *Chem. Rev.* **2010**, *110* (5), 2641–2684.

22 Sarder, P.; Maji, D.; Achilefu, S. Molecular Probes for Fluorescence Lifetime Imaging. *Bioconjug. Chem.* **2015**, *26*, 963–974.

23 Connally, R. E.; Piper, J. A. Time-Gated Luminescence Microscopy. *Ann. N. Y. Acad. Sci.* **2008**, *1130*, 106–116.

24 Pazos, E.; Vázquez, M. E. Advances in Lanthanide-Based Luminescent Peptide Probes for Monitoring the Activity of Kinase and Phosphatase. *Biotechnol. J.* **2014**, *9* (2), 241–252.

25 Heffern, M. C.; Matosziuk, L. M.; Meade, T. J. Lanthanide Probes for Bioresponsive Imaging. *Chem. Rev.* **2014**, *114* (8), 4496–4539.

26 Thibon, A.; Pierre, V. C. Principles of Responsive Lanthanide-Based Luminescent Probes for Cellular Imaging. *Anal. Bioanal. Chem.* **2009**, *394* (1), 107–120.

27 Cho, U.; Chen, J. K. Lanthanide-Based Optical Probes of Biological Systems. *Cell Chem. Biol.* **2020**, *27* (8), 921–936.

28 Bünzli, J. C. G. Lanthanide Luminescence for Biomedical Analyses and Imaging. *Chem. Rev.* **2010**, *110* (5), 2729–2755.

29 Bünzli, J.-C. G.; Eliseeva, S. V. Basics of Lanthanide Photophysics; 2010; pp 1–45.

30 Peterson, K. L.; Dang, J. V; Weitz, E. A.; Lewandowski, C.; Valérie, V.; Pierre, C. Effect of Lanthanide Complex Structure on Cell Viability and Association. *Inorg. Chem* **2014**, *53*, 6021.

31 Sy, M.; Nonat, A.; Hildebrandt, N.; Charbonnière, L. J. Lanthanide-Based Luminescence Biolabelling. *Chem. Commun.* **2016**, *52* (29), 5080–5095.

32 Fricker, S. P. The Therapeutic Application of Lanthanides. *Chem. Soc. Rev.* **2006**, *35* (6), 524–533.

33 Moore, E. G.; Samuel, A. P. S.; Raymond, K. N. From Antenna to Assay: Lessons Learned in Lanthanide Luminescence. *Acc. Chem. Res.* **2009**, *42* (4), 542–552.

34 Tremblay, M. S.; Halim, M.; Sames, D. Cocktails of Tb3+ and Eu3+ Complexes: A General Platform for the Design of Ratiometric Optical Probes. *J. Am. Chem. Soc.* **2007**, *129* (24), 7570–7577.

35 Dexter, D. L. A Theory of Sensitized Luminiscence in Solids. *J. Chem. Phys.* **1953**, *21*, 836.

36 Förster, T. 10th Spiers Memorial Lecture. Transfer Mechanisms of Electronic Excitation. *Discussions of the Faraday Society*. 1959, pp 7–17.

37 Haas, Y.; Stein, G. Pathways of Radiative and Radiationless Transitions in Europium (III) Solutions: The Role of High Energy Vibrations. *J. Phys. Chem.* **1971**, *75* (24), 3677–3681.

38 Cacheris, W. P.; Quay, S. C.; Rocklage, S. M. The Relationship between Thermodynamics and the Toxicity of Gadolinium Complexes. *Magn. Reson. Imaging* **1990**, *8* (4), 467–481.

39 Werts, M. H. V.; Jukes, R. T. F.; Verhoeven, J. W. The Emission Spectrum and the Radiative Lifetime of Eu3+ in Luminescent Lanthanide Complexes. *Phys. Chem. Chem. Phys.* **2002**, *4* (9), 1542–1548.

The principal aim of this Thesis was based in the study of new biosensors and their application in biological processes through innovative fluorescence microscopy techniques thanks to their availability in our nanoscopy laboratory. These include fluorescence microscopy, such as Fluorescence Lifetime Imaging Microscopy (FLIM) used to develop the results included in this work.

2.1 FLUORESCENCE IMAGING

Understanding the inner workings of cells and organism, which constitute complex machines led by a series of dynamic biological events closely organized in space and time, can only be achieved by observing their elements (e.g., proteins, nucleic acids, lipids, glycans, or metabolites) and how they interact[1]. Real-time monitoring or mapping of the subcellular microenvironment in a specific organelle[2] and of the levels of certain overexpressed markers often associated with disease states, known as biomarkers[3], improves the strategies for regulating biological phenomena, the early prognosis of disease status and therapeutics[4]. These characterization and quantification of biological processes at the cellular and subcellular level can be carried out by molecular imaging.

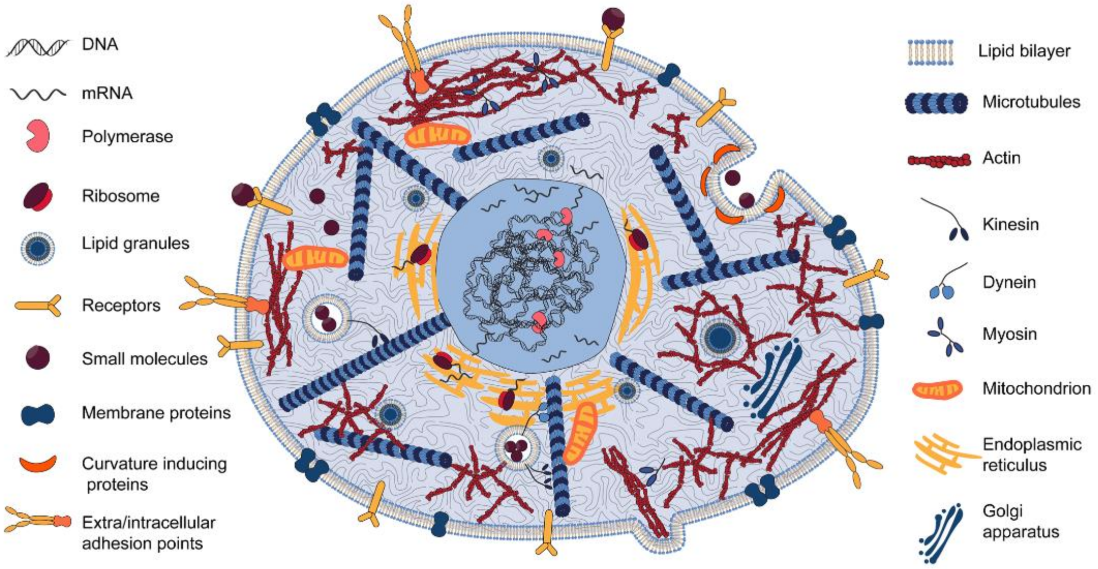

Figure 2.1. Illustration of the structure and contents of the cytoplasm of a normal living cell[5].

In the field of biological research, optical microscopy has represented a revolution among all available imaging modalities. In particular, fluorescence imaging microscopy of live cells and animals represents an essential technique to study and understand biological processes, as it allows a repetitive, non-invasive, uniform and relatively automated study[6].

Biological imaging has been improved by recent advances in optics and detectors, as well as the development of molecular fluorescent tools labelled to biomolecules[1]. On one hand, the visualization of intracellular processes or the ability to monitor changes in the concentration and distribution of key biomarkers depends largely on appropriated luminescent probes. Thus, desirable characteristics of a luminescent marker to increase the sensitivity of the detection process include a luminescence on response to specific recognition or in situ reactions with biomarkers as it translates in a favourable signal-to-noise ratio, and a fast response time[4]. On the other hand, as mentioned earlier, the progresses in optical microscopy techniques have revolutionized the way scientists can actually look at the sub-cellular world. Elegant combinations of photophysics, technical devices and mathematics have overcome the resolution limit, unavoidable for more than 100 years, giving rise to the so-called family of super-resolution microscopy techniques, also known as nanoscopy techniques. The impact of this contribution was such that its inventors Eric Betzig, W.E Moerner and Stefan Hell were awarded in 2014 with the Nobel prize in Chemistry[7]. This family of microscopy techniques allow to observe the dynamics of biomolecules in 3D at sub-second resolution and below the Abbe's diffraction limit[1]. This physical law establishes that the maximum resolution (d) achievable by a focused light beam of wavelength (λ) using an objective of NA numerical aperture is given by the expression: $d = \lambda/(2 \cdot NA)$. Hence, in conventional fluorescence microscopy, a 600-nm radiation through a NA 1.0 objective can reach a 300-nm maximum resolution. Even though detecting individual molecules or nanoparticles under a biological environment is possible thanks to advances in ultra-sensitive detection with high temporal and spatial resolution[7,8].

Research on single-molecule imaging and cell-analysis allow to explore the heterogeneity of individual cells, just as the kinetics of individual molecules in a chemical reaction can be revealed by the advances in optical microscopy techniques[5]. In contrast to conventional measurements, microscopy analysis with optical methods can provide statistical and dynamic information in situ mainly due to three points. Firstly, it allows the properties of the ensemble to be assessed from the statistics of a sufficient number of individual objects. Secondly, the spatial and temporal resolution of a single object analysis with optical microscopy is able to provide a precise relationship between structure and reactivity of molecules and nanoparticles. Finally, investigating the essence of reaction dynamics at the atomic and molecular scale is fundamental to understanding reaction pathways[9]. Single object analysis is of crucial importance, as many diseases are caused by errors at the single-molecule level, such as the mutation of a gene. As for example in the study of the DNA transcription process by polymerases, quantification with ensemble measurements (e.g., western blotting) masks the random intermittency of this continuous and linear process, and the step-by-step movement of polymerases[10,11]. Single-molecule imaging is therefore a powerful tool for elucidating native biological processes as well as the structure and dynamics of biomolecules[9,12].

2.2 FLUORESCENCE LIFETIME IMAGING MICROSCOPY (FLIM)

In the field of fluorescence microscopy, the need for dynamic technologies that can provide complete information form every pixel of an image is fulfilled by the Fluorescence Lifetime Imaging Microscopy (FLIM) technique, which offers additional information to conventional intensity-based fluorescence imaging.

Since Kusumi and co-workers were among the first to use time-resolved fluorescence imaging to study endosome fusion in single cells, calling the technique “flimscopy”[13] , FLIM has become in a powerful quantitative technique alternative to the ratiometric fluorescent methods. The multidimensional character of this technique allows mapping the spatial distribution of fluorescence intensity (total number of photons) and lifetimes within microscopic images of fixed and living cells. The fluorescence emission from molecules that have been excited by a finite light pulse shows exponential decay kinetics, with a lifetime usually in the order of several nanoseconds. The fluorescence decay time, commonly referred to as fluorescence lifetime τ can be considered as the average time that the fluorophores remain in the excited state, and in a physical sense as the time required for the fluorescence intensity to decrease to 1/e (=1/2.71) of its initial value I_0. Fluorescence lifetime is the reciprocal sum of the rate constants of all possible departure paths from the excited state defined as:

$$\tau = \frac{1}{k_r + k_{nr}}$$

where k_r corresponds to the radiative rate constant, and k_{nr} the non-radiative rate constant[14,15,16].

FLIM is a time-resolved image acquisition method that can operate in two technological categories: confocal scanning or multiphoton excitation where the image is acquired pixel-by-pixel by a non-imaging detector, e.g., a photomultiplier, and wide-field camera-based FLIM[15]. Also, the time-resolved information can be obtained in the time-domain or in the frequency-domain. In the first case, the sample is excited with a short optical pulse and observing the decay of the fluorescence intensity (with time-correlated single photon counting (TCSPC), gating, or a streak camera), in the second option the excitation source and/or detector is modulated to calculate the fluorescence decay time from the demodulation and the phase shift of the fluorescence. This uses the same 'heterodyne' principle as in a radio[16]. FLIM has also been combined with techniques such as fluorescence correlation spectroscopy (FCS)[17], scanning near-field optical microscopy (SNOM)[18], atomic force microscopy (AFM)[19], fluorescence recovery after photobleaching (FRAP)[19] among others.

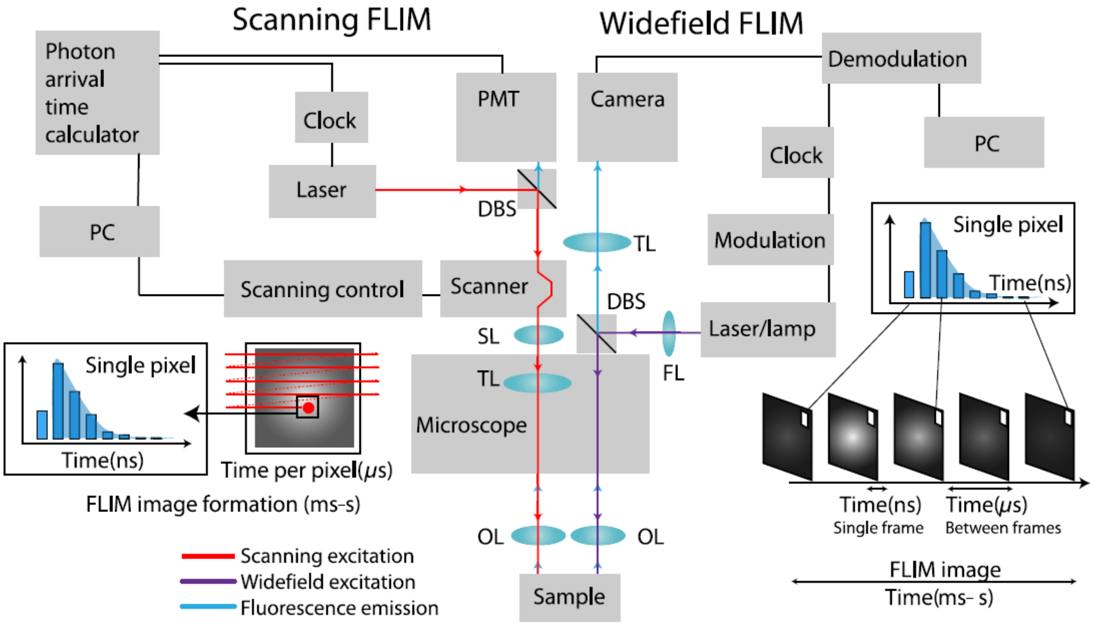

Figure 2.2. Schematic showing FLIM implementation in scanning and wide-field configurations[20].

In the time-domain FLIM by time-correlated single photon counting (TCSPC) it is measured the time between the sample excitation by a pulse laser and the arrival of the emitted photon at the detector. TCSPC requires a defined "start" signal, provided by the electronics steering the laser pulse or a photodiode, and a defined "stop" signal, realized by detection with single-photon sensitive detectors (e.g., Single Photon Avalanche Diodes, SPADs). The measurement of this time delay is repeated many times to account for the statistical nature of the fluorophore emission. The emission of a fluorescence photon from a fluorophore does not occur at a fixed time (black arrows). Instead, it is observed some moment distribution that can be described by an exponential decay function. The time constant characteristic of the decay is the time fluorescence. The delay times are sorted into a histogram that plots the occurrence of emission over time after the excitation pulse.

TCSPC is an excellent technique in the detection of low-level light signals providing a high precision and picosecond-time resolution with a potential photon efficiency. Moreover, the ability to resolve complex decay profiles and its tolerance to dynamic changes in the fluorescence decay parameters during the acquisition constitute some of the main advantages offered by this technique in lifetime imaging of biological systems[21,22].

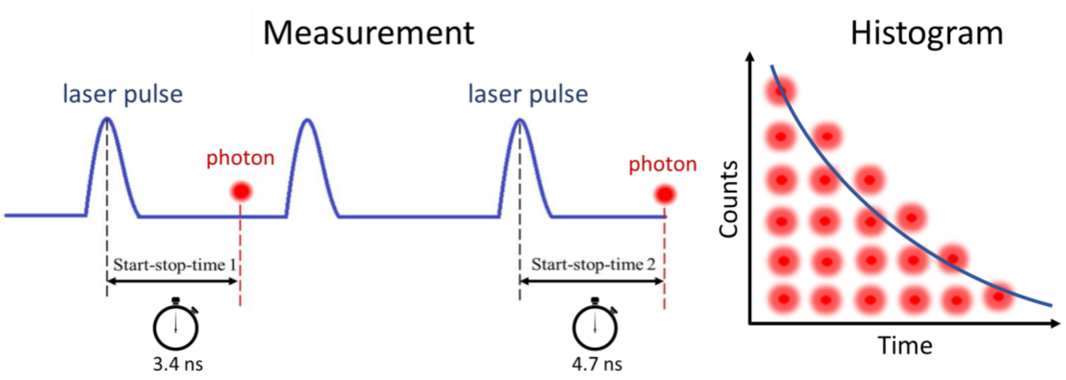

Figure 2.3. Scheme of Time-Correlated Single Photon Counting (TCSPC) procedure[23].

As mentioned above, FLIM represents an excellent alternative to fluorescence ratiometric measurements due to the advantages of the fluorescence lifetime, such as the independence of the fluorophore concentration and the excitation power, and the possibility of setting temporal filters for photon sorting. The latter is particularly interesting to discriminate photons emitted by the cell autofluorescence from photons emitted by fluorescent sensors displaying a long lifetime. This feature provides filtering tools to obtain the signal exclusively from the fluorescent sensor, avoiding interferences from the cell[24,25]. In addition, it also allows differentiating spectrally similar probes with the same detector. Furthermore, at moderate levels of photobleaching, lifetime measurements remain generally insensitive. However, the sensitivity of fluorophore lifetime to its local environment, such as the refractive index of the medium, changes in viscosity, pH, polarity, ions, temperature, etc. makes FLIM a robust and quantitative method without compromising the cell in biochemical assays. This feature forms the basis for mapping how the lifetime of a fluorophore is spatially distributed in relation to changes in its environment, thus providing information about biomolecules structure or status[14,16].

2.2.1 FLIM MICROSCOPY IN LOCAL ENVIRONMENT SENSING

FLIM measurements allow to determine how long a fluorophore remains in the excited energy state, which depends on the type of the molecule, its conformation and changes in its chemical and biological microenvironment. In general, the fluorescence lifetime can be affected by the local viscosity, pH, hydrophobic regions, polarity, temperature or refractive index, as well as interactions with other molecules. FLIM can provide information about the location of the fluorescent label or labelled protein. This ability to report on the environment of a fluorophore constitutes this imaging acquire technique as a powerful tool for cellular imaging studies, such as measurements of intracellular structure and function, metabolic, and protein-protein distances[16,26,27]. Therefore, the fluorescence lifetime information can be used in the following ways:

i. Physical parameters sensing

Temperature is one of the physical parameters of the environment that has been detected thanks to a combination of advances in FLIM and the development of temperature-sensitive polymers. These fluorescent polymeric thermometers suffer changes in their fluorescence lifetime near physiological temperature at 37 °C allowing to map temperature in different organelles of living cells. Thus, the results showed that the cytoplasm is one degree below the nucleus temperature depending on the cell cycle, as well as the thermogenesis observed in the mitochondria due to the cellular respiration[28]. Fluorescence decay measurements also allow to determinate the refractive index (n) of a fluorophore environment, because the radiative rate constant, kr, is a function of n. This effect has been used to measure fluorescence decay of GFP-tagged proteins, with proteins located in the cell membrane showing a faster decay than those in the cytoplasm due to higher refractive index of the membrane[29].

The FLIM technique has also been used to measure local viscosity through fluorophores whose fluorescent lifetime is affected by the viscosity of their medium, such as fluorescent molecular rotors. FLIM of suitable “molecular rotors” have been used to image viscosity in livings cells, as well as to monitor dynamic cellular processes in real time. Fluorescence lifetime measurements allow the detection of heterogeneous viscosity of the medium thanks to multi-exponential decays, potentially within a single pixel. Compared to ratiometric intensity imaging, FLIM intrinsically separates concentration and viscosity effects and does not require the use of a viscosity-independent fluorophore, allowing the free spectral region to be used to map another parameter such as polarity[27,30].

An example of the use of FLIM to determinate the polarity surrounding the probe have been carried out in this work, particularly in the detection of hydrophobic regions to study the aggregation kinetics of the β-amyloid peptide. As shown in Figure 2.4 the fluorescence lifetime images are obtained through the attribution of the photons to different pixels. This is achieved by storing the absolute arrival times of the photons together with the relative arrival time with respect to the laser pulse[31].

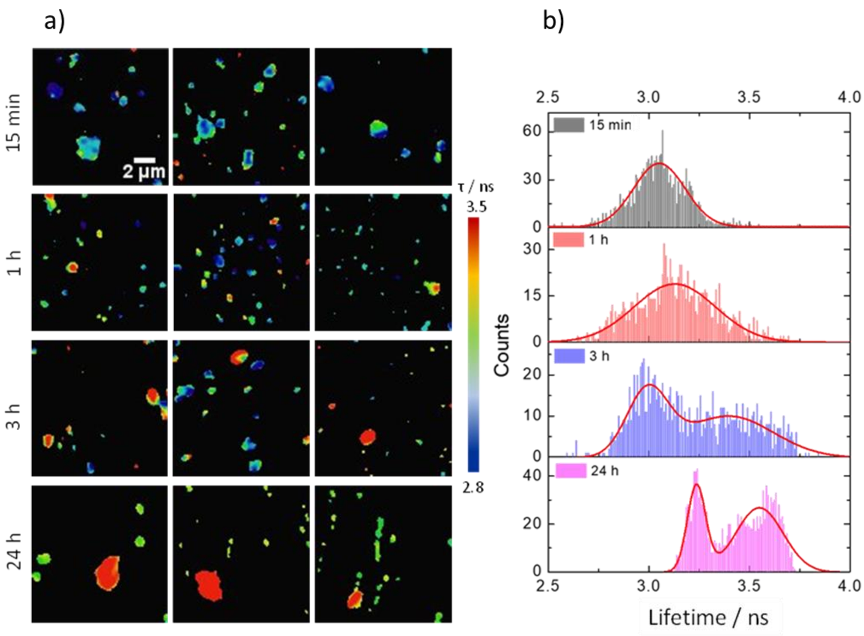

Figure 2.4. Aβ-42 aggregates in presence of the solvatochromic fluorophore 2-Me-4OMe-TM. (a) FLIM images at different time of incubation, with a lifetime range of 2.8 ns (blue) to 3.5 ns (red), indicating a decrease in polarity. (b) Histograms of the fluorescence lifetime at different incubation times, with contributions from shorter lifetimes around 3.0 ns in the early aggregates, and longer lifetimes around 3.6 ns in more mature aggregates.

ii. Solute concentration

As mentioned earlier, FLIM technique offers the advantage of fluorescence lifetime independence with respect to fluorophore concentration. This can be wide useful for mapping and measuring the concentration of ions that play a key role in living cells and organisms, such as Ca^{2+}, Cl^-, Na^+ and K^+. An example of ion sensing by FLIM was carried out to determine Cl^- concentrations in cockroach salivary glands using the fluorescence lifetime changes of the Cl^- sensing dye MQAE[32]. In this case, the sensitivity of the dye is due to collisional quenching by Cl^- ions. Oxygen is also another efficient fluorescence quencher, especially for fluorophores with longer fluorescence lifetime. Thus, metal-ligand complexes of ruthenium, platinum, palladium and europium can be used as optical oxygen sensors due to the decrease of their lifetime. The use of FLIM in oxygen detection offers great advantages compared to intensity-based fluorescence imaging where it is necessary to calibrate the intensity of the probe unquenched by oxygen and to know its concentration in the cell, which is impractical[27,30]. Thus, oxygen sensing by FLIM has made it possible to detect the oxygen concentrations in different cells types, such as in macrophages and to reveal cell subtypes with different oxygen gradient in isolated viable chondrocytes[33]. Another example of ion sensing was carried out in our group by mapping phosphate concentrations in living cells using FLIM[34]. It also possible to determinate the pH of the environment by fluorescent lifetime, as pH depends on the balance between the protonated and deprotonated forms of fluorescent molecules, each with a different lifetime[27]. In clinical imaging, measurements of fluorescence decay times of endogenous fluorophores, such as NADH and FAD, are of particular interest, as their concentration is an indicator of metabolic status. It has been possible to analyze the mitochondrial redox state or to distinguish between apoptosis and necrosis[35]. In addition, FLIM of skin autofluorescence represents a potential label-free tool for in vivo optical biopsies[36]. Other clinically relevant applications of autofluorescence FLIM have been carried out in the eye thanks to the autofluorescence of the retina, and in the teeth.

iii. Inter-intramolecular interactions

By far, the most extended application of FLIM in cell biology is in the identification of FRET phenomenon, which has become a wide useful tool in the localization of molecular interactions and conformational changes. FRET is an energy transfer process in which the energy of the excited state of a donor fluorophore is transferred by a non-radiative process to an acceptor molecule in the ground state. Thus, FRET constitutes a bimolecular fluorescence quenching process where the donor lifetime (τ_D) decreases. In that sense, FLIM-FRET measurements of the fluorescence lifetime τ_D provide a potential quantitative analysis of molecular interactions. By labelling proteins to the donor and the acceptor is possible to detect the distance between proteins on a nanometer scale[27,30,31].

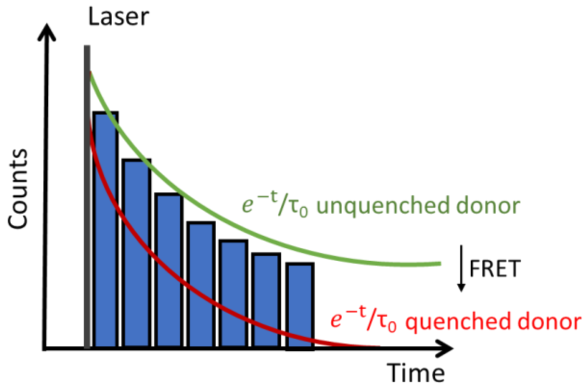

Figure 2.5. Representation of the donor decay function in FRET.

BIBLIOGRAPHY

1 Li, C.; Tebo, A. G.; Gautier, A. Fluorogenic Labeling Strategies for Biological Imaging. *Int. J. Mol. Sci.* **2017**, *18* (7), 1473.

2 Gao, P.; Pan, W.; Li, N.; Tang, B. Fluorescent Probes for Organelle-Targeted Bioactive Species Imaging. *Chemical Science*. 2019, pp 6035–6071.

3 Ouyang, J.; Sun, L.; Zeng, F.; Wu, S. Rational Design of Stable Heptamethine Cyanines and Development of a Biomarker-Activatable Probe for Detecting Acute Lung/Kidney Injuries: Via NIR-II Fluorescence Imaging. *Analyst* **2022**, *147* (3), 410–416.

4 Pramanik, S. K.; Das, A. Fluorescent Probes for Imaging Bioactive Species in Subcellular Organelles. *Chemical Communications*. 2021, pp 12058–12073.

5 Norregaard, K.; Metzler, R.; Ritter, C. M.; Berg-Sørensen, K.; Oddershede, L. B. Manipulation and Motion of Organelles and Single Molecules in Living Cells. *Chem. Rev.* **2017**, *117* (5), 4342–4375.

6 Willmann, J. K.; van Bruggen, N.; Dinkelborg, L. M.; Gambhir, S. S. Molecular Imaging in Drug Development. *Nature Reviews Drug Discovery*. 2008, pp 591–607.

7 Ehrenberg, M.; Betzig, E.; Hell, S. W.; Moerner, W. E. How the Optical Microscope Became a Nanoscope. *R. Swedish Acad. Sci.* **2014**, *50005*, 1–15.

8 Kapanidis, A. N.; Strick, T. Biology, One Molecule at a Time. *Trends in Biochemical Sciences*. 2009, pp 234–243.

9 Liu, H.; Ye, Z.; Wang, X.; Wei, L.; Xiao, L. Molecular and Living Cell Dynamic Assays with Optical Microscopy Imaging Techniques. *Analyst*. 2019, pp 859–871.

10 Abbondanzieri, E. A.; Greenleaf, W. J.; Shaevitz, J. W.; Landick, R.; Block, S. M. Direct Observation of Base-Pair Stepping by RNA Polymerase. *Nature* **2005**, *438* (7067), 460–465.

11 Wen, J. Der; Lancaster, L.; Hodges, C.; Zeri, A. C.; Yoshimura, S. H.; Noller, H. F.; Bustamante, C.; Tinoco, I. Following Translation by Single Ribosomes One Codon at a Time. *Nature* **2008**, *452* (7187), 598–603.

12 Luo, F.; Qin, G.; Xia, T.; Fang, X. Single-Molecule Imaging of Protein Interactions and Dynamics. *Annual Review of Analytical Chemistry*. 2020, pp 337–361.

13 Oida, T.; Sako, Y.; Kusumi, A. Fluorescence Lifetime Imaging Microscopy (Flimscopy). Methodology Development and Application to Studies of Endosome Fusion in Single Cells. *Biophys. J.* **1993**, *64* (3), 676–685.

14 Ishikawa-Ankerhold, H. C.; Ankerhold, R.; Drummen, G. P. C. Advanced Fluorescence Microscopy Techniques-FRAP, FLIP, FLAP, FRET and FLIM. *Molecules*. 2012, pp 4047–4132.

15 Elson, D.; Requejo-Isidro, J.; Munro, I.; Reavell, F.; Siegel, J.; Suhling, K.; Tadrous, P.; Benninger, R.; Lanigan, P.; McGinty, J.; et al. Time-Domain Fluorescence Lifetime Imaging Applied to Biological Tissue. *Photochem. Photobiol. Sci.* **2004**, *3* (8), 795–801.

16 Suhling, K.; French, P. M. W.; Phillips, D. Time-Resolved Fluorescence Microscopy. *Photochem. Photobiol. Sci.* **2005**, *4* (1), 13–22.

17 Oasa, S.; Krmpot, A. J.; Nikolić, S. N.; Clayton, A. H. A.; Tsigelny, I. F.; Changeux, J. P.; Terenius, L.; Rigler, R.; Vukojević, V. Dynamic Cellular Cartography: Mapping the Local Determinants of Oligodendrocyte Transcription Factor 2 (OLIG2) Function in Live Cells Using Massively Parallel Fluorescence Correlation Spectroscopy Integrated with Fluorescence Lifetime Imaging Microscopy (. *Anal. Chem.* **2021**, *93* (35), 12011–12021.

18 Kwak, E. S.; Kang, T. J.; Vanden Bout, D. A. Fluorescence Lifetime Imaging with Near-Field Scanning Optical Microscopy. *Anal. Chem.* **2001**, *73* (14), 3257–3262.

19 Micic, M.; Hu, D.; Suh, Y. D.; Newton, G.; Romine, M.; Lu, H. P. Correlated Atomic Force Microscopy and Fluorescence Lifetime Imaging of Live Bacterial Cells. *Colloids Surfaces B Biointerfaces* **2004**, *34* (4), 205–212.

20 Datta, R.; Heaster, T. M.; Sharick, J. T.; Gillette, A. A.; Skala, M. C. Fluorescence Lifetime Imaging Microscopy: Fundamentals and Advances in Instrumentation, Analysis, and Applications. *J. Biomed. Opt.* **2020**, *25* (07), 1.

21 Philip, J.; Carlsson, K. Theoretical Investigation of the Signal-to-Noise Ratio in Fluorescence Lifetime Imaging. *J. Opt. Soc. Am. A* **2003**, *20* (2), 368.

22 Becker, W. Advanced Time-Correlated Single Photon Counting Techniques. *Springer Series in Chemical Physics*. 2005.

23 Fu, C.; Zheng, H.; Wang, G.; Zhou, Y.; Chen, H.; He, Y.; Liu, J.; Sun, J.; Xu, Z. Three-Dimensional Imaging via Time-Correlated Single-Photon Counting. *Appl. Sci.* **2020**, *10* (6).

24 Herrero-Foncubierta, P.; Paredes, J. M.; Giron, M. D.; Salto, R.; Cuerva, J. M.; Miguel, D.; Orte, A. A Red-Emitting, Multidimensional Sensor for the Simultaneous Cellular Imaging of Biothiols and Phosphate Ions. *Sensors (Switzerland)* **2018**, *18* (1).

25 Garcia-Fernandez, E.; Pernagallo, S.; González-Vera, J. A.; Ruedas-Rama, M. J.; Díaz-Mochón, J. J.; Orte, A. Time-Gated Luminescence Acquisition for Biochemical Sensing: MiRNA Detection. In *Fluorescence in Industry*; Pedras, B., Ed.; Springer International Publishing: Cham, 2019; pp 213–267.

26 Gao, D.; Barber, P. R.; Chacko, J. V.; Sagar, M. A. K.; Rueden, C. T.; Grislis, A. R.; Hiner, M. C.; Eliceiri, K. W. FLIMJ: An Open-Source ImageJ Toolkit for Fluorescence Lifetime Image Data Analysis. *PLoS One* **2020**, *15* (12).

27 Becker, W. Fluorescence Lifetime Imaging - Techniques and Applications. *J. Microsc.* **2012**, *247* (2), 119–136.

28 Okabe, K.; Inada, N.; Gota, C.; Harada, Y.; Funatsu, T.; Uchiyama, S. Intracellular Temperature Mapping with a Fluorescent Polymeric Thermometer and Fluorescence Lifetime Imaging Microscopy. *Nat. Commun.* **2012**, *3*.

29 Van Manen, H. J.; Verkuijlen, P.; Wittendorp, P.; Subramaniam, V.; Van Den Berg, T. K.; Roos, D.; Otto, C. Refractive Index Sensing of Green Fluorescent Proteins in Living Cells Using Fluorescence Lifetime Imaging Microscopy. *Biophys. J.* **2008**, *94* (8).

30 Suhling, K.; Hirvonen, L. M.; Levitt, J. A.; Chung, P. H.; Tregidgo, C.; Le Marois, A.;

Rusakov, D. A.; Zheng, K.; Ameer-Beg, S.; Poland, S.; et al. Fluorescence Lifetime Imaging (FLIM): Basic Concepts and Some Recent Developments. *Medical Photonics*. 2015, pp 3–40.

31 Trautmann, S.; Buschmann, V.; Orthaus, S.; Koberling, F.; Ortmann, U. *Fluorescence Lifetime Imaging (FLIM) in Confocal Microscopy Applications*; 2013.

32 Lahn, M.; Dosche, C.; Hille, C. Two-Photon Microscopy and Fluorescence Lifetime Imaging Reveal Stimulus-Induced Intracellular Na+ and Cl- Changes in Cockroach Salivary Acinar Cells. *Am. J. Physiol. - Cell Physiol.* **2011**, *300* (6), 1323–1336.

33 Hosny, N. A.; Lee, D. A.; Knight, M. M. Single Photon Counting Fluorescence Lifetime Detection of Pericellular Oxygen Concentrations. *J. Biomed. Opt.* **2012**, *17* (1), 016007.

34 Paredes, J. M.; Giron, M. D.; Ruedas-Rama, M. J.; Orte, A.; Crovetto, L.; Talavera, E. M.; Salto, R.; Alvarez-Pez, J. M. Real-Time Phosphate Sensing in Living Cells Using Fluorescence Lifetime Imaging Microscopy (FLIM). *J. Phys. Chem. B* **2013**, *117* (27), 8143–8149.

35 Wang, H.-W.; Gukassyan, V.; Chen, C.-T.; Wei, Y.-H.; Guo, H.-W.; Yu, J.-S.; Kao, F.-J. Differentiation of Apoptosis from Necrosis by Dynamic Changes of Reduced Nicotinamide Adenine Dinucleotide Fluorescence Lifetime in Live Cells. *J. Biomed. Opt.* **2008**, *13* (5), 054011.

36 Galletly, N. P.; McGinty, J.; Dunsby, C.; Teixeira, F.; Requejo-Isidro, J.; Munro, I.; Elson, D. S.; Neil, M. A. A.; Chu, A. C.; French, P. M. W.; et al. Fluorescence Lifetime Imaging Distinguishes Basal Cell Carcinoma from Surrounding Uninvolved Skin. *Br. J. Dermatol.* **2008**, *159* (1), 152–161.

3.1 SOLVATOCHROMISM

As mentioned above, the absorption and emission properties of a solvatochromic dye that change its position and at times its fluorescence quantum yield is a function of polarity and hydration of its surroundings[1]. This phenomenon was named by Hantzsch as solvatochromism[2], and is considered "negative" when there is a hypsochromic (blue) shift of the absorption band, and "positive" when it occurs a bathochromic shift (red) as the polarity of the solvent increases[3]. The influence of solvent polarity on fluorescence can be explained through the diagram represented in Figure 3.1 and the different electronic states of the process. These fluorophores are surrounded by a sphere of solvent molecules in the electronic ground state (S_0) with an electric dipole moment which increases significantly upon excitation ($h\nu_A$) due to an intramolecular charge transfer from the electron donating to the accepting group, thus promoting to an excited single state (S_1). This transition occurs following the Franck-Condon principle[4] in the picosecond time scale, and results in a new, more ordered arrangement of the solvent sphere molecules around the fluorophore. This process is known as solvent relaxation and reduces the energy of the excited molecules to the S_1 state, also leading to a destabilization of the ground state, thus reducing the energy distance between these two states. The level of solvent relaxation is higher with increasing solvent polarity. This produces a return of the fluorophore to the ground state by a fluorescence decay whose emission is red-shifted (lower energy, $h\nu_F$). In addition, polar protic solvents show a strong tendency to return to the ground state trough non-radiative decay (K_{nr}), due to the reduced energy distance between S_0 and S_1 states which results in a decrease of the fluorescence quantum yield[5]. The reduced energy of the S_1 state is due to the H-bond interactions of these fluorophores, in this sense, water represents a strongly dipolar molecule with an outstanding H-bond donor[1]. Overall, depending on dipole moment of the fluorophore during the electronic transition upon excitation, a positive solvatochromism will occur if it increases ($\mu_g < \mu_e$) or negative if it decrease ($\mu_g > \mu_e$)[3].

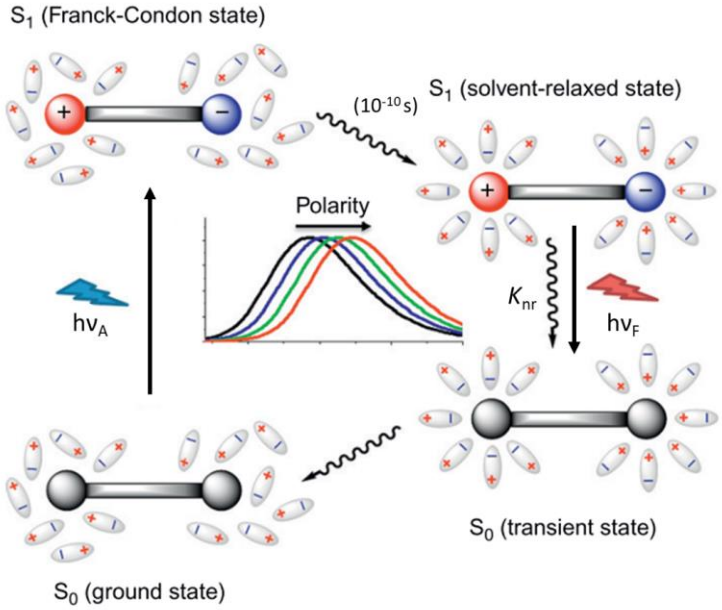

Figure 3.1. Simplified diagram of the solvatochromism phenomenon in fluorescence[1].

Despite its widespread use, solvatochromism remains a phenomenon to be further elucidated due to the different interactions and dynamic processes are involved. These interactions can be broadly divided into: (i) specific (e.g., hydrogen bonding, charge shift, probe-probe interactions, conformational changes) and (ii) non-specific, referring to the nature of the solvent (defined by the dielectric constant (ε) and the refractive index (n))[6]. This last is known as "solvent effects" and is attributed to the "polarity" of a solvent, which can be defined as its ability to dissolve charged or dipolar dissolved species. In a qualitative form, polarity is easy to understand, but not its quantitative measurements and precise definition. Because of its importance, efforts to define solvent polarity by empirical parameters has long been promoted, based on various solvent-sensitive reference processes. These efforts have been aimed at obtaining better solvent polarity parameters by possibly choosing standard solvent-dependent systems and studying the changes that occurs in the parameters of that system when the solvent is replaced[7]. The classification of the solvent can be established in a number of ways such as polarity, acidity, basicity, proton-donating properties, electron pair, etc. Among the solvent scales, those that do not distinguish between specific properties are considered general polarity scales, while others are identified to describe single intermolecular interactions[8].

3.1.2 SOLVENT POLARITY SCALES

3.1.2.1 BASED ON SPECTROSCOPIC MEASUREMENTS

These solvent polarity scales were developed by using empirical parameters from spectroscopic measurements. Therefore, the construction is carried out using a particular fluorophore, which usually has two energy states involved to the transition whose properties are influenced by the environment[9]. Depending on the parameter/s used for the study, a classification can be established between (i) single and (ii) multiparameter scales. Among the variety of scales available, those used in this work are discussed in more detail below.

i. Single parameter scales

- E_T (30): This solvent polarity parameter is based on the remarkable negative solvatochromism of the standard probe 2,6-diphenyl-4-(2,4,6-triphenyl-1-pyrido)phenolate, designated as betaine **30** in the literature[7,10], which represents its energy at the maximum of absorption band in a particular solvent. It is defined as the molar electronic transition energy (historically in kcal·mol^{-1}) of the dye 30:

$$E_T\ (30)(\mathrm{kcal}\cdot mol^{-1}\ ) = hcN_A\tilde{\mathrm{v}}_{max} =\ 28591/\,\lambda_{max}\ (1)$$

where h is the Planck's constant, c corresponds to speed of light, N_A is the Avogadro's constant, $\tilde{\mathrm{v}}_{\mathrm{max}}$ the wavenumber (cm^{-1}) and λ_{max} the wavelength (nm) of the longest wavelength absorption band in the UV-visible/near-IR of the spectrum, which correspond to an ICT transition from the phenolate moiety to the pyridinium ring upon excitation (Figure 3.2). Among the extent use of the E_T(30) parameter as an empirical measure of the polarity of several systems, including organic and ionic liquids, switchable-hydrophilicity solvents, polymers, surfaces or microheterogeneous solutions among others[11]. Moreover, E_T(30) is used as a good descriptor of hydrogen bonds as well as electrostatic interactions of solvents, because the intramolecular charge transfer (ICT) of betaine **30** also leads to a loss of electron density on the oxygen atom of the phenolate, thus decreasing its hydrogen bond acceptor character and its dipole moment[10].

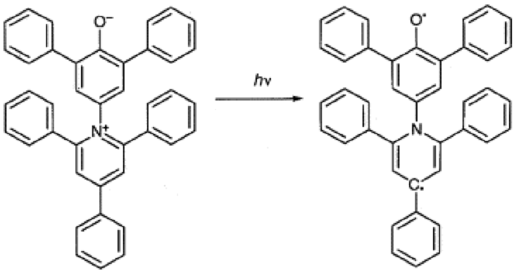

Figure 3.2. Scheme of the excitation process of betaine 30 dye.

ii. Multiparameter scales

- **Catalan:** This scale represents a multiparameter methodology to describe the solvent effect from the empirical measurements of solvent acidity (SA), basicity (SB), dipolarity (SdP), and polarizability (SP), with SA and SB representing specific scales, and SP and SdP general scales. Mathematically can be summarised in the equation:

$$A = A_0 + bSA + cSB + dSP + eSdP \qquad (2)$$

here *A* refers to a solvent-dependent physicochemical property in a particular solvent and A_0 is the statistical quantity corresponding to its value in the gas phase. SA, SB, SP and SdP denote independent and complementary solvent parameters, which report the different types of solute-solvent interactions, and *b* to *e* are the regression coefficients reporting the sensitivity of property *A* to the different solute-solvent interaction mechanisms.

Prior to the development of this multiparameter scale, Catalan constructed the SPP[12] (dipolarity and polarizability) scale through the absorption values of the probe **DMANF** (2-amino-7-nitrofluorene) and its homomorph **FNF** (2-fluoro-7-nitrofluorene). Subsequently, Catalan developed an empirical solvent polarizability (SP) scale using the probe **ttbP9** (3,20-di-tert-butyl-2,2,21,21-tetramethyl-5,7,9,11,13,15,17,19-docosanonaene) as a single molecular probe that responded exclusively to the polarizability to the medium as it does not possess any acidity or basicity. From these SP scale, the solvent polarity scale (SdP) was developed allowing to measure independently this parameter. The hydrogen-bond acceptor (HBA) basicity scale (SB scale) was developed through the use of 5-nitroindoline (**NI**) and its homomorph 1-methyl-5-nitroindoline (**MNI**). Finally, the solvent hydrogen-bond donor (HBD) acidity scale (SA scale) was constructed by the use of the homomorphic merocyanines *o-tert*-butylstilbazoliun betaine dye (**TBSB**) and *o,o'*-di-*tert*-butylstilbazolium betaine dye (**DTBSB**)[6,9].

This empirical scheme of Catalan, based on measures of the dipolarity, polarizability, HBD acidity, ad HBA basicity of the solvents (), allows prediction of the behaviour of any solvatochromic solute and provides information on solvent effects[6,13]. It also represents one of the most comprehensive solvent scales as it includes more than 300 solvents[9].

3.1.2.2 BASED ON THEORETICAL APPROACHES

- Lippert-Mataga: Applying general solvent effects theoretically provides a useful basis for studying solvent-dependent spectral shifts. No chemical interactions are included in this model, and therefore interactions such as hydrogen bonds or the formation of charge transfer states can be identified as deviations from the general theory. On the basis that solvent-fluorophore interactions influence the energy difference between the ground and excited states, the Lippert-Mataga equation describes this energy difference (cm^{-1}) as dependent on the solvent properties of refractive index (*n*) and dielectric constant (ε):[14,15]

$$\overline{\upsilon_A} - \overline{\upsilon_F} = \frac{2}{hc}\left(\frac{\varepsilon - 1}{2\varepsilon + 1} - \frac{n^2 - 1}{2n^2 + 1}\right)\frac{(\mu_E - \mu_G)^2}{a^3} + k \qquad (3)$$

h is the Planck constant (= 6.6256 x 10^{-27} ergs), *c represents* the light speed in vacuum (= 2.9979 x 10^{10} cm/s), *a* is the radius of the cavity where the dye is allocated, $\overline{\upsilon_A}$ and $\overline{\upsilon_F}$ are the absorption and emission wavenumber, respectively, and *k* is a constant representing the difference between the absorption and emission wavenumbers in the vacuum. Following this approach, the fluorophore is considered as a dipole plunged in a medium with equal dielectric constant at any point. The effects of ε and *n* on the Stokes shift can be explained as follows: an increase in *n* produces an instantaneous stabilization of the ground and excited states due to an electronic redistribution producing a decrease in the difference of the energy between the ground and excited state. This effect is the reason why most of the chromophores show a red-shift in the absorption spectra. However, although an increase in ε also stabilizes both states, it occurs in the excited state after a reorientation of solvent dipoles, i.e., this process requires the movement of the complete solvent molecules. The combination of both parameters is included in the Lippert-Mataga equation as orientation polarizability (Δf):

$$\Delta f = \frac{\varepsilon - 1}{2\varepsilon + 1} - \frac{n^2 - 1}{2n^2 + 1} \qquad (4)$$

The first term depending on ε explains the spectral shifts as a result of both solvent dipole reorientation and electron redistribution in the solvent molecules, while the second term depending on *n* is only explained by electron redistribution. Based on this simplified model, only a considerable Stokes shifts is predicted in the solvent reorientation, while refractive index and electronic redistribution affect the Stokes shift to a lesser extent[16].

3.2 SOLVATOCHROMIC FLUOROPHORES

The special design of environment-sensitive probes, also known as “smart molecules”, whose emission properties respond to changes in their local environment opened up the possibility of capturing physical modifications such as microenvironment polarity, viscosity, and biological analytes (ions), allowing to monitor biomolecular interactions, protein conformations and probe the local polarity of macrosystems. Based on their fluorescence changes, these dyes can be considered fluorogenic (based on changes in fluorescence intensity) and solvatochromic (based on changes in emission wavelength) and have become an essential tool in fluorescence sensing and bioimaging. Their ability of solvatochromic fluorophores to display shifts in their emission wavelengths, fluorescence lifetimes, and quantum yields in response to the polarity of their immediate surroundings, leading to solvatochromism being widely used in several fields of chemical and biological research[17,5,18]. The development of these solvatochromic probes improves their performance in the far-red and near-infrared range of the spectrum, reduces the non-specific interactions in biological systems, and improves the adaptation for advanced microscopy, such as *in vivo* bioimaging and superresolution allowing a quantitative analysis (combined with FLIM and/or ratiometric imaging) as they allow background-free imaging in the absence of washout conditions[18].

In these probes, it exists two main mechanisms involved (see Figure 3.3); a push-pull system that undergoes an intramolecular charge transfer (ICT) that redshift in more polar solvents when their excited state is highly polarized, or an excited-state intramolecular proton transfer (ESIPT). This dynamic performance along with their sensitivity to polarity and hydration make these dyes very useful for study biological membranes in lipid domains (rafts), apoptosis or endocytosis[18]. In addition, their use as fluorescents labels is well suited for the investigation of biomolecular interactions, especially with proteins, where they can report the state of a protein at the level of a single amino acid, i.e., in a very localized region of the molecule[5]. The study of proteins by solvatochromism has included intrinsic fluorophores such as the indole group of the natural amino acid tryptophan, whose sensitivity to solvent polarity blueshifts its emission when is buried in a native protein (N) and towards red when the protein is unfolded (U), making it widely used in folding and ligand binding studies[16]. Nevertheless, the development of extrinsic fluorophores with improved photophysical properties was necessary to overcome the short excitation wavelength required for indole and its relative abundance[5].

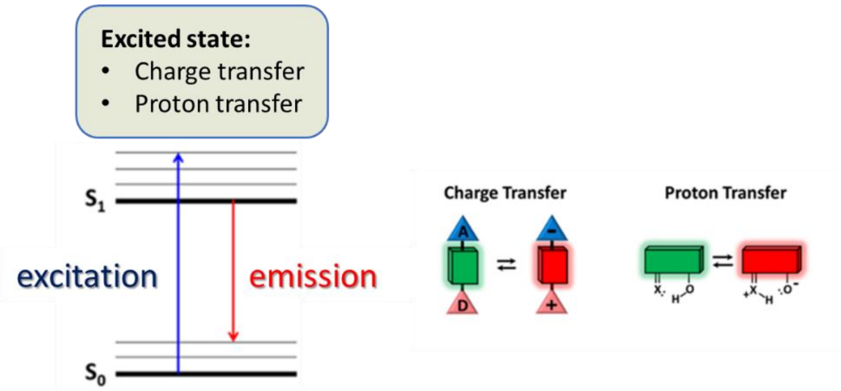

Figure 3.3. Simplified Jablonski diagram and the key mechanisms involved in the solvatochromic dyes[18].

i. Probes based on charge transfer

As mentioned above, so-called push-pull fluorophores represent classical environment-sensitive probes consisting of solvatochromic dyes with a D-A (electron donating and accepting groups) structure. After excitation, the push-pull system transfers the charge from the donor to the acceptor, producing a strongly dipolar excited state which upon interaction with the solvent dipoles relaxes and redshifts its single-band emission in more poler solvents. Recently, it has been shown that these fluorophores exhibit two tendencies. One, the formation of a triplet state especially in non-polar aprotic solvents, favours photo-oxidation thus reducing their photostability[19,20]. Two, trough electron transfer and twisted intramolecular charge transfer (TICT)[21] most of them are quenched in polar protic solvents (containing hydrogen atoms bound to oxygen –hydroxyl– or to nitrogen –amine, amide, etc.–), especially in water. The sensitivity to polarity of these push-pull fluorophores allows both the monitoring of biophysical properties of biomembranes, including polarity, hydration, electrostatics, etc[22]; and the detection of biomolecular interactions, as this results in an expulsion of local water molecules and thus a decrease in the polarity of the environment. Amino acid analogues of **Prodan**[23] and **4DMN**[24], in the UV-visible region, or **Nile Red** in the red spectral region represent some examples of push-pull dyes used in monitoring biomolecular interactions. Some of the most commonly used solvatochromic dyes that undergoes ICT are shown in Figure 3.4, including **Dansyl**, **Fluoroprobe**, **NBD**, **Dapoxyl**, the fluorene Prodan analogue **FR0**, etc.

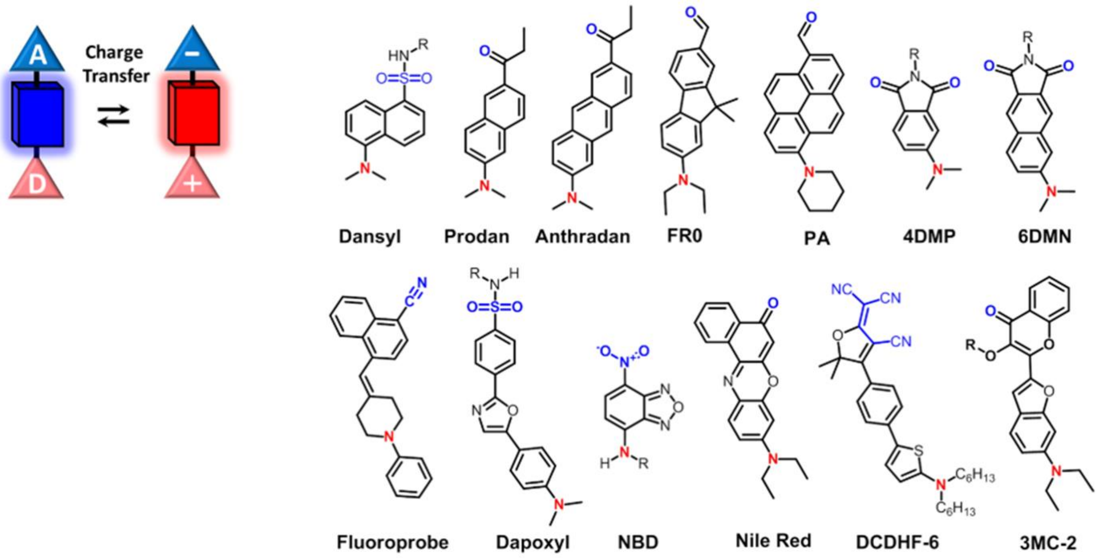

Figure 3.4. (Left) Outline of the concept of excited-state charge transfer. (Right) Examples of push-pull solvatochromic dyes[18]. Electron-donor and -acceptor groups are represented in red and blue, respectively.

ii. Probes based on intramolecular proton transfer

The other mechanism mentioned earlier whereby solvatochromic dyes can operate is excited-intramolecular proton transfer (ESIPT). The ESIPT pathway occurs when rotational freedom and donor/acceptor substituents weaken the intermolecular H-bonding, examples include **HBON**, **diCN-HBO** and **SAN** with the characteristic of a solvent-dependent double emission band[25]. In contrast to these six-membered cycles, dyes with a five-membered H-bond ring can easily perturb the H-bond, allowing their dual emission, consisting of the bands of the normal (N*) and tautomeric (T*) states, to be modulated. There is a change in the relative intensity of the two emissive tautomeric forms in response to the microenvironment. Polar and particularly protic solvents with the ability to donate H-bond suppress the ESIPT reaction, the intensity ratio (N*/T*) increases[1]. 3-hydroxychromone family (**3HC**) and its aza-analogues, 3-hydroxyquinolones (**3HQ**) are representative examples working in highly polar environments (in values between water and acetonitrile). In addition, 3HCs have been used in many types of biomolecular interactions in which the local polarity decreases, increasing the relative intensity of the ESIPT product. By comparison, the dyes **DMA-3HF** and **FA** operate in medium polarity solvents as their strong electron donating groups increase the dipole moment of the N* state[18].

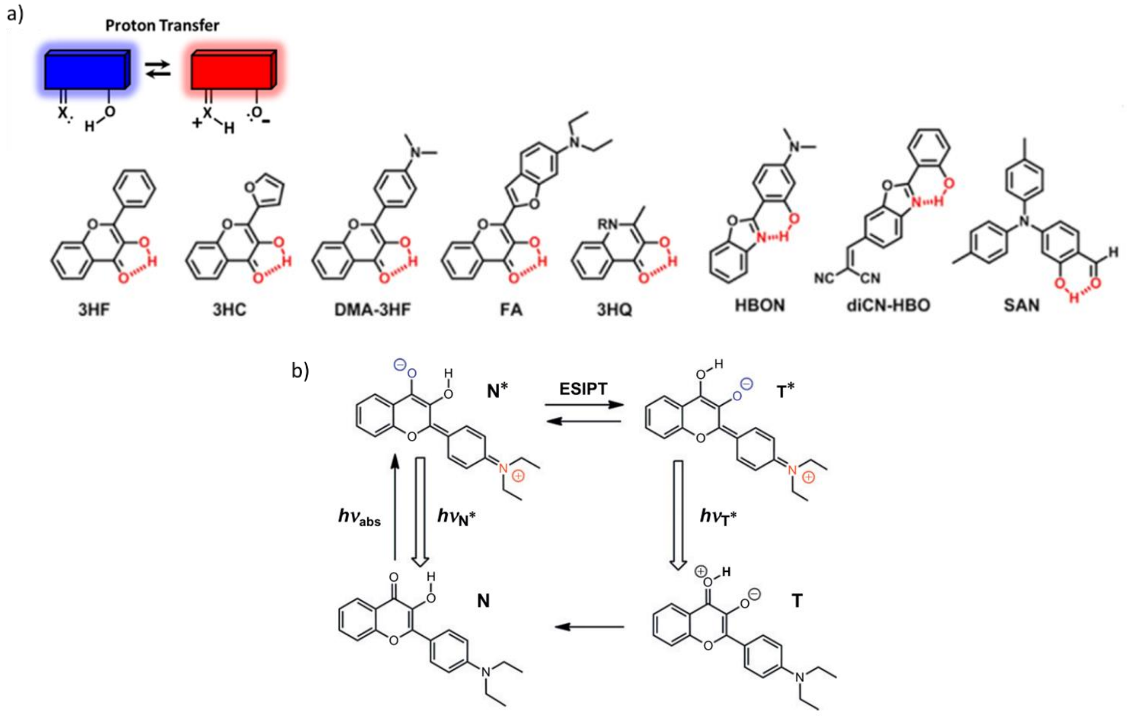

Figure 3.5. (a) Outline of the concept of proton transfer and examples of solvatochromic dyes that undergo excited-state intramolecular proton transfer (ESIPT)[18]. (b) Schematic photophysical cycle of the 3HC derivative 4'-(*N,N*-diethylamino)-3-hydroxyflavone. After excitation (N→N*), a charge transfer

occurs followed by an ESIPT process (N*→T*). Finally, after T*→T conversion, a zwitterionic T state is produced which rapidly transitions to the stable N state[1].

Bibliography

1 Klymchenko, A. S.; Mely, Y. Fluorescent Environment-Sensitive Dyes as Reporters of Biomolecular Interactions. In *Progress in Molecular Biology and Translational Science*; 2013; Vol. 113, pp 35–58.

2 Hantzsch, A. Über Die Halochromie Und »Solvatochromie« des Dibenzal-acetons Und Einfacherer Ketone, Sowie Ihrer Ketochloride. *Berichte der Dtsch. Chem. Gesellschaft (A B Ser.* **1922**, *55* (4), 953–979.

3 Reichardt, C. Solvatochromic Dyes as Solvent Polarity Indicators. *Chem. Rev.* **1994**, *94* (8), 2319–2358.

4 Condon, E. U. Nuclear Motions Associated with Electron Transitions in Diatomic Molecules. *Phys. Rev.* **1928**, *32* (6), 858–872.

5 Loving, G. S.; Sainlos, M.; Imperiali, B. Monitoring Protein Interactions and Dynamics with Solvatochromic Fluorophores. *Trends Biotechnol.* **2010**, *28* (2), 73–83.

6 Catalán, J. Toward a Generalized Treatment of the Solvent Effect Based on Four Empirical Scales: Dipolarity (SdP, a New Scale), Polarizability (SP), Acidity (SA), and Basicity (SB) of the Medium. *J. Phys. Chem. B* **2009**, *113* (17), 5951–5960.

7 Giernoth, R. Solvents and Solvent Effects in Organic Chemistry. 4th Ed. By Christian Reichardt and Thomas Welton. *Angew. Chemie Int. Ed.* **2011**, *50* (48), 11289–11289.

8 Katritzky, A. R.; Fara, D. C.; Yang, H.; Tämm, K.; Tamm, T.; Karelson, M. Quantitative Measures of Solvent Polarity. *Chemical Reviews*. 2004, pp 175–198.

9 Babusca, D.; Benchea, A. C.; Morosanu, A. C.; Dimitriu, D. G.; Dorohoi, D. O. Solvent Empirical Scales and Their Importance for the Study of Intermolecular Interactions. In *AIP Conference Proceedings*; 2017; Vol. 1796, p 4775.

10 Cerõn-Carrasco, J. P.; Jacquemin, D.; Laurence, C.; Planchat, A.; Reichardt, C.; Sraïdi, K. Solvent Polarity Scales: Determination of New ET(30) Values for 84 Organic Solvents. *J. Phys. Org. Chem.* **2014**, *27* (6), 512–518.

11 Reichardt, C. Pyridinium-N-Phenolate Betaine Dyes as Empirical Indicators of Solvent Polarity: Some New Findings. In *Pure and Applied Chemistry*; 2008; Vol. 80, pp 1415–1432.

12 Catalán, J.; Gómez, J.; Saiz, J. L.; Couto, A.; Ferraris, M.; Laynez, J. Calorimetric Quantification of the Hydrogen-Bond Acidity of Solvents and Its Relationship with Solvent Polarity. *J. Chem. Soc. Perkin Trans. 2* **1995**, No. 12, 2301–2305.

13 Catalán, J. On the Empirical Scales of Organic Solvents Established Using Probe/Homomorph Pairs. *J. Phys. Org. Chem.* **2021**, *34* (8), 1–5.

14 Lippert, E. Spektroskopische Bestimmung Des Dipolmomentes Aromatischer Verbindungen Im Ersten Angeregten Singulettzustand. *Zeitschrift für Elektrochemie,*

Berichte der Bunsengesellschaft für Phys. Chemie **1957**, *61* (8), 962–975.

15 Mataga, N.; Kaifu, Y.; Koizumi, M. Solvent Effects upon Fluorescence Spectra and the Dipolemoments of Excited Molecules. *Bull. Chem. Soc. Jpn.* **1956**, *29* (4), 465–470.

16 Lakowicz, J. R. *Principles of Fluorescence Spectroscopy*, Springer.; New York, 2006.

17 Marini, A.; Muñoz-Losa, A.; Biancardi, A.; Mennucci, B. What Is Solvatochromism? *J. Phys. Chem. B* **2010**, *114* (51), 17128–17135.

18 Klymchenko, A. S. Solvatochromic and Fluorogenic Dyes as Environment-Sensitive Probes: Design and Biological Applications. *Acc. Chem. Res.* **2017**, *50* (2), 366–375.

19 Kucherak, O. A.; Didier, P.; Mèly, Y.; Klymchenko, A. S. Fluorene Analogues of Prodan with Superior Fluorescence Brightness and Solvatochromism. *J. Phys. Chem. Lett.* **2010**, *1* (3), 616–620.

20 Niko, Y.; Didier, P.; Mely, Y.; Konishi, G. I.; Klymchenko, A. S. Bright and Photostable Push-Pull Pyrene Dye Visualizes Lipid Order Variation between Plasma and Intracellular Membranes. *Sci. Rep.* **2016**, *6*.

21 Grabowski, Z. R.; Rotkiewicz, K.; Rettig, W. Structural Changes Accompanying Intramolecular Electron Transfer: Focus on Twisted Intramolecular Charge-Transfer States and Structures. *Chemical Reviews*. 2003, pp 3899–4031.

22 Darwich, Z.; Klymchenko, A. S.; Kucherak, O. A.; Richert, L.; Mély, Y. Detection of Apoptosis through the Lipid Order of the Outer Plasma Membrane Leaflet. *Biochim. Biophys. Acta - Biomembr.* **2012**, *1818* (12), 3048–3054.

23 Cohen, B. E.; McAnaney, T. B.; Park, E. S.; Jan, Y. N.; Boxer, S. G.; Jan, L. Y. Probing Protein Electrostatics with a Synthetic Fluorescent Amino Acid. *Science (80-.).* **2002**, *296* (5573), 1700–1703.

24 Venkatraman, P.; Nguyen, T. T.; Sainlos, M.; Bilsel, O.; Chitta, S.; Imperiali, B.; Stern, L. J. Fluorogenic Probes for Monitoring Peptide Binding to Class II MHC Proteins in Living Cells. *Nat. Chem. Biol.* **2007**, *3* (4), 222–228.

25 Demchenko, A. P.; Tang, K. C.; Chou, P. T. Excited-State Proton Coupled Charge Transfer Modulated by Molecular Structure and Media Polarization. *Chem. Soc. Rev.* **2013**, *42* (3), 1379–1408.

4.1 AGGREGATION-INDUCED EMISSION

The concept of “aggregation-induced emission” (AIE) was introduced by Ben Zhong Tang’s group in 2001 when they found that a solution in ethanol of 1-methyl- 1,2,3,4,5-pentaphenylsilole showed a high increase in their fluorescence emission when adding water[1]. This phenomenon was attributed to aggregates/clusters formation, constituting the opposite effect of “aggregated-caused quenching” (ACQ). A few years later, in 2005, the AIE effect for this silole derivative was explained by the restriction of intramolecular vibrational and torsional motions. Thus, the restriction of intramolecular motions was abbreviated as RIM including both rotations (RIR) and vibrations (RIV)[2]. As can be observed in Figure 4.1, AIE luminogens (AIEgens) can consist of rotor-rich molecules, such as hexaphenylsilole (HPS) or tetraphenylethylene (TPE) whose properties are due to the RIR mechanism, and rotor-free molecules such as cyclooctatetrathiophene (COTh)[3] due to RIV effects. When the AIEgens with rotating units (e.g., phenyl rings) in a propelled-shaped structure are in dilute solution or in a soft matrix, the motion of these rotating units diffuses the energy of the excited state, leading to a non-radiative decay. However, upon aggregation, the RIR mechanism is activated and the motion of the rotating units is restricted because of steric hindrances, preventing π−π stacking. This favours the radiative decay pathways that enhance the fluorescence emission of the aggregates[4,5]. Due to intermolecular π−π stacking interaction the luminescence of an organic luminophore can be partially or completely quenched, and it was thought that molecules generally undergo ACQ effect upon aggregation[6,7]. The use of these traditional fluorogens is limited in terms of stability, sensitivity and efficacy, as organic dyes with multiple aromatic rings are hydrophobic and aggregate in aqueous or hydrophilic environments undergoing self-quenching. Hence, ACQ molecules should be used at low concentrations, which leads to a low signal-to-noise ratio and photobleaching of the small amount of molecules during the monitoring process[7,8].

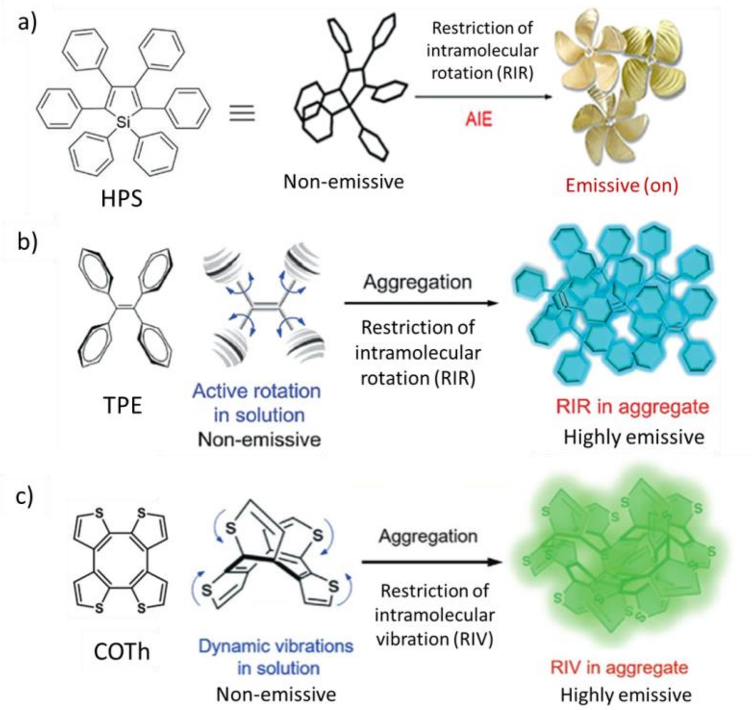

Figure 4.1. Schematic illustration of the RIM mechanism of AIE. (a) Non-planar HPS molecules with a propeller-shaped structure that prevent π–π stacking interactions promoting RIR effect in an aggregate state[5]. (b) TPE exhibits AIE activity by the RIR mechanism. (c) COTh is a non-emissive molecule in solution that becomes highly emissive upon aggregation due to the RIV mechanism[4].

Tang and coworkers took advantage of the RIR mechanism to develop AIE-based bioprobes as turn-on biosensor with applications in biosensing and bioimaging[5]. In this regard, the restriction of the intramolecular motions of an AIE luminogen when interacting with biomolecules in solution, within a cell or influenced by its local environment leads to the fluorescence light-up, detecting bioanalytes or biological processes[9]. In contrast to fluorescence turn-off sensors, AIE-based bioprobes feature higher sensitivity and a fast response, as they allow even to small emissive aggregates to be differentiated form the dark background[5]. Most of AIEgens show a monomeric emission due to their intramolecular rigidification when they aggregate or link to a biomacromolecule. However, in 1936 it was discovered by Scheibe and Jelley[10,11] that through increasing the concentration of pseudoisocyanine (PIC) in aqueous solutions, a new fluorescence band appeared due to intermolecular interactions. These so-called J-aggregates, characterized by a narrow band, represent another process by which the AIE phenomenon can occur, and continue to fascinate chemists and physicists because of their high brightness and the simultaneous high mobility of excitons along the aggregates[2]. Nowadays, it is known that depending on the aggregation pattern of the dyes, in addition to J-type they can also form H-type aggregates that exhibit changes in their absorption and photoluminescence spectra. Thus, J-aggregates exhibit a bathochromic shift (shifted to a longer wavelength) due to the π–π stacking of aromatic molecules, in which they are generally oriented “head-to-tail”. This is completely opposite to the H-aggregates, which show a hypsochromic shift (shifted to a shorter wavelength) with low or no fluorescence due to face-to-face stacking within the assembly[5,7,9,15].

Due to the advantages of AIE-based bioprobes, including intense emission upon aggregation, large Stokes shift, resistance to photobleaching, good biocompatibility and high specificity, AIEgens are suitable molecular probes for biomedical applications. The first generation of AIE molecules was developed to detect ions, enzymes, peptides, and DNA[8] by simple imaging of these biomolecules, such as the cyanine dye thiazole orange (TO) and its dimers (TOTOs) widely used in nucleic acid studies[2]. In contrast, the new AIE-based probes were developed focused on selective imaging of biological species, such as Gram-positive and Gram-negative bacteria, and different cellular organelles with emissions along the spectrum (from visible to near-IR). As cancer and bacterial infections have become urgent public health challenges, AIE-based molecules also have therasnostic applications in cancer cell ablation and bacterial killing[8,16].

4.2 AIE-BASED BIOPROBES FOR SPECIFIC ORGANELLE IMAGING

Organelles in eukaryotic cells including cytoplasm membrane, nucleus, mitochondria, lysosomes, lipid droplets (LDs), Golgi apparatus, endoplasmic reticulum, etc., play key roles in cellular function. The disfunction in biological activities of these organelles is always associated to a number of diseases such as diabetes, angiocardiopathy, neurodegenerative diseases and cancers among many others. This reveals the importance of visualizing and monitoring the morphology and activity changes of specific organelles, as they provide very useful information at the subcellular and molecular level that opens up opportunities for use in disease diagnosis and therapy. In this respect, the optical properties of AIE turn-on probes make them highly suitable molecules for the analysis of specific cell organelles. Therefore, several AIE bioprobes that can be targeted by physical interactions to specific cellular organelles have been developed as a very useful tool in imaging the cell membrane, mitochondria, lysosome, lipid droplets (LDs), and nucleus[7,8].

i. Cytoplasm membrane imaging

The cell membrane could be broadly defined as a phospholipid bilayer interspersed with proteins which separates the cellular interior from the external environment. It performs critical functions such as acting as a cell barrier, maintaining the stability of metabolism, nutrient uptake and waste removal, as well as signal transmission and cell recognition.

Based on their elements and functions, the design and development of membrane specific AIE bioprobes focuses on three main principles. (1) Since some components, such as proteins, can be particularly overexpressed in the plasma membrane, the binding of a bioprobe to a ligand of a membrane protein is a good strategy for cytoplasm membrane imaging[17]. As an example, the **TPS-2cRGD** AIE bioprobe allowed the identification of $\alpha_v\beta_3$-positive cancer cells, as the cyclic arginine-glycine-aspartic acid (cRGD) peptide can target the integrin $\alpha_v\beta_3$ overexpressed in tumor neovasculature[18]. (2) Due to similar hydrophobic properties, lipophilic structures can easily be trapped in the phospholipid bilayer and cell tracking can be carried out. For this reason, cell membrane-targeted dyes are usually amphiphilic or cationic, such as the commercial dyes DiO and DiI. The amphiphilic and cationic AIE-based probe **TPNPDA-C12** has a two-coloured fluorescence that allows staining the cell membrane with a red emission due to amphiphilic interaction, and also the mitochondria with yellow fluorescence due to electrostatic interaction[19]. (3) A good alternative to these approaches may also be bioorthogonal turn-on bioprobes that have the ability to react with the cell membrane allowing staining of the cell surface[20]. Bioorthogonal chemistry comprises a whole set of chemical reactions compatible with the biological components of a living being and which can therefore take place in the presence or within living cells[21]. It represents a potential tool for the application of bioprobes in the labelling of biological substrates. Generally, this approach is performed in two steps: the bioorthogonal functional group with a substrate is inserted into living systems (such as cell organelles) and then a probe with the corresponding functional group is added to react with the substrate, labelling it[22]. The selectivity and excellent signal-to-noise ratio of the turn-on AIEgens make them suitable bioprobes in this case for membrane imaging by bioorthogonal reaction. The water-soluble **TPETSAI** molecule represents an AIE specific bioorthogonal bioprobe that illuminates the cytoplasm membrane and also enables photodynamic ablation of cancer cells[23].

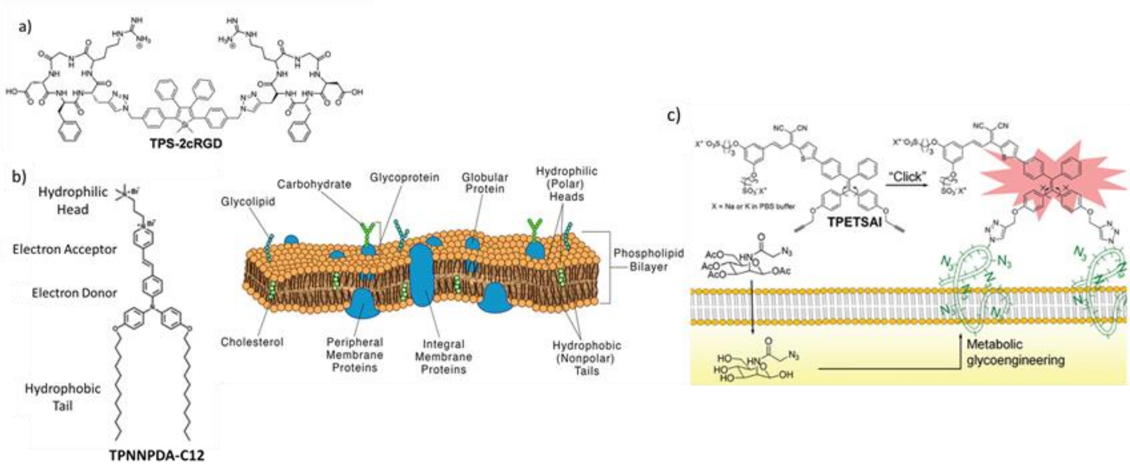

Figure 4.2. Schematic representation of the structure and different components of the cell membrane. Image via ScienceFacts.net. (a), (b) Chemical structures of the AIE bioprobes **TPS-2cRGD** and **TPNPDA-C12**, respectively. (c) Chemical structure of **TPETSAI** and its mechanism for membrane imaging through a bioorthogonal reaction[17].

ii. Mitochondria imaging

The mitochondrion is considered a semi-autonomous organelle with material genetic as it has its own DNA and carries out their replication and expression independently. It operates as a power plant for the oxidation of carbohydrates, fats and amino acids by storing the chemical energy it produces in form of the small molecule adenosine triphosphate (ATP)[24]. Direct visualization of mitochondrial changes by fluorescence imaging would provide useful information to help understand mitochondrial metabolism and diseases related to mitochondrial dysfunction. Moreover, the negative membrane potential of mitochondria several orders of magnitude higher than that of other organelles represent an opportunity to design suitable chemical ligands for specific targeting mitochondria[7,17]. In this respect, positively charged ligands accumulate in the mitochondria because of the proton gradient of the mitochondrial membrane. Triphenylphosphonium (TPP)[25] and pyridinium molecules are commonly used to introduce signalling probes into mitochondria. Performing a similar mechanism, cyanine and rhodamine dyes with lipophilic cations are also used as delivery vehicles[17]. Some of the main nontoxic AIE mitoprobes that allow visualisation of mitochondria and related processes are introduced below.

Since Tang's group reported the first AIE for mitochondria imaging in 2013, consisting of the integration of TPE and the mitochondrial ligand TPP (**TPE-TPP**)[26], numerous highly photostable and specific multicolour AIE probes have been developed[7,17]. Among the first AIE mitoprobes developed for mitochondrial imaging is also the green-emissive **AIE-MitoGreen-1**

[66]. To further reduce the influence of the autofluorescence, the following yellow- and red-emitting mitoprobes were developed. Thus, the yellow emissive AIE bioprobe **TPE-Py** was synthetized by introducing a pyridinium unit into the **TPE-TPP** molecule[27]. However, as the probe could not be sufficiently retained in the mitochondrion during the monitoring of cellular activities due to electrostatic and hydrophobic interactions, the **TPE-Py-NCS** bioprobe was developed. The covalent conjugation between the amine-reactive isothiocyanate (NCS) unit and mitochondrial proteins allows its use for mitochondria tracking[28]. In the monitoring of mitochondria-related bioprocesses, the red-emitting AIE mitoprobe, **AIE-Red**, was also reported to be very efficient for monitoring the mitophagy process[28], as well as the mitochondrial viscosity-sensitive **MitoAIE1**[29]. Red-emissive AIE bioprobes **TPE-indo** and **TPE-Ph-In** were also synthesized by introducing a positively charged indolium group that gives these probes the ability to monitor the membrane potential change of mitochondria through their fluorescence intensity changes[30,31]. In addition, the development of super-resolution imaging techniques has required specific fluorophores with remarkable photostability, such as the photoactivable AIE bioprobe ***o*-TPE-ON+** suitable for single-molecule localization microscopy (SLM)[32].

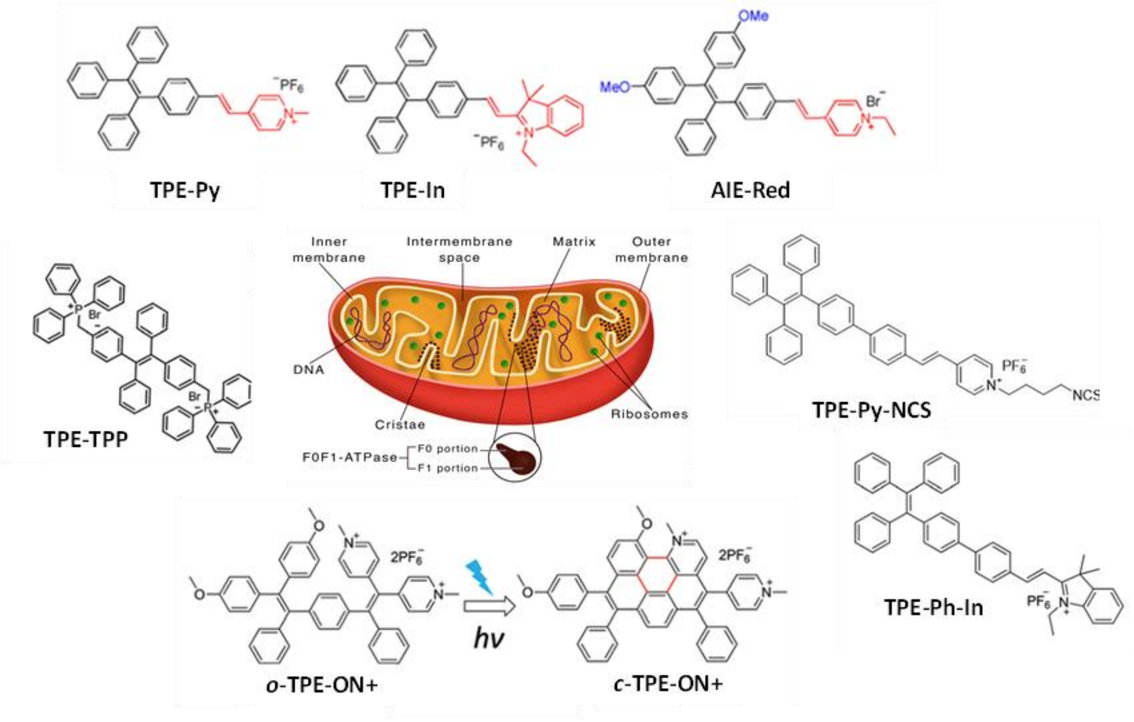

Figure 4.3. (Center) Schematic representation of the structure and different components of the mitochondria. Image via ScienceFacts.net. Chemical structures of different positively charged mitochondria-targeting ligands described above.

Recently, the possibility of designing a system that includes different probes using the same AIEgen core for imaging of different cellular organelles has emerged. To this end, Liu and co-workers carried out the synthesis of the four probes **TPAN, TPAPy, TPANPF6** and **TPAPyPF6** for monitoring organelles by modification functional groups of a single core. The results revealed that ionized **TPANPF6** and **TPAPyPF6,** due to the electrostatic attraction of the mitochondrial membrane, target mitochondria, whereas the non-ionized **TPAN and TPAPy** target LDs[8,33].

iii. Lysosome imaging

Lysosomes are digestive organelles that perform enzymatic degrative functions in synergy with cellular metabolism. These organelles originate from the Golgi apparatus and carry out the breakdown of absorbed biomacromolecules by endocytosis, providing the rest of the cell with the nutrients it needs, as well as degrading viruses and bacteria to safeguard cells[17]. Lysosomal autophagy also eliminates damaged or toxic components present in cells, such as disabled proteins and other organelles. Thus, abnormal functioning or enzyme mutation of lysosomes leads to excessive storage of molecules and results in accumulated diseases. Their ability to carry out functional activities can be monitored through their morphology, distribution and movement in living cells, which can be perform by fluorescence imaging[34]. Lysosome-specific fluorescent bioprobes are designed in two main approaches, either by making the bioprobe a lysosomal enzyme substrate or by combing it with a ligand specific for the acidic lysosomal environment (such as the weak base groups N, N-dimethyl amino and morpholine).

The first reported AIE-based lysosome bioprobe was the green emissive, highly lysosome specific **AIE-Lyso-1**[35]. The molecule contains lysosome ligand morpholines that direct it to the reactive site, and esterase substrate site acetoxyl groups to ensure its emission only in lysosomes. The blocked hydroxyl groups are hydrolysed by lysosomal esterase which can form intramolecular hydrogen bonds with nitrogen atoms, thus lighting up the lysosomes via the ESIPT and AIE processes. The yellow-emitting **AIE-LysoY** is a similar lysosome specific AIE bioprobe for monitoring the autophagy process[36]. It was also used to monitor lysosomal autophagy the viscosity sensing probe **LysoAIE2** with an indolium group and two hydroxyls to improve the water-solubility[37]. Recently, several AIE-based probes targeting lysosomes have been developed. Among them, the **T-BDP** probe is a D-A-D (donor-acceptor-donor) type molecule combining boron-dipyrromethene and triphenylamine with near-infrared AIE emission. Confocal laser scanning microscopy (CLSM) images of T-BDP nanoparticles demonstrated their specificity for cancer cells lysosomes[38].

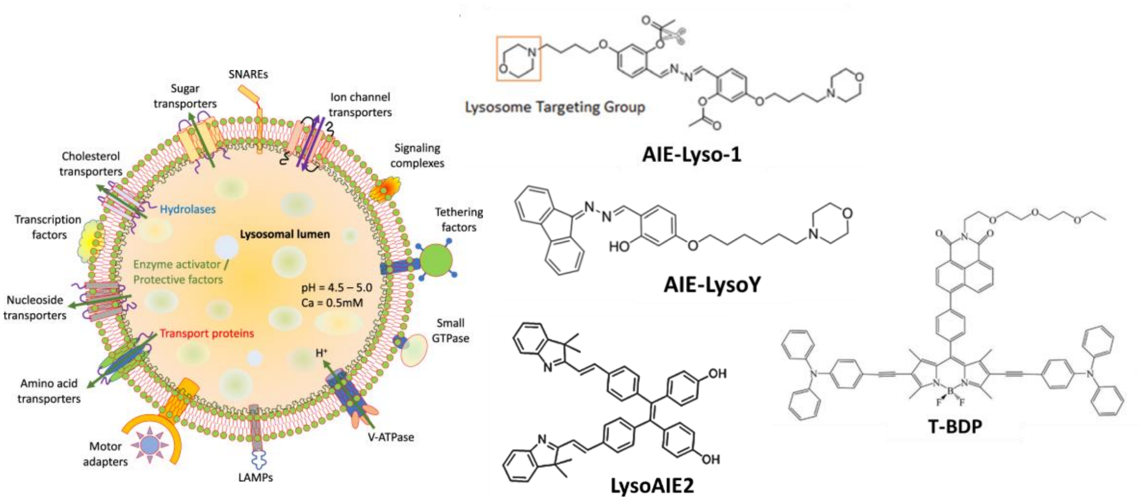

Figure 4.4. (Left) General structure and properties of lysosomes, including lipid bilayer with peripheral and integral membrane proteins with different functions[39]. (Right) Chemical structure of the AIE lysosome bioprobes **AIE-Lyso-1**, **AIE-LysoY**, **LysoAIE2** and **T-BDP.**

iv. Lipid droplets imaging

Lipid droplets (LDs), considered inert lipid-rich globules found mainly in adipose tissues, have been found to be involved in various cellular functions such as lipid storage, membrane synthesis, and protein degradation. Abnormal LDs quantity and activity involves diseases including diabetes mellitus, obesity, fatty liver diseases and inflammatory myopathy. Consequently, LDs have attracted increasing research interest and monitoring their location and distribution is very useful for early diagnosis. Due to their highly hydrophobic lipid environment, less polar than other cellular parts, polarity-sensitive AIEgens represents a potential LDs imaging[7,37].

Commercial fluorophores such as Nile red and BODIPY with twisted intramolecular charge transfer (TICT)[40] characteristics represent polarity-sensitive fluorescence probes that became strongly emissive in a non-polar environment and that therefore, represent good candidates for LD imaging. In this sense, the first AIE-based LD bioprobe reported, **TPE- AmAl,** was designed with TICT and solvatochromism plus AIE properties[41]. These characteristics were achieved by an electron donor (D) – electron acceptor (A) structure with the dimethyl-amino and formyl, respectively. The emissive properties of this LD bioprobe range from orange in aqueous solution to blue-green in non-polar environments, such as inside LDs. Furthermore, it was synthetized the red-emitting LD bioprobe **TPE-Ac** for *in vivo* imaging[42], and the **DPAS** and **FAS** "ESIPT + AIE" probes with yellow and orange emission, respectively[43]. In addition to the one photon excitation AIE-based LD fluorophores, the synthesis of **TPA-BI** and **IND-TPA** for two-photon fluorescence imaging was recently reported. Also recently, the AIE-based LD specific bioprobe dihydro-2-azafluorenone **1**, which undergoes photo-oxidative dehydrogenation to generate 2-azafluorenone **2** with AIE properties, proved to be an excellent photoactivatable AIEgen for LD imaging of living cells[44].

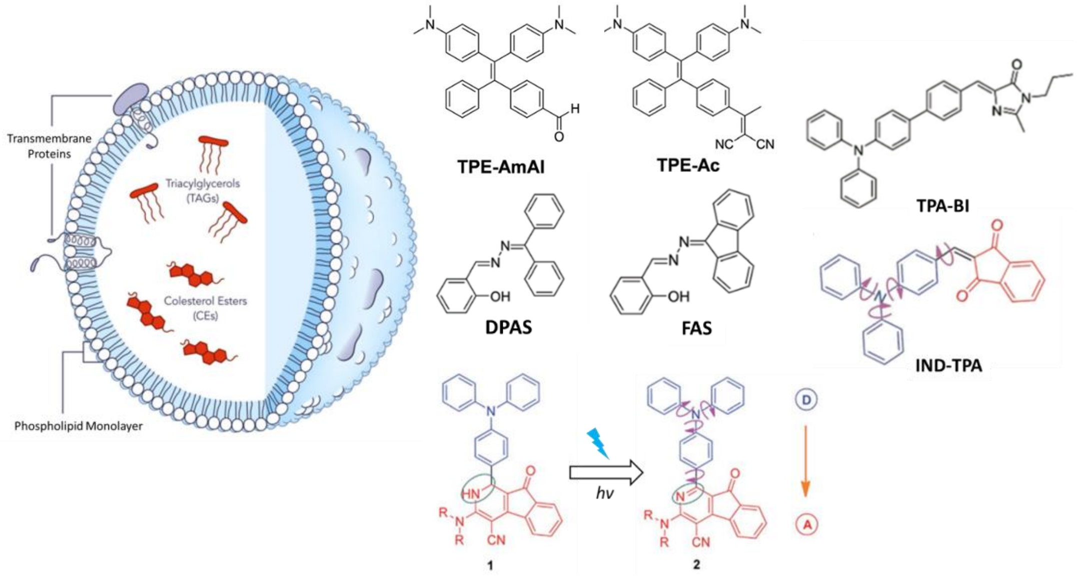

Figure 4.5. (Left) Schematic representation of lipid droplet structure and composition[45]. (Right) Chemical structure of the AIE LD bioprobes mentioned above.

v. Nucleus imaging

The nucleus is the largest organelle of a cell and represents its control unit, as it stores most the genetic material and regulates gene expression. For this reason, its biological and biomedical study has always been the main focus. In this sense, nucleus imaging provides a potential tool to show its activities and morphology. Due to the difficulty of penetrating the nuclear membrane, not many fluorophores have been described that stain the nucleus. However, AIEgens with superior properties than conventional fluorophores have proven to be good candidates for the study. In the design of nucleus specific bioprobes, the main principle is based on the introduction of DNA targeting sites, so that the probes target different parts of the DNA double helix framework. These include commercial dyes such as ethidium bromide (intercalant), DAPI (small groove fixative) or acridine orange (nucleic acid stain). In addition, staining of RNA in the nucleolus can also be used for the design of these nucleus-specific probes, as its negative charge is a potential target for positively charged probes[17,37].

ASCP is a new AIE-based bioprobe based on an α-cyanostilbene derivative with TICT characteristics and the unique ability to be used as a dual-color agent for mitochondria and nucleus imaging at different excitation and emission wavelengths[46]. **ASCP** incorporates a dimethylamino moiety that red-shifts the emission and a pyridinium unit that allows targeting of mitochondria. It was also recently revealed that its ability to target both mitochondria and the nucleus was explained by its affinity to bind RNA. In addition to **ASCP**, positively charged and hyperbranched polymers were developed, such as **TPPA-DBO,** which is highly specific for nuclei because of its affinity with DNA. These polymers also exhibit an excellent nuclear membrane permeability and tunable fluorescence, making them suitable for multiplex imaging[47]. The **TPE-NLS** bioprobe that conjugates the TPE group with a peptide sequence targeting was also successfully used in nucleus imaging[48].

Recently, an innovative strategy to improve the cell transfection efficiency for gene delivery into the cell nucleus, consisting in a smart non-viral gene vector, was reported. It was based on gemini-type amphiphiles composed of a backbone of 2,3-dicarboxylate-5,6-diphenyl-pyrazine (**DEDPP**) derivatives with AIE and two-photon absorption properties, inserted with triazole-[12]aneN_3 as the hydrophilic moiety and alkyl chains as the hydrophobic moiety. The DEDPP derivatives self-assembled into a micelle in aqueous solution, acting as a gene vector due to the electrostatic interaction between triazole-[12]aneN_3 group and DNA. In the presence of the cationic liposome DOPE (dioleoylphosphatidyl ethanola-mine) self-assembled to form a lipoplex (complexes between plasmid DNA and cationic lipids), thus improving the efficiency of cell transfection. This lipoplex structure could penetrate into the cell and cleavage of the ester bond of the DEDPP derivatives by lipase would release the DNA complexes to enter the nucleus. Once there, the pH change in the nucleus environment would break the pH-sensitive ester bonds of the triazole-[12]aneN_3 groups, thus releasing the DNA into the nucleus. By labelling the DNA with a commercial red dye, it might be possible to stain the nucleus red and blue, due to the commercial dye and the **DEDPP** derivatives, respectively[49,50].

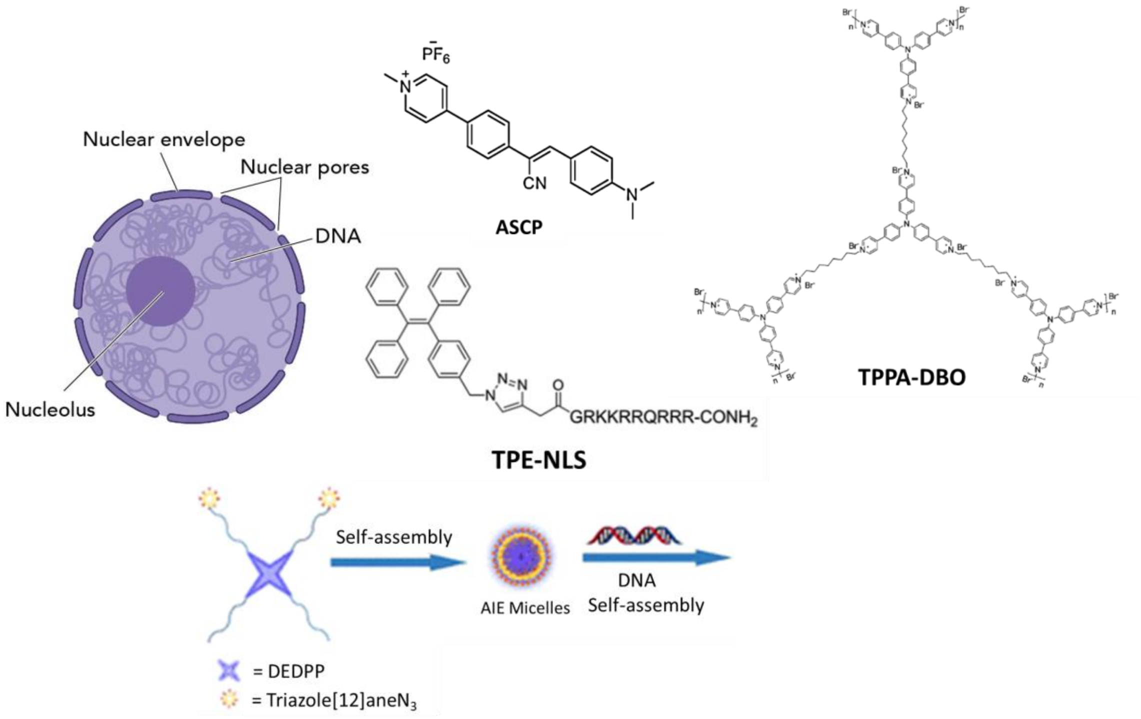

Figure 4.6. (Left) Schematic structure of nucleus with principal components. Image via Rsscience.com. (Right) Chemical structures of nucleus specific AIEgens **ASCP**, **TPPA-DBO** and **TPE-NLS**. (Bottom) Strategy of triazole-[12]aneN_3-based gemini-type amphiphiles (**DEDPP**) for gene delivery.

BIBLIOGRAPHY

1 Luo, J.; Xie, Z.; Lam, J. W. Y.; Cheng, L.; Chen, H.; Qiu, C.; Kwok, H. S.; Zhan, X.; Liu, Y.; Zhu, D.; et al. Communication Aggregation-Induced Emission of 1-Methyl-1,2,3,4,5-Pentaphenylsilole. *Chem. Commun* **2001**, 1740–1741.

2 Würthner, F. Aggregation-Induced Emission (AIE): A Historical Perspective. *Angewandte Chemie - International Edition*. 2020, pp 14192–14196.

3 Yang, Y.; Gu, Y.; Ma, Z.; Zhang, Y.; Xu, W.; Xu, L.; Wang, K.; Zou, B.; Wang, H. Aggregation-Induced Emission and Pressure-Dependent Fluorescence of Aryl Cyclooctatetrathiophenes. *Dye. Pigment.* **2021**, *184*, 108803.

4 Han, T.; Liu, L.; Wang, D.; Yang, J.; Tang, B. Z. Mechanochromic Fluorescent Polymers Enabled by AIE Processes. *Macromol. Rapid Commun.* **2021**, *42* (1).

5 Huang, L.; Dai, L. Aggregation-Induced Emission for Highly Selective and Sensitive Fluorescent Biosensing and Cell Imaging. *J. Polym. Sci. Part A Polym. Chem.* **2017**, *55* (4), 653–659.

6 v. Bünau, G. J. B. Birks: Photophysics of Aromatic Molecules. Wiley-Interscience, London 1970. 704 Seiten. Preis: 210s. *Berichte der Bunsengesellschaft für Phys. Chemie* **1970**, *74* (12), 1294–1295.

7 Mei, J.; Huang, Y.; Tian, H. Progress and Trends in AIE-Based Bioprobes: A Brief Overview. *ACS Applied Materials and Interfaces*. 2018, pp 12217–12261.

8 Cai, X.; Liu, B. Aggregation-Induced Emission: Recent Advances in Materials and Biomedical Applications. *Angewandte Chemie - International Edition*. 2020, pp 9868–9886.

9 Ding, D.; Li, K.; Liu, B.; Tang, B. Z. Bioprobes Based on AIE Fluorogens. *Acc. Chem. Res.* **2013**, *46* (11), 2441–2453.

10 JELLEY, E. E. Spectral Absorption and Fluorescence of Dyes in the Molecular State. *Nature* **1936**, *138* (3502), 1009–1010.

11 Scheibe, G. Variability of the Absorption Spectra of Some Sensitizing Dyes and Its Cause. *Angew. Chemie* **1936**, *49*, 563.

12 Wang, L.; Shen, Y.; Yang, M.; Zhang, X.; Xu, W.; Zhu, Q.; Wu, J.; Tian, Y.; Zhou, H. Novel Highly Emissive H-Aggregates with Aggregate Fluorescence Change in a Phenylbenzoxazole-Based System. *Chem. Commun.* **2014**, *50* (63), 8723–8726.

13 Würthner, F.; Kaiser, T. E.; Saha-Möller, C. R. J-Aggregates: From Serendipitous Discovery to Supramolecular Engineering of Functional Dye Materials. *Angewandte Chemie - International Edition*. 2011, pp 3376–3410.

14 Hestand, N. J.; Spano, F. C. Expanded Theory of H- and J-Molecular Aggregates: The Effects of Vibronic Coupling and Intermolecular Charge Transfer. *Chemical Reviews*. 2018, pp 7069–7163.

15 Más-Montoya, M.; Janssen, R. A. J. The Effect of H- and J-Aggregation on the Photophysical and Photovoltaic Properties of Small Thiophene–Pyridine–DPP Molecules

for Bulk-Heterojunction Solar Cells. *Adv. Funct. Mater.* **2017**, *27* (16).

16 Wang, J.; Zhang, L.; Li, Z. Aggregation-Induced Emission Luminogens with Photoresponsive Behaviors for Biomedical Applications. *Advanced Healthcare Materials*. 2021.

17 Hu, F.; Liu, B. Organelle-Specific Bioprobes Based on Fluorogens with Aggregation-Induced Emission (AIE) Characteristics. *Org. Biomol. Chem.* **2016**, *14*, 9921–10112.

18 Shi, H.; Liu, J.; Geng, J.; Tang, B. Z.; Liu, B. Specific Detection of Integrin α vβ 3 by Light-up Bioprobe with Aggregation-Induced Emission Characteristics. *J. Am. Chem. Soc.* **2012**, *134* (23), 9569–9572.

19 Zheng, Y.; Ding, Y.; Ren, J.; Xiang, Y.; Shuai, Z.; Tong, A. Simultaneously and Selectively Imaging a Cytoplasm Membrane and Mitochondria Using a Dual-Colored Aggregation-Induced Emission Probe. *Anal. Chem.* **2020**, *92* (21), 14494–14500.

20 Sletten, E. M.; Bertozzi, C. R. Bioorthogonal Chemistry: Fishing for Selectivity in a Sea of Functionality. *Angewandte Chemie - International Edition*. 2009, pp 6974–6998.

21 Scinto, S. L.; Bilodeau, D. A.; Hincapie, R.; Lee, W.; Nguyen, S. S.; Xu, M.; am Ende, C. W.; Finn, M. G.; Lang, K.; Lin, Q.; et al. Bioorthogonal Chemistry. *Nat. Rev. Methods Prim.* **2021**, *1* (1), 30.

22 Borrmann, A.; Van Hest, J. C. M. Bioorthogonal Chemistry in Living Organisms. *Chemical Science*. 2014, pp 2123–2134.

23 Yuan, Y.; Xu, S.; Cheng, X.; Cai, X.; Liu, B. Bioorthogonal Turn-On Probe Based on Aggregation-Induced Emission Characteristics for Cancer Cell Imaging and Ablation. *Angew. Chemie* **2016**, *128* (22), 6567–6571.

24 Boyman, L.; Karbowski, M.; Lederer, W. J. Regulation of Mitochondrial ATP Production: Ca2+ Signaling and Quality Control. *Trends in Molecular Medicine*. 2020, pp 21–39.

25 Zielonka, J.; Joseph, J.; Sikora, A.; Hardy, M.; Ouari, O.; Vasquez-Vivar, J.; Cheng, G.; Lopez, M.; Kalyanaraman, B. Mitochondria-Targeted Triphenylphosphonium-Based Compounds: Syntheses, Mechanisms of Action, and Therapeutic and Diagnostic Applications. *Chemical Reviews*. 2017, pp 10043–10120.

26 Leung, C. W. T.; Hong, Y.; Chen, S.; Zhao, E.; Lam, J. W. Y.; Tang, B. Z. A Photostable AIE Luminogen for Specific Mitochondrial Imaging and Tracking. *J. Am. Chem. Soc.* **2013**, *135* (1), 62–65.

27 Zhao, N.; Li, M.; Yan, Y.; Lam, J. W. Y.; Zhang, Y. L.; Zhao, Y. S.; Wongd, K. S.; Tang, B. Z. A Tetraphenylethene-Substituted Pyridinium Salt with Multiple Functionalities: Synthesis, Stimuli-Responsive Emission, Optical Waveguide and Specific Mitochondrion Imaging. *J. Mater. Chem. C* **2013**, *1* (31), 4640–4646.

28 Zhang, W.; Kwok, R. T. K.; Chen, Y.; Chen, S.; Zhao, E.; Yu, C. Y. Y.; Lam, J. W. Y.; Zheng, Q.; Tang, B. Z. Real-Time Monitoring of the Mitophagy Process by a Photostable Fluorescent Mitochondrion-Specific Bioprobe with AIE Characteristics. *Chem. Commun.* **2015**, *51* (43), 9022–9025.

29 Chen, W.; Gao, C.; Liu, X.; Liu, F.; Wang, F.; Tang, L. J.; Jiang, J. H. Engineering Organelle-Specific Molecular Viscosimeters Using Aggregation-Induced Emission Luminogens for

Live Cell Imaging. *Anal. Chem.* **2018**, *90* (15), 8736–8741.

30 Zhao, N.; Chen, S.; Hong, Y.; Tang, B. Z. A Red Emitting Mitochondria-Targeted AIE Probe as an Indicator for Membrane Potential and Mouse Sperm Activity. *Chem. Commun.* **2015**, *51* (71), 13599–13602.

31 Zhang, L.; Liu, W.; Huang, X.; Zhang, G.; Wang, X.; Wang, Z.; Zhang, D.; Jiang, X. Old Is New Again: A Chemical Probe for Targeting Mitochondria and Monitoring Mitochondrial Membrane Potential in Cells. *Analyst* **2015**, *140* (17), 5849–5854.

32 Gu, X.; Zhao, E.; Zhao, T.; Kang, M.; Gui, C.; Lam, J. W. Y.; Du, S.; Loy, M. M. T.; Tang, B. Z. A Mitochondrion-Specific Photoactivatable Fluorescence Turn-on Aie-Based Bioprobe for Localization Super-Resolution Microscope. *Adv. Mater.* **2016**, *28* (25), 5064–5071.

33 Liu, Z.; Zou, H.; Zhao, Z.; Zhang, P.; Shan, G. G.; Kwok, R. T. K.; Lam, J. W. Y.; Zheng, L.; Tang, B. Z. Tuning Organelle Specificity and Photodynamic Therapy Efficiency by Molecular Function Design. *ACS Nano* **2019**, *13* (10), 11283–11293.

34 Van Meel, E.; Klumperman, J. Imaging and Imagination: Understanding the Endo-Lysosomal System. *Histochem Cell Biol* **2008**, *129*, 253–266.

35 Gao, M.; Hu, Q.; Feng, G.; Tang, B. Z.; Liu, B. A Fluorescent Light-up Probe with “AIE + ESIPT” Characteristics for Specific Detection of Lysosomal Esterase. *J. Mater. Chem. B* **2014**, *2* (22), 3438–3442.

36 Leung, C. W. T.; Wang, Z.; Zhao, E.; Hong, Y.; Chen, S.; Kwok, R. T. K.; Leung, A. C. S.; Wen, R.; Li, B.; Lam, J. W. Y.; et al. A Lysosome-Targeting AIEgen for Autophagy Visualization. *Adv. Healthc. Mater.* **2016**, *5* (4), 427–431.

37 Zhou, Y.; Hua, J.; Tang, B. Z.; Tang, Y. AIEgens in Cell-Based Multiplex Fluorescence Imaging. *Sci. China Chem.* **2019**, *62* (10), 1312–1332.

38 Yang, M.; Deng, J.; Su, H.; Gu, S.; Zhang, J.; Zhong, A.; Wu, F. Small Organic Molecule-Based Nanoparticles with Red/near-Infrared Aggregation-Induced Emission for Bioimaging and PDT/PTT Synergistic Therapy. *Mater. Chem. Front.* **2021**, *5* (1), 406–417.

39 Allemailem, K. S.; Almatroudi, A.; Alrumaihi, F.; Almatroodi, S. A.; Alkurbi, M. O.; Basfar, G. T.; Rahmani, A. H.; Khan, A. A. Novel Approaches of Dysregulating Lysosome Functions in Cancer Cells by Specific Drugs and Its Nanoformulations: A Smart Approach of Modern Therapeutics. *International Journal of Nanomedicine*. 2021, pp 5065–5098.

40 Wang, C.; Chi, W.; Qiao, Q.; Tan, D.; Xu, Z.; Liu, X. Twisted Intramolecular Charge Transfer (TICT) and Twists beyond TICT: From Mechanisms to Rational Designs of Bright and Sensitive Fluorophores. *Chemical Society Reviews*. 2021, pp 12656–12678.

41 Wang, E.; Zhao, E.; Hong, Y.; Lam, J. W. Y.; Tang, B. Z. A Highly Selective AIE Fluorogen for Lipid Droplet Imaging in Live Cells and Green Algae. *J. Mater. Chem. B* **2014**, *2* (14), 2013–2019.

42 Kang, M.; Gu, X.; Kwok, R. T. K.; Leung, C. W. T.; Lam, J. W. Y.; Li, F.; Tang, B. Z. A Near-Infrared AIEgen for Specific Imaging of Lipid Droplets. *Chem. Commun.* **2016**, *52* (35), 5957–5960.

43 Wang, Z.; Gui, C.; Zhao, E.; Wang, J.; Li, X.; Qin, A.; Zhao, Z.; Yu, Z.; Tang, B. Z. Specific Fluorescence Probes for Lipid Droplets Based on Simple AIEgens. *ACS Appl. Mater.*

Interfaces **2016**, *8* (16), 10193–10200.

44 Gao, M.; Su, H.; Lin, Y.; Ling, X.; Li, S.; Qin, A.; Tang, B. Z. Photoactivatable Aggregation-Induced Emission Probes for Lipid Droplets-Specific Live Cell Imaging. *Chem. Sci.* **2017**, *8* (3), 1763–1768.

45 Antunes, P.; Cruz, A.; Barbosa, J.; Bonifácio, V. D. B.; Pinto, S. N. Lipid Droplets in Cancer: From Composition and Role to Imaging and Therapeutics. *Molecules*. 2022.

46 Yu, C. Y. Y.; Zhang, W.; Kwok, R. T. K.; Leung, C. W. T.; Lam, J. W. Y.; Tang, B. Z. A Photostable AIEgen for Nucleolus and Mitochondria Imaging with Organelle-Specific Emission. *J. Mater. Chem. B* **2016**, *4* (15), 2614–2619.

47 Ma, H.; Yang, Z.; Cao, H.; Lei, L.; Chang, L.; Ma, Y.; Yang, M.; Yao, X.; Sun, S.; Lei, Z. Materials Chemistry B Materials for Biology and Medicine One Bioprobe: A Fluorescent and AIE-Active Macromolecule; Two Targets: Nucleolus and Mitochondria with Long Term Tracking One Bioprobe: A Fluorescent and AIE-Active Macromolecule; Two Targets: Nucleolus and Mitochondria with Long Term Tracking †. *J. Mater. Chem. B 5*, 655.

48 Liang, J.; Feng, G.; Kwok, R. T. K.; Ding, D.; Tang, B.; Liu, B. AIEgen Based Light-up Probes for Live Cell Imaging. *Sci. China Chem.* **2016**, *59* (1), 53–61.

49 Ma, L. Le; Tang, Q.; Liu, M. X.; Liu, X. Y.; Liu, J. Y.; Lu, Z. L.; Gao, Y. G.; Wang, R. AneN3-Based Gemini-Type Amphiphiles with Two-Photon Absorption Properties for Enhanced Nonviral Gene Delivery and Bioimaging. *ACS Appl. Mater. Interfaces* **2020**, *12* (36), 40094–40107.

50 Song, N.; Xiao, P.; Ma, K.; Kang, M.; Zhu, W.; Huang, J.; Wang, D.; Tang, B. Z. Recent Advances of AIEgens for Targeted Imaging of Subcellular Organelles. *Chemical Research in Chinese Universities*. 2021, pp 52–65.

AIMS

The main aim of this PhD Thesis is the photophysical study of new fluorescent dyes and its usage as new tools in the study of challenging biological process. In particular, different dyes will be studied and applied in advanced imaging techniques.

The specific objectives proposed are the following:

1. Design, synthesis, photophysical and solvatochromic study of different fluorescent probes which are divided into environment-sensitive probes and long-life probes.

   Environment-sensitive probes:

   a. Photophysical study of solvatochromism and aggregation-induced emission (AIE) properties of 2-Me-4-OMe TM and PEMC dyes.

   Long-lifetime probes:

   a. Photophysical study and lanthanide sensitization of **dihydrocyclopenta[de]quinolin-2-one** derivative.

   b. Study of reactivity of **dihydrocyclopenta[de]quinolin-2-one** derivative.

2. Application of fluorescent probes in the study of biological processes of interest using the FLIM technique.

   a. Study of the behaviour of compounds inside the cell. Their accumulation in different organelles.

   b. Study of amyloid protein aggregation kinetics through the solvatochromic properties of the probe.

   c. Proof-of-concept studies of the application of this biothiol sensor to study cells of the immune.

INSTRUMENTATION

This section describes the instrumentation used for the experiments obtained in this work, which will be described in more detail in each chapter in the following Results section.

1.1 ABSORPTION SPECTROPHOTOMETER

Absorption spectra were recorded on a Perkin-Elmer Lambda 650 UV/Vis spectrophotometer with a temperature-controlled cell and it has a 0.17 nm UV/Vis resolution. It is a dual sampling compartment spectrophotometer and it is compatible with transmission and reflectance measurements. It is possible to work from 190-900 nm wavelengths. It has an automated polarizer/depolarizer drive in the large sample compartment that provides further depolarization or allows of oriented samples with polarized light. It is equipped with a beam depolarizer that corrects instruments bias. It has a deuterium and tungsten halogen light source which is pre-aligned and pre-focused for quick replacement and maximum uptime and there are double halographic grating monochromators for ultra-low stray light performance. The system and all the components that are part of it are controlled by a computer that is provided of some software to control the system.

Figure 1.1. Perkin-Elmer Lambda 650 UV/Vis spectrophotometer.

1.2 STEADY STATE SPECTROFLUOROMETER

Steady state fluorescence spectra were recorded using a Jasco FP-8300 spectrofluorometer. It is specifically designed for bio-applications and it is controlled by external software called Spectra Manager. Synchronization of the spectra is possible with a wavelength or constant energy difference. The light source is a Xenon lamp with shielded lamp house of 150 W. The detector is a silicon photodiode for excitation and a photomultiplier for emission with a wavelength covering from 200 to 900 nm. Measurements repeatability is ± 1 nm and a signal to noise ratio for Raman peak of water higher than 170:1 (peak to peak) and higher than 680:1 (rms) at 350 nm excitation wavelength, 2 s response time and 5 nm excitation and emission monochromator bandwidths. It is possible to select the slit band width between these values: 1, 2.5, 5, 10, 20 nm for excitation and emission. Wavelength scan speed is also a controllable parameter, speed from 20 to 20000 nm/min, it depends on the response and sensitivity selected. It is also possible to select filters for different wavelengths or transmittance attenuator. It has a 10 mm rectangular cell holder as sample compartment and it is nitrogen purgeable. For spectral correction there is a beam splitter that passes part of the incident current though a reference photodiode for excitation correction in contrast, some fields provided by the manufacturer itself by the software correct the emission.

1.3 TIME-RESOLVED FLUOROMETER

Time-resolved fluorescence measurements were done in a FluoTime 200 instrument (PicoQuant GmbH) based on Time-correlated single photon counting (TCSPC) methodology, and provided with several excitation laser sources.

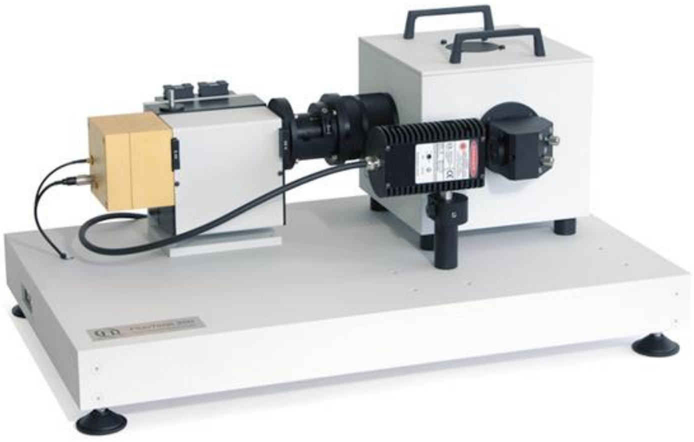

Figure 1.2. Time-resolved spectrofluorometer FluoTime 200 (PicoQuant).

1.3.1 LASER EXCITATION SOURCES

The excitation source employed in the collection of luminescence decay traces consisted on a high-power, pulsed picosecond diode laser, either of 440 nm (LDH-440), 470 nm (LDH-P-470), 485 nm (LDH-P-C-485), 530 nm (LDH-530) or 635 nm (LDH-P-635), all of them from PicoQuant GmbH. The train of pulses of the excitation source was controlled by a PDL 800 driver system (PicoQuant GmbH), which has a crystal oscillator that generates fluctuations lower than the mother frequency, allowing the pulse frequency to be divided by binary factors (1, 2, 4, 8 or 16) to generate a range of pulse frequencies of 40, 20, 10, 5 and 2.5 MHz. In this Thesis, we used a repetition rate for the train of pulses of 10 and 20 MHz and a pulse-width with a minimum amplitude of 40 ps.

In order to have stability on the measurements the room temperature is controlled by a thermostat that keeps the temperature in the laser source stable.

1.3.2 TCSPC SYSTEM

Through the time-correlated individual photon counting technique (TCSPC) technique, fluorescence decay traces are obtained, by building up a histogram of the arrival time of individual photons at the detector over many excitation / emission cycles. The arrival times are recorded in the histogram through relative times between the generation of the excitation laser pulse and arrival of the emission photons corresponding to the mentioned excitation. This technique was carried out on the already mentioned time-resolved fluorescence spectrophotometer FluoTime 200, based on an L-geometry and controlled by a computer equipped with the TCSPC TimeHarp 200 data acquisition card (PicoQuant GmbH).

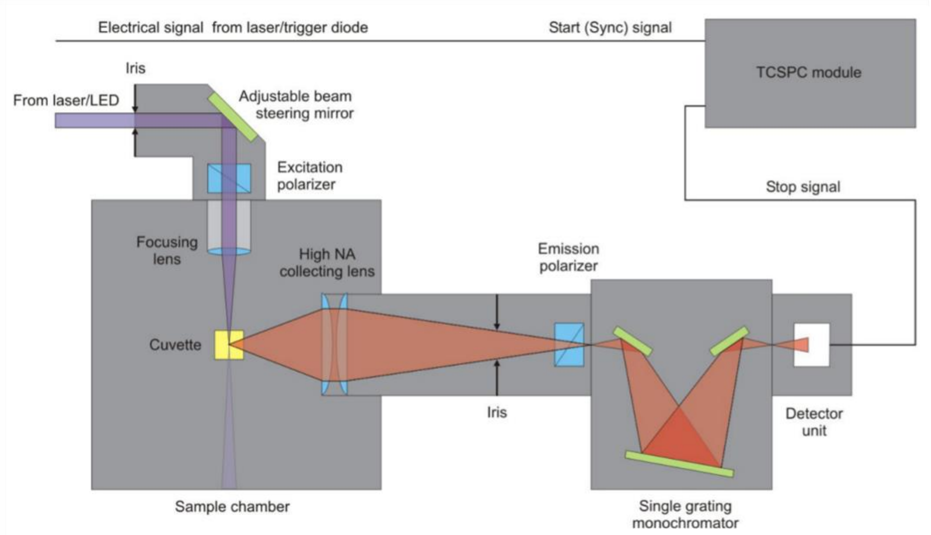

Figure 1.3. Scheme of the time-resolved fluorometer FluoTime 200 (PicoQuant).

The pulsating excitation radiation of the laser, as shown in Figure 1.3, is directed to the sample chamber through an optical fibre, there, by means of a lens the beam is focused towards the sample. The emission of the excited sample is collected and collimated through lenses at right angle with the respect to the excitation pathway. The emitted light passes through a laminar polarizer set at an angle of 54.7º respect to the direction of polarization of the excitatory light, in order to eliminate the effects of the rotational diffusion of the fluorophores in the fluorescence decays. Subsequently, the emitted light is focused on a Science Tech 9030 monochromator with technical specifications: f/3.5, concave holographic diffraction grating of 1200 lines/mm, 8 nm of angular dispersion and a spectral range from 350 to 800 nm. After passing through two slits of adjustable width, the detection of the emitted photons is carried out in a microchannel plate photomultiplier, whose signal serves as a START pulse and is connected, alongside the STOP pulse from the pulse-activated PDL 800 B oscillator. Both pulses are connected to a computer equipped with the TimeHarp 200 card and a control software which has integrated the two modules constant fraction discrimination (CFD): the time-amplitude converter (TAC) and the analog-digital converter (ADC). Histograms of fluorescence decays are collected along 1036 channels.

1.4 FLUORESCENCE LIFETIME IMAGING MICROSCOPY (FLIM)

The system used to perform Fluorescence Lifetime Imaging Microscopy (FLIM) measurements is based on a confocal microscope with pulsed laser excitation (MicroTime 200, PicoQuant GmbH). The instrument is capable of single-molecule sensitivity detection and Fluorescence Correlation Spectroscopy (FCS).

MicroTime 200 is composed of 4 main parts:

i. **Olympus IX71 Microscope**.

It consists of an inverted microscope that includes the infinity-corrected optical system (UIS), which allows not compromising the path of vision when intermediate accessories are added. It is equipped with WHN10x optical lenses and the following objectives: Plan-N-x40, Plan-N-x60, and immersion U-Plan-S-Apo-x100 (1.4 NA), being the last one used with immersion oil type DF that has a refraction index of 1.515. Figure 1.4 shows the general characteristics of the microscope. To image a region, the sample are raster-scanned with an x-y piezo-driven device (Physik Instrumente).

Figure 1.4. Olympus IX71 inverted microscope structure.

ii. **Excitation system.**

Although excitation diode lasers have already been discussed in the section *1.3.1 Laser excitation sources*, here the lasers have also been operated with a “Sepia II” driver (PicoQuant GmbH), allowing the simultaneous use of two different laser heads. The “Sepia II” driver also allows to generate trains of pulses with the frequencies of 40, 20, 10, 5 and 2.5 MHz. The laser placed on the second channel of the “Sepia II” driver was delayed with respect to the first laser, by an ORTEC DB463 delay box (AMETEK GmbH), to achieve pulsed interleaved excitation (PIE). The lasers and frequency used for this Thesis is explained in more detail in the Results section within the instrumentation subsection of each chapter entitled *FLIM bioimaging*.

iii. **Main Optical Unit (MOU).**

It comprises the following subunits:

a. The excitation segment: It is the part where the laser light beam that comes from the excitation system enters into the Main Optical Unit. It is incorporated by an optical fibre by means of an FC/APC connector and after reflection in a mirror, it passes through the excitation shutter (which can be controlled either by software, or manually). Once the beam passes through the shutter 10-20% of the intensity is directed to the photodiode that measures the excitation power.
b. The basic confocal unit: after passing through the excitation segment the light beam passes to the dichroic filter in a 45° geometry which redirects the light to the Olympus IX7 microscope objective focusing the light on the target sample.

c. The fluorescence emission as well as the reflected excitation light is collected back again by the microscope objective and redirected back to the dichroic mirror, which is optimized to let mainly pass the fluorescence emission radiation. The light transmitted in the dichroic passes a wheel of filters, in which a specific cut-off filter can be used to remove the remains of the excitation light coming to the detection pathway. Then, the light is directed towards an achromatic lens that focuses on an aperture pinhole of 75 µm diameter. The distance between the lens and the aperture is easily controllable to optimize the confocal plane. After the aperture, the beam is re-collimated by a second lens and guided to the detectors, described below.

d. Focal plane diagnosis: Part of the excitation light reflected and redirected to the dichroic is, in turn, reflected back towards the diagnosis segment of the focal plane. The optical design of the MicroTime 200 allows a continuous analysis of the excitation light, which makes it possible to control the position and quality of the focal plane and the excitation volume in the sample. There is a CCD camera (GANZ ZC-F10C2, with 500 x 582 pixels (1/3")) that allows the diagnosis and it permanently monitors the image seen by the lens. The obtained images are displayed on the computer. The light arriving at the camera can be regulated by filters of different optical density.

e. Detection channels: The collimated beam of the fluorescent emission reaches the detectors through the basic confocal unit. Up to two different detection channels are available, and the emitted light can be directed to just one of the detectors, or to both of them using a 50/50 beam splitter or specific 45° geometry dichroic filters. Each detection channel has a mechanical shutter and a lens to focus the incident radiation on the sensitive section of the detectors. The detectors used are single photon avalanche diodes (SPAD), SPCM-AQR-14 (PerkinElmer), with a detection wavelength range from 400 to 1100 nm, and high detection efficiency of more than 70% at 630 nm. It is possible to use a bandpass filter in front of the detectors to select the broadcast bands in each channel.

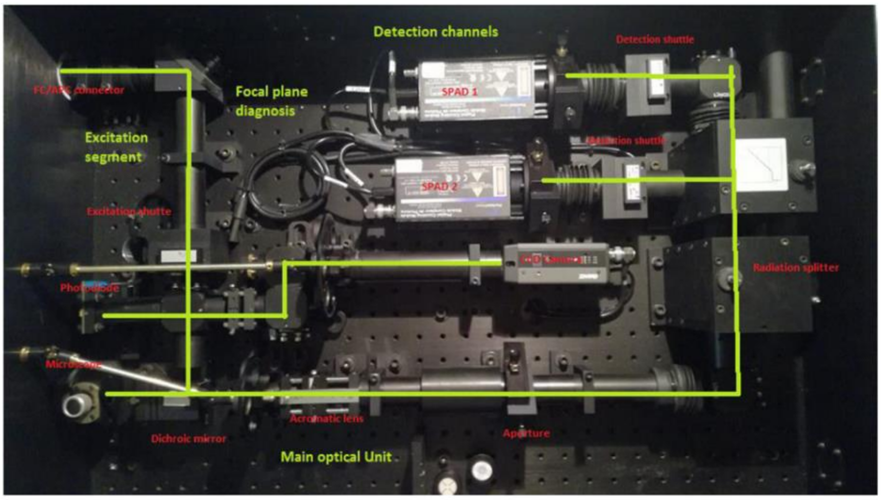

Figure 1.5. Main Optical Unit Scheme.

f. Data acquisition and electronic control: time-resolved photon arrival time information is collected using two TimeHarp 200 data collections cards (one for each detection channel). It is a TCSPC system that can operate in several ways, the most important is Time-Tagged-Time-Resolved methodology. The TTTR method allows the recording of the arrival time of each individual photon to the detectors. On the one hand, the START-STOP times of each photon with picosecond resolution are determined, more specifically it is the time elapsed between the excitation pulse (START) and the arrival of the photon (STOP signal), as the fluorescence time resolved by TCSPC mode is done. On the other hand, the arrival of the photons is recorded by an independent clock that measures the total time of each experiment and it labels each photon to its global time of arrival to the detector, respect to the overall measurement time. This allows identifying photons that come from the same molecule and also discriminating fluorescence blinking which is a feature of single molecule fluorescence experiments. Therefore, the most outstanding applications are: the detection of single molecule diffusion, FCS and single molecule blinking that is obtained by integrating fluorescence lifetimes.

Histograms are not performed in TTTR mode. Instead, the START-STOP time of each event is always recorded with a time tag of a separate clock, assigned at the time of arrival of the STOP photon. As a result, recordings made by TTTR mode occupy 12 bits for the START-STOP time and 16 bits for time tag. These 16 bits with the clock at 100 ns will cover a maximum range of 6.5536 ms. It should be noted that it is not possible to combine the START-STOP time of picoseconds and the time tag in the same figure, since the two times are not synchronized. The aim of these two times is, rather, to examine physical processes with two very different time scales and time references. However, analysis sophisticated methods use both times to extract as much information as possible from such physical processes, for example, the diffusion of individual molecules to a measure.

It is often desirable to synchronize TCSPC measurements with other information or with other records. In order to perform, for example, images of fluorescence lifetimes, it is also necessary to record the spatial location of the photons. To achieve this, a mechanism is needed that assigns the external synchronization information to the TCSPC data collected independently. To solve this problem, the data set generated by the TimeHarp 200 may contain markers for the synchronization information derived from the captured images. Figure 1.6 shows how the signal of the external marker signal is recorded in the data sequence.

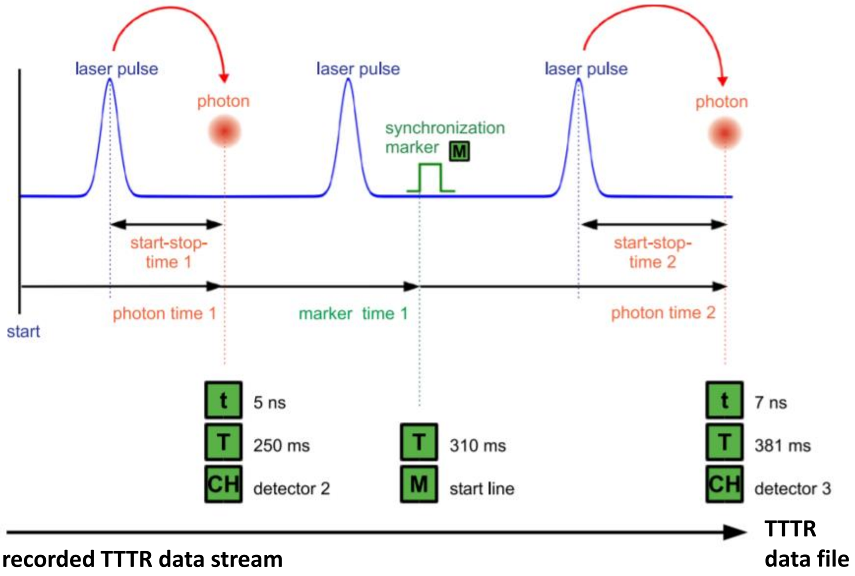

Figure 1.6. Measurement scheme of the Time-Tagged-Time-Resolved (TTTR).

Like in classical TCSPC the time difference between the moment of excitation and the arrival of the first fluorescence photon at the detector is measured. This TCSPC time (t) is stored into the TTTR data stream along with a global tag (T) and the information about the detection channel (CH). Additional external synchronization signals (markers, M) can be included in the data stream for imaging, for instance recording the XY coordinates of each pixel.

1.5 OTHER GENERAL LABORATORY EQUIPMENT

1.5.1 PH-METER

pH measurements have been done with a pH-meter Crison BASIC 20 that permits measurements from -2 to 16, mV: ±2000, -20-150° temperature. For its calibration they have been used Crison standard tampons: 4.01, 7 and 9.21. Measure error (± 1 digit): ≥ 0.01 pH, ≥ 1mV, ≥ 0.2°.

1.5.2 BALANCE

It has been used an electronic analytical Sartorious Balance A-120 S model provided with an internal and external calibration system. It has a standard deviation ± 0.1 mg and 3s time-response.

1.5.3 SONICATOR

An ultrasonic bath Ultrasons Selecta P model 513 with a 150W generator that produces 40 KHz sound waves has been employed. It has a synchronized timer with signaling lamp.

1.5.4 MAGNETIC STIRRER

A magnetic stirrer Bungen model MC8 has been used to perform several experiments.

1.5.5 SHAKER

An ElMI SkyLine DTS-2 thermoshaker for 2 microplates (ELME 10023) has been used in this work. The shaker features are a rotational speed between 100-1300 rpm, a rotation amplitude of 1.5 mm and a temperature control range between ambient +3 up to 60 °C.

1.5.6 CO_2 INCUBATOR

The cells were maintained in a Panasonic Incu*Safe* MCO-18AC-PE CO_2 Incubator in conditions of 5% humidification and 37 °C during the measurements, in order to keep them as long as possible in their optimal living conditions.

1.5.7 VERTICAL LAMINAR FLOW HOOD

The cells were washed and treated in a vertical laminar flow hood Telstar PV-100 for FLIM bioimaging measurements.

1.6 REAGENTS

The reagents used to carry out the experimental part of this Thesis are listed here, and will be developed in more detail in the following Results section within each subsection of *Material and methods* and *Supporting Information*.

- General chemical reagents:
  - 1,4-Dioxane. Sigma-Aldrich
  - 1-Butanol. Sigma-Aldrich
  - Acetone. Sigma-Aldrich
  - Acetonitrile. Sigma-Aldrich
  - Bovine Serum Albumin (BSA). Sigma-Aldrich
  - Calcium chloride. Merck
  - Chlorobenzene. Sigma-Aldrich
  - Chloroform. Sigma-Aldrich
  - Cyclohexane. Sigma-Aldrich
  - Dibutyl ether. Sigma-Aldrich
  - Dichloromethane. Sigma-Aldrich
  - Diethyl ether. Sigma-Aldrich
  - Dimethyl sulfoxide. Sigma-Aldrich
  - DL-Homocysteine. Sigma-Aldrich
  - Tris-EDTA buffer solution. Sigma-Aldrich
  - Ethanol. Sigma-Aldrich
  - Ethyl acetate. Sigma-Aldrich
  - L-Glutathione reduced. Sigma-Aldrich
  - Glycerol $\geq$ 99.5%. Sigma-Aldrich
  - L-Cysteine hydrochloride anhydrous. Fluka^{TM}
  - Methanol. Sigma-Aldrich
  - Phosphate buffer saline. Sigma-Aldrich
  - Potassium chloride. Merck
  - Potassium phosphate monobasic. Merck
  - Propanol. Sigma-Aldrich

  - Sodium chloride. Sigma-Aldrich
  - Sodium dodecyl sulphate. Sigma-Aldrich
  - Sodium hydroxide. Panreac
  - Sodium phosphate dibasic heptahydrate. Sigma-Aldrich
  - Sodium phosphate monobasic monohydrate. Sigma-Aldrich
  - Tetrahydrofuran. Sigma-Aldrich
  - Toluene. Sigma-Aldrich
  - Ultrapure water (18.2 MΩ·cm).

In general, the reagents were used without further purification, after checking the absence of fluorescent emission due to impurities. The chemicals were analytical or biochemical grade purity.

- 1-42 β-amyloid peptide fragment:
  - Aβ42, Sigma–Aldrich, CAS Number 107761-42-2.

- Mitochondrial membrane potential and organelle fluorescence microscopy tracking analysis probes:
  - MitoTracker^{TM} Green FM. Thermo Fisher

1.6.1 BUFFERS PREPARATION

- HEPES buffer: it was prepared in 0.5 M stock solution - work solution 50 mM, pH 7.4
- Krebs-Ringer phosphate (KRP) buffer: it was composed of 118 mM NaCl, 5 mM KCl, 1.3 mM $CaCl_2$, 1.2 mM KH_2PO_4 and 30 mM HEPES.

- Phosphate buffered saline solution (PBS): a commercial PBS 10X stock solution was used. The stock PBS buffer was diluted to a 1X working concentration in Mili-Q water at 7.5-8 pH at room temperature. The PBS was filtered by a Whatman Anotop^{TM} 0.2 µm filters prior to use.

- Sodium phosphate monobasic monohydrate ($NaH_2PO_4{\cdot}H_2O$) and sodium phosphate dibasic heptahydrate ($Na_2HPO_4 \cdot 7H_2O$) buffer: a 0.5 M stock solution was prepared. When necessary, the pH was adjusted using 0.1 M NaOH or 0.1 M $HClO_4$.

- SSPE buffer: it was prepared 20X buffer solution (1 mM EDTA, 149 mM NaCl, and 10 mM NaH_2PO_4) at pH 7.4 adjusted by the addition of HCl. The buffer was filtered through a Whatman Anotop^{TM} 0.02 µm filters for microscopy experiments prior to use.

1.7 CELL CULTURES

1.7.1 CELL LINE

The *in cellulo* experiments developed in this Thesis were carried out thanks to support of the Department of Biochemistry and Molecular Biology II, which provided the following cells lines:

- Embryonic kidney cells HEK-293 (ATCC no. CRL-1573).
- Human breast cancer cell line MDA-MB-231 (ATCC no.CRM-HTB-26).

1.7.1.1 REAGENTS

- Cell culture media:
  - DMEM (Dulbecco's Modified Eagle Medium). Gibco
- Cell culture reagents:
  - Fetal Bovine Serum (FBS) 10% (*v/v*). Gibco
  - Glutamine. Thermo Fisher
  - P/S (Penicillin/Streptomycin). Gibco
- Material:
  - Cell culture treated 6 well plastic plates. Corning
  - Coverslip ø 25 mm

1.7.2 PRIMARY CELL CULTURES

The primary cell cultures experiments included in this Thesis were developed in the Miguel Fribourg's laboratory at the Icahn School of Medicine at Mount Sinai, USA, and were obtained from mouse splenocytes:

- Male and female C57BL/6-Foxp3-YFP mice from Icahn School of Medicine at Mount Sinai, USA.
- Male and female Wild type B6 mice from Icahn School of Medicine at Mount Sinai, USA.

1.7.2.1 REAGENTS

- ACK lysis buffer. Roche

- Buffer 2% rat serum 2 mM EDTA
- Fluorescent Fixable viability dye:
  - eFluor 780. eBioscience, USA
- Isolation naïve CD4$^+$ T cells :
  - EasyStep^{TM} Mouse Naïve CD4$^+$ T Cell Isolation Kit. STEMCELL Kit
- Murine splenocytes (CD441Ocd62hi). EasyStep^{TM} Mouse Naïve CD4$^+$ T cell Isolation Kit. STEMCELL Technologies
- Phosphate buffered saline (PBS).
- Surface staining:
  - CD4, PE-cyanine 7 Anti-mouse CD4 (GK 1.5). TONBO biosciences, USA
- Mouse cultures reagents:
  - IL-2. Peprotech
  - TGFβ. Peprotech
  - αCD3/αCD28. Gibco

1.7.3 HUMAN CELLS

The experiments in human cells were carried out in peripheral blood mononuclear cells (PBMCs) from buffy coats obtained from Fully anonymous deidentified donors to the New York Blood Bank of the USA, and thus were determined by the institution not to constitute human subjects research.

1.7.3.1 REAGENTS

- Human peripheral blood mononuclear cells (CD45RA+CD45RO-). EasyStep^{TM} Human Naïve CD4$^+$ T Cell Isolation Kit. STEMCELL Technologies
- Isolation naïve CD4$^+$ T cells :
  - EasyStep^{TM} Human Naïve CD4$^+$ T Cell Isolation Kit. STEMCELL Kit
- Human cultures reagents:
  - IL-2. BD Pharmingen
  - TGFβ. Peprotech
  - αCD3/αCD28. Gibco

RESULTS

A SOLVATOFLUOROCHROMIC SILICON-SUBSTITUTED XANTHENE DYE USEFUL IN BIOIMAGING

Dyes and Pigments, Volume 168, September 2019, 264-272

IP: 4.613

Q1 (12/71)

Chemistry applied

Contribution: In this publication I have carried out the photophysical characterization together with the solvatochromic study using different solvent polarity scales.

1.1 ABSTRACT

In this work, we have performed an in-depth study of the photophysics and solvatofluorochromism of a red-emitting Si-xanthene dye, an analog of Tokyo Magenta (TM) historically developed by Egawa et al (*Chem. Commun.* **2011**, *47*, 4162-4164). The results show a strong dependency of the emission properties of 2-Me-4-OMe-TM on the polarity of the solvent. For instance, the dye exhibited an increase in its fluorescence lifetime with the decrease in solvent polarity. Therefore, in this work, this spectral behavior has been used as a new approach for determining the intracellular microenvironment polarity through the measurement of its fluorescence lifetime by Fluorescence Lifetime Imaging Microscopy (FLIM). Our experiments confirmed the ability of the dye to detect changes in polarity between different intracellular compartments.

1.2 INTRODUCTION

In the last few years, chemical modifications of the prototype fluorescein scaffold have produced a great variety of new fluorescent xanthene-based dyes with tailored photophysical properties[1]. However, all these derivatives present a common drawback: they exhibit absorption and emission wavelength maxima in the green region of the visible spectral range. On the other hand, the replacement of the oxygen atom at the 10´ positions of the xanthene moiety by a silicon atom has a significant impact on the photophysical properties, thus producing a usually desirable red-shift in their absorption and emission maxima[2]. For reviews, see can be found also[3]. These new derivatives are now synthetically accessible, and more importantly, their applications in biosensing and bioimaging has been demonstrated[4]. Within this context, our research group has recently described the presence of an excited-state proton transfer (ESPT) reaction promoted by the species of phosphate buffer in these fluorophores[5]. When an adequate proton donor/acceptor pair, as a phosphate buffer species, is present, this ESPT reaction produces a change in the fluorescence lifetime that depends on the total phosphate concentration and is therefore a useful method for phosphate detection. Remarkably, silicon-containing fluorophores are spontaneously incorporated into cells and can be used to monitor intracellular phosphate fluxes using fluorescence lifetime imaging microscopy (FLIM)[6]. FLIM is an excellent approach for studying biological systems because of the inherent advantages of this technique, such as fluorophore concentration independence or easy autofluorescence avoidance[7]. FLIM incorporates the advantages of fluorescence probes but uses fluorescence lifetime as a sensing parameter. In FLIM, intensity images are recorded together with fluorescence lifetime, allowing a multiparameter analysis of data. FLIM-based intracellular probes have been successfully used in the determination of pH[8], calcium[9] and phosphate[6] ions, temperature[10] and microviscosity[11]. The incorporation of the new family of fluorescein red derivatives in FLIM methodology thus opens new opportunities in the research of biological systems, where this technique is preferentially used. In this context, we designed, synthesized and described a modified fluorophore[12], 7-hydroxy-10(4-methoxy-2-methylphenyl)-5,5-dimethyldibenzo[b,e]silin-3(5H)-one (2-Me-4-OMe-TM), which could act as a dual multiplexed intracellular detector of biothiols and phosphate ions[12]. However, although the decrease in the fluorescence lifetime was consistent and allowed the phosphate flux in the cell to be monitored, an in-depth study of the buffer-mediated ESPT reaction was lacking. In this work, we unraveled the full excited-state behavior of 2-Me-4-OMe-TM. With this information in hand, we found that when this dye was employed in intracellular FLIM imaging, the fluorescence lifetime was less sensitive towards phosphate ions than the behavior predicted by the ESPT reaction. For this reason, a deep study has been conducted to unravel the reasons for this anomalous behavior. We considered that a combination of different effects might influence the dynamics of the excited state of 2-Me-4-OMe-TM. Because cytoplasm is a complex matrix with multiple compartments and macromolecules, we evaluated whether dye-macromolecule interactions or changes in the polarity of the microenvironment surrounding the dye could change the photophysical properties of 2-Me-4-OMe-TM. One of the reasons behind this anomaly could be the presence of solvatochromic effects in the red fluorescent 2-Me-4-OMe-TM dye. Solvatochromism is the characteristic of a chromophore that undergoes a shift in its absorption and/or emission wavelengths when the substance is dissolved in solvents with different polarities. For shifts in the emission spectra we refer to this phenomenon as solvatofluorochromism. This effect has multiple applications in biological and biomedical research to study local polarity in biological structures, changes in the protein conformation or biomolecule interactions[13]. Despite its wide use, solvatochromism is an unclear phenomenon[14] in which different interactions and dynamic processes are involved. These interactions are divided into two types: specific (e.g., hydrogen bonding, charge shift, probe-probe interactions, conformational changes) and nonspecific (when the shift is produced by the nature of the solvent, characterized by the dielectric constant and the refractive index)[15]

To shed light on the solvatofluorochromic behavior of 2-Me-4-OMe-TM, we have now carried out an in-depth photophysical study of this red dye using different solvents and different correlation approaches: the Lippert-Mataga equation, the Catalan and $E_T(30)$ analysis. The proper use of the solvatofluorochromic behavior of the dye could reveal the presence of the probe in environments with different polarities. To check this assertion, we have also incorporated the probe into a micellar system. We also found a strong solvatofluorochromic effect between protic and aprotic solvents due to specific interactions between the probe and solvent molecules. With all these data, we have reached a deeper understanding of the excited-state dynamics of the hetero-xanthene dye, facilitating its efficient use as a FLIM probe.

1.3 RESULTS AND DISCUSSION

1.3.1 SOLVATOFLUOROCHROMISM

The dye 2-Me-4-OMe-TM was prepared as described in the Appendix A (Scheme A1). 2-Me-4-OMe-TM was dissolved in 16 different solvents, and we measured its absorption spectra (Figure S1.1), steady-state fluorescence spectra (Figures S1.2 and S1.3), quantum yields (Table S1.1), and fluorescence lifetimes (Table S1.2). The comparison of the spectra showed important changes in the photophysical properties of the dye dissolved in different solvents. Interestingly, according to the dye's spectroscopic features, we found two different groups of solvents. In the first group, the dye's absorption was characterized by a band centered between 420 and 446 nm; in the second group, the dye presented two absorption bands, one centered between 434 and 474 nm and the other between 592 and 613 nm. The main feature of most of the solvents in which the dye displayed two absorption bands is their marked acidic character. This dual-band absorption was found when the dye was dissolved in alcohols, which are polar, proton donor solvents, with the exception of DMSO and acetonitrile. In contrast, the dye dissolved in aprotic solvents exhibited single-band absorption. Moreover, it is remarkable that the highest quantum yield values corresponded to the dye dissolved in protic solvents, in which the dye displayed two absorption bands. As representative examples of the aforementioned features, Figure 1.1 shows the normalized absorption and fluorescence emission of 2-Me-4-OMe-TM in acetone, acetonitrile and butanol, representing solvents in which the dye showed either one- or two-band spectral features.

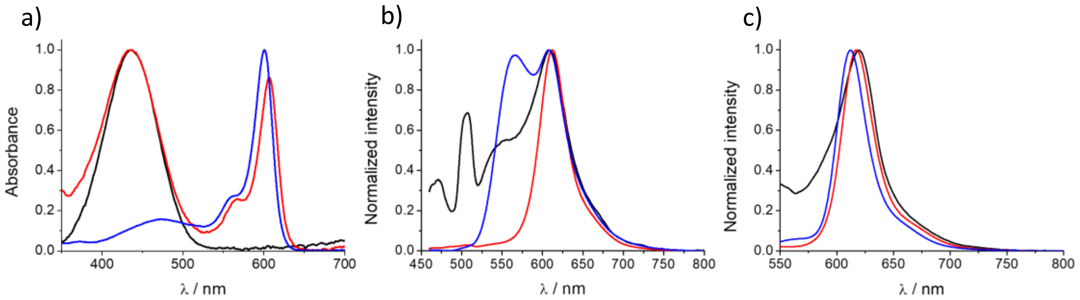

Figure 1.1. Representative normalized (a) absorption spectra and (b and c) emission spectra, with (b) λ_{ex} = 440 and (c) λ_{ex} = 530 nm, of compound 2-Me-4-OMe-TM in three solvents: acetone (black), acetonitrile (red) and butanol (blue).

Because on its lipophilic character, we have considered the possibility that 2-Me-4-OMe-TM may undergo aggregation in polar solvents, being these aggregates responsible of the red-band fluorescence emission. To unravel this, we measured the fluorescence intensity from concentrations as low as 1×10^{-7} M, up to high 2-Me-4-OMe-TM concentrations (1×10^{-5} M) in water (Figure S1.4a). As aggregation depends on the concentration, low quantities of 2-Me-4-OMe-TM should reduce aggregation. To unambiguously discard any aggregation, we plotted the emission intensity vs the 2-Me-4-OMe-TM concentration. Our results showed always the same emission shape in all the concentrations studied, except at the highest concentrations in which auto-absorption caused a slight red-shift in the emission band (see Figure S1.4b). However, selecting another wavelength with less inner filter effect (620 nm), we obtained a perfect linear behavior in the complete range studied. The fulfillment of the Kavanagh's Law suggests that aggregation in polar solvents can be considered negligible.

To study the solvent dependency based on solvent-dye nonspecific interactions, we followed the Lippert-Mataga equation (See Appendix A)[17]. This equation describes the Stokes shift ($\Delta\underline{\upsilon}$) as a consequence of the changes in the dipole moment after the excitation and the dipole energy in solvents with different dielectric constants (ε) and/or refractive index (n) (Table S1.3), where both parameters are included in the orientation polarizability (Δf).

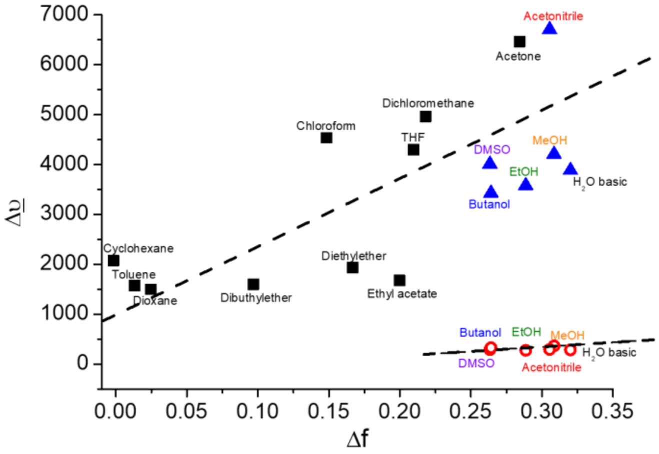

Figure 1.2. Lippert-Mataga representation of orientation polarizability of 2-Me-4-OMe-TM dissolved in different solvents.

Figure 1.2 shows the plot of the experimental Stokes shift values versus Δf, following the Lippert-Mataga representation. For solvents in which the dye presented a double absorption band, we calculated two values: one selecting the blue-shifted (triangles) and the other selecting the red-shifted (open circles) absorption band. We observed two main trends marked by dashed lines. The first trend is observed in those solvents for which the dye presented a single band (aprotic solvents) and for the blue-shifted band of the solvents in the protic group. The second trend involves the red-shifted band of the protic solvents. The difference in the trends between aprotic and protic solvents suggests that 2-Me-4-OMe-TM presents specific interactions with solvents such as butanol, ethanol, methanol, acetonitrile or water[18]. This interaction could be the formation of hydrogen bonds between the fluorophore and the solvent; in fact, with the exceptions of acetonitrile and DMSO, the rest of the solvents in this group stand out for their high acidity and proton donor capacity[19]. This fact supports the idea of different electronic densities of the 2-Me-4-OMe-TM dye depending on whether it is forming hydrogen bonds.

The presence of specific hydrogen bonding effects of the solvents makes the Lippert-Mataga formalism insufficient; therefore, we employed a complementary solvatochromic study based on the methodology reported by Catalan[15]. In brief, the analysis is based on four empirical solvent scales, i.e., polarizability (SP), dipolarity (SdP), acidity (SA) and basicity (SB), hence taking into account both general effects and specific hydrogen bonding features of the solvents. The major advantage of the Catalan methodology is that it allows the separation of the relative contribution of the four parameters in the solvatochromic shifts of $\tilde{\nu}_{abs}$ and and $\tilde{\nu}_{em}$, and hence, it provides insights on which of the solvent's features is the main one responsible for the spectroscopic behavior of the dye. Arithmetically, the effect of the solvent on the physicochemical properties observable (*A*) is expressed by a multilinear expression:

$$A = A_0 + b\,SA + c\,SB + d\,SP + e\,SdP$$

where *A* is a solvent-dependent physicochemical property in a specific solvent, $A_0$is the statistical quantity corresponding to the value of the property in the gas phase and *b* to *e* are the regression coefficients describing the sensitivity of property *A* to the different solute-solvent interactions[15]. As found in the Lippert-Mataga representation, and due to the dual absorption bands found in protic solvents, we separated them into two different groups, depending on the number of absorption bands. In the first dataset, all solvents were considered, using the blue-shifted absorption band for the solvents in which the dye displayed two bands. The second dataset was gathered with the red-shifted absorption band of the dye. We used the correlation coefficient *r* as the goodness-of-fit criterion, obtaining values of 0.954 and 0.996 for the $A = \tilde{\nu}_{abs}$ correlation in the first and the second datasets, respectively. When correlating $A = \tilde{\nu}_{em}$, we obtained 0.894 and 0.982 for the two datasets, respectively. These *r* values support a good correlation in all cases. To understand the importance of each of the solvent's properties, Catalan fitting was carried out, omitting one, two and three solvent scales.

Table S1.4 shows the correlation coefficient values obtained for all the performed fittings, including all parameters and omitting one of the solvent scales. For the first group, the changes in $\tilde{\nu}_{abs}$ were predominantly produced by the solvent acidity and, to a lower extent, basicity, as evidenced by the large negative values and low associated error. This result means that the acid-base features of the solvents are primarily controlling the energy of the transition. This analysis explains the presence of the double band in the acidic solvents (water, methanol, ethanol and butanol) and in those solvents with a combination of low acidity but large basicity (DMSO and acetonitrile).

In contrast, the $\tilde{\nu}_{em}$ was largely affected by the solvent's polarizability; hence, the general solvent stabilization of the excited-state is the major effect for the emission, so further stabilization in more dipolar solvents was observed. This result is in excellent agreement with the Lippert-Mataga approach when considering the Stokes shift. Interestingly, when considering the second, red-shifted band, the acidity of the solvent was found to be the major contributor in both $\tilde{\nu}_{abs}$and $\tilde{\nu}_{em}$, without a strong dependence on any other physicochemical parameter.

Therefore, using the Catalan approach, we conclude the following: although acidity is the main physicochemical parameter that affects all solvents and bands for absorption, both groups are affected by different physicochemical parameters for emission. Regarding the first band, the solvent dipolarity represents the primary physicochemical parameter that produces a red-shift in the fluorescence emission. In contrast, our results clearly support the idea of the second absorption and emission band arising from hydrogen bonding interactions with the solvent. Despite the difficulty in quantifying the solvatofluorochromic effects, due to the appearance of specific interactions, this behavior could be considered interesting; the strong differences among solvents due to these specific effects could allow the probe be applied to aqueous or nonaqueous phases[17], e.g., when the fluorophore enters disperse hydrophobic systems or interacts with a macromolecule.

In addition, we performed the (E_T30) solvent scale polarity[14b,20] analysis of the absorption and emission maxima (see Figure S1.5). The correlation of the emission maxima showed two different tendencies regarding the single and blue-shifted band and the red-shifted band. The first group showed a negative solvatofluorochromic behavior whereas the red shifted group exhibited a positive solvatofluorochromic behavior. These interesting differences could indicate the nature of the transition between ground- and excited- level, so that the first group is due to a $\pi \rightarrow \pi^*$ transition, whereas the red-shifted band corresponds to a $n \rightarrow \pi^*$ transition.

For a better understanding of the transition of the 2-Me-4-OMe-TM fluorescence properties from a polar to a nonpolar medium, we carried out absorption, steady-state and time-resolved fluorescence measurements of 2-Me-4-OMe-TM in different water: THF volume proportions. Figure 1.3 shows the transition of the absorption and normalized fluorescence intensity by absorption at two different excitation wavelengths (440 and 595 nm). The absorption spectra (Figure 1.3a) showed an evident red-shift of the ~570-nm absorption band and an increased intensity of the ~440-nm band when the THF proportion was increased. The red band completely disappeared in pure THF. The emission spectra also showed striking results. When exciting predominately at the nonpolar maximum (Figure 1.3b; λ_{ex} = 440 nm) and with increasing THF concentrations above 40%, the fluorescence showed a decrease in intensity along with a slight red-shift at approximately 600 nm and the appearance of an emission shoulder at approximately 550 nm. However, in pure THF, the 2-Me-4-OMe-TM fluorescence decreased strongly, as expected, given the very low quantum yield in THF (0.005). For a better visualization of the two-bands in the fluorescence, we have normalized these spectra (see Figure S1.6a) where the fluorescence splitting is unambiguously identified when THF is in the media.

Figure 1.3c shows the fluorescence emission using the absorption maximum as the excitation wavelength. As can be observed, there was an increase in intensity when the THF proportion was increased to 80%. Interestingly, a red-shift of the emission band was also observed, from 598 nm in water to 614 nm in 80% THF.

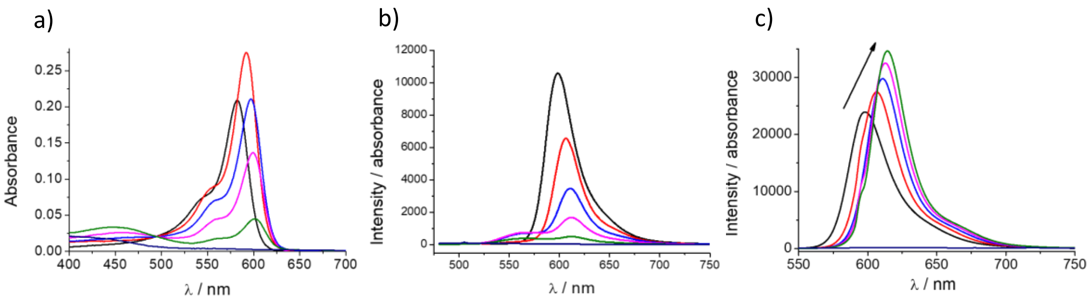

Figure 1.3. (a) Absorption and (b, c) emission spectra using an excitation wavelength of (b) 440 nm and (c) 595 nm in THF: Water mixtures with THF proportion of 0 (black), 20 (red), 40 (blue), 60 (pink), 80 (green) and 100% (dark blue).

We also performed a time-resolved fluorescence study of the dye dissolved in water: THF mixtures using either 530 nm (Figure 1.4) or 440 nm excitation (Figure S1.6). When 2-Me-4-OMe-TM was dissolved in water, the dye presented a single fluorescence lifetime of approximately 3 ns. However, when the THF proportion was increased, the long decay time increased to approximately 4.2 ns, and a second fluorescence lifetime appeared (of approximately 0.2 ns) with an increasing relative abundance. Similar trends were observed in both the emission wavelengths of 570 and 600 nm, but with a higher extent at 570 nm (see Figures 1.4 and S1.6). The appearance of the second, and even a third decay time (of approximately 1 ns) was even more noticeable using an excitation wavelength of 440 nm (Figure S1.6). Using 530 nm, we predominantly excited the 2-Me-4-OMe-TM species, forming hydrogen bonds in protic solvent (i.e., water, with τ = 3 ns, see Figure 1.4a. However, with the addition of THF, the contribution of this species decreased, favoring the species interacting with the aprotic solvent (see Figure 1.3a, where the intensity of the red-shifted peak decreased in favor of the blue-shifted peak); showing a decrease in the relative abundance associated with the 3 ns fluorescence lifetime; and increasing the relative abundance associated with the 0.2/1 ns fluorescence lifetimes (see Figure 1.4a and 1.4b, dashed lines). Because when the excitation wavelength of 530 nm was used, the 1-ns lifetime was not detected (Figure 1.4), we can assign this decay time to the probe interacting with the aprotic solvent, whereas the fast decay time of approximately 0.2 ns can be assigned to dynamics of the interconversion and formation of the hydrogen bonding species.

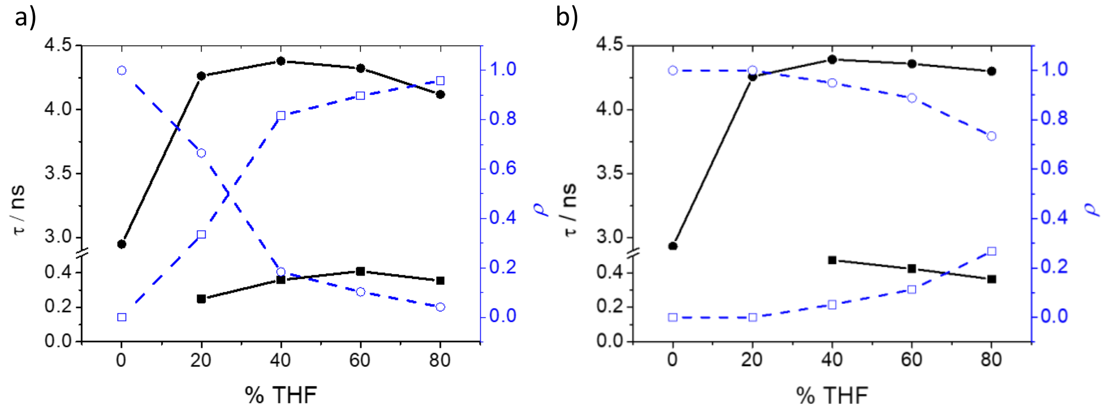

Figure 1.4. Fluorescence lifetime (τ) and relative abundance (ρ) at λ_{ex} = 530 nm at (a) λ_{em} = 570 and (b) 600 nm.

Considering the increase in the fluorescence lifetime during the transition from protic to aprotic solvent, we deliberated its applicability to detect polarity changes in the medium using the fluorescence lifetime as the analytical signal, hence making the approach suitable for fluorescence lifetime imaging microscopy (FLIM), as a polarity probe in cells. For this purpose, we suggest its use by selecting the best conditions where the sample maintains a monoexponential decay nature and with higher relative abundance (i.e., λ_{ex} = 530 nm and λ_{em} = 600 nm). For a more complete study of the changes in its properties and its behavior in the different compartments of the cells, we previously studied the photophysics of 2-Me-4-OMe-TM in a micellar system.

1.3.2 STUDY OF 2-ME-4-OME-TM EXCITED-STATE DYNAMICS IN WATER AND SDS MICELLES

Once the solvatofluorochromic behavior of 2-Me-4-OMe-TM was established, we investigated whether the interaction with the cellular membranes was the reason behind the decreased sensitivity towards phosphate. For this assessment, we compared the phosphate-mediated ESPT reaction of the dye in water and in SDS micelles.

As we showed with green-emitting xanthene dyes[6a], the presence of a phosphate-mediated ESPT reaction served as the basis for their use as intracellular phosphate sensors. Through a fluorogenic mechanism, we previously showed the application of a modified 2-Me-4-OMe-TM as a dual sensor for the simultaneous detection of intracellular phosphate ions and biothiols[12]. Since a full study of the ESPT reaction for the dye 2-Me-4-OMe-TM was lacking, we investigated its acid-base equilibrium around physiological pH by means of absorption, steady-state and time-resolved fluorescence spectroscopy (See SI, Figures S1.7 - S1.13). More interestingly, all the excited-state rate constants defining the excited-state process were calculated (Scheme 1.2, Figure S1.13 and Table S1.5). The presence of the ions of the phosphate buffer at near-neutral pH effectively promotes the ESPT reaction, causing a phosphate-dependent decrease in the fluorescence lifetime of the dye (Figure S1.13b). The solution of the excited-state kinetic scheme in the presence of phosphate would allow the use of 2-Me-4-OMe-TM as a FLIM sensor for phosphate in biological samples. However, when this dye was used intracellularly, the sensitivity was lower than expected, and specific calibration procedures were employed[12]. Therefore, as cytoplasm is a complex matrix with multiple compartments and microenvironments, we decided to evaluate the effects of membranous systems on the photophysical properties of 2-Me-4-OMe-TM. A simpler approach to studying the complex intracellular system is the use of micellar medium.

We carried out a study of the behavior of 2-Me-4-OMe-TM in SDS micelles at different phosphate concentrations and pH 7.35. Figure 1.5 shows the absorption and emission spectra at 1 mM SDS concentration and at different phosphate concentrations. Figures S1.14 and S1.15 show the absorption and emission spectra at different SDS concentrations. The addition of phosphate produced notable changes in the absorption spectra, causing a decrease in the 595 nm maximum and an increase at approximately 460 nm. This change may be due to the interaction of the dye with the micelles that formed in solution. This interaction may produce a change in the polarity of the surroundings of the dye, favoring aprotic interactions of the probe inside the micelles[21]. Following the fluorescence intensity, we calculated the critical micelle concentration (CMC) of the SDS (see Figure S1.16) in the presence of different concentrations of phosphate buffer. We found a decrease in the CMC from approximately 2.05 mM to 0.95 mM, indicating that the phosphate concentration favored micellar formation. This result can be attributed to the effect of the electrolyte on the micelle formation, which reduced the thickness of the ionic layer surrounding the polar moiety of the surfactant and allowed micellar formation via electrostatic forces[22].

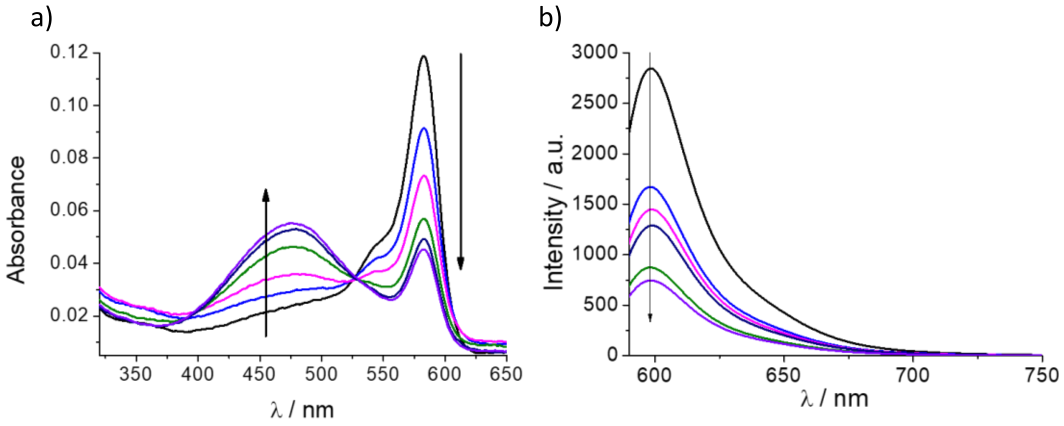

Figure 1.5. (a) Absorption and (b) Emission spectra (λ_{ex} = 583 nm) of 2-Me-4-OMe-TM at 1 mM of SDS and different phosphate concentration (5, 50, 100, 150, 175 and 200 mM) at pH 7.35. Arrows indicate the change in the spectra due to the increase in the phosphate concentration.

Next, we measured the time-resolved fluorescence of 2-Me-4-OMe-TM at different SDS and phosphate concentrations (Figure 1.6a). We observed two different behaviors: when the SDS concentration was below the CMC, between 0.1 and 1 mM, the dye's lifetime decreased with the addition of phosphate, in agreement with the buffer-mediated ESPT reaction. However, when the SDS concentration was above the CMC, between 3 and 20 mM, the lifetime of the dye increased due to the change in the polarity of the dye's surroundings and phosphate acting as a promoter of micelle formation.

Therefore, below the CMC, the effect of the phosphate buffer-mediated ESPT reaction prevailed, producing a decrease in the fluorescence lifetime[12]. In contrast, above the CMC, the phosphate buffer acted as a stabilizer of the micellar medium, and as a consequence, more micelles were formed. This process decreased the concentration of the anionic species of the dye but, at the same time, resulted in a solvent protective effect that caused an increase in the fluorescence lifetime.

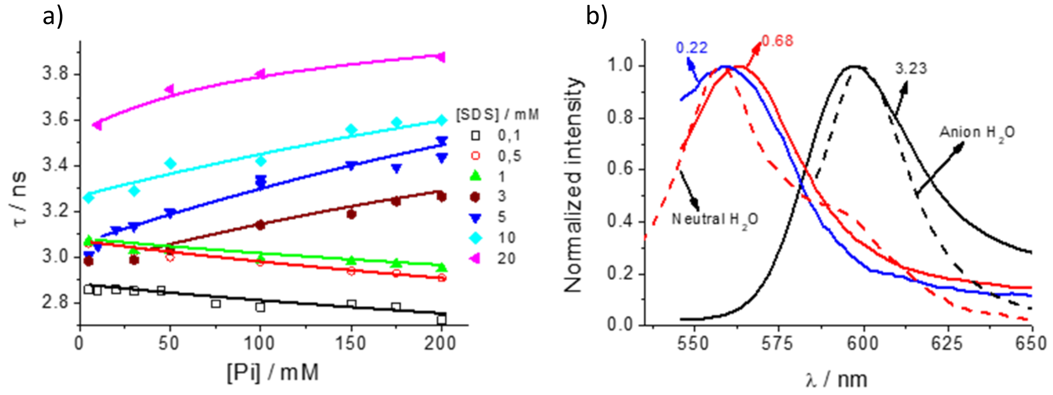

Figure 1.6. (a) Fluorescence lifetime of 2-Me-4-OMe-TM in the presence of different SDS and phosphate

concentrations, at pH 7.4. (b) SAEMS profiles of the different fluorescence lifetime components (0.22, blue; 0.68, red; and 3.23 ns, black) recovered in SDS micelles ([SDS] = 10 mM and [phosphate] = 5 mM). The normalized spectra from the anionic (dashed black line) and neutral (dashed red line) species of 2-Me-4-OMe-TM in aqueous solution are also plotted.

Finally, to identify each of the species in the micellar system unambiguously, through time-resolved data, we calculated the species-associated emission spectra (SAEMS) of each of the decay time components. Figure 1.6b shows the SAEMS obtained from the three fluorescence lifetimes obtained in the micellar medium ([SDS] = 10 mM and [phosphate] = 5 mM). Moreover, in Figure 1.6b, the emission spectra of the two prototropic species involved in aqueous solution (dashed lines) are also presented for comparison. The species with τ = 3.23 ns presented a maximum at 600 nm, which clearly overlapped with the anionic species in aqueous solution at pH 9.00. Therefore, this spectrum can be associated with the anionic species of the 2-Me-4-OMe-TM. We assign the slight red-shift to the difference in the polarity between the aqueous and SDS solutions. We used the same argument to identify the neutral species of the fluorophore, which prevails in aqueous solution at pH 4.00, overlapping with the SAEMS of the component with τ = 0.22 ns. The third component, with τ = 0.68 ns, presented a SAEMS with a maximum that was red-shifted with respect to the neutral species. The presence of this fluorescence lifetime can be associated with the interaction of the dye and the micelles, which could be produced in the interior of the micelles or in the interphase. A similar behavior was found in other xanthene derivatives when introduced in reverse micelles[23] or interacting with macromolecules[24].

Anionic species are most stabilized in the excited state by water molecules or other protic solvents, producing a decrease in the difference of energy between the ground and excited states. This stabilization is not present in aprotic solvents, as in micelles, avoiding this stabilization and producing a blue-shifted effect[25]. Both species are preferentially located in their microenvironment, so the longest fluorescence lifetime is associated with the anionic form that remains in the solvent despite the micelles. Although the quantity of anionic species is decreased, its fluorescence lifetime is dependent on the polarity of the solvent, which is determined by the number of micelles formed. We consider the micellar system as an approximation to simulate the cellular interior. The studied fluorophore could be used as a polarity sensor for different intracellular compartments.

1.3.3 BIOIMAGING

First, we checked the intracellular uptake and accumulation of 2-Me-4-OMe-TM in HEK293 cells. The fluorescence intensity images are presented in Figures 1.7a-c (and Figure S1.17), representing a time point 30 seconds after the fluorophore addition to the extracellular medium. These intensity images show a specific accumulation pattern similar to previous silicon-substituted xanthenes[5]. Moreover, the corresponding lifetime images (Figures 1.7d-f, and Figure S1.17) exhibited differences in the average lifetime values, which were dependent on the microenvironment polarity of the regions where the probe was located.

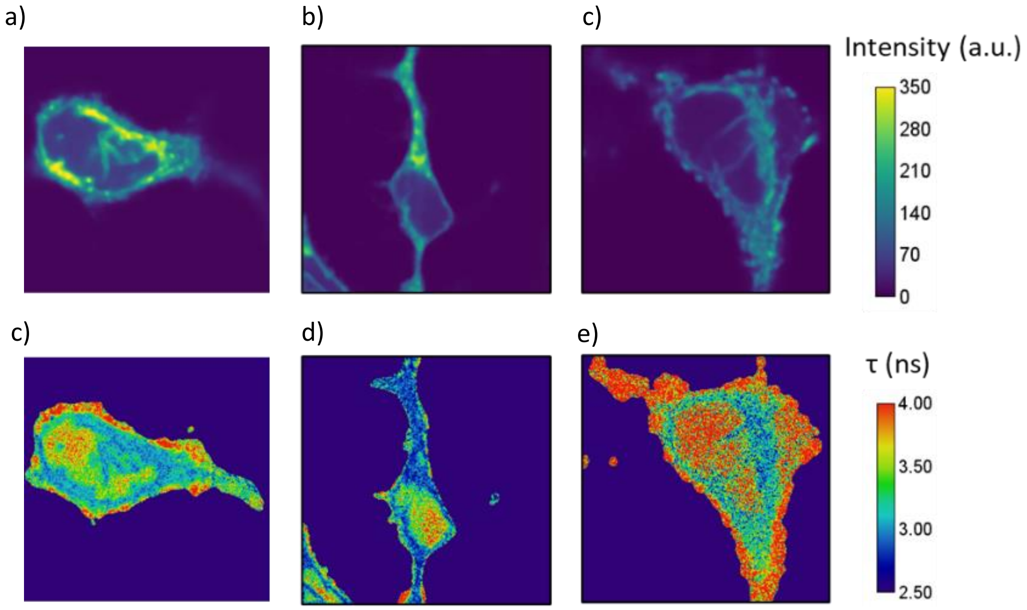

Figure 1.7. FLIM of 2-Me-4-OMe-TM in HEK293 cells. Images (a), (b) and (c) show the intensity images and (d), (e) and (f) the fluorescence lifetime images from (a), (b) and (c), respectively.

As observed in the FLIM images, there are three well-differentiated lifetimes in the cells: the structure surrounding the cell, the nuclei and the cytoplasmic regions. The three average fluorescence lifetimes recovered from these three regions of a total of seven cells were 3.96 ± 0.08, 3.67 ± 0.09 and 3.00 ± 0.09 ns, respectively. The anionic form was predominantly excited in these FLIM images, and it presented a longer lifetime in a nonpolar environment, such as the surrounding structures that can be associated with the plasma membranes and other structures associated with proteins and other macromolecules. The dye located at the nuclei also presented longer fluorescence lifetime values than that dissolved in the cytoplasm but lower than that incorporated in the plasma membrane structures. This result could be explained by the less polar microenvironment, typical of the interior of the nucleus[26]. Finally, the lowest fluorescence lifetime of the dye was found in the cytoplasm, which presented the highest polarity.

However, while we analyzed the cytoplasmic region as a whole, a more detailed inspection of the intensity images allowed the clear discrimination of different structures that could be associated with mitochondria and other intracellular organelles (see Figure 1.8 and Figure S1.18). Although the mechanism of the incorporation of the dye into these structures is not well known, there are some hypotheses that imply the chemical equilibrium between the neutral and anionic forms and the accumulation of the anion formic inside the mitochondria due to the slightly higher intramitochondrial pH[27]. According to these authors, only the more lipophilic neutral form is able to cross the mitochondrial membrane; inside mitochondria, the higher pH shifts the chemical equilibrium to favor the anionic form; and as this species is less lipophilic, it is retained inside the organelle. In any case, the accumulation of the probe in these structures allows easy discrimination of the regions with lower intensity and therefore isolation to study the polarity of these structures. Figures 1.8a-d and S1.18 show the complete FLIM images and the isolated regions using an intensity mask (where only the more intense pixels were selected), which correspond to different intracellular structures. Interestingly, the analyzed region of interest (Figure 1.9c-d and S1.18) presented two different fluorescence lifetimes, indicating different environments.

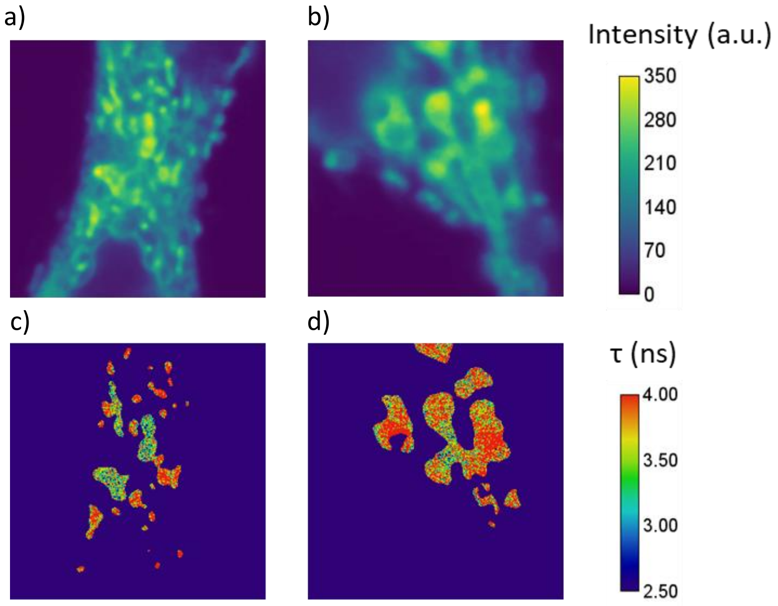

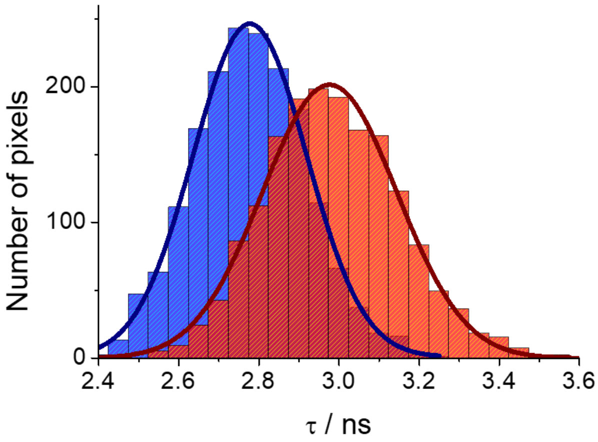

Figure 1.8. FLIM images of 2-Me-4-OMe-TM in HEK293 cells. (a) and (b) show the intensity images, where the accumulation of 2-Me-4-OMe-TM in some intracellular structures is observed. (c) and (d) show the fluorescence lifetime images from the isolated regions following a restrictive intensity-based threshold. (e) Fluorescence lifetime histograms from the two different intracellular structures recovered from Figures 1.11a-d and S1.17.

We calculated the histograms of fluorescence lifetimes coming from these two intracellular structures. The distributions are shown in Figure 1.9e, where two clearly different Gaussian curves were obtained. This probe accumulation in intracellular organelles together with the dye's capacity to measure polarity via the fluorescence lifetime could be useful in cancer-related biomedical research since polarity changes in tumoral mitochondria have been described[28].

1.4 CONCLUSIONS

In this work, we performed a thorough photophysical study of the probe 2-Me-4-OMe-TM. From this study, we found that the dye is suitable for detecting phosphate through a buffer-mediated ESPT reaction in aqueous solution. Moreover, it has been demonstrated that 2-Me-4-Ome-TM presents high sensitivity to the solvent's acidity, forming specific hydrogen bonding interactions, and polarity. The polarity affects the equilibrium of the prototropic species but also increases the fluorescence lifetime of the anionic form. The kosmotropic effect of the phosphate buffer on micelle formation was observed through the fluorescence emission of 2-Me-4-Ome-TM. Finally, we used the probe to detect differences in polarity between different regions of cells using FLIM microscopy. We found a specific pattern of intensity where the probe accumulates in some organelles. This finding allowed the isolation of these organelles to determine their polarity.

1.5 EXPERIMENTAL SECTION

1.5.1 INSTRUMENTATION

UV-visible absorption spectrophotometry and steady-state fluorimetry were carried out using a Lambda 650 UV-visible spectrophotometer (PerkinElmer, Waltham, MA, USA) and a Jasco FP-8300 spectrofluorometer (Jasco, Tokyo, Japan), respectively. Fluorescence lifetime decays were recorded by the single-photon timing method using a FluoTime 200 fluorometer (PicoQuant GmbH, Berlin, Germany). The excitation source was a pulsed diode laser, LDH−530 (PicoQuant), operated at a repetition rate of 20 MHz. Fluorescence decay histograms were collected at 600, 605 and 610 nm over 1320 channels, with a time increment per channel of 37 ps. Histograms of the instrument response functions (using a LUDOX scatterer) and sample decays were recorded until they reached 2×10^4 counts in the peak channel. The fluorescence decay traces were globally analyzed using an iterative deconvolution method with exponential models using FluoFit software (PicoQuant).

1.5.2 CELL CULTURE

HEK293 cells (ATCC: CRL-1573) were provided by the Cell Culture Facility, University of Granada. HEK cells were grown in Dulbecco´s modified Eagle´s medium (DMEM) supplemented with 10% (v/v) FBS, 2 mM glutamine, 100 U/mL penicillin and 0.1 μg/mL streptomycin in a humidified 5% CO_2 incubator.

For the FLIM microscopy experiments, cells were seeded onto 25 mm coverslips in 6-well plates at a density of 22.5×10^4 cells/well. For their visualization, the samples were washed three times using phosphate buffered saline (PBS) and bathed into Krebs-Ringer phosphate (KRP) buffer composed of 118 mM NaCl, 5 mM KCl, 1.3 mM $CaCl_2$, 1.2 mM KH_2PO_4 and 30 mM HEPES with 2×10^{-7} M of 2-Me-4-OMe-TM.

1.5.3 SPECIES-ASSOCIATED EMISSION SPECTRA (SAEMS)

Fluorescence decay traces were collected from 546 to 670 nm, with a $\Delta\lambda$ of 2 nm, in a discrete period of time, subsequently corrected and then normalized to the corresponding steady-state emission spectrum. The equation used to calculate the SAEMS for each detected species, *i*, was the following:

$$SAEMS\ (\lambda_{em})_i = \frac{A_{i,\lambda_{em}} \times \tau_i}{\sum(A_{i,\lambda_{em}} \times \tau_i)} \times I_{ss,\lambda_{em}}$$

where $A_{i,\lambda_{em}}$ is the amplitude of species *i* at the emission wavelength λ_{em}, τ_i is the fluorescence lifetime of species *i*, and $I_{ss,\lambda_{em}}$ is the steady-state emission spectrum.

1.5.4 FLIM BIOIMAGING

FLIM images were recorded on a MicroTime 200 fluorescence-lifetime microscope system (PicoQuant) using the same excitation source described earlier. The light beam passed through a dichroic mirror (532dcxr, Chroma) and through the oil immersion objective (1.4 NA, 100×) specific to an inverted microscope system (IX-71, Olympus). The fluorescence emitted light was collected back through the objective, filtered by a long-pass filter (550LP, AHF/Chroma), and directed to a 75-µm confocal aperture. The light was transmitted to a 630/60 bandpass filter (Thorlabs) and focused on single-photon avalanche diodes (SPCM-AQR 14, Perkin Elmer). The data were collected by a TimeHarp 200 TCSPC module (PicoQuant), and raw fluorescence lifetime images were acquired by a scanner with 512 × 512-pixel resolution. To obtain the fitted FLIM images, a spatial binning of 2 × 2 pixels was performed with SymphoTime software, and the matrix data were exported and analyzed by a home-coded Fiji ([Fiji Is Just] ImageJ) program[16].

BIBLIOGRAPHY

1 Ueno, T.; Urano, Y.; Setsukinai, K.; Takakusa, H.; Kojima, H.; Kikuchi, K.; Ohkubo, K.; Fukuzumi, S.; Nagano, T., Rational principles for modulating fluorescence properties of fluorescein. *J. Am. Chem. Soc.* **2004,** *126* (43), 14079-85.

2 Mottram, L. F.; Boonyarattanakalin, S.; Kovel, R. E.; Peterson, B. R., The Pennsylvania green fluorophore: A hybrid of Oregon Green and Tokyo Green for the construction of hydrophobic and pH-insensitive molecular probes. *Org. Lett.* **2006,** *8* (4), 581-584.

3 Martinez-Peragon, A.; Miguel, D.; Jurado, R.; Justicia, J.; Alvarez-Pez, J. M.; Cuerva, J. M.; Crovetto, L., Synthesis and photophysics of a new family of fluorescent 9-alkyl-substituted xanthenones. *Chemistry (Easton)* **2014,** *20* (2), 447-55.

4 Egawa, T.; Koide, Y.; Hanaoka, K.; Komatsu, T.; Terai, T.; Nagano, T., Development of a fluorescein analogue, TokyoMagenta, as a novel scaffold for fluorescence probes in red region. *Chem. Commun.* **2011,** *47* (14), 4162-4164.

5 Grimm, J. B.; Brown, T. A.; Tkachuk, A. N.; Lavis, L. D., General Synthetic Method for Si-Fluoresceins and Si-Rhodamines. *ACS Central Science* **2017,** *3* (9), 975-985.

6 Ikeno, T.; Nagano, T.; Hanaoka, K., Silicon-substituted Xanthene Dyes and Their Unique Photophysical Properties for Fluorescent Probes. *Chemistry – An Asian Journal* **2017,** *12* (13), 1435-1446.

7 Deng, F.; Xu, Z., Heteroatom-substituted rhodamine dyes: Structure and spectroscopic properties. *Chin. Chem. Lett.* **2018,** *in press DOI: https://doi.org/10.1016/j.cclet.2018.12.012*.

8 Kushida, Y.; Nagano, T.; Hanaoka, K., Silicon-substituted xanthene dyes and their applications in bioimaging. *Analyst* **2015,** *140* (3), 685-695.

9 Hirabayshi, K.; Hanaoka, K.; Takayanagi, T.; Toki, Y.; Egawa, T.; Kamiya, M.; Komatsu, T.; Ueno, T.; Terai, T.; Yoshida, K.; Uchiyama, M.; Nagano, T.; Urano, Y., Analysis of Chemical Equilibrium of Silicon-Substituted Fluorescein and Its Application to Develop a Scaffold for Red Fluorescent Probes. *Anal. Chem.* **2015,** *87* (17), 9061-9069.

10 Crovetto, L.; Orte, A.; Paredes, J. M.; Resa, S.; Valverde, J.; Castello, F.; Miguel, D.; Cuerva, J. M.; Talavera, E. M.; Alvarez-Pez, J. M., Photophysics of a Live-Cell-Marker, Red Silicon-Substituted Xanthene Dye. *J. Phys. Chem. A* **2015,** *119* (44), 10854-10862.

11 Paredes, J. M.; Giron, M. D.; Ruedas-Rama, M. J.; Orte, A.; Crovetto, L.; Talavera, E. M.; Salto, R.; Alvarez-Pez, J. M., Real-Time Phosphate Sensing in Living Cells using Fluorescence Lifetime Imaging Microscopy (FLIM). *J. Phys. Chem. B* **2013,** *117* (27), 8143-8149.

12 Zhang, Q.; Xiao, K.; Paredes, J. M.; Mamonova, T.; Sneddon, W. B.; Liu, H.; Wang, D.; Li, S.; McGarvey, J. C.; Uehling, D.; Al-awar, R.; Joseph, B.; Jean-Alphonse, F.; Orte, A.; Friedman, P. A., Parathyroid hormone initiates dynamic NHERF1 phosphorylation cycling and conformational changes that regulate NPT2A-dependent phosphate transport. *J. Biol. Chem.* **2019**.

13 Ruedas-Rama, M. J.; Alvarez-Pez, J. M.; Crovetto, L.; Paredes, J. M.; Orte, A., FLIM Strategies for Intracellular Sensing. In *Advanced Photon Counting: Applications, Methods, Instrumentation*, Kapusta, P.; Wahl, M.; Erdmann, R., Eds. Springer International Publishing: Cham, 2015; pp 191-223.

14 Hille, C.; Berg, M.; Bressel, L.; Munzke, D.; Primus, P.; Löhmannsröben, H. G.; Dosche, C., Time-domain fluorescence lifetime imaging for intracellular pH sensing in living tissues. *Analytical and Bioanalitical Chemistry* **2008,** *391*, 1871-1879.

15 Sagolla, K.; Lohmannsroben, H. G.; Hille, C., Time-resolved fluorescence microscopy for quantitative Ca2+ imaging in living cells. *Anal. Bioanal. Chem.* **2013,** *405* (26), 8525-8537.

16 Okabe, K.; Inada, N.; Gota, C.; Harada, Y.; Funatsu, T.; Uchiyama, S., Intracellular temperature mapping with a fluorescent polymeric thermometer and fluorescence lifetime imaging microscopy. *Nature Communications* **2012,** *3*.

17 Kuimova, M. K.; Yahioglu, G.; Levitt, J. A.; Suhling, K., Molecular rotor measures viscosity of live cells via fluorescence lifetime imaging. *J. Am. Chem. Soc.* **2008,** *130* (21), 6672-6673.

18 Shimolina, L. E.; Izquierdo, M. A.; Lopez-Duarte, I.; Bull, J. A.; Shirmanova, M. V.; Klapshina, L. G.; Zagaynova, E. V.; Kuimova, M. K., Imaging tumor microscopic viscosity in vivo using molecular rotors. *Sci. Rep.* **2017,** *7*.

19 Herrero-Foncubierta, P.; Paredes, J. M.; Giron, M. D.; Salto, R.; Cuerva, J. M.; Miguel, D.; Orte, A., A Red-Emitting, Multidimensional Sensor for the Simultaneous Cellular Imaging of Biothiols and Phosphate Ions. *Sensors* **2018,** *18* (1), 18.

20 Loving, G. S.; Sainlos, M.; Imperiali, B., Monitoring protein interactions and dynamics with solvatochromic fluorophores. *Trends Biotechnol.* **2010,** *28* (2), 73-83.

21 Klymchenko, A. S.; Mely, Y., Fluorescent Environment-Sensitive Dyes as Reporters of Biomolecular Interactions. In *Fluorescence-Based Biosensors: From Concepts to Applications*, Morris, M. C., Ed. 2013; Vol. 113, pp 35-58.

22 Marini, A.; Munoz-Losa, A.; Biancardi, A.; Mennucci, B., What is Solvatochromism? *J. Phys. Chem. B* **2010,** *114* (51), 17128-17135.

23. Reichardt, C., Solvatochromic Dyes as Solvent Polarity Indicators. *Chem. Rev.* **1994,** *94* (8), 2319-2358.

24. Machado, V. G.; Stock, R. I.; Reichardt, C., Pyridinium N-Phenolate Betaine Dyes. *Chem. Rev.* **2014,** *114* (20), 10429-10475.

25 Mera-Adasme, R.; Domínguez, M., A computationally-derived model for the solvatochromism of p-phenolates with high predictive power. *PCCP* **2018,** *20* (26), 18127-18132.

26 Catalan, J., Toward a Generalized Treatment of the Solvent Effect Based on Four Empirical Scales: Dipolarity (SdP, a New Scale), Polarizability (SP), Acidity (SA), and Basicity (SB) of the Medium. *J. Phys. Chem. B* **2009,** *113* (17), 5951-5960.

27 Schindelin, J.; Arganda-Carreras, I.; Frise, E.; Kaynig, V.; Longair, M.; Pietzsch, T.; Preibisch, S.; Rueden, C.; Saalfeld, S.; Schmid, B.; Tinevez, J. Y.; White, D. J.; Hartenstein, V.; Eliceiri, K.; Tomancak, P.; Cardona, A., Fiji: an open-source platform for biological-image analysis. *Nat. Methods* **2012,** *9* (7), 676-682.

28 Lakowicz, J. R., *Principles of Fluorescence Spectroscopy*. 3rd ed.; Springer: 2006.

29 Patra, D.; Barakat, C., Synchronous fluorescence spectroscopic study of solvatochromic curcumin dye. *Spectrochimica Acta Part a-Molecular and Biomolecular Spectroscopy* **2011,** *79* (5), 1034-1041.

30 Talone, C. J.; Gao, J. Y.; Lynch, J. R.; Tanu, R. M.; Deyrup, S. T., Determination of the ground- and excited-state dipole moments of bromocresol purple in protic and aprotic

solvents. *Spectrochimica Acta Part a-Molecular and Biomolecular Spectroscopy* **2016,** *156*, 138-142.

31 Cerón-Carrasco, J. P.; Jacquemin, D.; Laurence, C.; Planchat, A.; Reichardt, C.; Sraïdi, K., Solvent polarity scales: determination of new ET(30) values for 84 organic solvents. *J. Phys. Org. Chem.* **2014,** *27* (6), 512-518.

32 Mallick, A.; Bera, S. C.; Maiti, S.; Chattopadhyay, N., Fluorometric investigation of interaction of 3-acetyl-4-oxo-6,7-dihydro-12H indolo- 2,3-a quinolizine with bovine serum albumin. *Biophys. Chem.* **2004,** *112* (1), 9-14.

33 Fuguet, E.; Rafols, C.; Roses, M.; Bosch, E., Critical micelle concentration of surfactants in aqueous buffered and unbuffered systems. *Anal. Chim. Acta* **2005,** *548* (1-2), 95-100.

34 Orte, A.; Ruedas-Rama, M. J.; Paredes, J. M.; Crovetto, L.; Alvarez-Pez, J. M., Dynamics of Water-in-Oil Nanoemulsions Revealed by Fluorescence Lifetime Correlation Spectroscopy. *Langmuir* **2011,** *27* (21), 12792-12799.

35 Paredes, J. M.; Crovetto, L.; Orte, A.; Lopez, S. G.; Talavera, E. M.; Alvarez-Pez, J. M., Photophysics of the Interaction between a Fluorescein Derivative and Ficoll. *The Journal of Physical Chemistry A* **2011,** *115* (46), 13242-13250.

36 Mishra, P. P.; Koner, A. L.; Datta, A., Interaction of Lucifer yellow with cetyltrimethyl ammonium bromide micelles and the consequent suppression of its non-radiative processes. *Chem. Phys. Lett.* **2004,** *400* (1-3), 128-132.

37 Theillet, F.-X.; Binolfi, A.; Frembgen-Kesner, T.; Hingorani, K.; Sarkar, M.; Kyne, C.; Li, C.; Crowley, P. B.; Gierasch, L.; Pielak, G. J.; Elcock, A. H.; Gershenson, A.; Selenko, P., Physicochemical Properties of Cells and Their Effects on Intrinsically Disordered Proteins (IDPs). *Chem. Rev.* **2014,** *114* (13), 6661-6714.

38 Xiong, X. Q.; Song, F. L.; Chen, G. W.; Sun, W.; Wang, J. Y.; Gao, P.; Zhang, Y. K.; Qiao, B.; Li, W. F.; Sun, S. G.; Fan, J. L.; Peng, X. J., Construction of Long-Wavelength Fluorescein Analogues and Their Application as Fluorescent Probes. *Chemistry-a European Journal* **2013,** *19* (21), 6538-6545.

39 Zhu, H.; Fan, J.; Du, J.; Peng, X., Fluorescent Probes for Sensing and Imaging within Specific Cellular Organelles. *Acc. Chem. Res.* **2016,** *49* (10), 2115-2126.

SUPPORTING INFORMATION

SYNTHESIS

2-Me-4-OMe-TM has been synthesized as previously described.[1] In short, synthesis of the compound 2-Me-4-OMe-TM was carried out by nucleophilic addition of the organolithium derivative generated by the reaction of 4-bromo-3-methoxyphenol with *n*-BuLi to the previously described ketone (**I**, see Scheme S1.1).[2, 3] Later treatment with diluted HCl afforded compound 2-Me-4-OMe-TM in a 70% yield.

The purification of 2-Me-4OMe-TM was carried out by flash chromatography on Merck silica gel 50 using CH_2Cl_2:MeOH mixtures. A subsequent purification step was performed using preparative TLC in the same mixture of solvents. The determination and characterization of 2-Me-4OMe-TM was carried out by ^{1}H-NMR, ^{13}C-NMR and high resolution mass spectrometry (HRMS).

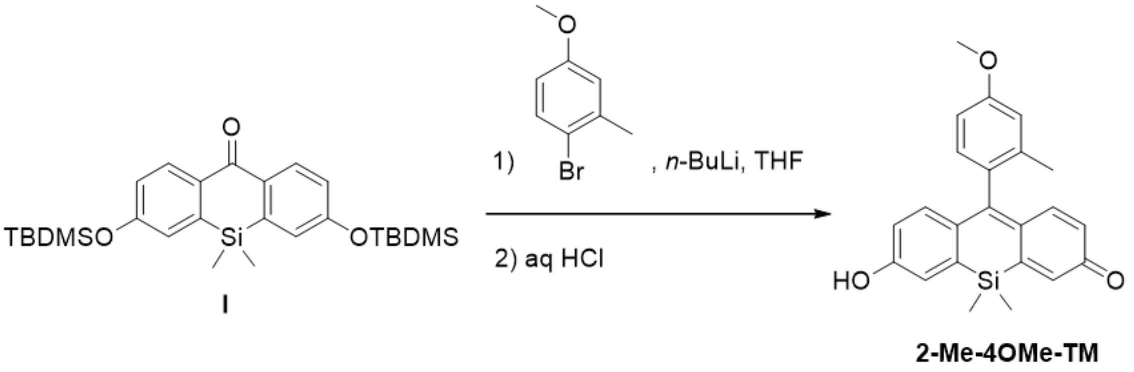

Scheme S1.1. Synthesis of 2-Me-4OMe-TM.

SAMPLE PREPARATION

A stock solution of 2-Me-4-OMe-TM was prepared by dissolving the purified solid in DMSO at a concentration of 4×10^{-4} M. The buffer reagents used were $NaH_2PO_4\cdot H_2O$ and $Na_2HPO_4\cdot 7H_2O$ (Sigma-Aldrich, Spain). Stock solutions (0.5 M) of these reagents were prepared. All the aqueous solutions were prepared with ultrapure water (18.2 MΩ-cm). When necessary, the pH was adjusted using 0.1 M NaOH or 0.1 M $HClO_4$. 1-Butanol, acetone, acetonitrile, chloroform, cyclohexane, dibutylether, diethylether, dioxane, DMSO, ethyl acetate, ethanol, methanol, THF and toluene were all from Sigma-Aldrich. A stock solution of 50 mM SDS, ($NaC_{12}H_{25}SO_4$) (Sigma-Aldrich) was prepared. Micelle samples were prepared using different SDS concentrations and adding different phosphate concentrations from the stock solutions. The pH values were maintained at 7.35.

QUANTUM YIELD CALCULATION

The relative fluorescence quantum yield values were determined using the following formula[4]:

$$\Phi = \Phi_R \cdot \frac{\mathrm{I}}{I_R} \cdot \frac{OD_R}{\mathrm{OD}} \cdot \frac{n^2}{n_R^2}$$

Where Φ and Φ_R denote the fluorescence quantum yield of the sample and the reference respectively, I and I_R the integrated fluorescence spectra of the sample and the reference, OD and OD_R the absorption at the excitation wavelength of the sample and the reference and n and n_R the refractive index of the solvent where the sample and reference are dissolved. As references, we have used fluorescein in 0.01 M NaOH ($\Phi = 0.91$)[5] for samples that were excited at 440 nm with a range of emission corresponding to the blue-shifted peaks, and rhodamine 101 in ethanol ($\Phi = 0.98$)[6] for samples that were excited at 530 nm and a range of emission corresponding to the red-shifted peaks. The emission spectra were measured at excitation wavelength of 440, and 530 nm, using 5nm and 2.5nm for excitation and emission slits at room temperature.

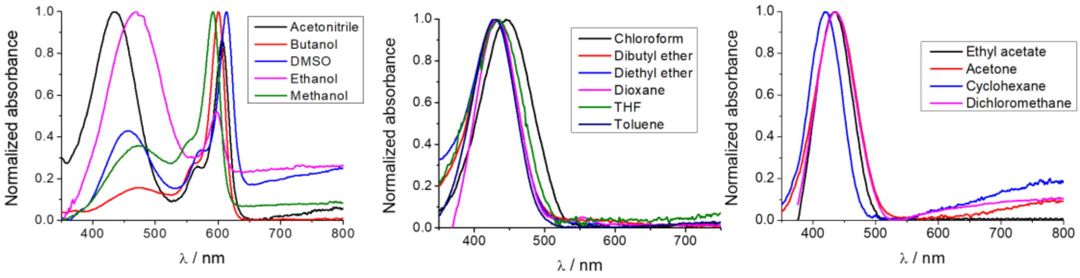

Figure S1.1. Normalized absorption spectra of 2-Me-4-OMe-TM in different solvents. The spectra are represented in separate panels for clarity.

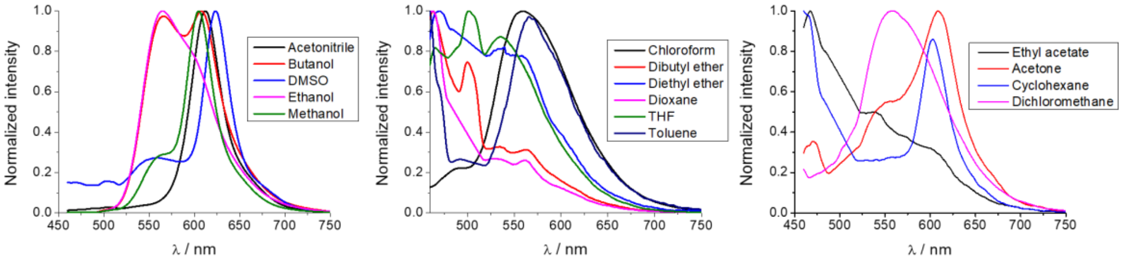

Figure S1.2. Normalized fluorescence emission spectra (λ_{ex}= 440 nm) of 2-Me-4-OMe-TM in different solvents. The spectra are represented in separate panels for clarity.

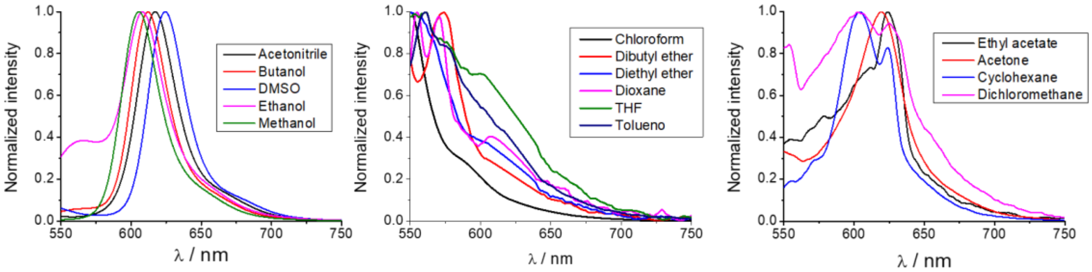

Figure S1.3. Normalized fluorescence emission spectra (λ_{ex}= 530 nm) of 2-Me-4-OMe-TM in different solvents. The spectra are represented in separate panels for clarity.

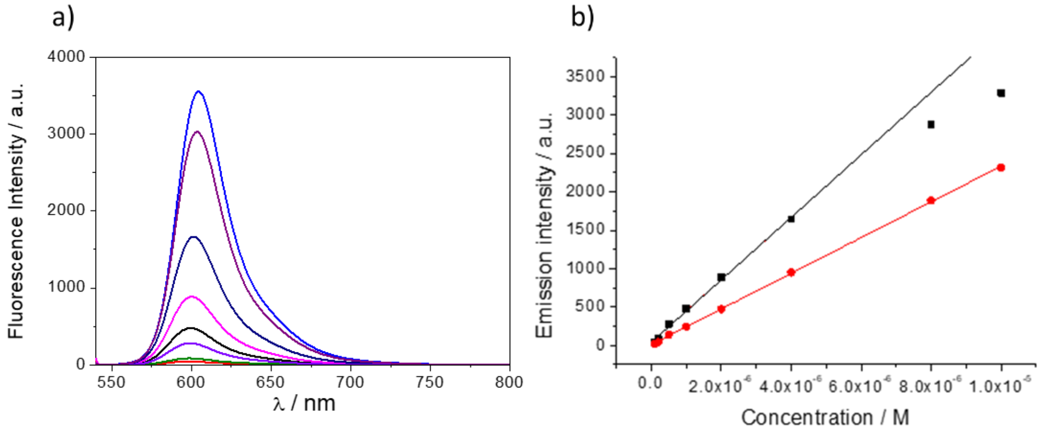

Figure S1.4. (a) Fluorescence emission spectra (λ_{ex}= 530 nm) of different concentration of 2-Me-4-OMe-TM (from $1{\times}10^{-7}$ M until $1{\times}10^{-5}$ M) in aqueous solution. (b) Kavanagh's Law at two different emission wavelengths (black squares 599 nm and red circles 620 nm).

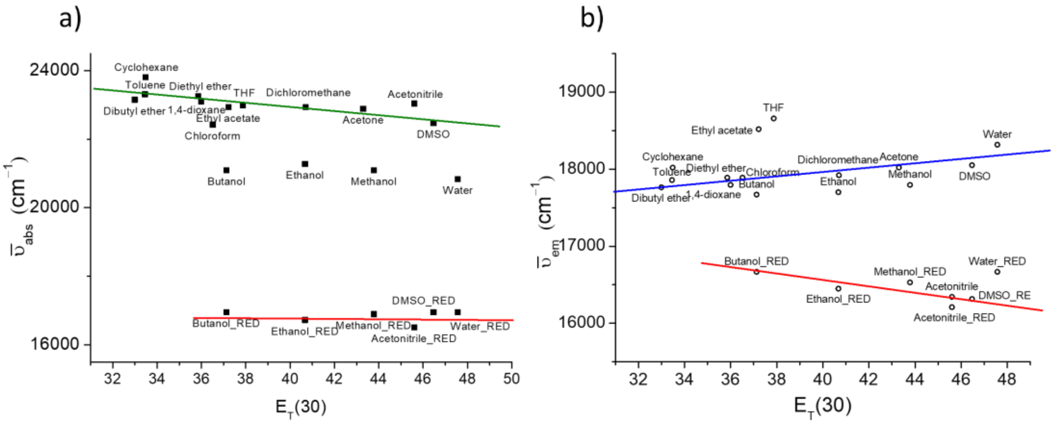

Figure S1.5. Plot of the absorption (a) and emission (b) maxima wavenumber as a function of the $E_T(30)$ parameter of the different solvents marked. Red lines and solvent with _RED inserted indicate the red-shifted band of the dye.

Table S1.1						
Solvent	**λ^{max}_{abs} / nm**[a]		**λ^{max}_{em} / nm**[b]		**QY**	
			(λ_{ex} = 440 nm)	**(λ_{ex} = 530 nm)**	**440**	**530**
Acetone	437	–	609	619	< 0.001	–
Acetonitrile	434 (100%)	606 (87%)	612	617	0.007	0.009
Butanol	474 (17%)	600 (100%)	566/608	612	0.110	0.297
Cyclohexane	420	–	460/602	604	0.004	–
Chloroform	446	–	559	550	0.011	0.023
Dibutylether	432	–	464	574	0.001	–
Dichloromethane	437	–	558	604	0.001	–
Diethylether	430	–	469	552	0.001	–
Dioxane	433	–	463	555	0.002	–
DMSO	456 (12%)	613 (100%)	555	590	0.071	0.107
Ethyl acetate	434	–	468	611	0.001	–
Ethanol	470 (100%)	598 (32%)	565/(s 608)	(565)/608	0.081	0.060
Methanol	474 (28%)	592 (100%)	(s 562) /605	605	0.058	0.267
THF	435	–	535	557	0.005	–
Toluene	429	–	460/567	560	0.001	–
Water (aqNaOH)	–	583	590	600		0.44

[a] In solvents in which the dye exhibited two absorption bands, numbers in brackets represent the relative height of the two peaks.

[b] The excitation wavelengths were selected according to the availability of excitation laser sources in our laboratory. These two excitation lasers approximately correspond to the first and second absorption band, respectively

Table S1.2. Amplitudes and fluorescence lifetimes obtained from 2-Me-4-OMe-TM in different solvents

Solvent	**A_1 / %**	**τ_1 / ns**	**A_2/ %**	**τ_2 / ns**	**A_3 / %**	**τ_3 / ns**	**τ_{av}/ ns***
Acetone	1.13	3.72	98.62	0.018	0.25	1.11	2.55
Acetonitrile	1.44	4.05	98.47	0.013	0.09	1.12	3.27
Butanol	0.26	4.19	88.65	0.018	11.09	1.02	1.15
Cyclohexane	1.69	3.27	96.17	0.026	2.14	1.24	2.00
Chloroform	0.37	5.26	49.81	0.040	49.81	0.25	0.36
Dibutyl ether	39.47	14.38	57.86	0.075	2.67	1.41	9.92
Dichloromethane	–	–	99.65	0.102	0.35	1.16	0.14
Diethyl ether	0.71	14.16	97.44	0.049	1.85	2.32	7.96
Dioxane	0.98	16.69	94.20	0.074	4.82	1.71	9.11

DMSO	0.01	5.79	99.93	0.015	0.05	1.05	0.34
Ethyl acetate	5.15	11.16	69.58	0.704	25.27	2.77	4.93
Ethanol	–	–	58.73	0.042	41.27	0.64	0.58
Methanol	4.11	4.45	95.89	0.149	--	--	2.57
THF	12.03	16.36	38.76	0.515	49.21	3.47	9.86
Toluene	8.35	18.22	72.60	0.637	19.05	3.97	11.32

- τav is calculated-based in the equation $\tau_{av} = \frac{\sum_i A_i \tau_i^2}{\sum_i A_i \tau_i}$

Table S1.3. Dielectric constant and refractive index values used in this work*

Solvent	***ε***	***n***
1-Butanol	17.8	1.399
Acetone	21.01	1.359
Acetonitrile	36.64	1.34423
Chloroform	4.81	1.446
Cyclohexane	2.02	1.426
Dibutyl ether	3.1	1.399
Diethyl ether	4.267	1.353
Dioxane	2.21	1.422
DMSO	47	1.358
Ethyl acetate	5.99	6.02
Ethanol	24	1.524
Methanol	33	1.329
THF	7.5	1.405
Toluene	2.4	1.4961
Water	80.1	1.33

*Refractive index used in this work come from the Refractive index database (https://refractiveindex.info) and dielectric constant from[7]

LIPPERT-MATAGA EQUATION

$$\overline{\upsilon_A} - \overline{\upsilon_F} = \frac{2}{hc}\left(\frac{\varepsilon - 1}{2\varepsilon + 1} - \frac{n^2 - 1}{2n^2 + 1}\right)\frac{(\mu_E - \mu_G)^2}{a^3} + k$$

In the Lippert-Mataga equation, *h* is the Planck constant, *c* represents the light speed in vacuum, *a* is the radius of the cavity where the dye is allocated, $\overline{\upsilon_A}$and $\overline{\upsilon_F}$ are the absorption and emission wavenumber, respectively, and k is a constant representing the difference between the absorption and emission wavenumbers in the vacuum. Following this approach, the fluorophore is considered as a dipole plunged in a medium with equal dielectric constant at any point. The effects of ε and *n* on the Stokes shift can be explained as follows: an increase in *n* produces an instantaneous stabilization of the ground and excited states due to an electronic redistribution producing a decrease in the difference of the energy between the ground and excited state. This effect is the reason why most of the chromophores show a red-shift in the absorption spectra. However, although an increase in ε also stabilizes both states, it occurs in the excited state after a reorientation of solvent dipoles, i.e., this process requires the movement of the complete solvent molecules[4]. Orientation polarizability (Δf) is the combination of both parameters as indicated in the equation and is included in the Lippert-Mataga equation.

$$\Delta f = \frac{\varepsilon - 1}{2\varepsilon + 1} - \frac{n^2 - 1}{2n^2 + 1}$$

Table S1.4. Estimated coefficients ± standard errors and correlation coefficient (r) for the multilinear regression analyses of $\tilde{\nu}_{abs}$ and$\tilde{\nu}_{em}$ The estimates are expressed in cm^{-1}.

			A₀	*b (SA)*	*c (SB)*	*d (SP)*	*e (SdP)*	*r*
Aprotic +	Et_2O	$\tilde{\nu}_{abs}$	(2.62 ± 0.14) × 10^4	-2554 ± 339	-1286 ± 349	-3280 ±1843	-769 ± 343	0.9537
	Acetone		(2.46 ± 0.33) × 10^4		-1013 ± 825	-726 ± 4306	-1966 ± 723	**0.6652**
	EtOAc		(2.23 ± 0.17) × 10^4	-2424 ± 482		-149 ± 2341	-640 ± 489	0.8932

	Bu$_2$O THF Chloroform 1,4-Dioxane CH$_2$Cl$_2$ Cyclohexane DMSO Toluene MeOH MeCN EtOH BuOH DMSO Water		$(2.38 \pm 0.03) \times 10^4$	-2443 ± 362	-1000 ± 336		-642 ± 365	0.9399
			$(252 \pm 0.15) \times 10^4$	-2905 ± 347	-1206 ± 401	-2424 ± 482		0.9318
		$\tilde{\nu}_{em}$	$(2.72 \pm 0.48) \times 10^4$	-687± 1148	-1115 ± 1182	-5715 ± 6242	-6272 ± 1162	0.8934
			$(2.68 \pm 0.46) \times 10^4$		-1042 ± 1143	-5028 ± 5969	-6595 ± 1003	0.8897
			$(2.48 \pm 0.40) \times 10^4$	-574 ± 1136		-2999 ± 5514	-6051 ± 1129	0.8842
			$(2.29 \pm 0.08) \times 10^4$	-494 ± 1121	-617 ± 1042		-6051 ± 1129	0.8847
			$(1.89 \pm 0.83) \times 10^4$	-3553 ± 1860	-465 ± 2149	1285 ± 1136		
Dual-band solvents (red-shifted absorption)	MeOH MeCN EtOH BuOH DMSO Water	$\tilde{\nu}_{abs}$	$(0.97 \pm 0.32) \times 10^4$	645 ± 83	1766 ± 640	4536 ± 2877	3422 ± 1206	0.9960
			$(2.07 \pm 1.59) \times 10^4$		-758 ± 3058	-4568 ± 14576	-808 ± 5971	0.7095
			$(1.83 \pm 0.12) \times 10^4$	529 ± 148		-3119 ± 1586	118 ± 306	0.9646
			$(1.47 \pm 0.04) \times 10^4$	592± 100	793 ± 224		1561 ± 329	0.9858
			$(1.87 \pm 0.08) \times 10^4$	539 ± 157	-36 ± 166	-3451 ± 1263		0.9628
		$\tilde{\nu}_{em}$	$(1.11 \pm 0.65) \times 10^4$	593 ± 169	1312 ± 1305	3274 ±5869	2649 ± 2460	0.9817
			$(2.13 \pm 1.51) \times 10^4$		-1006 ± 2898	-5089 ±13812	-1237 ± 5658	
			$(1.76 \pm 0.12) \times 10^4$	507 ± 146		-2413 ± 1563	194 ± 302	0.9630
			$(1.48 \pm 0.05) \times 10^4$	554 ± 125	610 ±281		1306 ±411	0.9760
			$(1.81 \pm 0.08) \times 10^4$	511 ± 157	-83 ± 166	-2908 ± 1259		0.9602

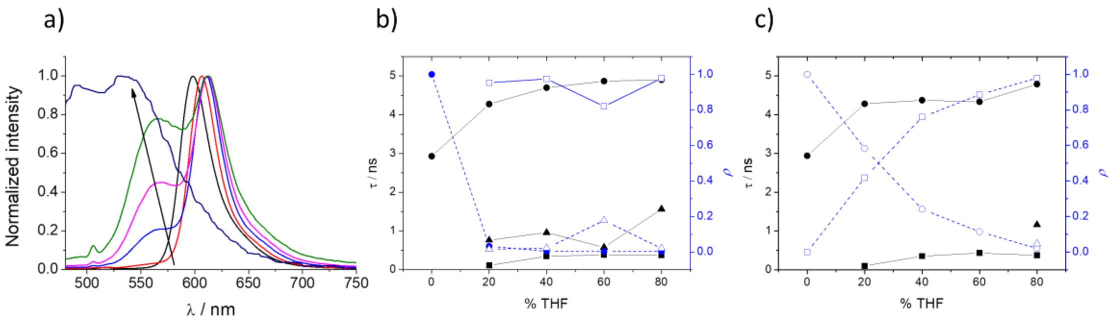

Figure S1.6. Normalized intensity emission (a) at λ_{ex}=440 nm and fluorescence lifetimes (τ) and the relative abundances (ρ) of 2-Me-4-OMe-TM in different water:THF proportions determined using (b) λ_{ex}=440 nm and λ_{em}= 570 nm and using (c) λ_{ex}=440 nm and λ_{em}= 600 nm.

ABSORPTION STUDIES

If a system that is formed by two species follows Beer's law, at any wavelength (λ_{abs}) and pH, the absorbance (*A*) is given by the expression

$$A(pH, \lambda_{abs}) = c\left(\sum_i \alpha_i(pH, pK_a)\varepsilon_i(\lambda_{abs})\right)d$$

where *c* is the total concentration of the dye, *d* is the optical path length, $\varepsilon_i(\lambda_{abs})$ is the wavelength-dependent molar absorption coefficient of the *i*th prototropic form of the dye, and α_i(p*H*, p*K*$_a$) is the fraction of the dye in the *i*th prototropic form, which depends on both p*H* and p*K*$_a$.

$$\alpha_1 = \frac{[H^+]}{[H^+] + K_a}$$

$$\alpha_2 = \frac{K_a}{[H^+] + K_a}$$

Substituting and operating properly, we obtain the next equation that is used to plot individual values versus pH to obtain the ε_N and the p*K*$_a$

$$\frac{A(pH, \lambda_{abs})}{\varepsilon_A c} = \left(\frac{\varepsilon_N}{\varepsilon_A}(\lambda_{abs})\frac{10^{-pH}}{10^{-pH} + 10^{-pk_a}} + \frac{10^{-pk_a}}{10^{-pH} + 10^{-pk_a}}\right)d$$

SPECTROSCOPY AND PHOTOPHYSICAL PROPERTIES OF 2-ME-4-OME-TM IN AQUEOUS SOLUTION AND SENSITIVITY TOWARDS PHOSPHATE IONS

To understand the prototropic equilibrium of 2-Me-4-OMe-TM in aqueous solution, we studied the pH dependency through spectrophotometry and spectrofluorimetry around physiological pH. The absorption spectra of 2-Me-4-OMe-TM at different pH values showed a similar shape as that of previously described silicon magenta xanthene dyes[2] (see Figure S1.7). The presence of an isosbestic point at approximately 520 nm suggests the presence of two species. Using the fundamental equations of the chemical equilibrium and the Lambert-Beer law, we recovered the molar absorptivity coefficients of the two involved species, i.e., the neutral and anionic forms (see Scheme S1.2 and Figure S1.8), and a pK_a value of 7.09 ± 0.03 (see Figure S1.9). At basic pH, the anionic form exhibited an absorption maximum at 583 nm and a shoulder at approximately 543 nm. On the other hand, under acidic conditions, corresponding to the neutral form, the absorption was largely decreased and blue-shifted. The neutral species showed a broad and poorly defined absorption band centered at 480 nm. Regarding the chemical equilibrium and using dyes of the same family as reference[2, 8-10], we propose scheme S1.2 for the chemical equilibrium in aqueous solution, where a zwitterionic form is included[9-11]. Interestingly, the fluorescence emission of this dye in aqueous solution is characterized by "on/off" properties, i.e., although the anionic form was very fluorescent, the neutral species presented a very low fluorescence emission in aqueous solution (see Figures S1.10, S1.11 and S1.12).

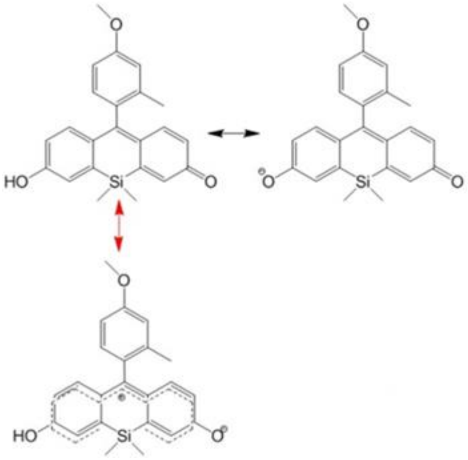

Scheme S1.2. Chemical equilibrium proposed between the prototropic neutral and anionic species of 2-Me-4-OMe-TM. Two resonance structures are included for the neutral species.

Similar to other xanthene derivatives, the presence of an adequate proton donor/acceptor can promote an ESPT reaction. As a consequence, the fluorescence decay times are dependent on the total phosphate concentration, so this mechanism has been used in the determination of intracellular phosphate concentration using FLIM imaging[1, 12]. For a better understanding of the phosphate sensitivity of this dye through the ESPT reaction, we have studied the excited-state dynamics through time-resolved fluorescence spectroscopy. The basis of this study is well established[13] and can be resolved by measuring a data set of fluorescence decay traces at different pH values and buffer concentrations. Intracellular phosphate is an important parameter for many different physiological processes[14]; hence, since the species of the phosphate buffer can act as an adequate proton donor/acceptor pair, we have resolved the dynamics of the excited-state processes of 2-Me-4-OMe-TM in the presence of phosphate buffer. The scheme of the excited-state reactions and the corresponding rate constants is presented in Figure S1.13a.

The analysis of the fluorescence decay traces of 2-Me-4-OMe-TM at different pH values and phosphate concentrations exhibited two decay times. The long decay time varied in the range of 2-3 ns, with an increasing trend as pH values increased and with lower values at higher phosphate concentrations (Fig. S11B). The short decay time varied between 80 and 200 ps, with less obvious trends, ultimately caused by the difficulty of accurately determining such short decay times. These decay time values can be fitted to the general equations of the buffer-mediated ESPT reaction, following the methodology previously described (see Appendix A, Buffer mediated ESPT reaction studies). Using the pH range in the experimental conditions, k_{12} can be considered negligible because $[H_3O^+]$ is small. Moreover, the shortest lifetime τ_1 is the sum of the rate constant of the process that produces the disappearance of 1* (k_{01} and k_{21}). We recovered the rate constants shown in Table S1.5, which successfully describe the pH and phosphate dependency of the fluorescence decay times, as seen in the comparison of the estimated (lines) and experimental times (points) in Figure S1.13b. As can be observed, there is a very good concordance between these values. It is important to highlight that at physiological pH and below 400 mM of phosphate, the fluorescence decay is characterized by a monoexponential character, which is a requirement for improved fluorescence lifetime-based sensors. Using k_{21}^B and k_{12}^B, we obtained the excited-state pK_a^* of the dye[15], resulting in a value of 6.85 ± 0.08. This pK_a^* can be compared with that obtained through steady-state fluorescence measurements using a high phosphate concentration. Figure S1.13c shows that the fit of the steady-state fluorescence data results in a pK_a^* value of 6.58 ± 0.06. Although the dye is slightly more acidic in the excited state than in the ground state, as with other xanthene derivatives[2, 9, 10], the pK_a^* is similar enough to the pK_a so that strong spontaneous ESPT reaction is negligible.

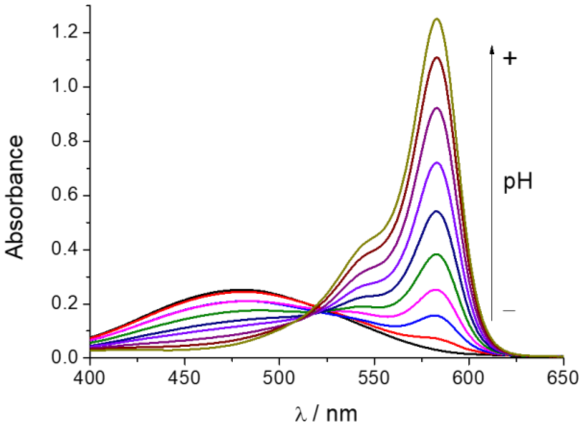

Figure S1.7. Absorption spectra of (at 4 × 10^{-6} M) in phosphate buffer 0.01 M at pH values between 4.88 and 8.94. The arrow indicates increasing pH vales.

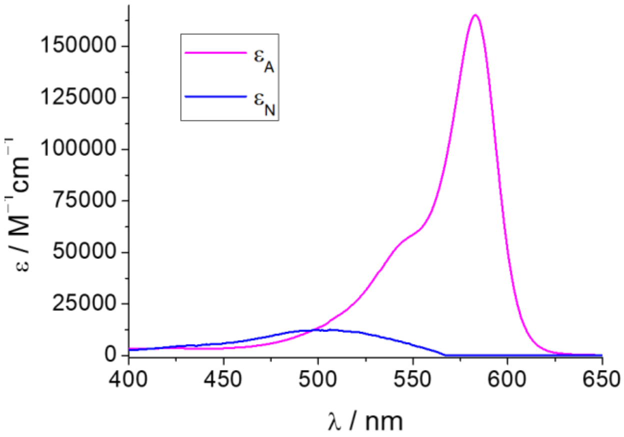

Figure S1.8. Recovered molar absorption coefficients of the neutral (blue line) and anionic (pink line) 2-Me-4-OMe-TM species in 0.01 M phosphate buffer.

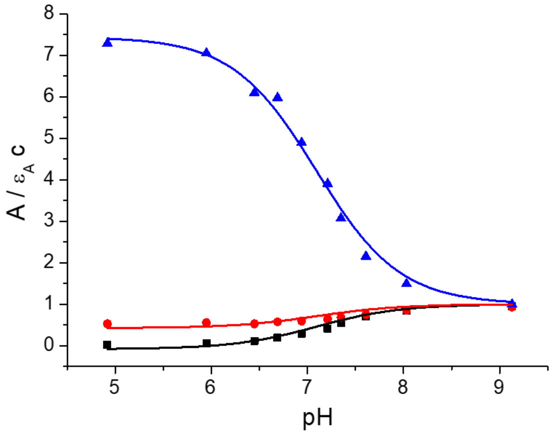

Figure S1.9. Global fitting of the A/(ε_A C) at 440 (blue triangles), 530 (red circles) and 585 (black squares) nm versus pH curves of 2-Me-4-OMe-TM solutions in 0.01 M phosphate buffer.

STEADY-STATE FLUORESCENCE STUDIES

The total fluorescence emission $F(\lambda_{ex}, \lambda_{em}, [H^+])$ at proton concentration $[H^+]$ produced by an excitation wavelength (λ_{ex}) and observed at emission wavelength (λ_{em}) can be expressed as:

$$F(\lambda_{ex}, \lambda_{em}, [H^+]) = \frac{F_{min}[H^+] + F_{max}K_a}{K_a + [H^+]}$$

where F_{min} indicates the fluorescence signal of the neutral form of the dye and F_{max} denotes the fluorescence signal of the anionic form of 2-Me-4-OMe-TM.

Quantum yield values from the steady-state fluorescence measurements were calculated using fluorescein in 0.1 M NaOH (ϕ = 0.79)[16] and rhodamine 101 in ethanol + 0.01% HCl (ϕ = 1.00)[17] as references for the measurements for λ_{ex}=440 nm and λ_{ex}=530 nm, respectively.

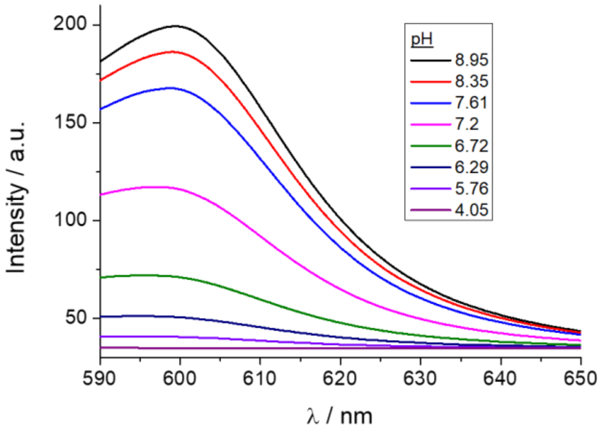

Figure S1.10. Steady-state emission spectra (λ_{ex} = 582 nm) of 4 ×10^{-6} M 2-Me-4-OMe-TM aqueous solutions at different pH values.

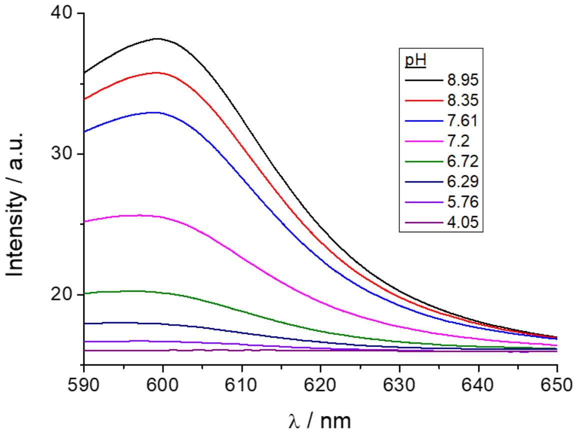

Figure S1.11. Steady-state emission spectra (λ_{ex} = 530 nm) of 4 ×10^{-6} M 2-Me-4-OMe-TM aqueous solutions at different pH values.

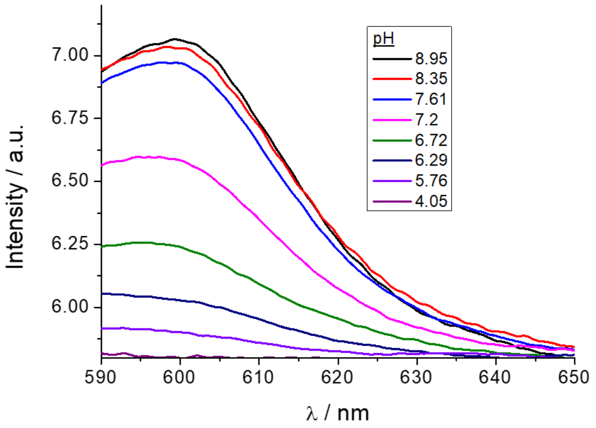

Figure S1.12. Steady-state emission spectra (λ_{ex} = 470 nm) of 4 $\times 10^{-6}$ M 2-Me-4-OMe-TM aqueous solutions at different pH values.

BUFFER-MEDIATED ESPT REACTION STUDIES

The theory and methods of solving buffer-mediated ESPT reactions are well established[9, 13, 18, 19].

Under experimental conditions where the buffer-mediated ESPT reaction occurs rapidly during its excited lifetime, the normalized fluorescence intensity can be expressed as[20].

$$\frac{I}{A} = \frac{\phi_1}{1 + 10^{(pH - pK_a^*)}} + \frac{\phi_2}{1 + 10^{(pK_a^* - pH)}}$$

where I/A is the fluorescence intensity at λ_{em}, normalized by absorbance at the excitation wavelength, ϕ_1 and ϕ_2 are the relative fluorescence efficiencies of the neutral and anionic forms at λ_{em}, and pK_a^* is the pK_a for the excited-state proton reaction $1^* \rightleftharpoons 2^* + H^+$.

If the photophysical system, as shown in Figure S1.3a is excited by an infinitely short light pulse that does not significantly alter the concentrations of the ground-state species, then the fluorescence δ-response function, $f(\lambda_{em}, \lambda_{ex}, t)$, at emission wavelength λ_{em} due to excitation at λ_{ex} is given by

$$f(\lambda_{ex}, \lambda_{em}, t) = p_1 e^{\gamma_1 t} + p_2 e^{\gamma_2 t} \qquad t \geq 0$$

in which this equation has been written in the common biexponential character, where

$$\gamma_{1,2} = \frac{-(a + c) \pm \sqrt{(c - a)^2 + 4bd}}{2}$$

$$a = k_{01} + k_{21} + k_{21}^{B}[R]$$

$$b = k_{12}[H^{+}] + k_{12}^{B}[RH]$$

$$c = k_{02} + k_{12}[H^{+}] + k_{12}^{B}[RH]$$

$$d = k_{21} + k_{21}^{B}[R]$$

[*R*] and [*RH*] are the concentration of the basic and acidic prototropic forms of the buffer and are related to the total buffer concentration as c^B=[*R*]+[*RH*]. They can be expressed as [*RH*] = $c^B[H^+]/([H^+]+ K_a^B)$ and [*R*] = $C^B K_a^B/([H^+]+ K_a^B)$, where K_a^B is the dissociation constant for the reversible reaction $RH \rightleftharpoons R + H^+$. k_{01}, k_{02}, k_{12}, k_{21}, $k^B{}_{12}$ and $k^B{}_{21}$ are the kinetic constants shown in Figure 1.1a.

The γ factors are related to the fluorescence lifetimes τ_1 and τ_2 by the expression

$$\tau_{1,2} = -\frac{1}{\gamma_{1,2}}$$

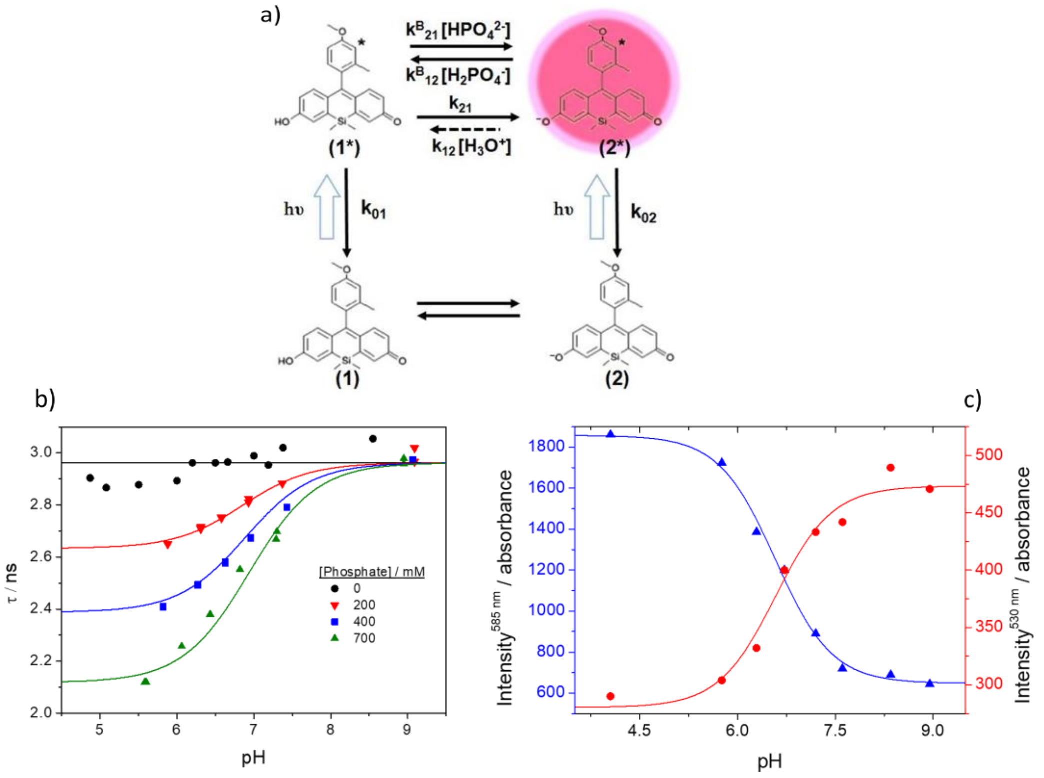

Figure S1.13. (a) Proposed kinetic model of ground- and excited-state proton-transfer reactions of 2-Me-4-OMe-TM in the presence of phosphate buffer. (b) Global fitting (solid lines) of the theoretical equations (see SI) to the long decay time at different pH values and phosphate buffer concentrations (circles: 0, invert triangles: 200, squares: 400 and triangles: 700 mM). (c) Global normalized fluorescence emission plot vs pH of 2-Me-4-OMe-TM in phosphate buffer solution (0.7 M) at 585 (blue triangles) and 530 (red circles) nm. The lines represent the global fit used to determine the pK_a^*.

Table S1.5

Rate constants	Value
$k_{01}\ (s^{-1})$	1.33 (± 0.89) × 10^9
$k_{02}\ (s^{-1})$	3.37 (± 0.01) × 10^8
$k_{21}\ (s^{-1})$	7.82 (± 0.92) × 10^9
$k_{21}^{B}\ (M^{-1}s^{-1})$	2.03 (± 1.34) × 10^9
$k_{12}^{B}\ (M^{-1}s^{-1})$	1.95 (± 0.99) × 10^9

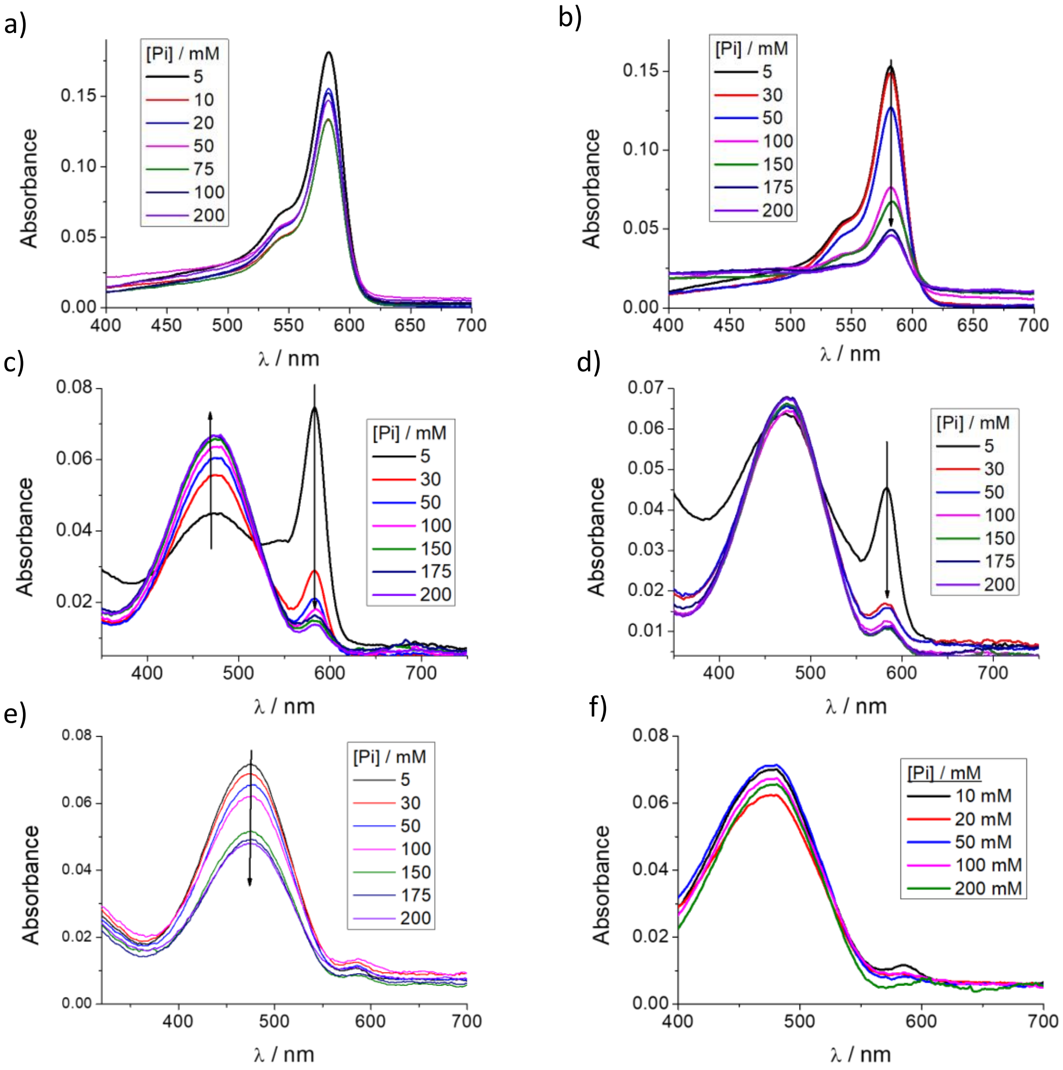

Figure S1.14. Absorption spectra at different SDS concentrations, (a) 0.1 mM, (b) 0.5 mM, (c) 3 mM, (d) 5 mM, (e) 10 mM and (f) 20 mM, and increasing phosphate concentrations. pH 7.35.

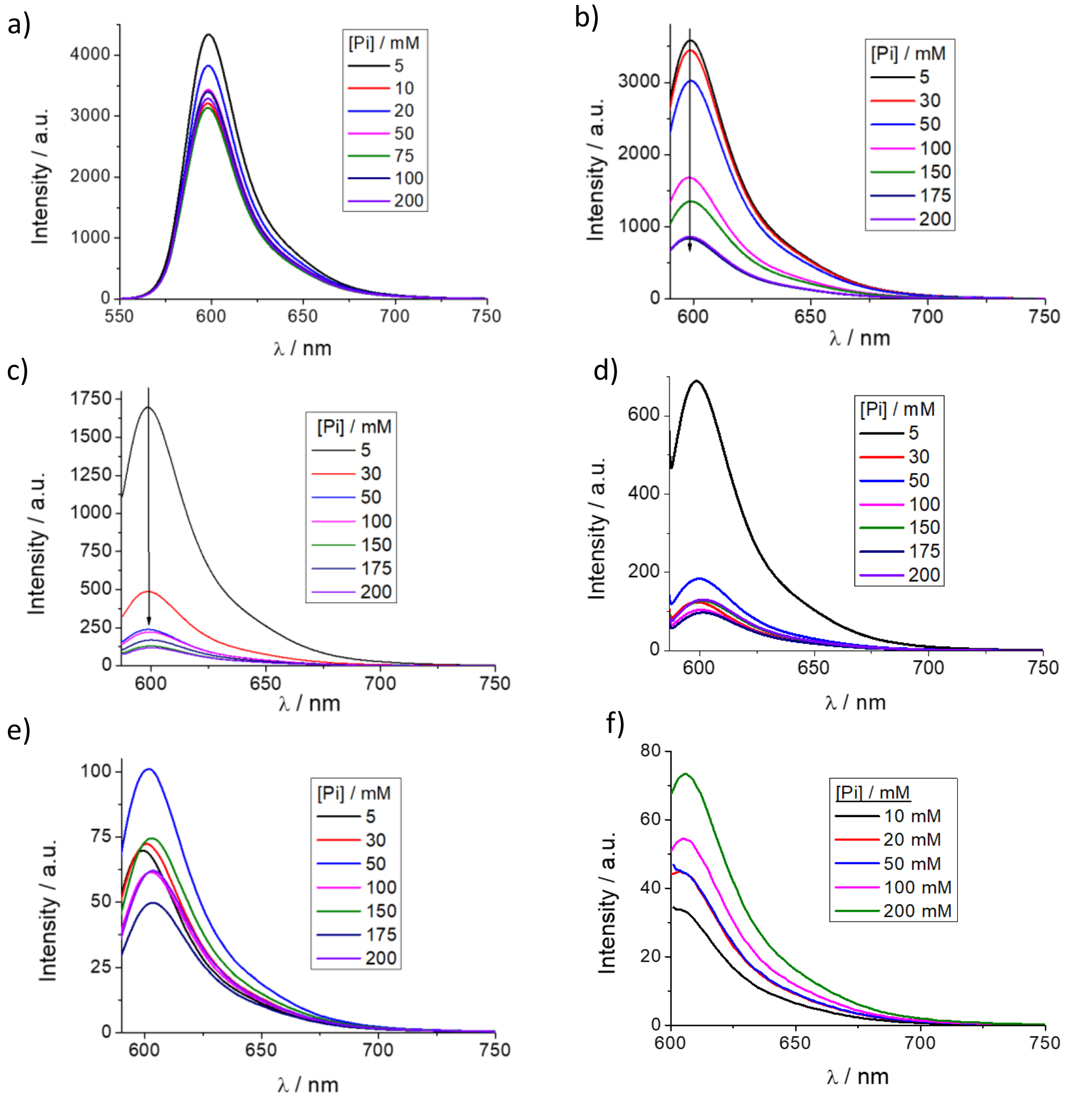

Figure S1.15. Fluorescence spectra at different SDS concentrations, (a) 0.1 mM, (b) 0.5 mM, (c) 3 mM, (d) 5 mM, (e) 10 mM and (f) 20 mM, and increasing phosphate concentrations. pH 7.35.

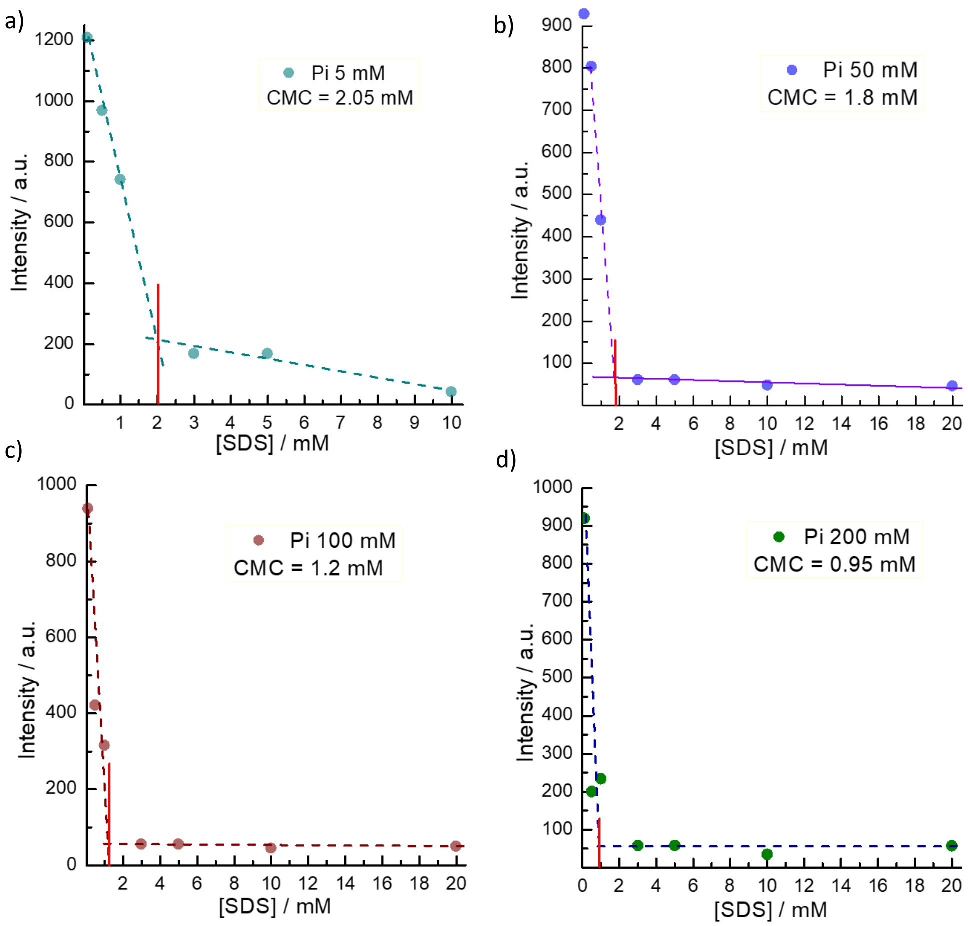

Figure S1.16. CMC estimation through change in the fluorescence maxima between different solutions at (a) [Pi] =5 mM, (b) 50 mM, (c) 100 mM and (d) 200 mM. The red line indicates the CMC estimation.

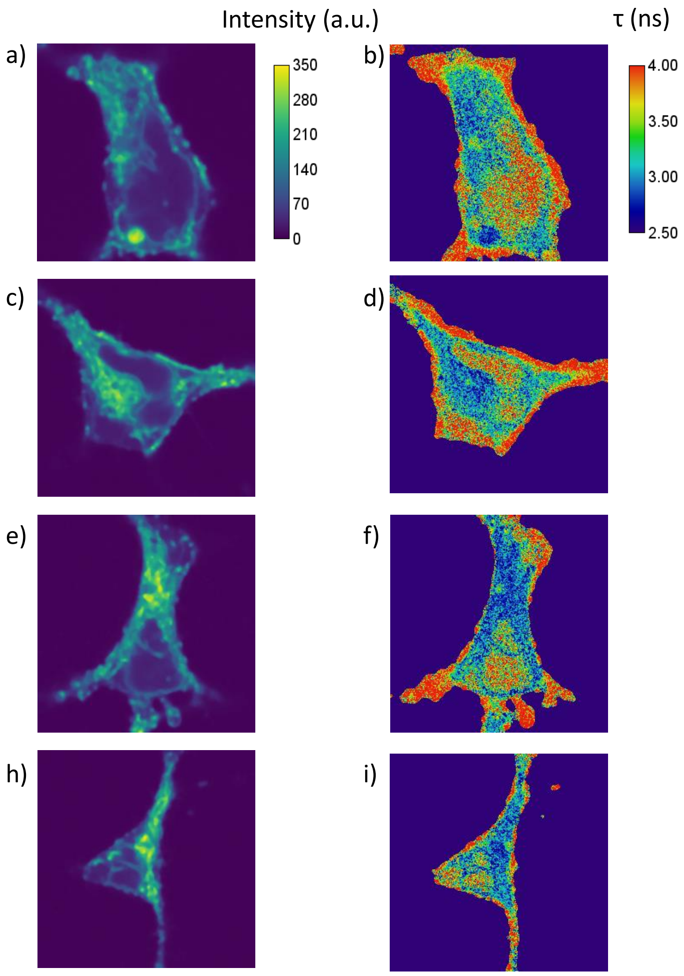

Figure S1.17. FLIM of 2-Me-4-OMe TM in HEK293 cells. Images (a), (c), (e) and (g) show the intensity images and (b), (d), (f) and (h) the fluorescence lifetime images from (a), (c), (e) and (g), respectively.

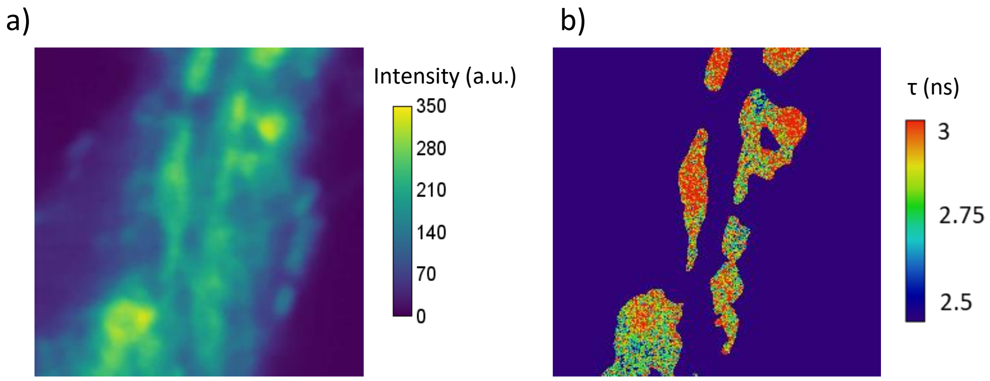

Figure S1.18. FLIM images of HEK293. (a) shows the intensity images, where the accumulation of 2-Me-4-OMe TM is observed in some intracellular structures. (b) shows the fluorescence lifetime images from the isolated regions following a restrictive intensity-based threshold.

BIBLIOGRAPHY

1 Herrero-Foncubierta, P.; Paredes, J. M.; Giron, M. D.; Salto, R.; Cuerva, J. M.; Miguel, D.; Orte, A., A Red-Emitting, Multidimensional Sensor for the Simultaneous Cellular Imaging of Biothiols and Phosphate Ions. *Sensors* **2018,** *18* (1), 18.

2 Crovetto, L.; Orte, A.; Paredes, J. M.; Resa, S.; Valverde, J.; Castello, F.; Miguel, D.; Cuerva, J. M.; Talavera, E. M.; Alvarez-Pez, J. M., Photophysics of a Live-Cell-Marker, Red Silicon-Substituted Xanthene Dye. *J. Phys. Chem. A* **2015,** *119* (44), 10854-10862.

3 Best, Q. A.; Sattenapally, N.; Dyer, D. J.; Scott, C. N.; McCarroll, M. E., pH-Dependent Si-Fluorescein Hypochlorous Acid Fluorescent Probe: Spirocycle Ring-Opening and Excess Hypochlorous Acid-Induced Chlorination. *J. Am. Chem. Soc.* **2013,** *135* (36), 13365-13370.

4 Lakowicz, J. R., *Principles of Fluorescence Spectroscopy*. 3rd ed.; Springer: 2006.

5 Porres, L.; Holland, A.; Palsson, L. O.; Monkman, A. P.; Kemp, C.; Beeby, A., Absolute measurements of photoluminescence quantum yields of solutions using an integrating sphere. *Journal of Fluorescence* **2006,** *16* (2), 267-272.

6 Karpiuk, J.; Grabowski, Z. R.; Deschryver, F. C., PHOTOPHYSICS OF THE LACTONE FORM OF RHODAMINE-101. *J. Phys. Chem.* **1994,** *98* (13), 3247-3256.

7 Wohlfarth, C., *Static Dielectric Constants of Pure Liquids and Binary Liquid Mixtures*. Springer, Berlin, Heidelberg: 2015.

8 Puente-Munoz, V.; Paredes, J. M.; Resa, S.; Ortuno, A. M.; Talavera, E. M.; Miguel, D.; Cuerva, J. M.; Crovetto, L., Efficient acetate sensor in biological media based on a selective Excited State Proton Transfer (ESPT) reaction. *Sensors and Actuators B-Chemical* **2017,** *250*, 623-628.

9 Crovetto, L.; Paredes, J. M.; Rios, R.; Talavera, E. M.; Alvarez-Pez, J. M., Photophysics of a Xanthenic Derivative Dye Useful as an 'On/Off' Fluorescence Probe. *Journal of Physical Chemistry A* **2007,** *111* (51), 13311-13320.

10 Paredes, J. M.; Crovetto, L.; Rios, R.; Orte, A.; Alvarez-Pez, J. M.; Talavera, E. M., Tuned lifetime, at the ensemble and single molecule level, of a xanthenic fluorescent dye by means of a buffer-mediated excited-state proton exchange reaction. *Physical Chemistry Chemical Physiscs* **2009,** *11* (26), 5400-5407.

11 Orte, A.; Ruedas-Rama, M. J.; Paredes, J. M.; Crovetto, L.; Alvarez-Pez, J. M., Dynamics of Water-in-Oil Nanoemulsions Revealed by Fluorescence Lifetime Correlation Spectroscopy. *Langmuir* **2011,** *27* (21), 12792-12799.

12 Zhang, Q.; Xiao, K.; Paredes, J. M.; Mamonova, T.; Sneddon, W. B.; Liu, H.; Wang, D.; Li, S.; McGarvey, J. C.; Uehling, D.; Al-awar, R.; Joseph, B.; Jean-Alphonse, F.; Orte, A.; Friedman, P. A., Parathyroid hormone initiates dynamic NHERF1 phosphorylation cycling and conformational changes that regulate NPT2A-dependent phosphate transport. *J. Biol. Chem.* **2019**.

13 Crovetto, L.; Orte, A.; Talavera, E. M.; Alvarez-Pez, J. M.; Cotlet, M.; Thielemans, J.; De Schryver, F. C.; Boens, N., Global compartmental analysis of the excited-state reaction between fluorescein and (+/-)-N-acetyl aspartic acid. *J. Phys. Chem. B* **2004,** *108* (19), 6082-6092.

14 Paredes, J. M.; Giron, M. D.; Ruedas-Rama, M. J.; Orte, A.; Crovetto, L.; Talavera, E. M.; Salto, R.; Alvarez-Pez, J. M., Real-Time Phosphate Sensing in Living Cells using

Fluorescence Lifetime Imaging Microscopy (FLIM). *J. Phys. Chem. B* **2013,** *117* (27), 8143-8149.

15 Orte, A.; Crovetto, L.; Talavera, E. M.; Boens, N.; Alvarez-Pez, J. M., Absorption and Emission Study of 2',7'-Difluorofluorescein and Its Excited-State Buffer-Mediated Proton Exchange Reactions. *Journal of Physical Chemistry A* **2005,** *109* (5), 734-747.

16 Umberger, J. Q.; LaMer, V. K., The Kinetics of Diffusion Controlled Molecular and Ionic Reactions in Solution as Determined by Measurements of the Quenching of Fluorescence1,2. *J. Am. Chem. Soc.* **1945,** *67* (7), 1099-1109.

17 Karstens, T.; Kobs, K., Rhodamine B and rhodamine 101 as reference substances for fluorescence quantum yield measurements. *The Journal of Physical Chemistry* **1980,** *84* (14), 1871-1872.

18 Alvarez-Pez, J. M.; Ballesteros, L.; Talavera, E.; Yguerabide, J., Fluorescein Excited-State Proton Exchange Reactions: Nanosecond Emission Kinetics and Correlation with Steady-State Fluorescence Intensity. *Journal of Physical Chemistry A* **2001,** *105* (26), 6320-6332.

19 Martinez-Peragon, A.; Miguel, D.; Jurado, R.; Justicia, J.; Alvarez-Pez, J. M.; Cuerva, J. M.; Crovetto, L., Synthesis and photophysics of a new family of fluorescent 9-alkyl-substituted xanthenones. *Chemistry (Easton)* **2014,** *20* (2), 447-55.

20 Yguerabide, J.; Talavera, E.; Alvarez, J. M.; Quintero, B., Steady-State Fluorescence Method for Evaluating Excited-State Proton Reactions - Application to Fluorescein. *Photochem. Photobiol.* **1994,** *60* (5), 435-441.

A SOLVATOFLUOROCHROMIC DYE AS A FLUORESCENT LIFETIME-BASED PROBE OF Β-AMYLOYD AGGREGATION

Dyes and Pigments, Volume 202, June 2022, 110274

IP: 4.889 (in 2020)

Q1 (16/74)

Chemistry applied

Contribution: I have carried out all the experiments and participated in the writing of this article.

2.1 ABSTRACT

In Alzheimer's disease (AD), the initial stages of the aggregation process of the β-amyloid peptide (Aβ) present a particular interest to understand the origin of the development of this disease. In this work, we present a sensor with the property of solvatofluorochromism that allows a fluorophore to undergo a shift in its emission wavelengths when placed in environments of different polarity. We used the natural adsorption binding of the dye 2-Me-4-OMe-TM, a silicon-modified xanthene derivative, to macrostructures and its solvatofluorochromic behaviour to detect, in real time, modifications in the environment polarity around the dye during the initial stages of Aβ aggregation process, using steady-state, time resolved fluorescence spectroscopy and advanced fluorescence imaging techniques as fluorescence lifetime imaging microscopy (FLIM). During this progression, formation of pre-amyloid aggregates produces strong local changes in hydrophobicity that can be monitored by the fluorescent dye 2-Me-4-OMe-TM. In particular, this dye has two different emission bands and by establishing a polarity scale based on the ratiometric value of the average fluorescence lifetimes between both bands, we were able to quantify the hydrophobicity of the detected aggregates and established a method for distinguishing between aggregates of different types.

2.2 INTRODUCTION

Neurodegenerative disorders, such as Alzheimer's disease (AD), have become one of the most important problems to public health because of the increase in life expectancy in developed countries[1]. Currently, there are no effective treatments despite high investments in research against AD and other neurodegenerative diseases. Furthermore, these disorders are diagnosed in the late stages, where the neurodegenerative damage is advanced and symptoms are evidenced. One important achievement is to have an effective and early diagnosis of AD and other neurodegenerative diseases. Therefore, the discovery of robust biomarkers for early diagnosis and disease monitoring are critical for a more efficacious therapy.

In the development of AD, one of the critical steps is the initial aggregation process of the β-amyloid peptide (Aβ) forming oligomers, because this represents the initial stage when the disease can develop[2] and has been reported as the main toxic agent to cells[3-5]. These oligomers are able to form mature fibrils and, in later stages, neuritic plaques, one of the main hallmarks of AD[6,7]. For this reason, one of the approaches to obtain information about the disease process is monitoring the evolution of the main steps of Aβ aggregation. To this end, several techniques have been reported for in vitro assays, such as electron microscopy (EM), NMR and cryo-EM[8]. However, one of the best approaches is through fluorescence-based techniques, a set of powerful and noninvasive procedures permitting the real-time visualization of biomolecular interactions and aggregation, even down to single-molecule resolution[9-12] or in living systems[7,13,14], facilitating monitoring and quantifying aggregated proteins in solution. Accordingly, the development of novel fluorophores, markers of amyloid aggregation, is a very active field of research[7,15-18], with many reported fluorescent trackers that overcome the limitations of traditionally used markers, such as Thioflavin T or Congo Red[19,20]. In some fundamental studies, Aβ peptides have been covalently modified to follow the aggregation process[21], but this chemical modification can produce a perturbation during the aggregation process, since the environment and monomer concentration are critical in the efficiency of nucleation[22]. To overcome this issue, in the last few years, there have been many reported fluorescent probes capable of visualizing the dynamic process of β-amyloid aggregation through fluorescence without the need for previous chemical binding[7,23-25] or based on measuring autofluorescence of the aggregates of amyloids[26,27]. Due to the increase in the hydrophobicity during the formation of the Aβ aggregates[28,29], one of the most common mechanisms of action of these fluorophores is their ability to modify their fluorescence with changes in the polarity environment[30].

In a previous work, we have studied the compound 7-hydroxy-10(4-methoxy-2-methylphenyl)-5,5-dimethyldibenzo[b,e]silin-3(5H)-one (2-Me-4-OMe-TM), a silicon-substituted xanthene fluorescent dye[31] (Scheme 2.1). 2-Me-4-OMe-TM presents a maximum absorption at approximately 590 nm and a red fluorescence with a maximum emission at approximately 650 nm. Red fluorescence presents several advantages in biological applications, such as minimizing background interference from biological samples and the use of lower energy excitation light, among others. Moreover, we found an exciting property in this dye: the solvatofluorochromism[31], a characteristic of a fluorophore that undergoes a shift in its emission wavelengths when placed in environments of different polarities. Solvatofluorochromism is a very interesting behaviour with important potential applications in biomedical approaches to study local polarity in biological structures, changes in the protein conformation or biomolecule interactions[32]. In addition to an evident shift in the emission maximum due to a strong dependency of the emission properties on the solvent polarity, which in extreme conditions can be from 460 to 620 nm, we found that 2-Me-4-OMe-TM shows an increase in the fluorescence intensity and lifetime when the environment of the dye changes from hydrophilic to hydrophobic.

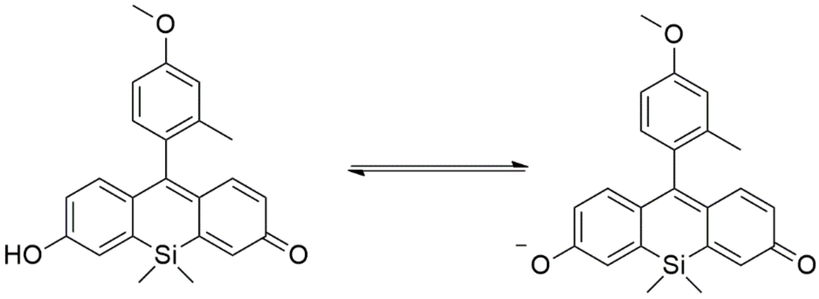

Scheme 2.1. Chemical structure of the neutral (left) and anionic (right) forms of 2-Me-4-OMe-TM.

In this work, we used the natural adsorption binding of 2-Me-4-OMe-TM to macrostructures and its solvatofluorochromic behaviour to detect, in real time, modifications in the environmental polarity around the dye during the initial stages of the Aβ aggregation process using steady-state and time-resolved fluorescence spectroscopy. Moreover, we implemented its use in advanced fluorescence imaging techniques such as fluorescence lifetime imaging microscopy (FLIM)[33], a tool that allows visualization of seeding and growth in the pathway of protein aggregation[10,34-36]. The use of FLIM (imaging based on fluorescence lifetime) overcomes many of the limitations of fluorescence-intensity methods. The most important advantage is that the fluorescence lifetime does not depend on the dye concentration or the power of the excitation source and it is possible to perform a time-gated analysis of the decay curves to discriminate photons coming from autofluorescence[33,37]. During the process of growing amyloid fibrils, the formation of preamyloid aggregates produces strong local changes in hydrophobicity[28,29]. To qualitatively determine the surrounding environment of the dye when interacting with Aβ aggregates, we established a polarity scale using alkyl alcohols of different chain lengths. Our data confirmed the potential use of the fluorescent dye 2-Me-4-OMe-TM as a sensor to study the initial stages of Aβ fibrillation.

2.3 MATERIAL AND METHODS

2.3.1. KINETIC AGGREGATION

The 1-42 β-amyloid peptide fragment (Aβ42, Sigma−Aldrich, CAS Number 107761-42-2) was resuspended at 442 µM in NaOH 0.01 M pH 12 solution and cryopreserved to avoid aggregation. Aggregation experiments were performed using solutions with different total concentrations of Aβ42 peptide (10, 50, and 100 µM) dissolved in buffer SSPE (1 mM EDTA, 149 mM NaCl, and 10 mM NaH_2PO_4, at pH 7.4 adjusted by the addition of HCl), and the addition of 2-Me-4-OMe-TM to a final concentration of 6 µM. The buffer was preheated at 37 °C and filtered through 0.02 µm filters (Whatman) for microscopy experiments prior to use.

Aggregation kinetics were followed in real time for 24 h, upon the addition of 2-Me-4-OMe-TM, at 37 °C and continuous stirring between 245 and 360 rpm, in order to accelerate aggregation, facilitate contact and break up long fibers, generating more secondary nucleation points. Sample aliquots at incubation times of 0, 15 min, 1, 3 and 24 h were extracted, fast-frozen in liquid nitrogen and cryopreserved for FLIM imaging. The incubated sample was heated and stirred on an ELMI SkyLine DTS-2 thermoshaker for 2 microplates (ELME 10023). The aggregation process was monitored at different total concentrations of 10, 50 and 100 µM Aβ42.

2.3.2 INSTRUMENTATION

STEADY-STATE AND TIME-RESOLVED FLUORIMETRY

Steady-state emission spectra were collected using a 10x2 mm cuvette (Hellma 105.201-QS) in a Jasco FP-8300 spectrofluorometer (Jasco, Tokyo, Japan) at an excitation wavelength of 582 nm.

Fluorescence lifetime decays were recorded using a FluoTime 200 time-resolved fluorometer (PicoQuant GmbH, Berlin, Germany) employing a 530-nm pulsed diode laser and LDH-530 (PicoQuant) as the excitation source, with a repetition rate of 20 MHz. Fluorescence decay histograms of 2-Me-4-OMe-TM were collected at 550 and 600 nm.

Time-resolved emission spectra (TRES), which provide emission spectra of different emissive species with time resolution, were obtained by recording the decay traces at different wavelengths from 540 to 640 nm with $\Delta\lambda = 5$ nm. Decay traces were fitted to a biexponential decay equation using iterative deconvolution methods built-in the FluoFit software (PicoQuant). Preexponential coefficients at each wavelength were normalized to the same count number in the decay. Thus, the decay traces were proportional to the steady-state fluorescence intensity.

The preexponential factors were also corrected for the different sensitivities of the detector using a factor that related the total emission during the decay (p1 × τ1 + p2 × τ2) to the steady-state-intensity emission. TRES spectra were calculated using the following equation:

$$I_\lambda\,(t) = \sum_{i=I}^{n} p_{i,\lambda}\,.\;e^{-t/\tau_i}$$

Here, $I_\lambda\,(t)$ is the time-dependent fluorescence intensity at each wavelength, n is the number of exponential decay components, p_i is the amplitude of each decay component at λ wavelength and τ_i is the lifetime of each component.

The species-associated emission spectra (SAEMS) show the spectral contribution of each species i to the global fluorescence spectrum and are estimated by the following equation:

$$I_{i,\lambda} = \frac{p_i\,.\;\tau_i}{\sum_{i=I}^{n} p_i\,.\;\tau_i} I_{SS,\lambda}$$

where $I_{SS,\lambda}$ is the corrected fluorescence intensity in the steady state.

FLUORESCENCE LIFETIME IMAGING MICROSCOPY

Images of the fluorescence lifetime were collected using a time-resolved confocal MicroTime 200 fluorescence lifetime microscope system (PicoQuant GmbH, Berlin, Germany). The excitation source was a 530 nm pulsed laser (LDH-P-C-530, PicoQuant) at a repetition rate of 20 MHz. The light beam passed through an achromatic quarter-wave plate (AQWP05M-600, Thorlabs, NJ, USA), disposed at 45° from the polarization plane of the laser, and was focused by a 532 DCXR dichroic mirror (AHF/Chroma, Germany) to the oil immersion objective (1.4 NA, 100X) specific to an inverted microscope system (IX-71, Olympus, Tokyo, Japan). Fluorescence emission was conducted with a 550 nm longpass filter (AHF/Chroma, Germany) and directed to a 75 µm pinhole. The fluorescence photons were collected into two detection channels using a 600 DCXR dichroic beam splitter (AHF/Chroma, Germany) and carried to two single-photon avalanche diodes (SPADs) (SPCM-AQR 14, Perkin-Elmer) after passing two bandpass filters, D600/40M (Semrock/AHF) and D550/40M (Semrock/AHF), for SPAD 1 and 2, respectively (see Figure 2.1).

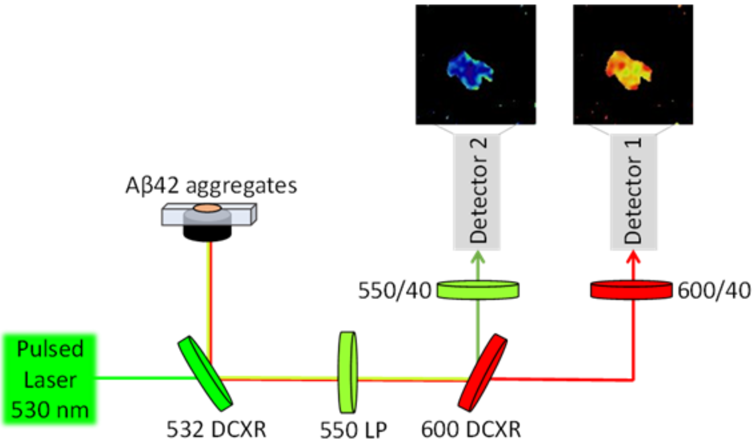

Figure 2.1. Scheme of the dual-color FLIM instrumentation employed to follow the aggregation of Ab42 with the dye 2-Me-4-OMe-TM.

The excitation laser was focused into 2 µL of Aβ42 peptide at different aggregation times, which was mixed with 20 µL of SSPE buffer and deposited onto the slide for FLIM image acquisition. The glass slide was previously cleaned and treated for single-molecule imaging.

Individual photon time tagging was carried out by a TimeHarp 200 module (PicoQuant) with a time resolution of 29 ps per channel on the single-photon timing scale (microtime). A total of 15 images for each sample were collected with an area of 12 μm^2 raster-scanned with an x-y piezo-driven device (Physik Instrumente, Freiburg, Germany) of the region of interest and a spatial resolution of 512 x 512 pixels using a collection time of 0.60 ms per pixel.

FLIM images were obtained by fitting with a single exponential decay function to the photon decay trace in each pixel of the image, after having applied a spatial binning of 2x2 pixels with SymPhoTime 32 software. The matrix data were further analyzed by a home-coded macro of Fiji ([Fiji Is Just] ImageJ) software [38].

The ratio data of FLIM images were obtained through matrix operations in Fiji [38] and Origin 8.5 software (OriginLab Corp., Northampton, MA, USA). First, we measured the ratio images between red and green channels at different incubation times, and we extracted their individual pixel values to construct the histogram chart. To construct the box and whisker chart, we calculated the mean and standard deviation of 10 – 12 images at each incubation time.

2.4 RESULTS

2.4.1 MONITORING AB42 PEPTIDE AGGREGATION USING STEADY-STATE FLUORESCENCE

In aqueous solution around physiological pH, 2-Me-4-OMe-TM presents two prototropic species (neutral and anion, see Scheme 2.1). Due to the strong difference in quantum yields and in absorptivity coefficients (See Table S2.1 and Figure S2.1, Supporting Information) between the anion and neutral species in aqueous solution of silicon-xanthene derivatives[39] in these conditions only it is possible to recover the emission band of the anion form. The origin of the solvatochromism in 2-Me-4-OMe-TM was studied in our previous work[31] where we performed a study based on the methodology reported by Catalan[40]. We found that 2-Me-4-OMe-TM fluorescence is affected by two main causes, first the solvent dipolarity, being the primary specific physicochemical parameter and second the hydrogen bonding interactions with the solvents, supporting the idea of a new emission band arising when this interaction appears. The strong dependency of the emission properties of 2-Me-4-OMe-TM on the polarity of the surrounding environment makes it a suitable candidate for monitoring protein−protein interactions in real time. The interesting photophysics and solvatofluorochromic characteristics of the fluorophore 2-Me-4-OMe-TM prompted us to use it as a reporter for monitoring Aβ42 aggregation, as supported by previous results of 2-Me-4-OMe-TM interacting with micelles and intracellular organelles, resulting in a redshift and intensity increase of the emission when the environmental polarity near the fluorophore decreased[31]. In fact, micellar structures were recently reported as mediators of amyloid nucleation in the aggregation pathway of the Aβ42 peptide[22], and thus, 2-Me-4-OMe-TM would be appropriate for monitoring such structures.

Thus, we measured the emission spectra of the anion form of 2-Me-4-OMe-TM in the presence of Aβ42 peptide under aggregating conditions at three different total concentrations of Aβ42 (10, 50 and 100 µM). Initially, we observed a decrease in the fluorescence intensity, mainly at the lowest concentrations of Aβ42. This behaviour can be explained by the interaction between 2-Me-4-OMe-TM and the initial step of aggregation of the peptide, as we demonstrated in our previous study where the 2-Me-4-OMe-TM interacts with the SDS micelles, decreasing their intensity[31]. Later, during this initial period, we observed an increase in the emission intensity over time (see Figure 2.2). This observation reveals the interaction of the fluorophore with a more hydrophobic environment, corresponding to the emergence of nonpolar patches of aggregated Aβ42. Therefore, an initial interaction exists when the aggregation could be in the micellar step[22] that produces a decrease in the emission of the 2-Me-4-OMe-TM, and later, when the aggregation proceeds beyond this step, the local environment becomes more nonpolar, thereby increasing the emission intensity of 2-Me-4-OMe-TM.

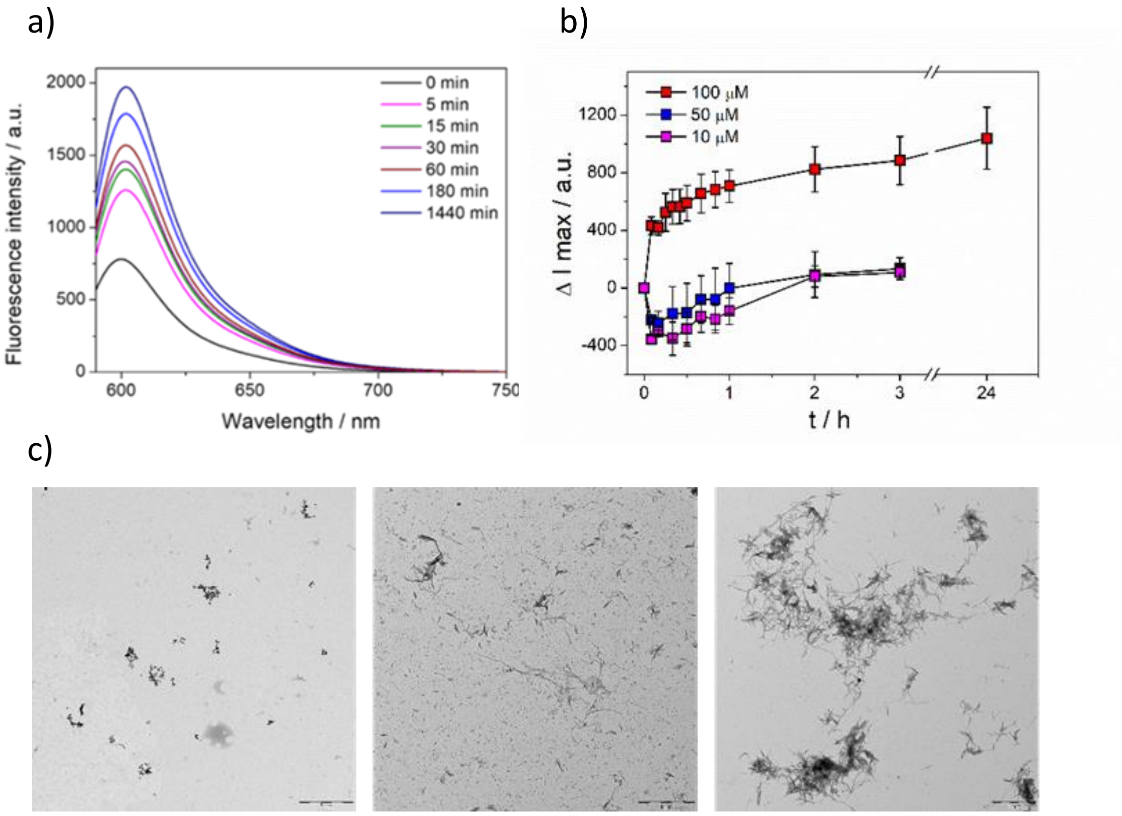

Figure 2.2. (a) Emission spectra of 2-Me-4-OMe-TM (λ_{ex} = 581 nm) in the presence of 100 µM Aβ42 incubated for 24 h at 37 °C. (b) Change in the fluorescence emission intensity of 2-Me-4-OMe-TM at 600 nm (λ_{ex} = 581 nm) with the incubation time of Aβ42 at 10, 50 and 100 µM. Error bars represent the SD of triplicate experiments (c) Representative TEM images of 100 µM Aβ42 aggregates after 15 min (left), 60 min (middle) and 24 h (right) of incubation.

In our experiments, we used Aβ42 peptide concentrations below and above its critical micellar concentration (CMC) of 25 µM[22]. In all cases, the fluorophore was able to monitor the aggregation for the first 24 h, showing an increase in the steady-state fluorescence intensity over time (Figure 2.2 and S2.2). The changes in the fluorescence intensity when micelles are formed is supported by our previous work in which we studied the effect of SDS micelle formation on the fluorescence of 2-Me-4-OMe-TM[31]. There, we found two opposite effects upon micelle formation, first the solvatochromic effect due to the changes in the solvent dipolarity producing an increase on the fluorescence lifetime and intensity of the anion form, and second a decrease of the anionic species concentration due to the interaction of the neutral form with the micelles. In our experiment with Aβ42 peptide, the predominant effect is the change in the hydrophobicity environment that produces an increase in the intensity. Our data show a stronger fluorescence increase at 100 µM, corresponding to aggregation to a larger extent, as confirmed by TEM images. In contrast, 2-Me-4-OMe-TM exhibited a lessened fluorescence intensity increase in aggregating samples at peptide concentrations of 10 and 50 µM (Figure 2.2b). This change in the fluorescence intensity confirms the spontaneous interaction of the fluorophore with Aβ42 aggregates and, owing to its solvatofluorochromic properties, its ability to monitor the decrease in the environmental polarity due to the formation of peptide aggregates and therefore its potential applicability in the *in vitro* study of the early stages of aggregation of these biomarkers present in AD. The intensity changes plots do not show the typical initial lag phase due to the spontaneous and fast adsorption of the 2-Me-4-OMe-TM, even with the initial aggregates.

We verified, through the use of transmission electron microscopy (TEM), that amyloid aggregation proceeded as expected. Figure 2.2c shows curly protofibrillar structures at the earliest incubation time of 15 min, whereas aggregates became longer after 60 min of incubation and appeared as tangled amyloid fibrils after 24 h. These fibrils formed tangles with many crossed and branched fibers piled in multiple clusters[41].

2.4.2 IMAGING THE POLARITY OF AB42 PEPTIDE AGGREGATES

In our previous study, we found that not only the emission intensity of 2-Me-4-OMe-TM but also the fluorescence lifetime (τ) showed dependency on the surrounding polarity[30]. FLIM has been demonstrated to be a powerful tool to monitor aggregation through hydrophobicity maps[18,28,42]. Therefore, the use of FLIM where intensity images are recorded in combination with the fluorescence lifetime, allowing multiparameter analysis of data, is especially interesting.

The polarity dependence of the differences in the average fluorescence lifetime values are due to the excited-state kinetics of 2-Me-4-OMe-TM. This dye exhibits two emissive species: a long decay time with polarity-dependent values between 3.0 and 4.2 ns and a short decay time of approximately 0.2 ns with a larger contribution in low-polarity environments[31]. These two different fluorescence lifetimes were associated to the anionic and neutral species. In aqueous solution and near-neutral pH, only the long decay species, associated with the anionic species of 2-Me-4-OMe-TM (free in solution), is the main emissive form at 610 nm. However, when the polarity decreases, the increase of the quantum yield of the neutral species allows its detection in the band at 560 nm. In this work, we further studied the effect of different polarity scales on the emissive properties of the dye. For this, we first used as solvents different alcohols of different chain lengths to observe the changes in the emission properties of 2-Me-4-OMe-TM due to its solvatofluorochromic behaviour. A decrease in the polarity of the solvent produces two effects on the 2-Me-4-OMe-TM emission: a redshift in the maxima and the appearance of a new band at approximately 560 nm[31] (see Figures 2.3 and S2.3, Supporting Information). Figures 2.3a and 2.3b show the calculated SAEMS of each of the decay time components in methanol and octanol. SAEMS allow to identify each of the species in both solvents. Figure 3a shows the redshift of the anionic species when the polarity decreases and Figure 2.3b shows the appearance of a new emission band at approximately 560 nm associated to the neutral species in non−polar solvents as was demonstrated in our previous work[31]. Similar results as been obtained using different DMSO:water proportions (see Figure S2.4, Supporting Information).

We also measured the polarity dependence of the fluorescence lifetime in both bands (τ_G represents the fluorescence lifetime using a green filter band (550/40) and therefore associated to the neutral species and τ_R represents the fluorescence lifetime using a red filter band (600/40) and therefore associated to the anionic species) at different dielectric constant solvents obtained from different THF:water proportions[43]. In our fluorescence lifetime measurements, we selected a laser excitation source of 530 nm, because it produces a simultaneous excitation of both species. As observed in Figure 2.3c, from the dielectric constant of water until reaching a value of approximately 65, the average lifetime measured undergoes an opposite effect in both bands, while in the red emission (λ_{em} = 610 nm) the lifetime increases with the dielectric constant, it decreases in the green band (λ_{em} = 560 nm). In the red band, when the polarity starts to decrease from that of water, τ_R increases until reaching a dielectric constant lower than 50, where the contribution of the short-decay species is larger and decreases the average fluorescence lifetime. In contrast, at 560 nm, it emits mainly short-decay species associated with the neutral form of 2-Me-4-OMe-TM, so that τ_G is controlled by the short lifetime, especially at low dielectric constants, and therefore producing a decrease in the average fluorescence lifetime with the decrease in polarity.

These data collected for the excited-state behaviour of 2-Me-4-OMe-TM allow us to establish a quantitative scale of such properties with the polarity of the surrounding environment thanks to the fact that the ratio between both lifetimes (τ_R/τ_G) presents a linear relationship with the dielectric constant (see Figure 2.3d). This linear relation makes the fluorescence of 2-Me-4-OMe-TM very interesting to use in FLIM to measure changes in polarity within this range of dielectric constant values.

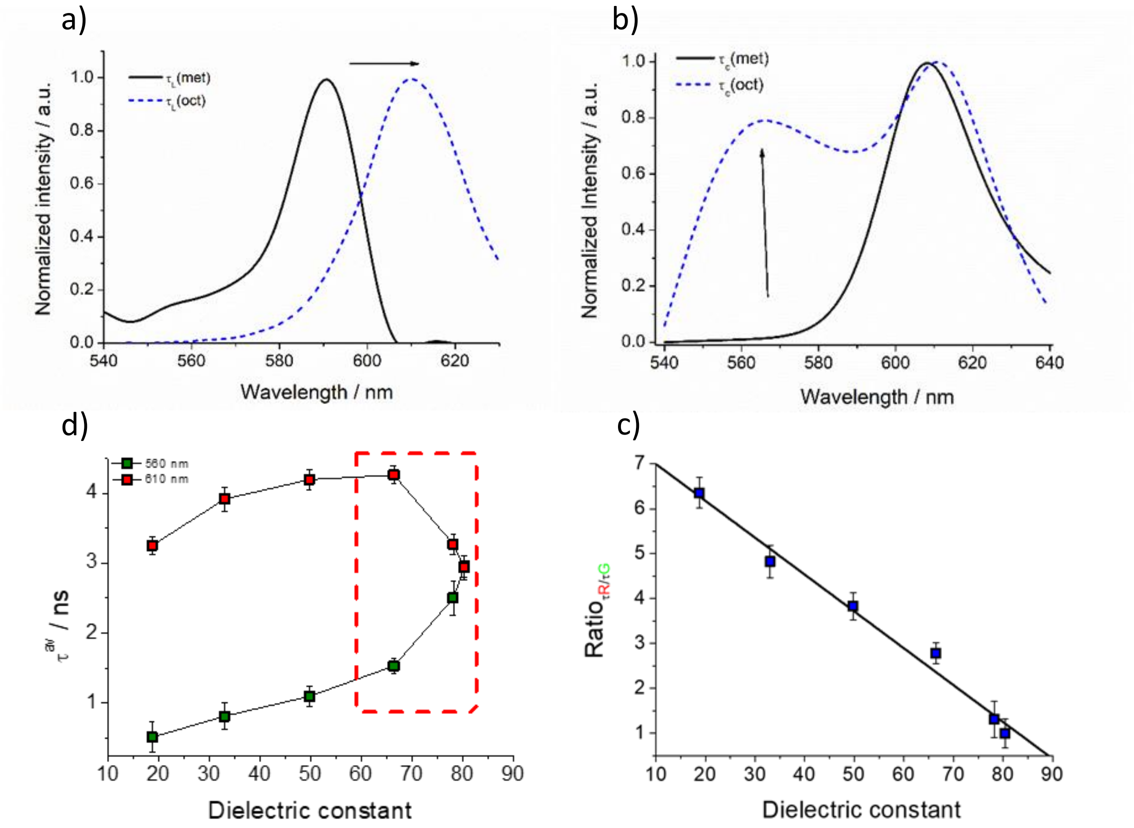

Figure 2.3 SAEMS spectra of the two emissive forms of 2-Me-4-OMe-TM in methanol (black) and octanol (green). Spectral distribution of the large (a) and short (b) lifetime of Me-4-OMe-TM in each alcohol. (c) Average lifetime of 2-Me-4-OMe-TM in solutions with different dielectric constant obtained from different THF:water proportions by volume, obtained at an excitation wavelength of 530 nm and emissions in the green and red regions at 560 and 610 nm, respectively. (d) Ratio values of average lifetimes obtained at 610 nm (τ_R) and 560 nm (τ_G).

With these results, we monitored Aβ42 aggregation in the presence of 2-Me-4-OMe-TM by dual-color FLIM microscopy, focusing on two detection bands, namely, 550/40 for the emission band due to the more hydrophobic ambient environment and 600/40 nm for the emission band corresponding to the more hydrophilic ambient environment, as indicated in Figure 2.1. Focusing on FLIM images collected on the 600/40 detection channel, because the intensity of 2-Me-4-OMe-TM in a hydrophilic environment is low, the segmentation analysis procedure allowed us to analyze pixels where the dye interacts with peptide aggregates. Figures 4 and S5 clearly show that as incubation proceeded, 2-Me-4-OMe-TM exhibited longer decay times. The histograms showed the presence of two populations. The first population appears at the beginning from the very early stages of incubation (15 min), the histogram was centered at 3.05 ± 0.13 ns, but at later incubation times, the fluorescence lifetime of this population showed an increase in the value, reaching 3.24 ± 0.06 ns, where the errors represent the SD of the gaussian fits. The second population appeared after 3 hours of incubation with a fluorescence lifetime of 3.40 ± 0.22 ns and in samples incubated for 24 h it appearing centered at 3.55 ± 0.12 ns. This increase in the average lifetime with incubation is in agreement with our results obtained in solution as shown in Figure 2.3, where a decrease in the dielectric constant is related to an increase in the average fluorescence lifetime. Likewise, these lifetime values allowed assigning a change in the polarity value to the detected aggregates, owing to the polarity scale established with the THF:water proportions.

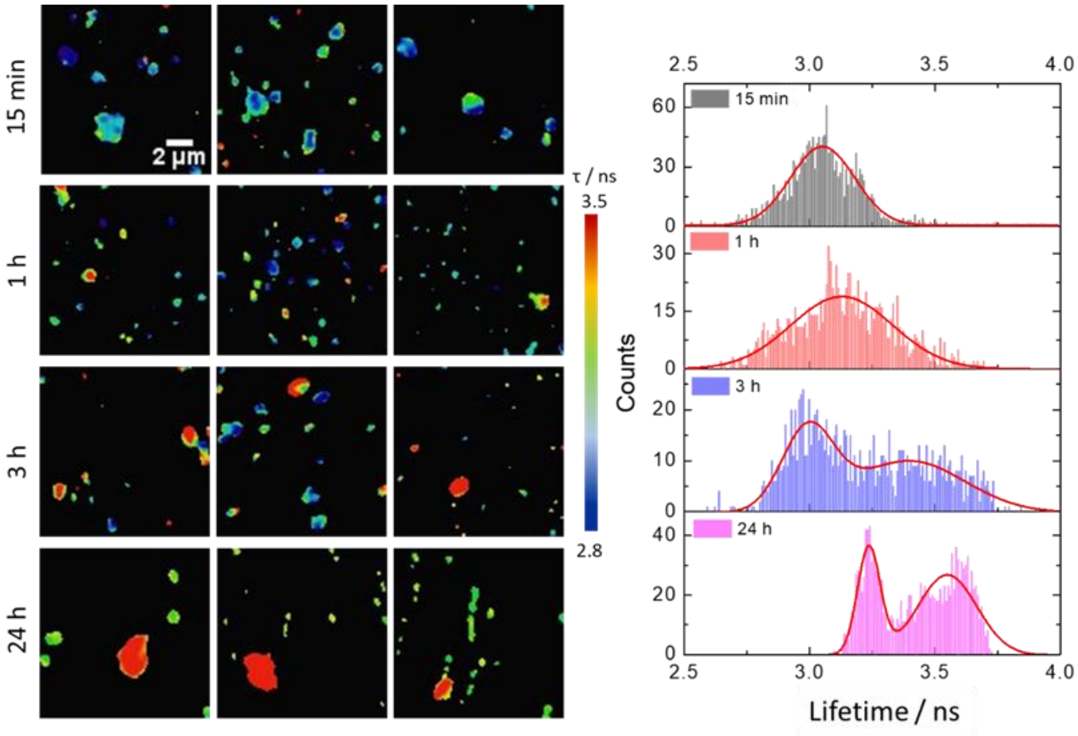

Figure 2.4. (Left) FLIM images of 2-Me-4-OMe-TM in the red channel in 100 μM Aβ42 peptide incubated at 37 °C for 15 min and 1, 3 and 24 h. The size of each image is 12 x 12 μm. Scale bar represents 2 μm (Right) Fluorescence lifetime histograms in the 600/40 channel from the FLIM images represented in the figure.

Interestingly, by focusing on the 550/40 nm emission channel, we pay attention to the short-decay time species of 2-Me-4-OMe-TM, with a larger contribution in hydrophobic environments, as demonstrated in the experiments with the organic alcohol series (time-resolved fluorimetry, SAEMS in Figure 2.3 and steady-state fluorimetry Figure S2.3, Supporting Information) or using different DMSO:water proportion (Figure S2.4, Supporting Information). In this detection channel, the fluorescence contribution of the neutral species was stronger and increased with the hydrophobicity of the environment. Therefore, an increasing hydrophobicity produces a decrease in the average fluorescence lifetime measured at 560 nm (Figure 2.3c).

When we measured the FLIM images of 2-Me-4-OMe-TM in the 550/40 nm channel in the presence of incubated Aβ42 peptide, we found that the average fluorescence lifetime shifted to shorter decay times as the incubation time increased (Figures 2.5 and S2.6). Our data showed a population of aggregates in which the lifetime of 2-Me-4-OMe-TM was centered at 2.80 ± 0.01 ns after 15 min of incubation, shifting to 2.50 ± 0.01 ns at later stages. Finally, the emergence of a second population of aggregates at 2.05 ± 0.02 ns was detected after 24 h of incubation. As expected, this behavior is different from that detected in the 600/40 nm channel. However, this outcome is justified because of the short fluorescent lifetime components of the neutral species of the dye favored at the 550 nm emission wavelength. This finding is in agreement with the data obtained from the 600/40 channel and the fact that fibrils formed in the late stages are more hydrophobic and with other works where it is measured an increase on hydrophobicity during the aggregation process of different oligomers[28,44] .

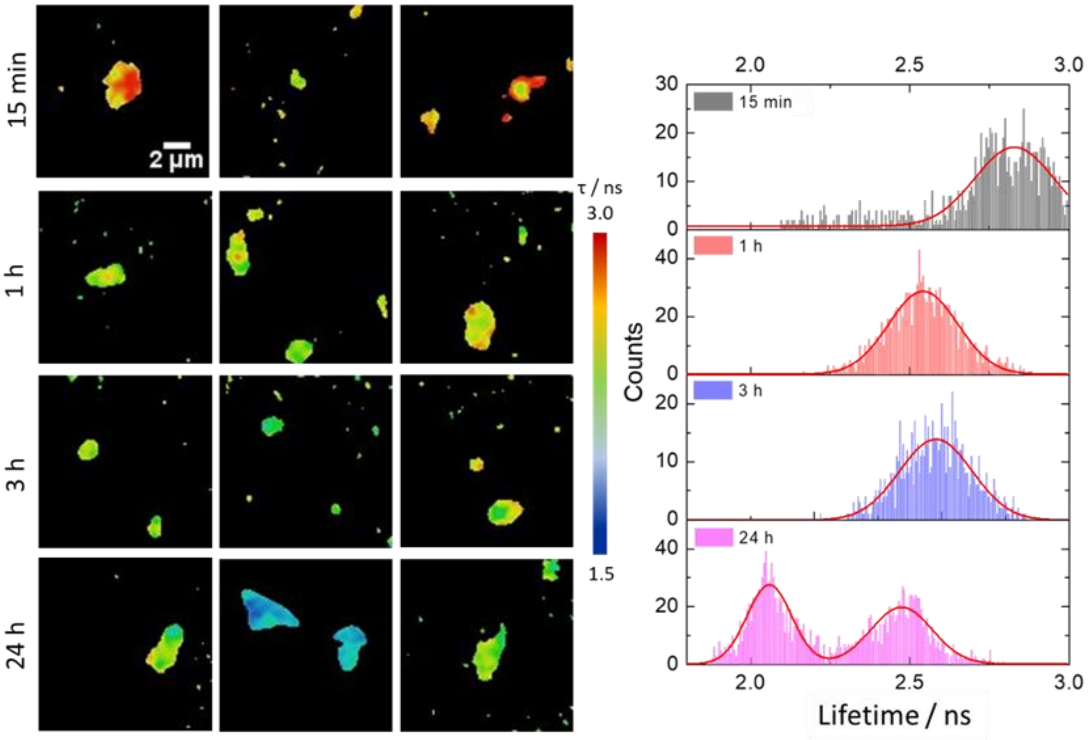

Figure 2.5. (Left) FLIM images of 2-Me-4-Ome-TM in the green channel in 100 µM Aβ42 incubated at 37 °C for 15 min and 1, 3 and 24 h. The size of each image is 12 x 12 µm. Scale bar represents 2 µm. (Right) Corresponding fluorescence lifetime histograms in the 550/40 channel from the FLIM images represented in the figure.

Since the average fluorescence lifetime recovered in both channels presented opposite trends upon aggregation, we envisaged that using fluorescence lifetime ratio images (Figure 2.6) could provide further sensitivity in the detection of changes in the aggregates and directly relate them with the dielectric constant of the microenvironment using the calibration in Figure 2.2. The histograms from these images are represented in Figure S2.6. Figure 2.6b presents the average ratio value from images at different incubation times. The lifetime ratio increased from 0.96 ± 0.14 at 15 min until 2.59 ± 0.24 after 24 h of incubation. The increase in the lifetime ratio values corresponds to a decrease in the polarity of the aggregates, as is indicated in Figure 2.3b.

Several approaches take advantage of measuring the fluorescence lifetime to monitor different aggregation states with the use of intrinsic fluorescence[45,46] or extrinsic fluorescence[7,9,47,48]. Owing to the solvatochromic behaviour of 2-Me-4-OMe-TM, our system is based on the opposite changes in the fluorescence lifetime of the dual band emission of this dye. In this way, we reported an approach that combines the advantage of both methods: the measure of fluorescence lifetime provides independence from the concentration of the dye, allows compatibility with other imaging techniques or easily removes autofluorescence[33]; and the ratiometric measurement enables reducing the noise affecting both channels simultaneously, obtaining a more stable and robust readout for biological contexts, e.g., in samples where both lifetimes are artificially increased or reduced.

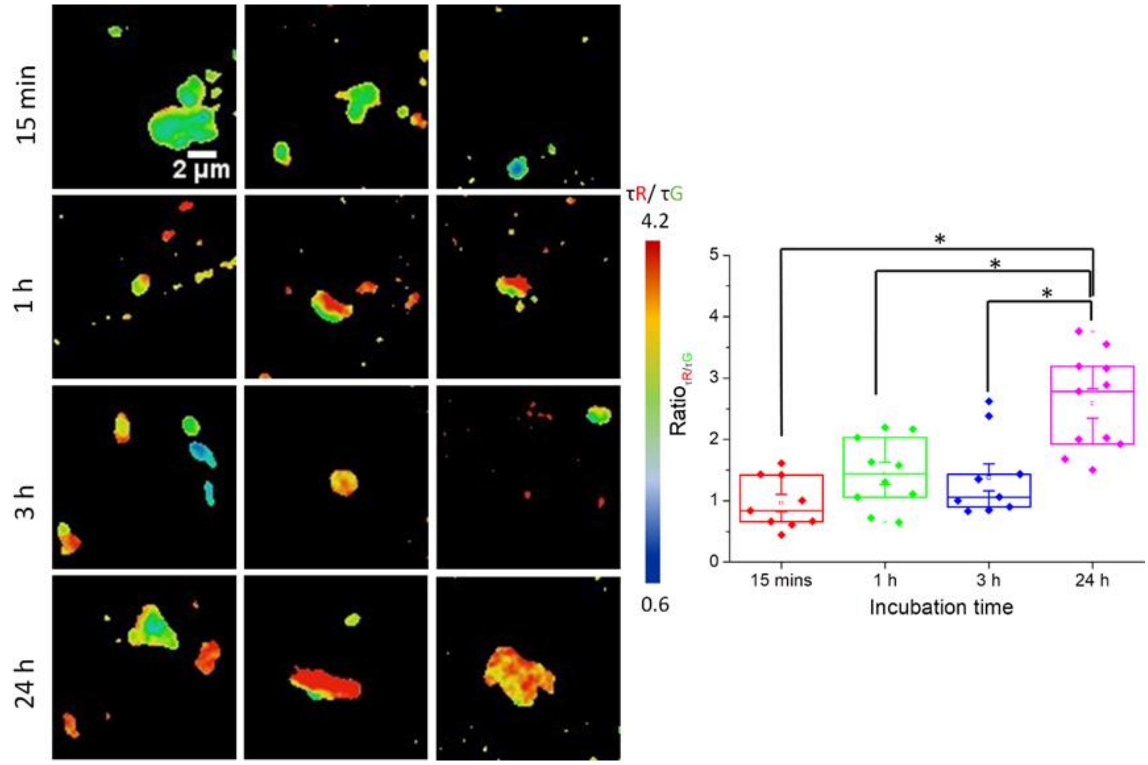

Figure 2.6. (Left) FLIM ratio red/green images 2-Me-4-OMe-TM in 100 µM Aβ42 incubated at 37 °C for 15 min and 1, 3 and 24 h. Scale bar represents 2 µm (Right) Corresponding fluorescence lifetime ratio at different incubation times. The size of each image is 12 x 12 µm. The whisker in the charts (Figure 2.6 right) represents the standard deviation, and the box limits correspond to the 25th and 75th percentiles.

The asterisks indicate a significant difference between populations based on a non-parametric statistical one-way ANOVA test at the 0.05 level.

2.5 CONCLUSION

In this work, through steady-state fluorescence and FLIM, we confirmed the use of the solvatofluorochromic dye 2-Me-4-OMe-TM as a fluorescent probe for the initial stages of Aβ42 amyloid aggregation. In particular, by establishing a polarity scale based on the ratiometric value of the average fluorescence lifetimes between two different emission bands, we were able to detect changes in the hydrophobicity of the aggregates and established a method for distinguishing between aggregates of different types. FLIM has proven to be an excellent approach for studying amyloidogenic aggregation because of the inherent advantages of the fluorescence lifetime technique, such as fluorophore concentration independence or easy autofluorescence avoidance, which supports the use of the xanthenic derivative 2-Me-4OMe TM for noninvasive detection of preamyloid aggregates.

BIBLIOGRAPHY

1 Temussi, P. A.; Masino, L.; Pastore, A., From Alzheimer to Huntington: why is a structural understanding so difficult? *EMBO J.* **2003,** *22* (3), 355-361.

2 Bucciantini, M.; Calloni, G.; Chiti, F.; Formigli, L.; Nosi, D.; Dobson, C. M.; Stefani, M., Prefibrillar amyloid protein aggregates share common features of cytotoxicity. *J. Biol. Chem.* **2004,** *279* (30), 31374-82.

3 Chafekar, S. M.; Baas, F.; Scheper, W., Oligomer-specific A beta toxicity in cell models is mediated by selective uptake. *BBA-Mol. Basis Dis.* **2008,** *1782* (9), 523-531.

4 Glabe, C. G., Structural Classification of Toxic Amyloid Oligomers. *J. Biol. Chem.* **2008,** *283* (44), 29639-29643.

5 Sengupta, U.; Nilson, A. N.; Kayed, R., The Role of Amyloid-beta Oligomers in Toxicity, Propagation, and Immunotherapy. *Ebiomedicine* **2016,** *6*, 42-49.

6 Naslund, J.; Haroutunian, V.; Mohs, R.; Davis, K. L.; Davies, P.; Greengard, P.; Buxbaum, J. D., Correlation between elevated levels of amyloid beta-peptide in the brain and cognitive decline. *Jama-Journal of the American Medical Association* **2000,** *283* (12), 1571-1577.

7 Fueyo-Gonzalez, F.; Gonzalez-Vera, J. A.; Alkorta, I.; Infantes, L.; Jimeno, M. L.; Aranda, P.; Acuna-Castroviejo, D.; Ruiz-Arias, A.; Orte, A.; Herranz, R., Environment-Sensitive Probes for Illuminating Amyloid Aggregation In Vitro and in Zebrafish. *Acs Sensors* **2020,** *5* (9), 2792-2799.

8 Ono, K.; Watanabe-Nakayama, T., Aggregation and structure of amyloid beta-protein. *Neurochem. Int.* **2021,** *151*.

9 Paredes, J. M.; Casares, S.; Ruedas-Rama, M. J.; Fernandez, E.; Castello, F.; Varela-Alvarez, L.; Orte, A., Early Amyloidogenic Oligomerization Studied through Fluorescence Lifetime Correlation Spectroscopy. *Int. J. Mol. Sci.* **2012,** *13* (8), 9400-9418.

10 Castello, F.; Paredes, J. M.; Ruedas-Rama, M. J.; Martin, M.; Roldan, M.; Casares, S.; Orte, A., Two-Step Amyloid Aggregation: Sequential Lag Phase Intermediates. *Sci. Rep.* **2017,** *7*.

11 Novo, M.; Freire, S.; Al-Soufi, W., Critical aggregation concentration for the formation of early Amyloid-beta (1-42) oligomers. *Sci. Rep.* **2018,** *8*.

12 Yang, J.; Perrett, S.; Wu, S., Single Molecule Characterization of Amyloid Oligomers. *Molecules* **2021,** *26* (4).

13 Bertoncini, C. W.; Celej, M. S., Small Molecule Fluorescent Probes for the Detection of Amyloid Self-Assembly In Vitro and In Vivo. *Curr. Protein Peptide Sci.* **2011,** *12* (3), 206-220.

14 Ruiz-Arias, A.; Paredes, J. M.; Di Biase, C.; Cuerva, J. M.; Giron, M. D.; Salto, R.; Gonzalez-Vera, J. A.; Orte, A., Seeding and Growth of beta-Amyloid Aggregates upon

Interaction with Neuronal Cell Membranes. *International Journal of Molecular Sciences* **2020,** *21* (14).

15 Dzyuba, S. V., BODIPY Dyes as Probes and Sensors to Study Amyloid-beta-Related Processes. *Biosensors-Basel* **2020,** *10* (12).

16 Pravin, N.; Kumar, R.; Tripathi, S.; Kumar, P.; Mohite, G. M.; Navalkar, A.; Panigrahi, R.; Singh, N.; Gadhe, L. G.; Manchanda, S.; Shimozawa, M.; Nilsson, P.; Johansson, J.; Kumar, A.; Maji, S. K.; Shanmugam, M., Benzimidazole-based fluorophores for the detection of amyloid fibrils with higher sensitivity than Thioflavin-T. *J. Neurochem.* **2021,** *156* (6), 1003-1019.

17 Sulatskaya, A. I.; Sulatsky, M. I.; Povarova, O. I.; Rodina, N. P.; Kuznetsova, I. M.; Lugovskii, A. A.; Voropay, E. S.; Lavysh, A. V.; Maskevich, A. A.; Turoverov, K. K., Trans- 2- 4-(dimethylamino)styryl -3-ethyl-1,3-benzothiazolium perchlorate - New fluorescent dye for testing of amyloid fibrils and study of their structure. *Dyes and Pigments* **2018,** *157*, 385-395.

18 Ruiz-Arias, A.; Jurado, R.; Fueyo-Gonzalez, F.; Herranz, R.; Galvez, N.; Gonzalez-Vera, J. A.; Orte, A., A FRET pair for quantitative and superresolution imaging of amyloid fibril formation. *Sensors and Actuators B-Chemical* **2022,** *350*.

19 Arad, E.; Green, H.; Jelinek, R.; Rapaport, H., Revisiting thioflavin T (ThT) fluorescence as a marker of protein fibrillation - The prominent role of electrostatic interactions. *J. Colloid Interface Sci.* **2020,** *573*, 87-95.

20 Frieg, B.; Gremer, L.; Heise, H.; Willbold, D.; Gohlke, H., Binding modes of thioflavin T and Congo red to the fibril structure of amyloid-beta(1-42). *Chem. Commun.* **2020,** *56* (55), 7589-7592.

21 Narayan, P.; Meehan, S.; Carver, J. A.; Wilson, M. R.; Dobson, C. M.; Klenerman, D., Amyloid-β Oligomers are Sequestered by both Intracellular and Extracellular Chaperones. *Biochemistry* **2012,** *51* (46), 9270-9276.

22 Morel, B.; Carrasco, M. P.; Jurado, S.; Marco, C.; Conejero-Lara, F., Dynamic micellar oligomers of amyloid beta peptides play a crucial role in their aggregation mechanisms. *PCCP* **2018,** *20* (31), 20597-20614.

23 Yu, H. J.; Zhao, W.; Xie, M. T.; Li, X. Q.; Sun, M.; He, J.; Wang, L.; Yu, L., Real-Time Monitoring of Self-Aggregation of beta-Amyloid by a Fluorescent Probe Based on Ruthenium Complex. *Anal. Chem.* **2020,** *92* (4), 2953-2960.

24 Sang, J. C.; Lee, J. E.; Dear, A. J.; De, S. M.; Meisl, G.; Thackray, A. M.; Bujdoso, R.; Knowles, T. P. J.; Klenerman, D., Direct observation of prion protein oligomer formation reveals an aggregation mechanism with multiple conformationally distinct species. *Chemical Science* **2019,** *10* (17), 4588-4597.

25 Jiang, B.; Aliyan, A.; Cook, N. P.; Augustine, A.; Bhak, G.; Maldonado, R.; McWilliams, A. D. S.; Flores, E. M.; Mendez, N.; Shahnawaz, M.; Godoy, F. J.; Montenegro, J.; Moreno-Gonzalez, I.; Marti, A. A., Monitoring the Formation of Amyloid Oligomers Using Photoluminescence Anisotropy. *J. Am. Chem. Soc.* **2019,** *141* (39), 15605-15610.

26 Obstarczyk, P.; Lipok, M.; Grelich-Mucha, M.; Samoc, M.; Olesiak-Banska, J., Two-Photon Excited Polarization-Dependent Autofluorescence of Amyloids as a Label-Free Method of Fibril Organization Imaging. *J. Phys. Chem. Lett.* **2021,** *12* (5), 1432-1437.

27 Ziaunys, M.; Sneideris, T.; Smirnovas, V., Exploring the potential of deep-blue autofluorescence for monitoring amyloid fibril formation and dissociation. *Peerj* **2019,** *7*.

28 Bongiovanni, M. N.; Godet, J.; Horrocks, M. H.; Tosatto, L.; Carr, A. R.; Wirthensohn, D. C.; Ranasinghe, R. T.; Lee, J. E.; Ponjavic, A.; Fritz, J. V.; Dobson, C. M.; Klenerman, D.; Lee, S. F., Multi-dimensional super-resolution imaging enables surface hydrophobicity mapping. *Nature Communications* **2016,** *7*.

29 Kremer, J. J.; Pallitto, M. M.; Sklansky, D. J.; Murphy, R. M., Correlation of beta-amyloid aggregate size and hydrophobicity with decreased bilayer fluidity of model membranes. *Biochemistry* **2000,** *39* (33), 10309-10318.

30 Gregoire, S.; Irwin, J.; Kwon, I., Techniques for monitoring protein misfolding and aggregation in vitro and in living cells. *Korean J. Chem. Eng.* **2012,** *29* (6), 693-702.

31 Espinar-Barranco, L.; Luque-Navarro, P.; Strnad, M. A.; Herrero-Foncubierta, P.; Crovetto, L.; Miguel, D.; Giron, M. D.; Orte, A.; Cuerva, J. M.; Salto, R.; Alvarez-Pez, J. M.; Paredes, J. M., A solvatofluorochromic silicon-substituted xanthene dye useful in bioimaging. *Dyes and Pigments* **2019,** *168*, 264-272.

32 Staderini, M.; Martin, M. A.; Bolognesi, M. L.; Menendez, J. C., Imaging of beta-amyloid plaques by near infrared fluorescent tracers: a new frontier for chemical neuroscience. *Chem. Soc. Rev.* **2015,** *44* (7), 1807-1819.

33 Ruedas-Rama, M. J.; Alvarez-Pez, J. M.; Crovetto, L.; Paredes, J. M.; Orte, A., FLIM Strategies for Intracellular Sensing. In *Advanced Photon Counting: Applications, Methods, Instrumentation*, Kapusta, P.; Wahl, M.; Erdmann, R., Eds. Springer International Publishing: Cham, 2015; pp 191-223.

34 Lu, M.; Kaminski, C. F.; Schierle, G. S. K., Advanced fluorescence imaging of in situ protein aggregation. *Phys. Biol.* **2020,** *17* (2).

35 Castello, F.; Casares, S.; Ruedas-Rama, M. J.; Orte, A., The First Step of Amyloidogenic Aggregation. *J. Phys. Chem. B* **2015,** *119* (26), 8260-8267.

36 Jurado, R.; Adamcik, J.; Lopez-Haro, M.; Gonzalez-Vera, J. A.; Ruiz-Arias, A.; Sanchez-Ferrer, A.; Cuesta, R.; Dominguez-Vera, J. M.; Calvino, J. J.; Orte, A.; Mezzenga, R.; Galvez, N., Apoferritin Protein Amyloid Fibrils with Tunable Chirality and Polymorphism. *J. Am. Chem. Soc.* **2019,** *141* (4), 1606-1613.

37 Ruedas-Rama, M. J.; Orte, A.; Hall, E. A. H.; Alvarez-Pez, J. M.; Talavera, E. M., Effect of Surface Modification on Semiconductor Nanocrystal Fluorescence Lifetime. *Chemphyschem* **2011,** *12* (5), 919-929.

38 Schindelin, J.; Arganda-Carreras, I.; Frise, E.; Kaynig, V.; Longair, M.; Pietzsch, T.; Preibisch, S.; Rueden, C.; Saalfeld, S.; Schmid, B.; Tinevez, J. Y.; White, D. J.; Hartenstein, V.; Eliceiri, K.; Tomancak, P.; Cardona, A., Fiji: an open-source platform for biological-image analysis. *Nat. Methods* **2012,** *9* (7), 676-682.

39 Egawa, T.; Koide, Y.; Hanaoka, K.; Komatsu, T.; Terai, T.; Nagano, T., Development of a fluorescein analogue, TokyoMagenta, as a novel scaffold for fluorescence probes in red region. *Chem. Commun.* **2011,** *47* (14), 4162-4164.

40 Catalan, J., Toward a Generalized Treatment of the Solvent Effect Based on Four Empirical Scales: Dipolarity (SdP, a New Scale), Polarizability (SP), Acidity (SA), and Basicity (SB) of the Medium. *J. Phys. Chem. B* **2009,** *113* (17), 5951-5960.

41 Lin, T. W.; Chang, C. F.; Chang, Y. J.; Liao, Y. H.; Yu, H. M.; Chen, Y. R., Alzheimer's amyloid-beta A2T variant and its N-terminal peptides inhibit amyloid-beta fibrillization and rescue the induced cytotoxicity. *PLoS One* **2017,** *12* (3).

42 Gonzalez-Garcia, M. C.; Pena-Ruiz, T.; Herrero-Foncubierta, P.; Miguel, D.; Giron, M. D.; Salto, R.; Cuerva, J. M.; Navarro, A.; Garcia-Fernandez, E.; Orte, A., Orthogonal cell polarity imaging by multiparametric fluorescence microscopy. *Sensors and Actuators B-Chemical* **2020,** *309*.

43 Wohlfarth, C., *Static Dielectric Constants of Pure Liquids and Binary Liquid Mixtures*. Springer, Berlin, Heidelberg: 2015.

44 Lee, J. E.; Sang, J. C.; Rodrigues, M.; Carr, A. R.; Horrocks, M. H.; De, S.; Bongiovanni, M. N.; Flagmeier, P.; Dobson, C. M.; Wales, D. J.; Lee, S. F.; Klenerman, D., Mapping Surface Hydrophobicity of alpha-Synuclein Oligomers at the Nanoscale. *Nano Lett.* **2018,** *18* (12), 7494-7501.

45 Chan, F. T. S.; Schierle, G. S. K.; Kumita, J. R.; Bertoncini, C. W.; Dobson, C. M.; Kaminski, C. F., Protein amyloids develop an intrinsic fluorescence signature during aggregation. *Analyst* **2013,** *138* (7), 2156-2162.

46 Amaro, M.; Kubiak-Ossowska, K.; Birch, D. J. S.; Rolinski, O. J., Initial stages of beta-amyloid A beta(1-40) and A beta(1-42) oligomerization observed using fluorescence decay and molecular dynamics analyses of tyrosine. *Methods and Applications in Fluorescence* **2013,** *1* (1).

47 Wang, Y.; Clark, T. B.; Goodson, T., Two-Photon and Time-Resolved Fluorescence Conformational Studies of Aggregation in Amyloid Peptides. *J. Phys. Chem. B* **2010,** *114* (20), 7112-7120.

48 Rovnyagina, N. R.; Budylin, G. S.; Vainer, Y. G.; Tikhonova, T. N.; Vasin, S. L.; Yakovlev, A. A.; Kompanets, V. O. Fluorescence Lifetime and Intensity of Thioflavin T as Reporters of Different Fibrillation Stages: Insights Obtained from Fluorescence Up-Conversion and Particle Size Distribution Measurements. *International Journal of Molecular Sciences* **2020,** *21* (17).

SUPPPORTING INFORMATION

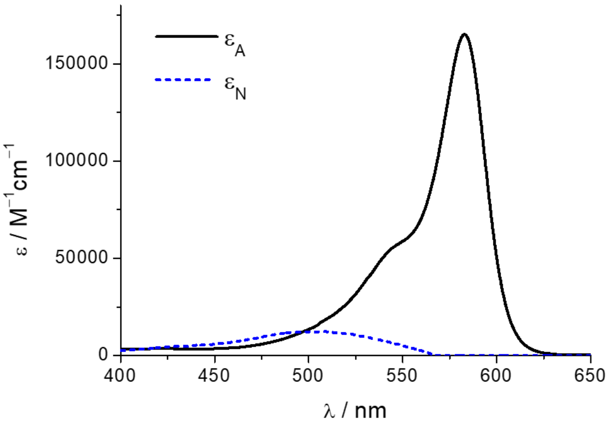

Figure S2.1. Absorptivity coefficients from anion and neutral species of 2-Me-4-OMe-TM in water solution.

Table S2.1. Quantum yields and fluorescence lifetimes obtained from 2-Me-4-OMe-TM in different solvents.

Solvent	QY (440)	QY (530)	τ_{av} / ns
Water	–	0.440	2.95
DMSO	0.071	0.107	0.34
Methanol	0.058	0.267	3.06
Ethanol	0.075	0.101	4.14
Butanol	0.110	0.297	3.42
Pentanol	0.141	0.886	3.81
Octanol	0.187	–	1.41

QY(440) indicates the experimental quantum yield of the dye using a wavelength excitation of 440 nm where we predominantly excite the neutral species. QY(530) indicates the experimental quantum yield of the dye using a wavelength excitation of 530 nm where it predominantly excites the anionic species.

QUANTUM YIELD CALCULATION

The relative fluorescence quantum yield values were determined using the following formula[1]:

$$\Phi = \Phi_R \frac{I}{I_R} \frac{OD_R}{OD} \frac{n^2}{n_R^2}$$

Where Φ and Φ_R indicates the fluorescence quantum yield of the dye and the reference respectively, *I* and I_R the integrated fluorescence spectra of the dye and the reference, *OD* and OD_R the absorption at the excitation wavelength of the dye and the reference and *n* and n_R the refractive index of the solvent where the dye and reference are dissolved. As references, we have used fluorescein in 0.01 M NaOH ($\Phi = 0.91$)[2] for the dye when is excited at 440 nm with a range of emission corresponding to the 480-600 band, and rhodamine 101 in ethanol ($\Phi = 0.98$)[3] for the dye when is excited at 530 nm and a range of emission corresponding to the 560-700nm.

TIME RESOLVED EXPERIMENTS

Fluorescence decay traces of 2-Me-4-OMe-TM in different solvents were measured in a Fluotime 200 fluorometer (PicoQuant GmbH) by the time correlated single photon counting, (TCSPC) method. The excitation sources were 440 nm or 530 nm LDH pulsed laser (PicoQuant GmbH). The pulse repetition rate was 20 MHz. Fluorescence decay traces were registered at two different emission wavelengths (560 and 610 nm), until the peak channel reached 20000 counts. Except water, all the solvents were fitted to tri-exponential fitting curves.

Average lifetime is calculated based in the next expression:

$$\tau_{av} = \frac{\sum_i A_i \tau_i^2}{\sum_i A_i \tau_i}$$

Where A_i is the pre-exponential fit and τ_i the fluorescence lifetime of the *i* exponential.

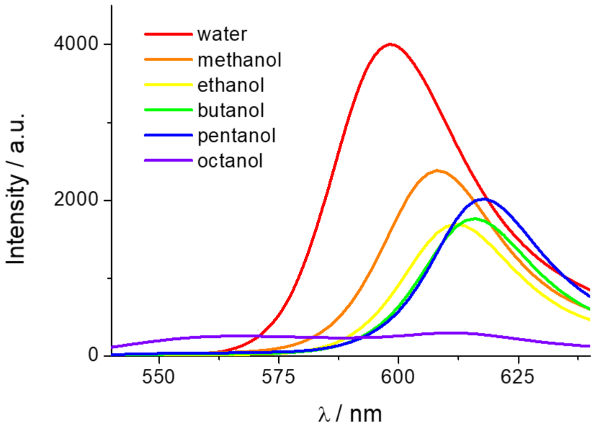

Figure S2.3. Fluorescence emission spectra (λ_{ex} = 530 nm) of 2-Me-4-OMe-TM in six different solvents.

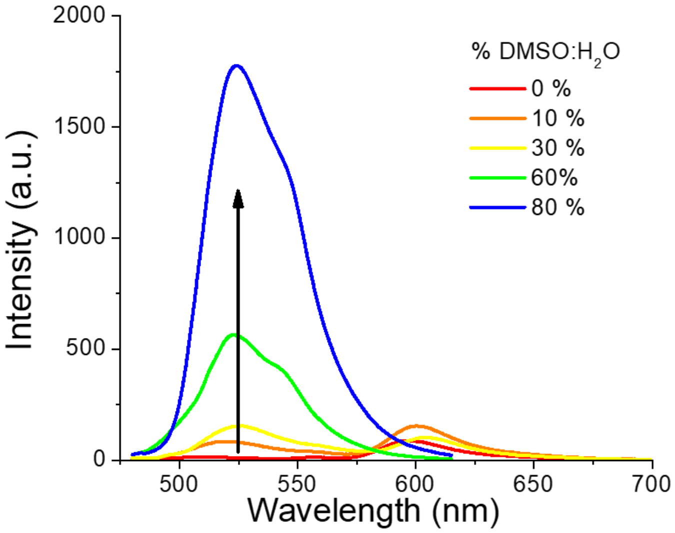

Figure S2.4. Fluorescence spectra (λ_{ex} = 470 nm) of 2-Me-4-OMe-TM in different DMSO:water proportions.

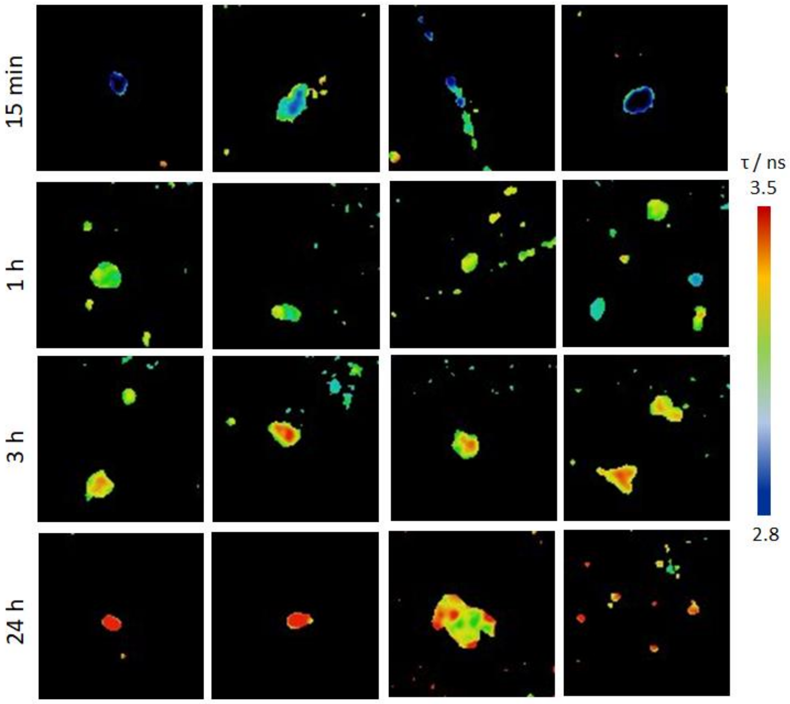

Figure S2.5. FLIM images of 2-Me-4-OMe-TM in the red channel in 100 µM Aβ42 peptide incubated at 37 °C for 15 min, 1, 3 and 24 h. The size of each image is 12 x 12 µm.

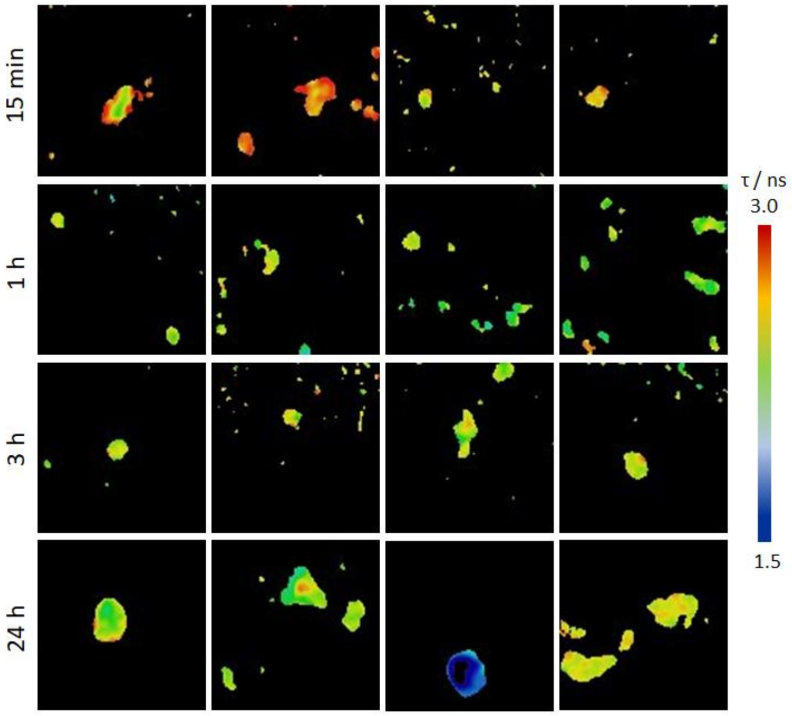

Figure S2.6. FLIM images of 2-Me-4-OMe-TM in the green channel in 100 μM Aβ42 peptide incubated at 37 °C for 15 min, 1, 3 and 24 h. The size of each image is 12 x 12 μm.

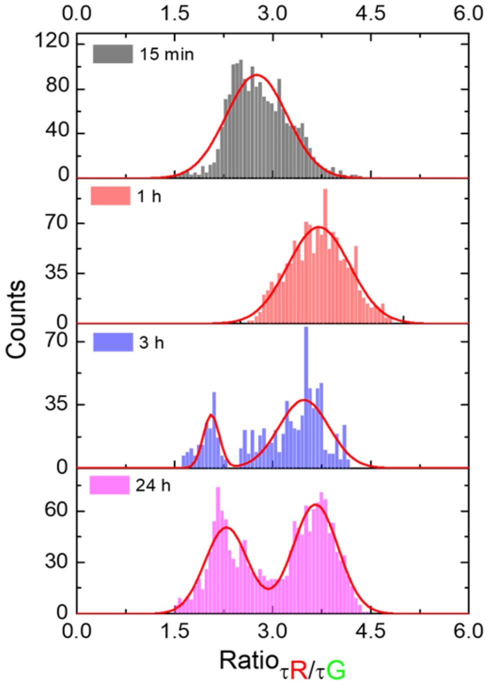

Figure S2.7. Histograms of the ratio of fluorescence lifetimes in the red and green channels from the FLIM images represented in the figure 6 of main text.

BIBLIOGRAPHY

1 Lakowicz, J. R. *Principles of Fluorescence Spectroscopy*, Springer.; New York, **2006**.

2 L. Porres, A. Holland, L. O. Palsson, A. P. Monkman, C. Kemp, A. Beeby, *Journal of Fluorescence* **2006**, *16*, 267-272.

3 J. Karpiuk, Z. R. Grabowski, F. C. Deschryver, *Journal of Physical Chemistry* **1994**, *98*, 3247-3256.

SYNTHESIS, PHOTOPHYSICS, AND SOLVATOCHROMIC STUDIES OF AN AGGREGATED-INDUCED-EMISSION LUMINOGEN USEFUL IN BIOIMAGING

Sensors, Volume 19, Issue 22, 4932

IP: 3.275

Q1 (15/64)

Instrument and instrumentation

Contribution: I have carried out all the experiments except the synthesis of the molecule PEMC.

3.1 ABSTRACT

Biological samples are a complex and heterogeneous matrix where different macromolecules with different physicochemical parameters cohabit in reduced spaces. The introduction of fluorophores into these samples, such as in the interior of cells, can produce changes in the fluorescence emission properties of these dyes, caused by the specific physicochemical properties of cells. This effect can be especially intense with solvatofluorochromic dyes, where changes in the polarity environment surrounding the dye can drastically change the fluorescence emission. In this article, we studied the photophysical behavior of a new dye and confirmed the aggregation-induced emission (AIE) phenomenon with different approaches, such as by using different solvent proportions, increasing the viscosity, forming micelles, and adding bovine serum albumin (BSA), through analysis of the absorption and steady-state and time-resolved fluorescence. Our results show the preferences of the dye for nonpolar media, exhibiting AIE under specific conditions through immobilization. Additionally, this approach offers the possibility of easily determining the critical micelle concentration (CMC). Finally, we studied the rate of spontaneous incorporation of the dye into cells by fluorescence lifetime imaging and observed the intracellular pattern produced by the AIE. Interestingly, different intracellular compartments present strong differences in fluorescence intensity and fluorescence lifetime. We used this difference to isolate different intracellular regions to selectively study these regions. Interestingly, the fluorescence lifetime shows a strong difference in different intracellular compartments, facilitating selective isolation for a detailed study of specific organelles.

3.2 INTRODUCTION

When one dye has weak emission in dilute solutions but its aggregation causes strong emission, we call this behavior aggregation-induced emission (AIE). Moreover, the aggregation effects can include changes on other dye fluorescence properties such as shifts in its spectral position. For example, this effect has been observed in a coumarin-based fluorogen[1] and acridine orange in reverse micelles[2] or porphyrins[3]. Since its discovery in 2001[4], this phenomenon has received much attention[5-7] and has been developed in several applications, such as organic light-emitting devices, bioimaging[9], ion sensors[10,11], and environmental analysis[12]. AIE is therefore a very interesting behavior present in many molecules, with multiple uses in different scientific fields.

Biological samples are a complex and heterogeneous matrix where different macromolecules with different physicochemical parameters cohabit in reduced spaces. The introduction of a fluorophore in these samples, such as in the interior of cells, can produce changes in the fluorescent emission properties of these dyes caused by the specific physicochemical properties of cells[13]. This effect can be especially intense with solvatofluorochromic dyes, where the changes in the polarity environment surrounding the dye can drastically change the fluorescence emission[14]. The crowded environment typical of intracellular media can produce AIE by restricting the intramolecular motion of the dye due to immobilization upon interaction with intracellular macromolecules. AIE makes these molecules excellent probes in the fields of biomedicine and life sciences[15]. AIE probes have been used for biosensing and/or bioimaging in DNA[16] and ATP[17] detection, as a mitochondria marker[18], for determining lipid droplet and mitochondria membrane potential[19], and for detecting multiple ions and species such as Al^{3+} in food and cells[20], intracellular cyanide[21], bilirubin and Fe^{3+}[22]. These molecules present a promising future as probes in in vivo diagnosis and therapy[23].

The study and development of new AIE luminogens is currently an interesting research topic with important potential uses. However, prior to application, it is important to understand their photophysical and solvatochromic behavior. This consideration is especially important in fluorescence lifetime imaging microscopy (FLIM) for correct interpretation of the data obtained. FLIM is an innovative multiparametric tool in which intensity and fluorescence lifetime are recovered in an image. Apart from intensity, the fluorescence lifetime can reveal different environments and be affected by analytes[24-26] but with the advantage of being independent of the luminogen concentration. In this article, we have synthesized and studied the solvatochromic properties of the dye 2-((4-((E)-2-((E)-3-((E)-3-(4-cyano-5-(dicyanomethylene)-2-

phenyl-2-(trifluoromethyl)-2,5-dihydrofuran-3-yl) allylidene)-5,5-dimethylcyclohex-1-enyl) vinyl) phenyl) (ethyl)amino) ethyl methacrylate (PEMC) (see Scheme 3.1 and SI) using different approaches such as the Catalan and Lippert–Mataga analyses. We also measured the effect on fluorescence-forming sodium dodecyl sulfate (SDS) micelles and added bovine serum albumin (BSA), analyzing the absorption and steady-state and time-resolved fluorescence. Finally, we measured the behavior in live cells through FLIM.

3.3 RESULTS AND DISCUSSION

3.3.1 SOLVATOCHROMISM

An initial solvatochromic study using 14 different solvents was performed (Figure 3.1). We measured the absorption, emission, and fluorescence lifetime of the dye PEMC. We observed a strong dependency on the nature of the solvent used, with maxima shifts of 57 and 50 nm of dye PEMC absorption and emission, respectively. Moreover, we have calculated the relative quantum yield in every solvent using Nile Blue A as a reference. The main spectral parameters and quantum yield are included in Table 3.1.

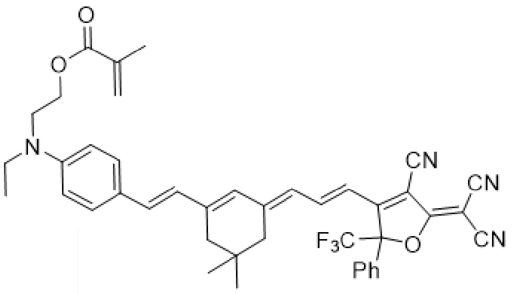

Scheme 3.1. Molecular structure of PEMC.

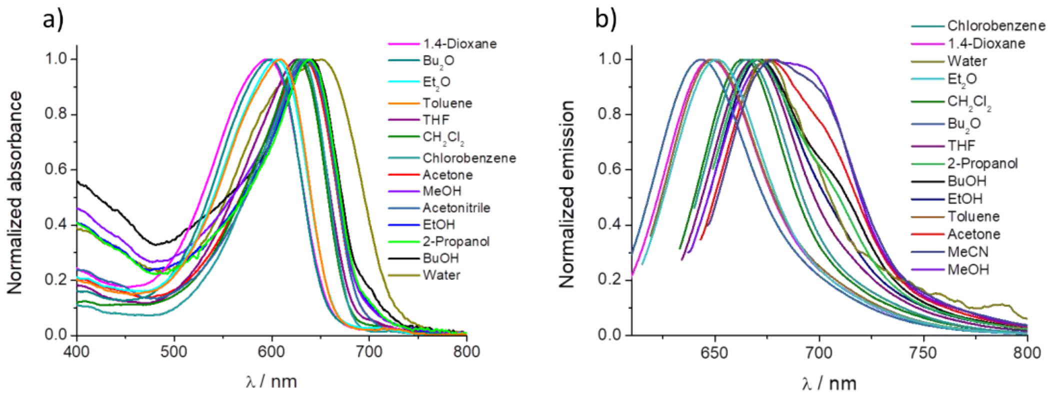

Figure 3.1. Normalized absorption (a) and emission (b) of PEMC in different solvents. The list indicates the solvent ordered from blue to red.

Solvent	Dielectric Constant	λ^{max}_{abs}/nm	λ^{max}_{em}/nm	τ_{av}/ns	Quantum Yield
Chlorobenzene	5.62	630	666	0.68	0.266
Toluene	2.38	609	649	0.58	0.202
Dibutyl ether	3.08	598	644	0.35	0.188
Diethyl ether	4.20	605	651	0.27	0.126
Butanol	17.51	642	670	0.36	0.058
2-Propanol	19.92	639	678	0.34	0.049
Ethanol	24.55	637	672	0.56	0.049
THF	7.58	624	671	0.21	0.044
1,4-Dioxane	2.21	595	648	0.57	0.041
Dichloromethane	8.93	648	665	0.31	0.022
Methanol	32.66	627	676	1.88	0.014
Acetone	20.56	633	676	0.1	0.012
Acetonitrile	35.94	636	679	2.34	0.011
Water	78.36	650	676	0.47	0.001
Nile Blue A (see [28])	-	630	659	-	0.27

Table 3.1. Absorption and emission maxima, fluorescence lifetime, and quantum yield of PEMC in different solvents with their dielectric constants (from [27]).

As solvatochromism is essential to understand the behavior of dyes in biological samples and allows us to determine a correct interpretation of the fluorescence signal, we performed a study using the Catalan approach[29] and the Lipper–Mataga equation. The Lipper–Mataga equation reveals a slight decrease in the spectral shift and polarizability (Δf; see Figure S3.1), a term that represents the changes in the dipole moment and energy after excitation. This term includes the dielectric constant and refractive index of the solvent. However, the deeper and stronger Catalan approach can reveal the influence of four physicochemical parameters (acidity, basicity, dipolarity, and polarizability) on the changes in absorption and emission spectral properties. Our study revealed a good relationship between the experimental and theoretical data using the four parameters obtained from the Catalan approach (see Figure S3.2). After removing the parameters one by one, the parameter responsible for decreasing the good relationship is determined to be the critical physicochemical parameter that affects the spectral shift in absorption and emission. Table S3.1 reveals the fitting of the Catalan approach. As can be observed, for absorption and emission, we obtain *r* values supporting good correlations (0.9420 and 0.9736, respectively) that remain high when we remove every parameter except dipolarity, which reduces the values to 0.6602 and 0.6175. To confirm that dipolarity is the only parameter that affects solvatochromism, we also obtained data using only one physicochemical parameter. As can be observed in Table S3.1, our fitting shows low *r* values, except when we used the dipolarity parameter, which remains high, indicating a good correlation (0.8856 and 0.9538 for absorption and emission, respectively). Therefore, our results show that dipolarity is the main physicochemical parameter that affects the spectral shift in absorption and emission. This finding is in good accordance with the Lipper–Mataga representation because dipolarity is not included in the polarizability term (Δf). For this reason, the Lipper–Mataga representation does not show any strong change with polarizability.

As expected, for solvatochromic dyes, the dependence of the fluorescence properties on the dipolarity can be used as sensing in bioimaging, because inside cells, it can be found important changes in the dipolarity in the microenvironments. The increase in fluorescence from water to nonpolar solvents makes this molecule an interesting probe to detect its incorporation into nonpolar structures (micelles, proteins, membranes, etc.) from aqueous solvent. Moreover, these structures can cause a restriction in the intramolecular motion of the dye, leading to AIE.

3.3.2 AGGREGATION-INDUCED EMISSION

We checked the enhancement of fluorescence intensity by aggregation increasing the concentration of PEMC in ethanol. Figure 3.2a shows a plot of maxima intensities at different concentrations and spectra are in Figure S3.3. At lowest concentrations we observed a linear increase in intensity (as predicted by Kavanagh's law). This linearity is broken when concentration becomes high enough. However, at very high concentrations, aggregation happens, enhancing strongly the fluorescence intensity. In the other hand, to evaluate whether dipolarity is also key in the AIE process, we measured PEMC in different polarity environments containing different proportions of water: THF. As can be observed in Figures 3.2b and S3.4, the intensity rapidly increases in the presence of a low percentage of THF, with a maximum at 2.5% THF, decreases from 5% to 30% THF, and then increases slightly until 100% THF. Because in THF, the quantum yield of PEMC is higher than that in water, the fluorescence measured is higher in THF than in water. The fast increase at 2.5% THF can be explained as follows. The molecules start to form small aggregates as a result of electrostatic interaction with the solvent mixture leading to AIE. When the proportion of THF molecules increases, aggregates are broken or form even larger aggregates which are non-fluorescent probably as a result of aggregation induced quenching. PEMC becomes more widely distributed and therefore loses its local aggregation, causing decreased fluorescence due to AIE. So, 2.5% is the critical concentration when AIE is maximum.

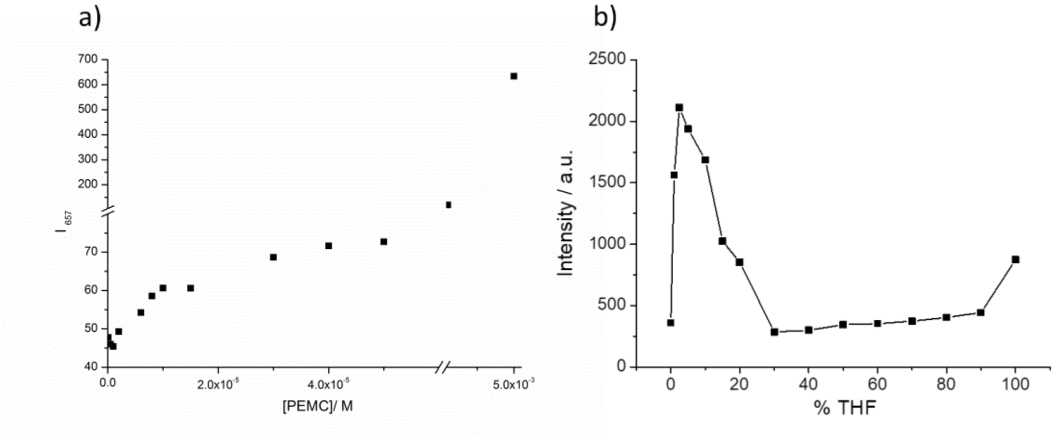

Figure 3.2. (a) Fluorescence intensity with λ_{ex} = 635 nm recovered at λ_{em} = 657 nm from PEMC in ethanol solution at different concentration. (b) Fluorescence intensity of PEMC in the presence of increasing proportions of THF to water.

Another approach to corroborate the AIE behavior is by limiting the rotational freedom of the dye, such as by increasing the viscosity of the solvent or studying incorporation of the dye into a macromolecular structure. In the first case, we added glycerin to increase the viscosity of the sample. Figure 3.3a shows the increase in fluorescence when 25% and 50% glycerin is present in the solution, indicating that PEMC can also be considered as a probe of viscosity.

In contrast, AIE can be used to observe the spontaneous incorporation of macromolecules such as proteins. To follow this behavior, we added BSA to a previously prepared solution of PEMC. Two additions of BSA were performed. As observed in Figure 3.3b, the incorporation of 20 µg of BSA produces a two-fold fluorescence intensity increase, and the addition of 50 µg of BSA produces a stronger effect, enhancing the fluorescence intensity by ten-fold.

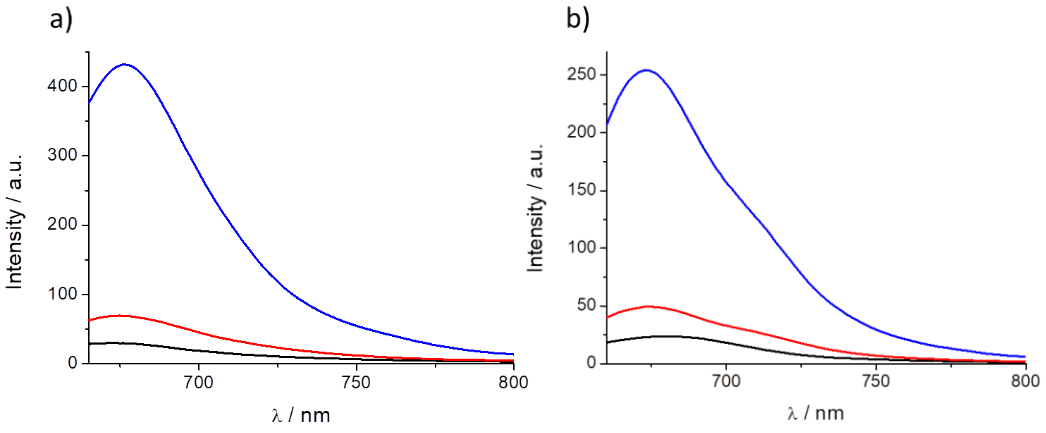

Figure 3.3. Fluorescence intensity of PEMC in the presence of different amounts of glycerin (0%, black; 25%, red; and 50%, blue) (a) and BSA (0 µg, black; 20 µg, red; and 50 µg, blue) (b).

Based on the previous data and according to the characteristic that the dye fluorescence is highly dependent on the surrounding dipolarity and exhibits AIE when immobilized, we hypothesized to use the dye as a probe to detect micelle formation. For this purpose, SDS was selected as it can be mixed at different concentrations to study the influence on PEMC before and after micelle formation. Figure 3.4a shows the fluorescence intensity of PEMC at different SDS concentrations. The dye is almost nonfluorescent when it is dissolved in water or even at an SDS concentration lower than 1 mM. However, above an SDS concentration of 3 mM, and until 5 mM, the fluorescence of PEMC is enhanced. This increase in the fluorescence is attributed to the incorporation of the dye molecules into the SDS micelles when they are formed. Therefore, the solvent can be used to determine the CMC and the formation of micelles when it is confined in this small volume to produce AIE. At higher CMC values, the fluorescence intensity exhibited a slight decrease, as shown in Figure 3.4b.

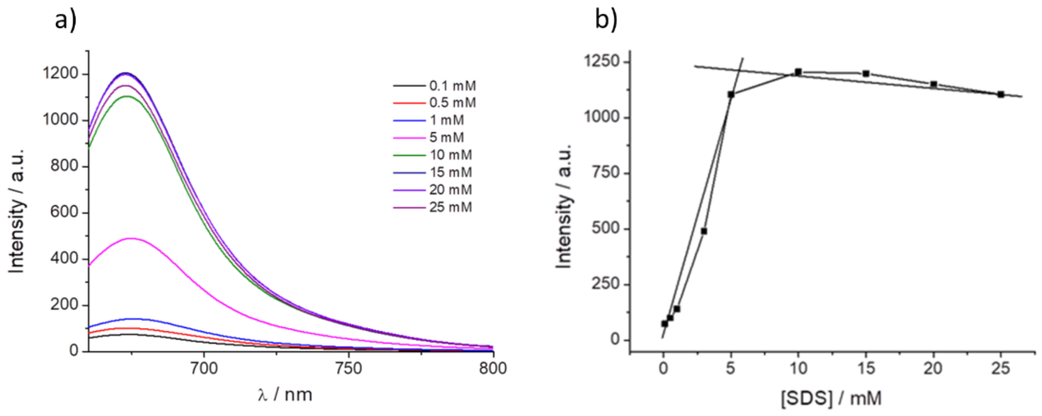

Figure 3.4. Fluorescence intensity of PEMC at different SDS concentrations (a) and the (b) CMC values obtained through emission spectra of PEMC at different SDS concentrations (from 0.1 to 25 mM).

All these characteristics of PEMC make it useful in further applications for bioimaging. As the interiors of cells are characterized by a complex matrix, AIE can be considered an advantageous behavior to identify and as a marker of internal organelles. For this reason, we performed FLIM, studying the rate of spontaneous introduction and the internal fluorescence pattern of PEMC.

3.3.3 FLIM

First, we verified whether PEMC spontaneously enters the interior of cells by measuring the incorporation into the MDA-MB-231 cell line under experimental conditions where autofluorescence is negligible. Figure 3.5a shows the kinetics of intracellular fluorescence after the addition of 5 µL of PEMC (EtOH) in 1 mL of phosphate buffered saline (PBS) for a final concentration of 5×10^{-6} M PEMC. As can be observed, the incorporation is spontaneous, but it takes a period of time to achieve equilibrium, approximately 70 min (see Figure 3.5b). FLIM can recover the fluorescence lifetime and when a sufficient level of intensity is achieved to collect this signal, this parameter is independent of the dye concentration. We have observed that after 10 min, we obtain an interesting intracellular pattern where different structures are well defined in the intensity images (see Figure 3.5a), and marked with higher fluorescence lifetimes in FLIM images (see Figure S3.5). Figure S3.6 collects the average fluorescence lifetime from Figure 3.5.

a)

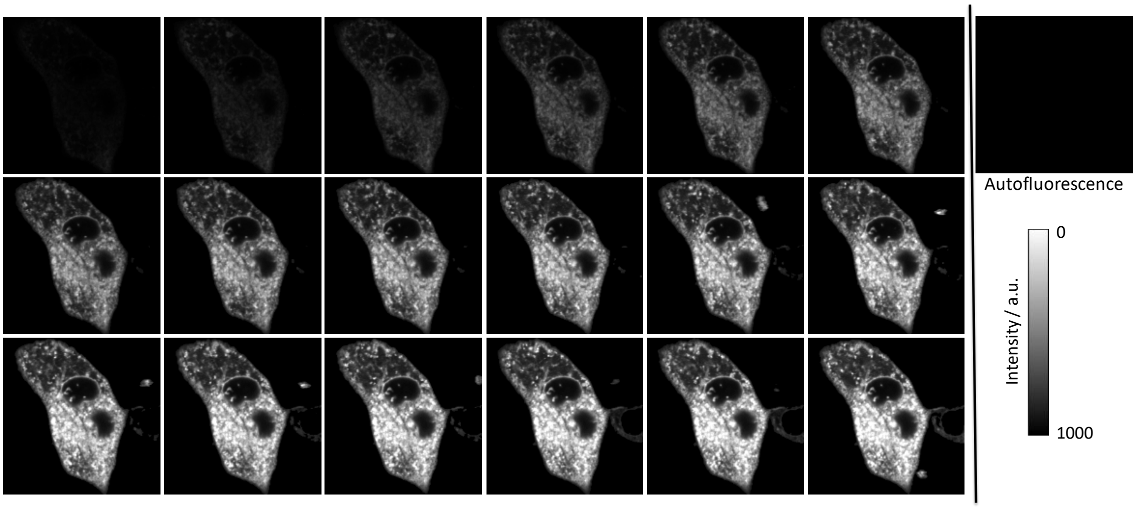

b)

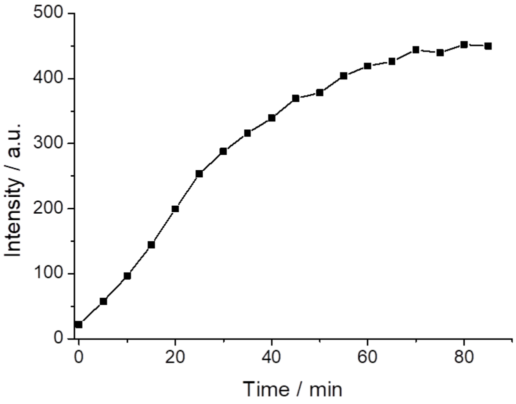

Figure 3.5. Intensity images of the autofluorescence and input kinetics of PEMC in MDA-MB-231 cells (a) and the maxima of fluorescence intensity (b) of every image from (a). The images were taken every 5 min.

In addition to the MDA-MB-231 cell line, we used HEK cells to observe the intracellular pattern as much in intensity as in the fluorescence lifetime. Interestingly, peripheral F-actin structures at the plasma membrane in HEK293 cells[30] present a low intensity signal but a higher fluorescence lifetime, as shown in Figures 3.6a and S3.7. Peripheral F-actin is clearly identifiable in this cell line, because their typical structures around the cells avoid any mistake with other organelles[30]. Respecting other intracellular structures, an enhancement of the fluorescence intensity is observed, with a corresponding higher value of the fluorescence lifetime. A similar intracellular pattern (with the exception of the peripheral F-actin structures) is found in the MDA-MB-231 cells (Figure 3.6b).

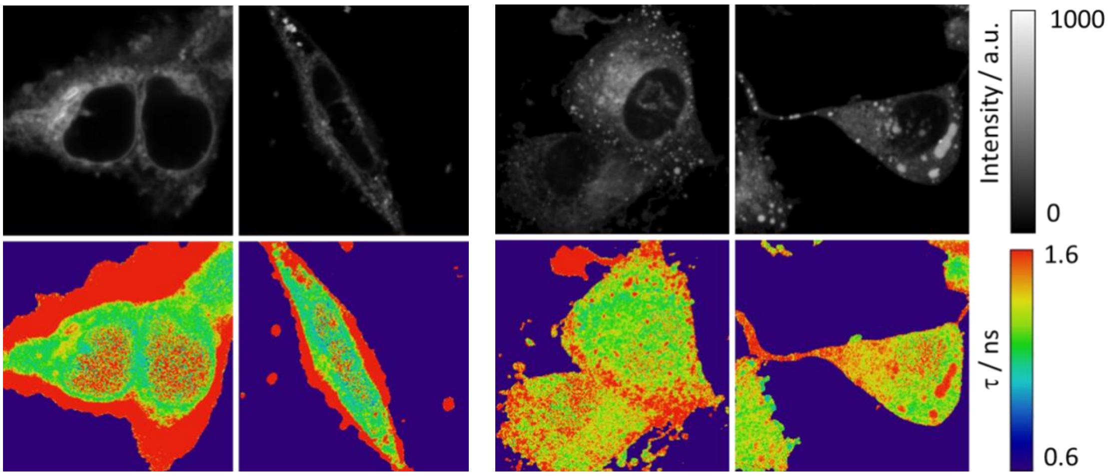

a)

b)

Figure 3.6. (a) FLIM of PEMC in HEK and (b) MDA-MB-231 cells. The top of the figure shows the intensity images and the bottom shows the corresponding fluorescence lifetime images.

AIE is intracellularly produced in some internal structures. The difference in intensity can be used to isolate different organelles based on the intensity threshold. Briefly, as different structures have different intensities values, we used intensity images to select different regions of interest (ROI) through appropriate thresholds (see Figure S3.8). The ROI selected can be used to isolate these regions in the fluorescence lifetime images and obtain the fluorescence lifetime of PEMC in these structures. Therefore, this approach can efficiently study independent organelles based on fluorescence lifetime. Figure 3.7a shows HEK cells segmented with the resulting fluorescence lifetime image maps and histograms. Interestingly, we observed that three different isolated regions of the cells present well-differentiated fluorescence lifetimes (Figure 3.7b).

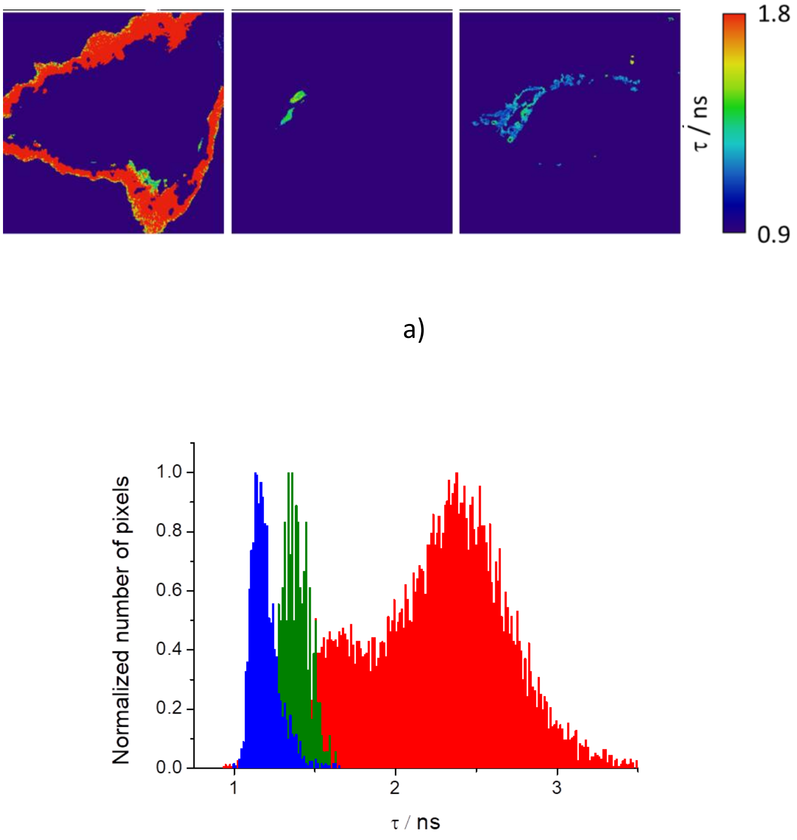

a)

b)

Figure 3.7. Fluorescence lifetime images maps of isolated organelles from HEK cells (a) and the histograms (b) with three different regions of the cells.

To go further in the investigation of these intracellular structures, we used a commercial mitochondria biomarker. Following an alternate excitation (470 nm to mitochondria biomarker and 635 nm to PEMC), and recovering their fluorescence in two different channels (green for mitochondria biomarker and red for PEMC), we selected the pixel where in both channels collocated to isolate the mitochondria and studied the fluorescence lifetime in these compartments. Figure S3.9 shows the co-localization images, the complete FLIM image, and the mitochondria-isolated FLIM images. As can be observed, the mitochondria biomarker presents some artifacts marking some structures that are not mitochondria (placed in peripheria). These artifacts are easily identifiable by studying the mitochondria-isolated FLIM images because they show a different fluorescence lifetime.

3.4 DISCUSSION

AIE is an interesting phenomenon that can be used as a tool to determine different biological and/or biomedical mechanisms, including intracellular processes. However, the use of AIE requires the complete knowledge of the photophysical properties of a given dye for proper interpretation and use. For this reason, we first realized the photophysical characterization of the dye diluted in different solvents following two different approaches, the Lipper–Mataga equation and the Catalan approach. From our analysis, the Lipper–Mataga analysis does not show any dramatic changes, except for a slight decrease in polarizability (Δf), a parameter that takes into account the effect of the solvent to change the dipole moment of the dye. However, the deeper Catalan approach allows the discrimination of which of four different physicochemical parameters (acidity, basicity, polarizability and dipolarity) affects the absorption and emission behavior. Following this analysis, we found that dipolarity is the only parameter that affects the behavior. Dipolarity is the capacity of the solvent to contain a dipolar system. Based on this result, and according to the data from the photophysical characterization in which the dye presents different relative quantum yields in the solvents, to verify the AIE, we mixed different proportions of water and THF. At a very low THF proportion (1%), we found a strong increase in the fluorescence signal. We explain this behavior as follows: because PEMC presents a higher affinity for this solvent, it accumulates around THF molecules, and therefore, the dye molecules become very closely packed, producing AIE. However, increasing the THF proportion produces a decrease in the intensity because the higher amount of THF molecules allows PEMC to disperse widely, losing its aggregation state and, therefore, the AIE behavior. When the THF proportion is further increased, the fluorescence intensity slightly increases due to the higher quantum yield of the dye in this solvent. To confirm aggregation is responsible of the enhancement of fluorescence, we increased the concentration of PEMC using ethanol as a solvent until it achieved aggregation. Once this condition was obtained, we observed a very strong enhancement of fluorescence.

Another approach to confirm the AIE is the immobilization of the dye by increasing the viscosity or binding it to certain substances. This is a very interesting behavior with useful applications in biological and biomedical fields. To observe the effect of the immobilization of the dye, we realized both approaches, first by increasing the solvent viscosity, and then, by taking advantage of the spontaneous incorporation of PEMC into nonpolar media, we used SDS molecules to study the behavior of the dye before and after the formation of micelles. Increasing the viscosity has a strong effect on fluorescence intensity. The addition of glycerol to the solvent produces a strong enhancement of the intensity. In the other approach, adding SDS to the solvent, below the CMC, the dye exhibits increased fluorescence due to the higher proportion of SDS in the medium. This behavior is probably due to the same effect previously discussed regarding the addition of THF. Once the CMC is reached and micelles are spontaneously formed, the dye exhibits its maximum fluorescence intensity due to AIE caused by the immobilization of the dye. After further increasing the SDS proportion, a slight decrease in the fluorescence intensity of PEMC was observed. This result occurs because a higher proportion of SDS can produce micelles with higher volumes in which the dye can become partially less immobilized. To confirm that this approach can be extended to study changes in the conformation or denaturation of proteins, we also added BSA protein to a solution of PEMC. We performed two different additions: 30 and 50 µg of BSA. We observed that when BSA is incorporated, the fluorescence of the dye increases drastically due to the self-introduction of the dye within the less polar interior of the protein, causing immobilization of the dye or even a self-interaction of the dye molecules in the interior of the proteins. Both cases cause AIE, with a ten-fold increase in the fluorescence intensity when 50 µg of BSA is added to the solution.

Finally, we studied the time of spontaneous incorporation of PEMC into live cells. In contrast to xanthenic dyes[14,25,26,31] (where the incorporation is very fast), PEMC achieves equilibrium approximately 70 min after addition of this luminogen. After this period of time, our data showed a plateau in the intracellular intensity signal. Following the fluorescence lifetime images, the lifetime remains almost invariable due to the concentration independence of this parameter. However, it takes approximately 20 min to observe a characteristic pattern where intracellular structures are clearly marked with higher fluorescence lifetime. This effect is probably due to AIE, where the PEMC molecules are immobilized in these structures, achieving a higher fluorescence intensity and a higher fluorescence lifetime. More interesting is the potential application in image analysis that can be performed owing to AIE behavior inside the cells. The differences in the intensity fluorescence can be used to isolate intracellular compartments in different regions of the cell. For this purpose, we isolated three different regions from HEK cells (see Figure 3.7). First, we selected the peripheral F-actin, where the luminogen presents lower intensity than that in other regions but a very high fluorescence lifetime. In the second and third regions, we differentiated between two different intracellular compartments. In the second region, PEMC exhibits very high intensity and intermediate fluorescence lifetime, and the third segmented region is characterized by multiple organelles with intermediate intensity but lower fluorescence lifetimes. For better characterization of the sensing aspect of this dye, we used a mitochondria biomarker to specifically isolate these compartments and measured the fluorescence lifetime in these organelles (Figure S3.9).

3.5 CONCLUSIONS

We studied the photophysical behavior of a new luminogen. We confirmed the AIE phenomenon with different approaches by using different solvent proportions, increasing the viscosity and forming micelles. In all cases, we observed a strong enhancement of the fluorescence produced by reducing the intrarotational mobility of the dye. Finally, we studied the rate of spontaneous incorporation of the dye into cells and observed the intracellular pattern produced by AIE. Interestingly, different intracellular compartments present strong differences in fluorescence intensity and fluorescence lifetime. We used this difference to isolate different intracellular regions to allow us to selectively study these regions. Finally, we have demonstrated the use of this luminogen in bioimaging with a mitochondria biomarker to analyze these organelles through their fluorescence lifetimes.

3.6 EXPERIMENTAL SECTION

3.6.1 GENERAL INFORMATION

The dye PEMC was dissolved in EtOH, and 15 µL was added to a final volume of 1500 µL to different solvents with a final concentration of 5×10^{-6} M. The solvents used were butanol, acetone, cyclohexane, 1,4-dioxane, ethanol, methanol, dichloromethane, tetrahydrofuran, dibutyl ether, diethyl ether, chlorobenzene, toluene, propanol, dimethyl sulfoxide, acetonitrile, and acidic and basic water.

3.6.2 INSTRUMENTATION

Absorption spectra were performed on a Lambda 650 UV-visible spectrophotometer (PerkinElmer, Waltham, MA, USA). Fluorescence emission spectra were collected on a Jasco FP-

8300 spectrofluorometer (Jasco, Tokyo, Japan) at the maximum absorption wavelength for each solvent. Fluorescence quantum yields were obtained using Nile Blue A as a reference (see Supplementary Material). Fluorescence lifetime decays were recorded by the single-photon timing method using a FluoTime 200 fluorometer (PicoQuant GmbH, Berlin, Germany). The excitation source was a pulsed diode laser at λ = 635 nm LDH-635, (PicoQuant), at a repetition rate of 40 MHz. Fluorescence decay histograms were collected at the maximum emission of each solvent, between 640 and 680 nm over 1320 channels, with increments per channel of 37 ps. Histograms of the instrument response functions (using a LUDOX scatterer) and sample decays were recorded until they reached 2×10^4 counts in the peak channel. The fluorescence decay traces were globally analyzed using an iterative deconvolution method with exponential models using FluoFit software (PicoQuant).

3.6.3 CELL CULTURE

Embryonic kidney cells HEK-293 (ATCC no. CRL-1573™) were grown at 37 °C in Dulbecco's modified Eagle's medium (DMEM) supplemented with 10% (*v*/*v*) fetal bovine serum (FBS), 2 mM glutamine and 100 U/mL penicillin. Cell cultures were maintained in an incubator at 37 °C with 95% humidity and 5% CO2.

For the FLIM experiments, cells were seeded onto circular coverslips (diameter of 25 mm) in six-well plates at a density of 2.3×10^5 cells per well.

3.6.4 FLIM BIOIMAGING

Images of fluorescence emission intensities and fluorescence lifetime were performed on a MicroTime 200 fluorescence-lifetime microscope system (PicoQuant GmbH, Berlin, Germany) using the same excitation source described earlier. The light beam was directed through a dichroic mirror (PIE 470/635 dcxr, Chroma) and through an oil immersion objective (1.4 NA, 100×) specific to an inverted microscope system (IX-71, Olympus, Tokyo, Japan). The fluorescence emission was carried to a 500-nm long-pass filter (AHF/Chroma) and focused to a 75-µm confocal aperture. The fluorescence emission passed through a bandpass filter (D685/70M, Chroma) and focused on single-photon avalanche diodes (SPCM-AQR 14, Perkin Elmer). The data were obtained by a TimeHarp 200 TCSPC module (PicoQuant), and raw fluorescence lifetime images were collected by scanner at a 512 × 512-pixel resolution.

Images were analyzed using home-coded macros of *Fiji Is Just ImageJ* software. For the experiments performed on mitochondria, we used the MicroTime 200 fluorescence-lifetime microscope system (PicoQuant GmbH, Belin, Germany) described earlier with the same configuration, adding a bandpass filter (D520/40M, Chroma). The mitochondria biomarker used was the MitoTracker Green FM (ThermoFisher).

BIBLIOGRAPHY

1 Yan, L.Q.; Kong, Z.N.; Xia, Y.; Qi, Z.J. A novel coumarin-based red fluorogen with AIE, self-assembly, and TADF properties. *New J. Chem.* **2016**, *40*, 7061–7067.

2 Falcone, R.D.; Correa, N.M.; Biasutti, M.A.; Silber, J.J. Acid-base and aggregation processes of acridine orange base in n-heptane/AOT/water reverse micelles. *Langmuir* **2002**, *18*, 2039–2047.

3 Guo, B.; Cai, X.L.; Xu, S.D.; Fateminia, S.M.A.; Liu, J.; Liang, J.; Feng, G.X.; Wu, W.B.; Liu, B. Decoration of porphyrin with tetraphenylethene: Converting a fluorophore with aggregation-caused quenching to aggregation-induced emission enhancement. *J. Mater. Chem. B* **2016**, *4*, 4690–4695.

4 Luo, J.; Xie, Z.; Lam, J.W.Y.; Cheng, L.; Chen, H.; Qiu, C.; Kwok, H.S.; Zhan, X.; Liu, Y.; Zhu, D.; et al. Aggregation-induced emission of 1-methyl-1,2,3,4,5-pentaphenylsilole. *Chem. Commun.* **2001**, 18, 1740–1741.

5 Mei, J.; Leung, N.L.C.; Kwok, R.T.K.; Lam, J.W.Y.; Tang, B.Z. Aggregation-Induced Emission: Together We Shine, United We Soar! *Chem. Rev.* **2015**, *115*, 11718–11940.

6 Mei, J.; Hong, Y.; Lam, J.W.Y.; Qin, A.; Tang, Y.; Tang, B.Z. Aggregation-Induced Emission: The Whole Is More Brilliant than the Parts. *Adv. Mater.* **2014**, *26*, 5429–5479.

7 Hong, Y.N. Aggregation-induced emission-fluorophores and applications. *Methods Appl. Fluoresc.* **2016**, *4*, 022003.

8 Matsuoka, K.; Albrecht, K.; Yamamoto, K.; Fujita, K. Mulifunctional Dendritic Emitter: Aggregation-Induced Emission Enhanced, Thermally Activated Delayed Fluorescent Material for Solution-Processed Multilayered Organic Light-Emitting Diodes. *Sci. Rep.* **2017**, *7*, 41780.

9 Malakar, A.; Kumar, M.; Reddy, A.; Biswal, H.T.; Mandal, B.B.; Krishnamoorthy, G. Aggregation induced enhanced emission of 2-(2′-hydroxyphenyl)benzimidazole. *Photochem. Photobiol. Sci.* **2016**, *15*, 937–948.

10 Ding, A.-X.; Shi, Y.-D.; Zhang, K.-X.; Sun, W.; Tan, Z.-L.; Lu, Z.-L.; He, L. Self-assembled aggregation-induced emission micelle (AIE micelle) as interfacial fluorescence probe for sequential recognition of Cu^{2+} and ATP in water. *Sens. Actuators B Chem.* **2018**, *255*, 440–447.

11 He, T.; Ou, W.; Tang, B.Z.; Qin, J.; Tang, Y. In vivo Visualization of the Process of Hg^{2+} Bioaccumulation in Water Flea Daphnia carinata by a Novel Aggregation-Induced Emission Fluorogen. *Chem. Asian J.* **2019**, *14*, 796–801.

12 Dalavi, D.K.; Suryawanshi, S.B.; Kolekar, G.B.; Patil, S.R. AIEE active SDS stabilized 2-naphthol nanoparticles as a novel fluorescent sensor for the selective recognition of crystal violet: Application to environmental analysis. *Anal. Methods* **2018**, *10*, 2360–2367.

13 Theillet, F.-X.; Binolfi, A.; Frembgen-Kesner, T.; Hingorani, K.; Sarkar, M.; Kyne, C.; Li, C.; Crowley, P.B.; Gierasch, L.; Pielak, G.J.; et al. Physicochemical Properties of Cells and Their Effects on Intrinsically Disordered Proteins (IDPs). *Chem. Rev.* **2014**, *114*, 6661–6714.

14 Espinar-Barranco, L.; Luque-Navarro, P.; Strnad, M.A.; Herrero-Foncubierta, P.; Crovetto, L.; Miguel, D.; Giron, M.D.; Orte, A.; Cuerva, J.M.; Salto, R.; et al. A solvatofluorochromic silicon-substituted xanthene dye useful in bioimaging. *Dyes Pigments* **2019**, *168*, 264–272.

15 Ding, D.; Li, K.; Liu, B.; Tang, B.Z. Bioprobes Based on AIE Fluorogens. *Acc. Chem. Res.* **2013**, *46*, 2441–2453.

16 Wang, G.; Zhang, R.; Xu, C.; Zhou, R.; Dong, J.; Bai, H.; Zhan, X. Fluorescence Detection of DNA Hybridization Based on the Aggregation-Induced Emission of a Perylene-Functionalized Polymer. *ACS Appl. Mater. Interfaces* **2014**, *6*, 11136–11141.

17 Li, H.; Guo, Z.J.; Xie, W.C.; Sun, W.Y.; Ji, S.; Tian, J.; Lv, L. A label-free fluorometric aptasensor for adenosine triphosphate (ATP) detection based on aggregation-induced emission probe. *Anal. Biochem.* **2019**, *578*, 60–65.

18 Zhang, W.J.; Kwok, R.T.K.; Chen, Y.L.; Chen, S.J.; Zhao, E.G.; Yu, C.Y.Y.; Lam, J.W.Y.; Zheng, Q.C.; Tang, B.Z. Real-time monitoring of the mitophagy process by a photostable fluorescent mitochondrion-specific bioprobe with AIE characteristics. *Chem. Commun.* **2015**, *51*, 9022–9025.

19 Zhou, Y.; Hua, J.; Barritt, G.; Liu, Y.; Tang, B.Z.; Tang, Y. Live Imaging and Quantitation of Lipid Droplets and Mitochondrial Membrane Potential Changes with Aggregation-Induced Emission Luminogens in an in Vitro Model of Liver Steatosis. *ChemBioChem Eur. J. Chem. Biol.* **2019**, *20*, 1256–1259.

20 Wu, Y.Q.; Wen, X.Y.; Fan, Z.F. Selective and Sensitive Fluorescence Probe for Detection of Al^{3+} in Food Samples Based on Aggregation-Induced Emission and Its Application for Live Cell Imaging. *Food Anal. Methods* **2019**, *12*, 1736–1746.

21 Deng, K.L.; Wang, L.; Xia, Q.; Liu, R.Y.; Qu, J.Q. A turn-on fluorescent chemosensor based on aggregation-induced emission for cyanide detection and its bioimaging applications. *Sens. Actuators B Chem.* **2019**, *296*, 126645.

22 Srinivasan, V.; Jhonsi, M.A.; Dhenadhayalan, N.; Lin, K.C.; Ananth, D.A.; Sivasudha, T.; Narayanaswamy, R.; Kathiravan, A. Pyrene-based prospective biomaterial: In vitro bioimaging, protein binding studies and detection of bilirubin and Fe^{3+}. *Spectrochim. Acta Part Mol. Biomol. Spectrosc.* **2019**, *221*, 117150.

23 Qi, J.; Chen, C.; Ding, D.; Tang, B.Z. Aggregation-Induced Emission Luminogens: Union Is Strength, Gathering Illuminates Healthcare. *Adv. Healthc. Mater.* **2018**, *7*, 1800477.

24 Naskar, B.; Dhara, A.; Maiti, D.K.; Kukulka, M.; Mitoraj, M.P.; Srebro-Hooper, M.; Prodhan, C.; Chaudhuri, K.; Goswami, S. Aggregation-Induced Emission-Based Sensing Platform for

Selective Detection of Zn^{2+}: Experimental and Theoretical Investigations. *ChemPhysChem* **2019**, *20*, 1630–1639.

25 Paredes, J.M.; Giron, M.D.; Ruedas-Rama, M.J.; Orte, A.; Crovetto, L.; Talavera, E.M.; Salto, R.; Alvarez-Pez, J.M. Real-Time Phosphate Sensing in Living Cells using Fluorescence Lifetime Imaging Microscopy (FLIM). *J. Phys. Chem. B* **2013**, *117*, 8143–8149.

26 Puente-Munoz, V.; Paredes, J.M.; Resa, S.; Ortuno, A.M.; Talavera, E.M.; Miguel, D.; Cuerva, J.M.; Crovetto, L. Efficient acetate sensor in biological media based on a selective Excited State Proton Transfer (ESPT) reaction. *Sens. Actuators B Chem.* **2017**, *250*, 623–628.

27 Reichardt, C.; Welton, T. Appendix A. Properties, Purification, and Use of Organic Solvents. In *Solvents and Solvent Effects in Organic Chemistry*; Reichardt, C., Welton, T., Eds.; Wiley-VCH Verlag GmbH & Co. KGaA , Hoboken, New Jersey, United States, 2010; pp. 549–586.

28 Brouwer, A.M. Standards for photoluminescence quantum yield measurements in solution (IUPAC Technical Report). *Pure Appl. Chem.* **2011**, *83*, 2213–2228.

29 Catalan, J. Toward a Generalized Treatment of the Solvent Effect Based on Four Empirical Scales: Dipolarity (SdP, a New Scale), Polarizability (SP), Acidity (SA), and Basicity (SB) of the Medium. *J. Phys. Chem. B* **2009**, *113*, 5951–5960.

30 Haghparast, S.M.A.; Kihara, T.; Miyake, J. Distinct mechanical behavior of HEK293 cells in adherent and suspended states. *PeerJ* **2015**, *3*, e1131.

31 Crovetto, L.; Orte, A.; Paredes, J.M.; Resa, S.; Valverde, J.; Castello, F.; Miguel, D.; Cuerva, J.M.; Talavera, E.M.; Alvarez-Pez, J.M. Photophysics of a Live-Cell-Marker, Red Silicon-Substituted Xanthene Dye. *J. Phys. Chem. A* **2015**, *119*, 10854–10862.

SUPPORTING INFORMATION

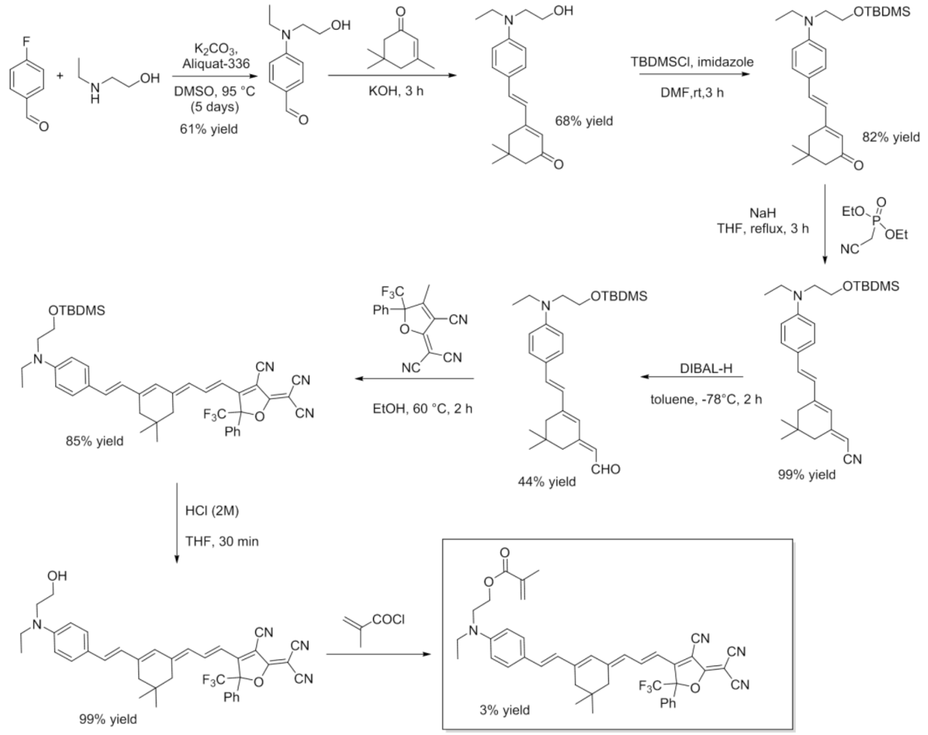

Scheme S3.1. Synthesis of dye: 2-((4-((*E*)-2-((*E*)-3-((*E*)-3-(4-cyano-5-(dicyanomethylene)-2-phenyl-2-(trifluoromethyl)-2,5-dihydrofuran-3-yl)allylidene)-5,5-dimethylcyclohex-1-en-1-yl)vinyl)phenyl)(ethyl)amino)ethyl methacrylate.

QUANTUM YIELD CALCULATION

The relative fluorescence quantum yield values were determined using the following formula[1]:

$$\Phi = \Phi_R \cdot \frac{\mathrm{I}}{I_R} \cdot \frac{OD_R}{\mathrm{OD}} \cdot \frac{n^2}{n_R^2}$$

Where Φ and Φ_R denote the fluorescence quantum yield of the sample and the reference respectively, I and I_R the integrated fluorescence spectra of the sample and the reference, OD and OD_R the absorption at the excitation wavelength of the sample and the reference and n and n_R the refractive index of the solvent where the sample and reference are dissolved. As references, we have used Nile Blue A in EtOH ($\Phi = 0.27$)[2]. The samples were excited at the maximum absorption of each solvent.

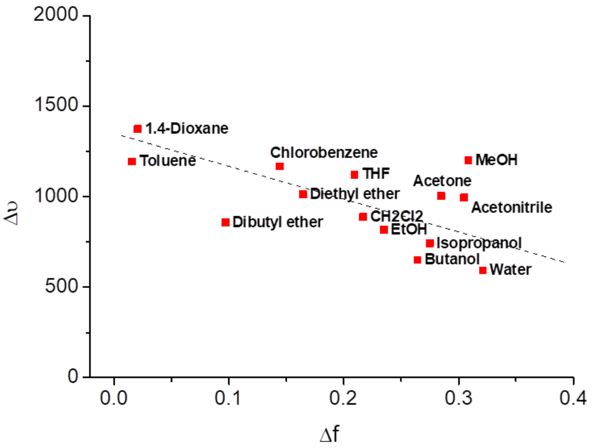

Figure S3.1. Lippert-Mataga representation of orientation polarizability of PEMC dissolved in different solvents.

LIPPERT-MATAGA EQUATION

$$\overline{\upsilon_A} - \overline{\upsilon_F} = \frac{2}{hc}\left(\frac{\varepsilon - 1}{2\varepsilon + 1} - \frac{n^2 - 1}{2n^2 + 1}\right)\frac{(\mu_E - \mu_G)^2}{a^3} + k$$

In the Lippert-Mataga equation, *h* is the Planck constant, *c* represents the light speed in vacuum, *a* is the radius of the cavity where the dye is allocated, $\overline{\upsilon_A}$ and $\overline{\upsilon_F}$ are the absorption and emission wavenumber, respectively, and *k* is a constant representing the difference between the absorption and emission wavenumbers in the vacuum.

$$\Delta f = \frac{\varepsilon - 1}{2\varepsilon + 1} - \frac{n^2 - 1}{2n^2 + 1}$$

Orientation polarizability (Δf) is the combination of both parameters as indicated in the equation and is included in the Lippert-Mataga equation.

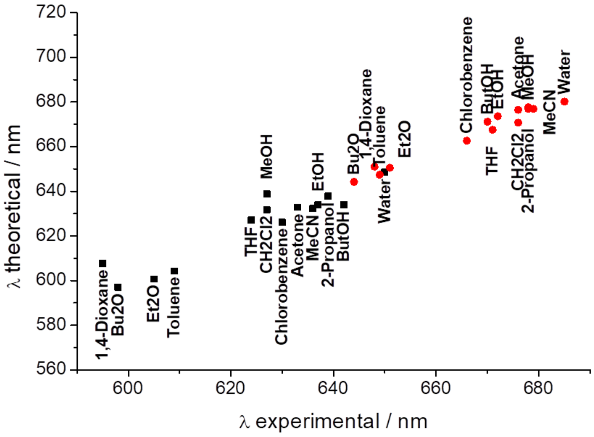

Figure S3.2. Experimental and theoretical wavelength (obtained from the Catalan approach data) of the 14 solvents used.

CATALAN EQUATION

$$A = A_0 + b\ SA + c\ SB + d\ SP + e\ SdP$$

The analysis is based on four empirical solvent scales: polarizability (*SP*), dipolarity (*SdP*), acidity (*SA*) and basicity (*SB*), hence taking into account both general effects and specific hydrogen bonding features of the solvents.

Where *A* is a solvent-dependent physicochemical property in a specific solvent, A_0 is the statistical quantity corresponding to the value of the property in the gas phase and *b* to *e* are the regression coefficients describing the sensitivity of property *A* to the different solute-solvent interactions.

Table S3.1. Estimated coefficients ± standard errors and correlation coefficient (r) for the multilinear regression analyses of $\tilde{\nu}_{abs}$ and $\tilde{\nu}_{em}$ The estimates are expressed in cm^{-1}.

	A_0	*b (SA)*	*c (SB)*	*d (SP)*	*e (SdP)*	*r*
$\tilde{\nu}_{abs}$	19501 ± 970	-401 ±180	-606 ± 271	-3125 ± 1157	-1518 ±240	0.9420
	18803 ± 1071		-357 ± 288	-2213 ± 1262	-1724 ±258	0.9119
	17819 ±717	-235 ± 191		-1266 ± 941	-1367 ± 269	0.9116
	16919 ± 207	-229 ± 211	-81 ±237		-1274 ± 278	0.8974
	16484 ± 1804	-840 ± 354	-123 ± 555	-365 ± 2288		**0.6602**
	16945 ± 153				-1451 ± 211	**0.8856**
	15013 ± 1312			1384 ± 1898		**0.1983**
	15840 ± 229		297 ± 460			**0.1762**
	16169 ±112	-793 ± 251				**0.6583**
$\tilde{\nu}_{em}$	16658 ± 432	-89 ± 80	-325 ± 121	-1093 ± 515	-1112 ± 107	0.9736
	16504 ± 413		-269 ± 111	-891 ± 487	-1158 ± 99	0.9703
	15758 ± 342	0 ± 91		-98 ± 449	-1031 ± 128	0.9540
	15755 ± 84	-29 ± 86	-141 ± 96		-1027 ± 113	0.9615
	14448 ± 1236	-410 ± 243	30 ± 380	930 ± 1567		**0.6175**
	15685 ± 65				-1022 ± 89	**0.9538**
	13901 ± 821			1590 ± 1188		**0.3480**

	14955 ± 152		95 ± 305			**0.0858**
	15114 ± 79	-466 ± 176				**0.5915**

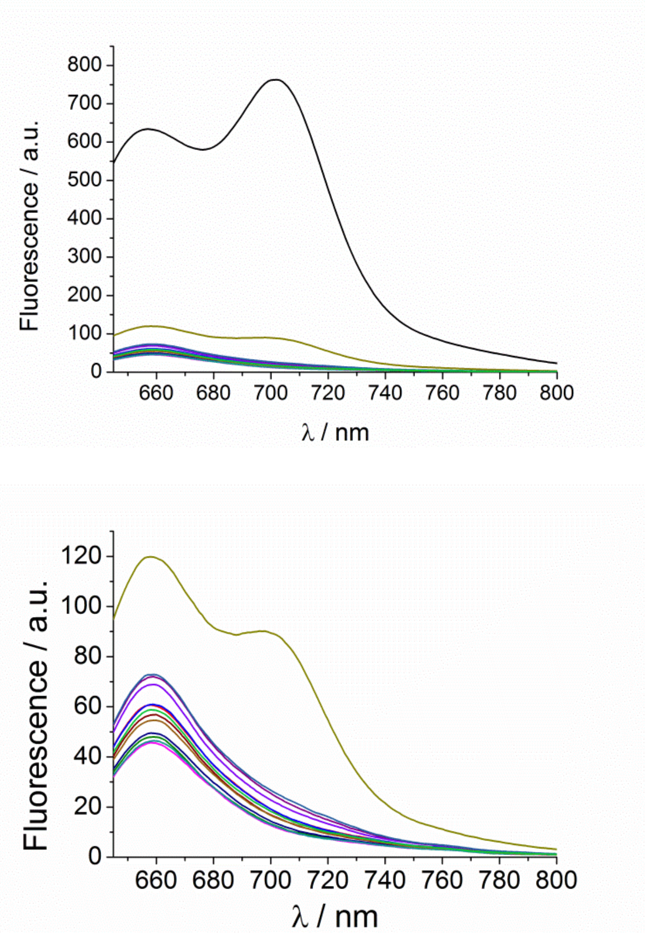

Figure S3.3. Fluorescence spectra in ethanol as solvent at different PEMC concentration. (Top) including 5x10^{-3} M (highest value) to see AIE effect. (Bottom) without 5x10^{-3} M to see in detail the Kavanagh law.

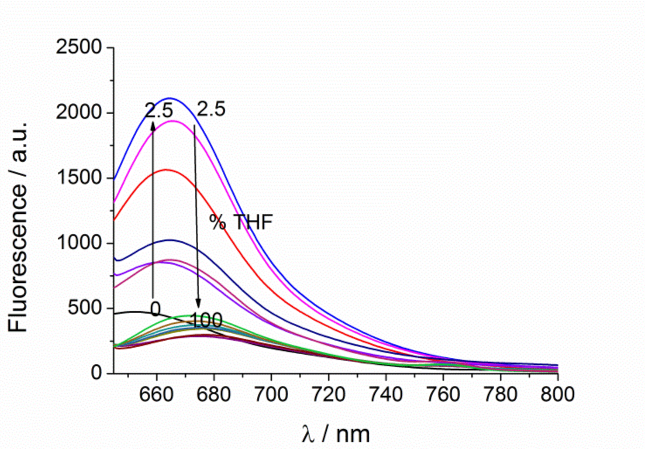

Figure S3.4. Fluorescence spectrum of PEMC in the presence of increasing proportions of THF to water.

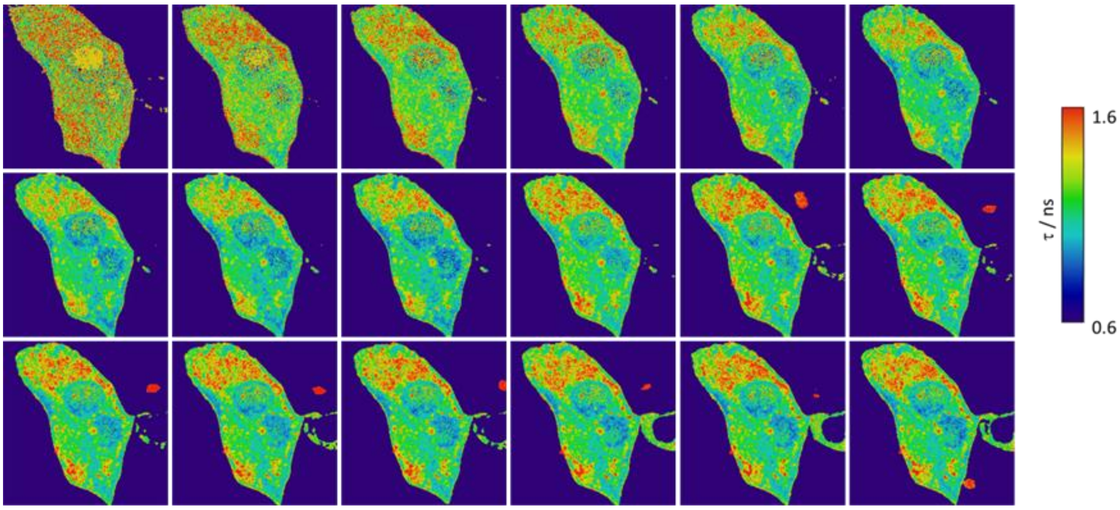

Figure S3.5. FLIM images of input kinetics of PEMC in MDA-MB-231 cells.

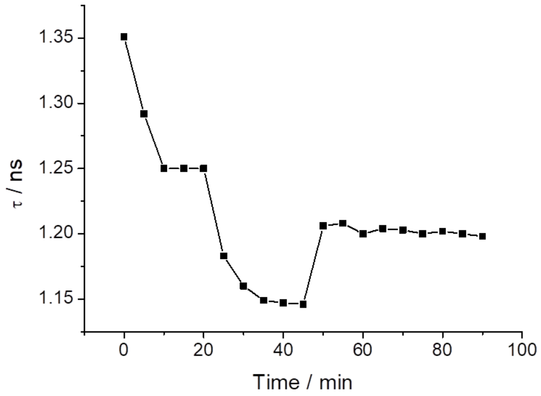

Figure S3.6. Fluorescence lifetime recovered from the input kinetics of PEMC in MDA-MB-231 cells from Figure S3.3.

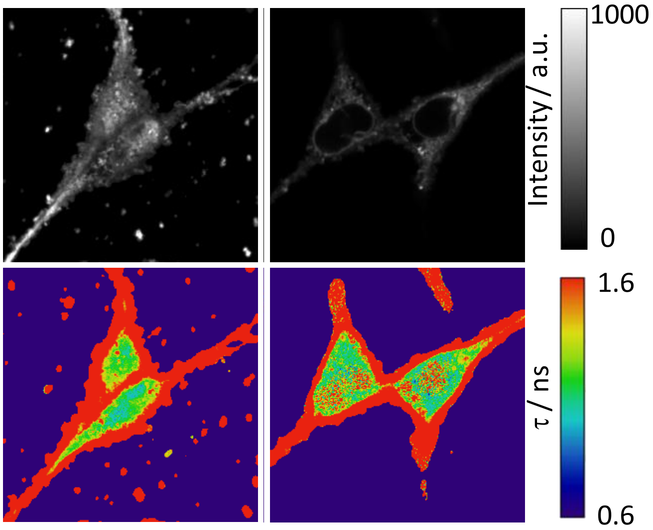

Figure S3.7. FLIM images of PEMC in HEK cells.

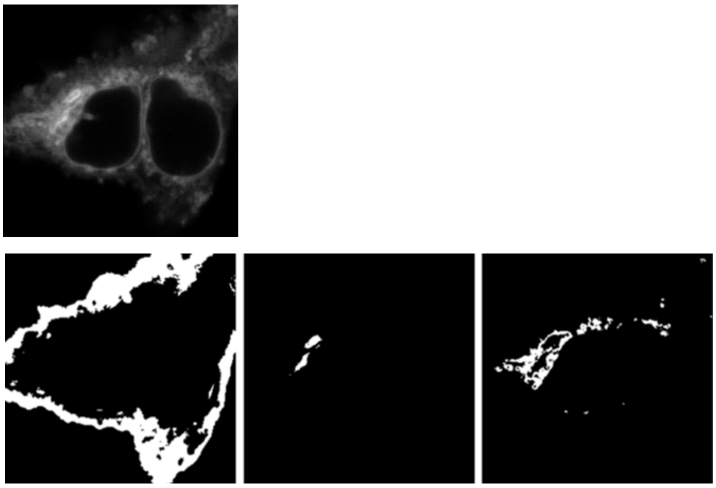

Figure S3.8. Intensity images of different organelles isolated by intensity threshold.

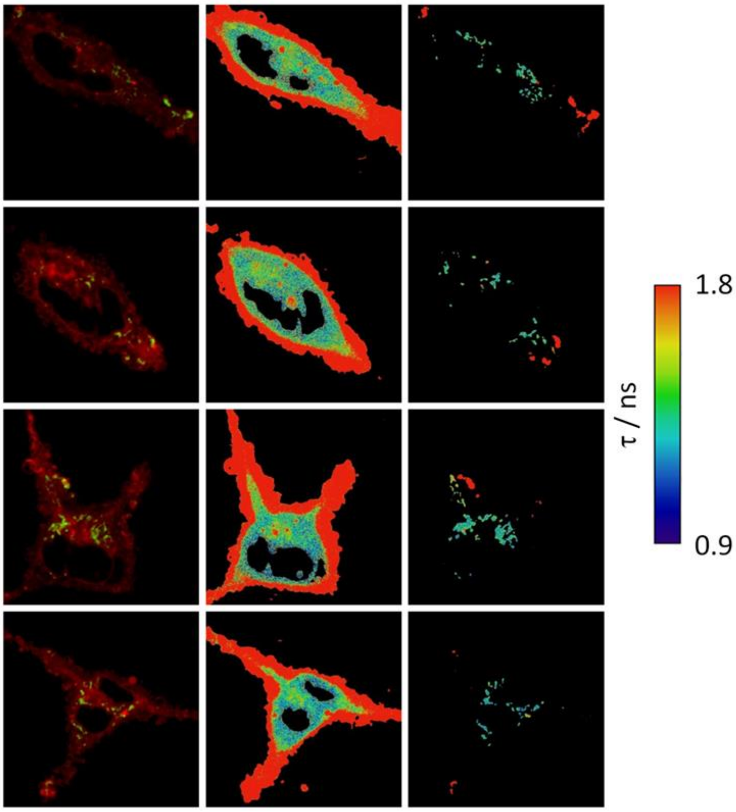

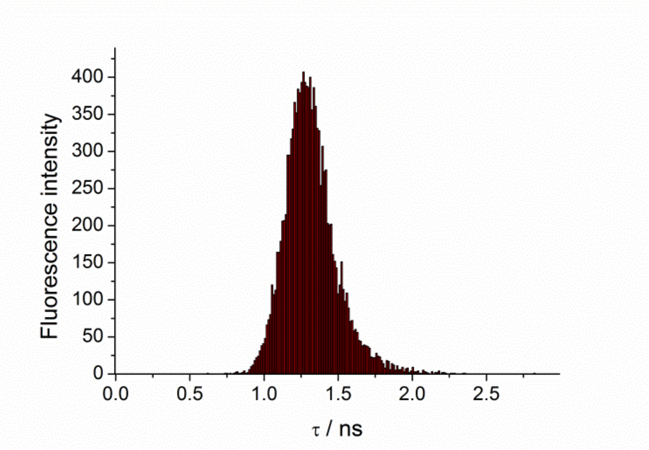

Figure S43.9. (Up) Fluorescence intensity images maps of HEK cells with MitoTracker Green and PEMC (left), fluorescence lifetime of PEMC separating the red signal (in the middle) and isolating the colocation region (Right) (Bottom) Histograms of PEMC in the mitochondria region of the cells.

BIBLIOGRAPHY

1 Lakowicz, J. R. *Principles of Fluorescence Spectroscopy*, Springer.; New York, 2006.

2 Brouwer, A. M. Standards for Photoluminescence Quantum Yield Measurements in Solution (IUPAC Technical Report). *Pure and Applied Chemistry*. **2011**, pp 2213–2228.

SELF-ASSEMBLED LANTHANIDE ANTENNA GLUTATHIONE SENSOR FOR THE STUDY OF IMMUNE CELLS

ACS Sensors, 2022, 7, 1, 322-330

IP: 7.711 (in 2020)

Q1 (33/179)

Chemistry, multidisciplinary

Contribution: In this publication, I have carried out the photophysical characterization of this molecule.

4.1 ABSTRACT

The small molecule 8-methoxy-2-oxo-1,2,4,5-tetrahydrocyclopenta[de]quinoline-3-carboxylic acid (**2b**) behaves as a reactive non-fluorescent Michael acceptor, which after reaction with thiols, becomes fluorescent and an efficient Eu^{3+} antenna, after self-assembling with this cation in water. This behavior makes **2b** a highly selective GSH biosensor, which has demonstrated high potential for studies in murine and human cells of the immune system ($CD4^+$ T, $CD8^+$ T, and B cells) using flow cytometry. GSH can be monitored by the fluorescence of the product of addition to **2b** (445 nm) or by the luminescence of Eu^{3+} (592 nm). **2b** was able to capture baseline differences in GSH intracellular levels amongst murine and human $CD4^+$ T, $CD8^+$ T, and B cells. We also successfully used **2b** to monitor intracellular changes in GSH associated with the metabolic variations governing the induction of $CD4^+$ naïve T cells into regulatory T cells (Treg).

4.2 INTRODUCTION

Biologically-active thiols known as biothiols, which includes cysteine (Cys), homocysteine (Hcy), glutathione (GSH) and hydrogen sulfide (H_2S), play a central role in the intracellular regulation of redox homeostasis and in the maintenance of cellular functions, such as post-translational modifications, biocatalysis, metal binding, and xenobiotic detoxification[1, 2]. Oxidative stress is a key feature of a wide variety of chronic and degenerative diseases and changes in the levels of biothiols have been associated to various diseases[3-8]. Distinct responses to metabolic stimuli (bioenergetic signatures) have been associated with differences in immune function[9, 10]. In recent years, several studies have shed light on the dynamic and sophisticated connection between metabolic programmes and the function of specialized cells in the immune system[10, 11]. This crucial role of metabolism in the control of immune processes, including inflammation, has led to the emergence of the new field of immunometabolism[11-13]. It is increasingly recognized that biothiols play a key role in regulating metabolic adaptability, and thereby function, of cells of the immune system[14-21]. One of the latest discoveries in this field is the regulation of functions through the synthesis and release of various biothiols, in particular GSH, which affects the metabolism and function of the immune system's effector cells.[12, 22, 23 24-26]. Consequently, the interest in developing tools to monitor biothiol levels in immune cells in clinical samples has grown exponentially.

To this aim, diverse probes and techniques have been developed for the detection of biothiols. Among the methods used, those based on fluorescence emission are among those that provide the greatest advantages due to their simplicity, low detection limits and ease of use[27-30]. However, selective and sensitive methods to detect and monitor GSH in cells with flow cytometry, a fluorescence-based, gold-standard tool for the identification and classification of cellular populations, remain an unmet need in the immunology field. Yet, current methods to measure GSH lack selectivity and sensitivity and their suitability to flow cytometry remains largely unexplored. The few that have been studied with this technique in immune cells include monochloro (bromo) bimane[31], mercury orange[32], *o*-phthaldialdehyde and chloromethyl fluorescein diacetate[33], but none of them is selective for GSH[34].

Many probes for biothiol sensing are based on Michael acceptors, in which following a nucleophilic attack of the sulfhydryl group and its addition to a double bond of the probe, their fluorescence increases notably. Luminescent sensors based on lanthanide complexes present several advantages over classical organic fluorophores, such as very high luminescence lifetime and narrow emission bands, which allow an increase in sensitivity and signal-to-noise ratio, avoiding natural background fluorescence in time-resolved luminescence spectroscopy[35-37]. Among the few lanthanide-based biothiol sensors reported in the literature[38,39], to our knowledge, no lanthanide antenna-based sensors, which self-assemble in water have yet been reported.

In this field, we have recently reported the discovery of the small and simple structure lanthanide antenna in organic solvents **1a** (Scheme 4.1)[40]. The lanthanide sensitization by **1a** is quenched by H_2O addition, setting the basis for its demonstrated application as H_2O sensor. In our screening for potential lanthanide antennas, we observed that the free acid **1b**[41] (Scheme

4.1) was also able to sensitize the emission of Tb^{3+} and more extensively Eu^{3+} in H_2O. For the design of a suitable biothiol sensor from **1b**, we synthesized the oxidized analogue 2-oxo-1,2-dihydrocyclopenta[*de*]quinoline-3-carboxylic acid, **2b**, which showed high Michael acceptor reactivity against thiols and an excellent fluorogenic behavior upon reaction. Herein we report the design and synthesis of this free acid, the photophysical properties and lanthanide sensitization of **1b** and **2b**, the reactivity of **2b** and proof-of-concept studies of the application of this biothiol sensor to study cells of the immune system. Strikingly, the results described herein, demonstrate that **2b** is a selective GSH sensor, which after its reaction with this biothiol, self-assembles in water with a lanthanide cation and, as an antenna, transfers its energy to the lanthanide ion resulting in the long-lived luminescence emission of the lanthanide.

4.3 RESULTS AND DISCUSSION

4.3.1 SYNTHESIS OF 2B

As shown in Scheme 4.1, the free acid **2b** was obtained in good yield from the methyl ester **1a** by oxidation to **2a**, with 2,3-dichloro-5,6-dicyano-1,4-benzoquinone (DDQ) in refluxing toluene, followed by saponification to the corresponding free acid **2b** by heating with 2 N NaOH.

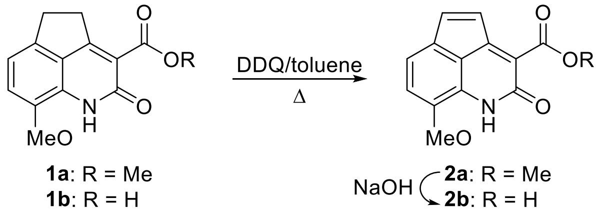

Scheme 4.1. Synthesis of 8-methoxy-2-oxo-1,2-dihydrocyclopenta[*de*]quinoline-3-carboxylic acid (2b).

1.3.2 PHOTOPHYSICAL PROPERTIES OF 1B AND 2B

The photophysical properties of **1b** and **2b** in CH_3CN and H_2O are shown in Table 4.1. The UV/visible spectrum of **1b** showed an absorption maximum at 320 nm, with a small shoulder at around 375 nm, while the oxidized analogue **2b** showed a broad absorption band centered around 390 nm, with no significant influence of the solvent polarity in both cases. As expected, due to the extension of the conjugation in the chromophore moiety, the absorption maximum of **2b** was shifted approximately 70 nm towards longer wavelengths when compared to that of **1b**. In fact, solutions of **1b** were colorless, while those of **2b** were orange by the naked eye.

Regarding emission properties, interestingly, the oxidized compound **2b** showed almost negligible emission (Φ_F of **2b** was almost 20-times lower than that of **1b**).

Compd[a]	Solvent	λ_{max}^{abs} (nm)	ε ($M^{-1}cm^{-1}$)	λ_{max}^{em} (nm)	Φ_F[b]
1b	CH_3CN	320, 375	4720	450	0.09
	H_2O	320, 373	5451	472	0.11
2b	CH_3CN	392	2125	462	0.008
	H_2O	390	3050	471	0.006

Table 4.1. Photophysical properties of the free carboxylic acids 1b and 2b. [a]Measured in duplicate at a 12 μM concentration. [b]Quantum yields calculated with reference to quinine sulfate (in 0.1 M H_2SO_4).

This low fluorescence emission of **2b** could be due to an antiaromatic character of its 2-oxo-1,2-dihydrocyclopenta[*de*]quinoline [4*n*]π-electron system, according to the Hückel's rules[42-44]. To clarify this hypothesis, TD-DFT calculations were carried out with the B3LYP functional and the 6-31+G(d,p) basis set[45-48], within the Gaussian-16 package[49] to determine the minimum energy structures of the free carboxylic acids **1b** and **2b** in their singlet ground energy state (S_0) and in the excited states S_1 and T_1, and their respective harmonic oscillator model of aromaticity (HOMA) values[50-54] for the common fused ring of 2-oxo-quinoline. Four tautomeric/rotamer structures were considered in the study of the geometries of the S_0, S_1 and T_1 energy states of **1b** and **2b**, one with a keto group at position 2 (**1A** and **2A** in Figure S4.1 of the ESI) and the other three with an enol group at that position (**1B**-**1D** and **2B**-**2D** in Figure S4.1). Calculations (Table S4.1) showed that the keto tautomer **A** is the minimum energy form for both **1b** and **2b** in the ground state S_0, and in the T_1 state of **2b**, while the enol tautomer **D** was that of minimum energy in the excited states S_1 and T_1 of **1b** and in the S_1 of **2b**, although in the latter case its energy was very near of the keto tautomer **A** (1.6 kJ mol^{-1}). These results indicate that excitation induces tautomerization in **1b** and **2b**. Calculations of the HOMA index values for the 2-oxo-quinoline fused ring common in **1b** and **2b** showed lower values for **2b** than for **1a** in the three energy states S_0, S_1 and T_1 (Table S4.2) and therefore a lower aromatic character in **2b**. Interestingly, a small decrease in the aromatic character of the six-membered rings of acenaphthylene compared to naphthalene has been reported[55]. The calculated HOMA values for the peripheral tricyclic skeleton of the 1,2-dihydrocyclopenta[*de*]quinoline system of **2b** (Table S4.3) indicated an aromatic character for the three energy states.

On the other hand, when comparing NMR data of the oxidized compound **2b** with those of **1b** (Table S4.4), the most significant changes with respect to aromaticity were a 0.21 ppm displacement of 7-H towards higher field in **2b** with respect to that of **1b**, and the displacements of carbons C_{3a} (29.8 pm), C_{8a} (8.3 pm) and C_{8b} (11.8 pm) also towards higher field in **2b** with respect to those of **1b**. These data are indicative of a decrease in the deshielding of the aromatic ring current in **2b** respect to **1b**, and, therefore, a lower aromatic character, which could explain their photophysical behavior.

The ability of compounds **1b** and **2b** to directly bind lanthanide ions in H_2O solution (54 µM) and sensitize their emission was spectroscopically analyzed by the addition of 1 and 2 equivalents of $TbCl_3$, $EuCl_3$, $DyCl_3$ and $SmCl_3$. As shown in Figure S4.2, the free carboxylic acid **1b** sensitized the luminescence of the cations Tb^{3+} and Eu^{3+}, but preferably that of the $^5D_4 \rightarrow {}^7F_6$ (490 nm) and $^5D_4 \rightarrow {}^7F_5$ (540-550 nm) Tb^{3+} bands. However, under the same conditions, the oxidized free carboxylic acid **2b** only sensitized the luminescence of Eu^{3+}, but with a much lower intensity than **1b** (Figure S4.3).

4.3.3. 2B BEHAVES AS A SELECTIVE AND SENSITIVE BIOTHIOL SENSOR

The photophysical properties According to the structure of **2b**, we hypothesized that this molecule could be a good Michael acceptor, in particular against thiols. This hypothesis was confirmed by following the reaction of **2b** (5 µM) with Cys (500 µM) in Hepes buffer pH 7.4 by HPLC-MS. As shown in Figure S4.4, when Cys was added just at the time of injection the product of addition of Cys to the double bond of **2b** was rapidly detected (t_R = 4.25 min).

Considering the good reactivity of **2b** against Cys and the photophysical properties of **2b** and **1b**, we propose that **2b** could be employed as a fluorogenic biothiol sensor (Figure 4.1), and consequently we studied its time-dependent reactivity toward GSH, Hcy, Cys and H_2S in Hepes buffer (50 mM, pH 7.4) using luminescence spectroscopy. The addition of 100 equivalents of GSH to **2b** (5 µM) resulted in a notable fluorescence increase at 445 nm (λ_{ex} = 320 nm) with the reaction time from 0 to 3h (Figure 4.2a). By contrast, upon the treatment of **2b** (5 µM) with 100 equivalents of Cys, Hcy or H_2S, this fluorescent increase was significantly lower (Figure 4.2b), which highlighted the selectivity of our sensor for GSH. This selectivity was confirmed upon addition of 5 or 10 equivalents of GSH, Hcy, Cys and H_2S, as only GSH led to a fluorescence increase (Figure 4.2c and Figure 4.2d). Furthermore, no obvious changes were detected when other amino acids, such as Ala, or potential interferent species (H_2O_2 and Fe^{2+}) were added (Figure S4.5) further emphasizing its selectivity towards thiols.

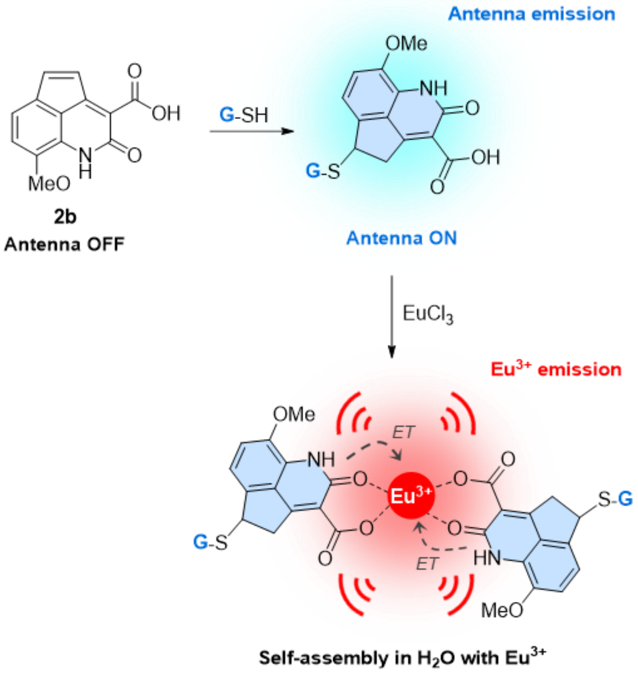

Figure 4.1. Schematic representation of the biosensor **2b**. After the addition of GSH to the Michael acceptor **2b**, the resulting antenna will increase its fluorescence.

Moreover, if lanthanide ions are present, the antenna will self-assemble and intramolecularly transfer its energy (ET) to the metal, resulting in a significant increase in the red long-lived luminescence emission of Eu^{3+}.

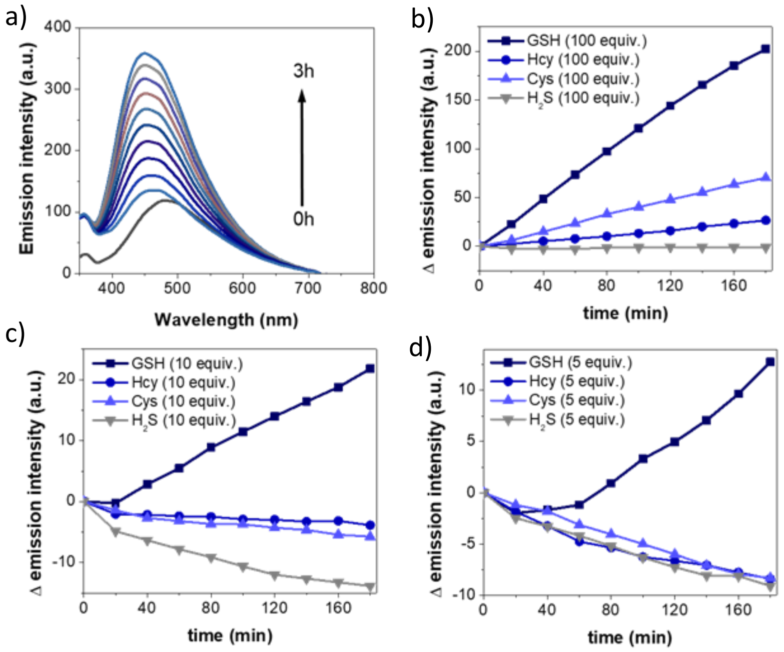

Figure 4.2. (a) Time-dependent fluorescence emission spectra of **2b** (5 μM, λ_{ex} = 320 nm) after the addition of 100 equivalents of GSH. (b-d) Changes in the fluorescence emission intensity of **2b** (5 μM) at 445 nm

(λ_{ex} = 320 nm) over time, after the addition of (b) 100, (c) 10 and (d) 5 equivalents of GSH, Hcy, Cys and H_2S.

Given that **1b** acted as a suitable lanthanide antenna, an alternative strategy in the design of the biothiol sensor would entail the addition of lanthanide ions to the reaction product of the biothiol to **2b** (**2b**-SR) (Figure 4.1). To explore this strategy, we next studied the ability of the product **2b**-GSH to directly bind lanthanide ions in solution sensitizing their luminescence, thus resulting on a red-shifted fluorogenic sensing reaction and with extraordinary potential to apply time-gated luminescence analysis due to the long luminescence lifetime of lanthanide ions[37] We carried out the reaction of **2b** (5 µM) with 100 equivalents of GSH for 3h (in Hepes 50 mM, pH 7.4), and then a titration of the corresponding addition product with increasing concentrations of $TbCl_3$, $EuCl_3$, $DyCl_3$ and $SmCl_3$ was performed (Figures 4.3a and S4.6). This led to the appearance of significant bands of sensitized luminescence of the lanthanide cation, mainly the $5D^0 \rightarrow 7F^2$ Eu^{3+} band at 615 nm and, in a lower extent, the $^5D_4 \rightarrow ^7F_6$ (490 nm) and $^5D_4 \rightarrow ^7F_5$ (540-550 nm) Tb^{3+} bands (Figure 4.3b). The luminescence lifetimes (τ) of the Eu^{3+} and Tb^{3+}emission for their complexes with **2b**-GSH were 122 ± 5 µs and 350 ± 1 µs, respectively, indicating a great potential to use time-resolved and time-gated analysis in the detection of biothiols. On the other hand, we also prepared the addition products of Hcy, Cys or H_2S to **2b** (**2b**-Hcy, **2b**-Cys and **2b**-H_2S) and performed a titration with increasing concentrations of $EuCl_3$. Compared to **2b**-GSH, which showed a significant energy transfer to the metal (Figure 4.3c), Eu^{3+} titration curves of **2b**-Hcy, **2b**-Cys and **2b**-H_2S led to a modest or negligible luminescent increase (Figures 4.3d and S4.7). Consequently, the τ of the Eu^{3+} emission for the complex of **2b**-GSH was higher than the ones of the complexes **2b**-Hcy and **2b**-Cys (Figure S4.8). The experimental data of the titrations fitted adequately to a binding isotherm with variable Hill slope (see SI for details). The fittings provided values for the apparent microscopic dissociation constant of 0.213 ± 0.005 mM, 0.235 ± 0.013 mM and 2.493 ± 0.092 mM, obtained for **2b**-GSH, **2b**-Hcy and **2b**-Cys, respectively (Figure 4.3d). This confirmed the preference of Eu^{3+} to directly assemble **2b**-GSH or **2b**-Hcy, and with much less affinity to **2b**-Cys. However, the higher Eu^{3+} luminescence intensity and lifetime exhibited by **2b**-GSH indicates a more effective protection against quenching caused by water molecules in the complex with **2b**-GSH than with **2b**-Hcy[56,57]. This protection of the lanthanide ion in **2b**-GSH is probably favored by the carboxylate group of the Glu residue present in GSH, which could aid in the formation of an extended coordination cage with the ion[58-60]. To demonstrate this, the geometry of a proposed structure of the europium complex with two units **2b**-GSH has been optimized with the RM1 semiempirical method (Figure 4.4).

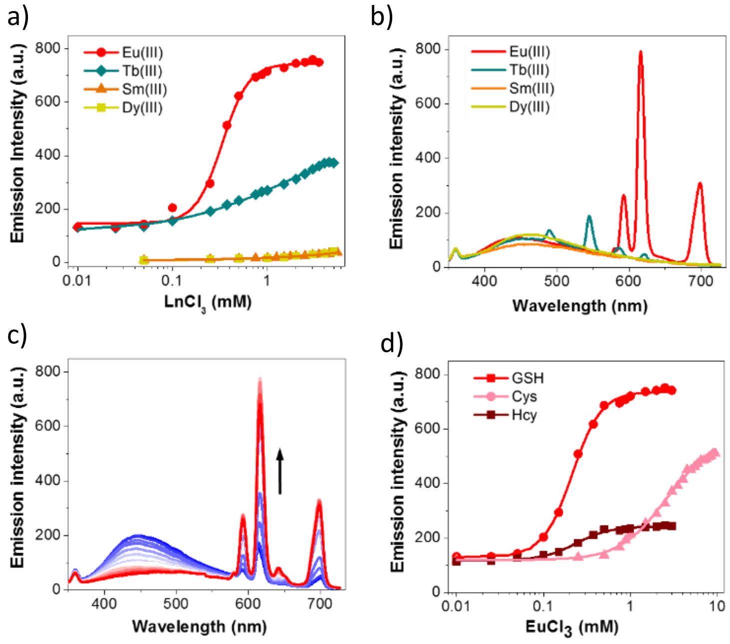

Figure 4.3. (a) Tb^{3+}, Eu^{3+}, Sm^{3+} and Dy^{3+} luminescence at their maximum emission wavelengths in the presence of **2b**-GSH (5 µM of **2b** and 100 equivalents of GSH, λ_{ex} = 320 nm) as a function of added $EuCl_3$, $TbCl_3$, $DyCl_3$ and $SmCl_3$ molar concentration (0.01-5.5 mM). (b) Emission spectra of **2b**-GSH (5 µM, λ_{ex} = 320 nm) after the addition of 100 equivalents of $EuCl_3$, $TbCl_3$, $DyCl_3$ and $SmCl_3$. (c) Titration spectra of **2b**-GSH (5 µM, λ_{ex} = 320 nm) with increasing molar concentration of $EuCl_3$ (0.025-3.0 mM, increase indicated by the arrow). (d) Eu^{3+} luminescence in the presence of the reaction products **2b**-GSH, **2b**- Hcy, or **2b**- Cys (5 µM of **2b** and 100 equivalents of biothiol, λ_{ex} = 320 nm) at 615 nm as a function of added $EuCl_3$ molar concentration (0.025-6.0 mM). Lines represent the fittings to a binding isotherm with variable Hill slope equation model.

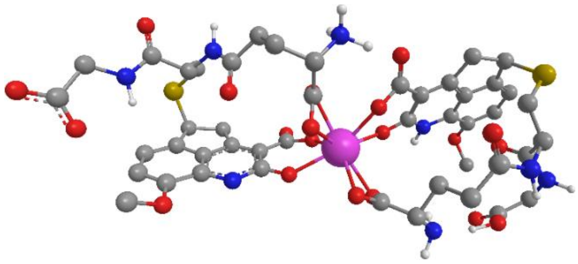

Figure 4.4. Proposed structure of the coordination of GSH-**2b** with Eu^{3+}. The geometry of the europium complex has been optimized with the RM1 semiempirical method,[61,62] as implemented in the MOPAC2016[63].

The greater reactivity of **2b** with GSH and the greater sensitization of the Eu^{3+} luminescence would enhance the selectivity of the sensor for GSH in subsequent cell studies, apart from the much higher intracellular concentration of GSH (1–10 mM) than that of Cys or Hcy (30–200 µM)[64-66]. We thus focused our attention on the reactivity of our sensor **2b** against

GSH (**2b**-GSH) and the selective sensitization of Eu^{3+} ions. We studied the reaction kinetics for the addition of 100 equivalents of GSH to **2b** (5 µM, Hepes 50 mM, pH 7.4), in the presence of $EuCl_3$ (1.5 mM). This led to a significant luminescence increase (λ_{ex} = 320 nm) in both the emission of the antenna (at 480 nm) and Eu^{3+} (Figure 4.5). Since Eu^{3+} ions are added at the beginning of the reaction, they can be pre-coordinated with unreacted **2b** probe. This may slightly change the surroundings of the lanthanide ions upon reaction, resulting in different areas of the $5D^0$ - $7F^1$ (592 nm) and $5D^0$ - $7F^2$ (616 nm) Eu^{3+} bands, when compared to the situation in which the lanthanide ions are added after completion of the reaction. These results open the door to the use **2b** as a self-assembled europium sensitizer to selectively report on the levels of GSH in real time, allowing the reaction to be monitored *in situ* at different wavelengths, broadening the palette for multiplexing applications. Nevertheless, we recommend using the 592 nm Eu^{3+} emission band, since its magnetic dipole nature makes it less sensitive to the environment[67]. The initial rates, obtained by analyzing the enhancement of luminescence intensity at 592 nm, exhibited an excellent linear relationship with the initial concentration of GSH (in logarithmic scale) (Figure S4.9). The linear fitting yielded a slope of 0.52 ± 0.07. This means a reaction order of ½ with respect to GSH, which indicates that the reaction mechanism is complex, possibly involving reversibility[68,69].

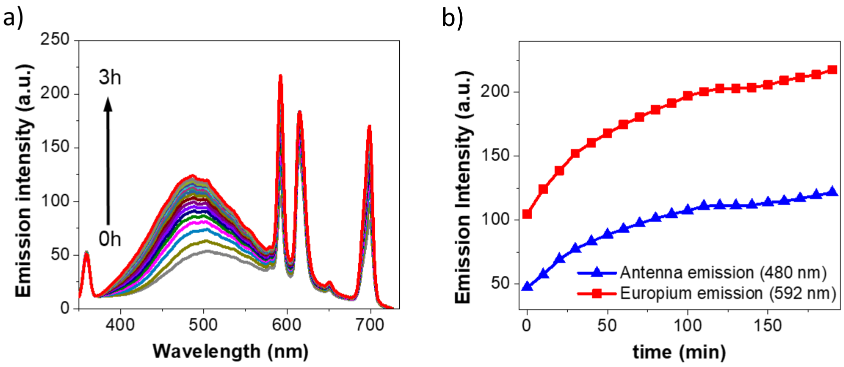

Figure 4.5. (a) Time-dependent luminescence emission spectra of **2b** (5 µM, λ_{ex} = 320 nm) in the presence of $EuCl_3$ (1.5 mM) after the addition of 100 equivalents of GSH. (b) The corresponding luminescence intensity at the emission of the antenna (480 nm, blue symbols) and the Eu^{3+} (592 nm, red symbols).

4.3.4 2B CAN BE USED TO MONITOR INTRACELLULAR GSH LEVELS IN MURINE AND HUMAN IMMUNE CELLS

To assess the applicability of **2b** to study intracellular GSH in primary cells we focused on the immune system. We first utilized **2b** to evaluate the differences in biothiol levels at baseline within different subpopulations ($CD4^+$ T cells, $CD8^+$ T cells, and B cells) of mouse splenocytes and human peripheral mononuclear cells (PBMCs) using flow cytometry. Of note, the sensor was not toxic and did not affect cell viability at a wide range of concentrations (0-50 µM) (Figure S4.10). To maximize the dynamic range of the measurements and capture differences within immune cell compartments, we used the sensor at 25 µM. Incubating the cells at this concentration, we were able to capture differences in the intracellular biothiol levels between CD4$^+$ T cells, CD8$^+$ T cells, and B cells, in both murine and human cells (Figure 4.6). Whereas we observed similar mouse intracellular biothiol levels in CD4$^+$ and CD8$^+$ T cells, B cells showed significantly lower levels (Figures 4.6a and 4.6b), suggesting that these cells might have lower baseline metabolic rates. Interestingly, we observed a different distribution in PBMCs, with baseline biothiol levels of CD4$^+$ T cells and human B cells being similar, and higher levels in CD8$^+$ T cells (Figure 4.6c). These results confirm that **2b** can be used in combination with flow cytometry to capture differences in intracellular biothiol levels within primary immune cell types.

Based on our previous outcomes where **2b** also acted as a europium antenna after reacting with biothiols, we applied this alternate version of the sensor to study changes in immune cell intracellular biothiol levels, in this case using a time-resolved, time-gated intensity analysis adapted to detect the long luminescence lifetime of Eu^{3+}. We cultured splenocytes from wild-type mice and studied the time-resolved, time-gated luminescence spectrum between 550 to 750 nm after adding either the **2b** biosensor (25 µM), europium ($EuCl_3$ at 250 µM) or both (Figure 4.6d). As expected, we only observed changes in the luminescence intensity when the **2b** sensor was added together with europium with the detected emission bands perfectly matching those of Eu^{3+} emission. This result indicates that the sensor was able to intracellularly sensitize europium luminescence, which could only happen if the sensor and the cation Eu^{3+} successfully entered the cells and reacted with intracellular biothiols. Once the conditions for the time-resolved, time-gated analysis on splenocytes were optimized, we studied the sensitized emission of Eu^{3+} in splenocytes in response to biothiol levels for 14 hours. Europium luminescence reached peak levels at the beginning of the experiment, slowly decreasing with time (within hours) (Figure S4.11), indicating that the Eu-based version of the sensor is an option for biological questions in which an increased signal-to-noise ratio (SNR) is required.

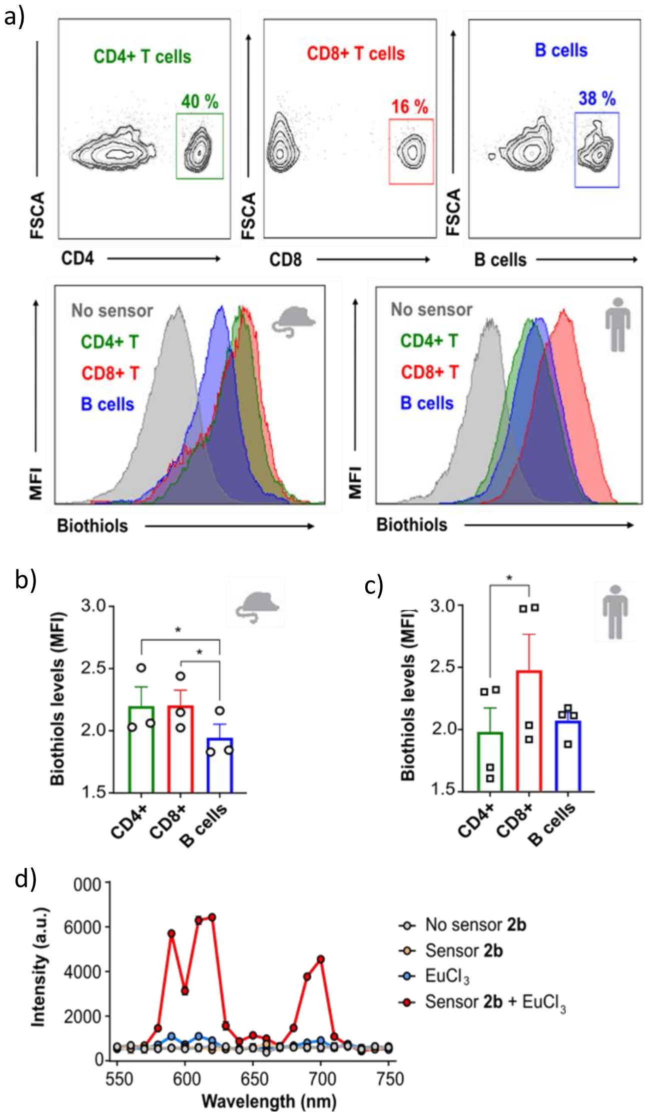

Figure 4.6. Study of the intracellular biothiol levels in murine and human immune cells with the sensor **2b**. (a) Gating flow cytometry strategy to identify the different cell subpopulations (CD4$^+$ T cells in green, CD8$^+$ T cells in red, and B cells in blue) and representative mean fluorescence intensities in the PacBlue channel either from murine or human cells (MFI, associated with intracellular biothiol levels); (b), (c) Flow cytometry quantification of the intracellular biothiol levels measured using the sensor at 25 µM from different subpopulations of immune cells in mouse (MFI normalized to control without **2b**) (b) and human (c) (n=3 animals/group or n=4 human samples/group from three independent experiments, ANOVA with Tukey HSD t-test, * p<0.05). (d) Time-resolved, time-gated luminescence spectra from splenocytes in the presence or absence of **2b**, $EuCl_3$ (250 µM) or both (λ_{ex} = 320 nm).

4.3.5 B CAPTURES GSH DYNAMIC CHANGES IN T$_{REG}$

Regulatory T cells (Treg) are one of the main mediators of central and peripheral tolerance and thus play a key role in autoimmune diseases, organ transplant rejection, and also anti-tumor immune responses[70-72]. GSH is vital for T cell effector function and proliferation and for preserving Treg function function[22], making the levels of this intracellular species in T cells a particularly relevant signal to monitor.

We decided to test the ability of the **2b** sensor to measure GSH intracellular changes in Treg induction cultures. To this aim, we isolated naïve splenic CD4$^+$ T cells (defined as CD44^{lo} CD62L^{hi} purity >95%) from C57BL/6-Foxp3-YFP mice and set up Treg induction cultures by culturing them for 5 days with αCD3/αCD28 activating beads under Treg polarizing conditions (IL-2 and TGFβ). In these mice, cells express a yellow fluorescent protein (YFP) fused to Foxp3 which can be detected as naïve T cells become Treg (CD4$^+$Foxp3$^+$), allowing us to selectively study GSH levels in this subpopulation. We monitored these levels in the culture daily by incubating with the sensor for 30 min and analyzing the cells by flow cytometry (Figure 4.7a). As it has been previously well established in these cultures, we observed an increase in the percentage of Treg in the culture as a function of time which peaked at day 5 (Figure 4.7b)[73, 74]. Interestingly, we observed a sharp increase in Treg GSH levels at day 1, followed by a decrease at days 2 and 3, and then increasing again up to day 5 (Figure 4.7c). This result suggests that different metabolic processes act at different times in the process of becoming Treg.

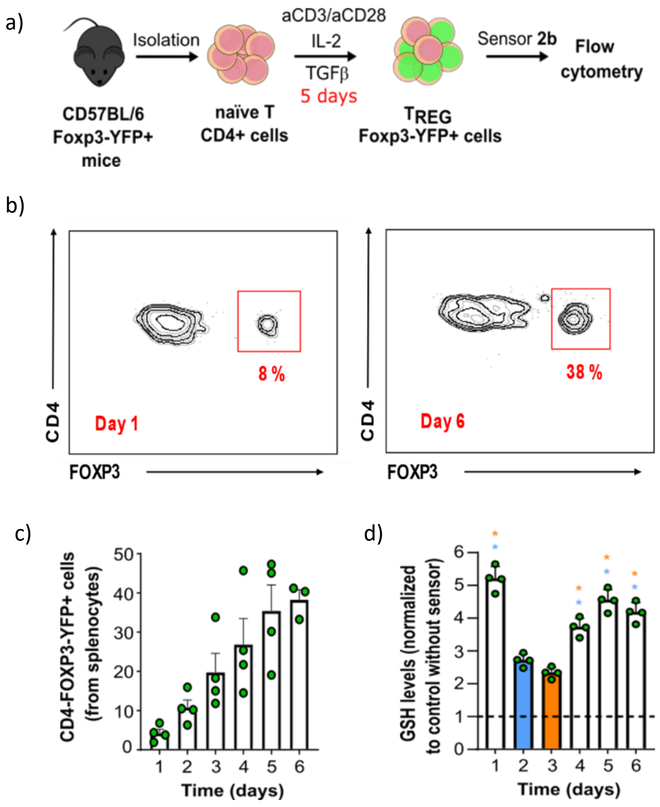

Figure 4.7. Study of biothiol metabolism in Treg with the sensor **2b**. (a) Schematic of the Treg induction protocol used to monitor intracellular biothiol levels. (b) Representative scatter plots of flow cytometry

analysis and quantification (c) of the number of CD4$^+$ Foxp3-YFP$^+$ cells in the culture at different days (1 to 6); (d) Flow cytometric quantification and statistical analysis of the intracellular biothiol levels in Treg at different days (n=4 animals/group from three independent experiments, ANOVA with Tukey HSD t-test, * $p<0.05$, blue: comparison with t=2 days, orange comparison with t=3 days).

4.4 CONCLUSIONS

In conclusion, the results herein described show that the small, non-fluorescent, Michael acceptor **2b**, after its reaction with biothiols, becomes fluorescent and an efficient Eu^{3+} antenna, which self-assembles with the cation in water. This property makes **2b** a highly selective GSH biosensor, which can be monitored through either the increase of the fluorescence of the antenna or the luminescence of Eu^{3+}, opening the possibility to multiplexing applications. We have demonstrated the potential of **2b** as a GSH biosensor to study murine and human cells of the immune system with flow cytometry (CD4$^+$ T, CD8$^+$ T, and B cells), and to monitor changes in their metabolism as naïve CD4$^+$ T cells polarize to Treg. Together, these experiments constitute a proof-of-concept of the use of **2b** to monitor biothiols in immune cells, filling the gap for GSH-metabolic studies in flow cytometry to address biological questions and pave the way to its application to study clinical samples.

BIBLIOGRAPHY

1 Poole, L. B. The basics of thiols and cysteines in redox biology and chemistry. *Free Radical Biol. Med.* **2015,** 80, 148-157.

2 Wang, Y.; Zhu, M.; Jiang, E.; Hua, R.; Na, R.; Li, Q. X. A Simple and Rapid Turn On ESIPT Fluorescent Probe for Colorimetric and Ratiometric Detection of Biothiols in Living Cells. *Sci. Rep.* **2017,** 7, 1-9.

3 Paulsen, C. E.; Carroll, K. S. Cysteine-mediated redox signaling: Chemistry, biology, and tools for discovery. *Chem. Rev.* **2013,** 113, 4633-4679.

4 Wang, X. F.; Cynader, M. S. Pyruvate released by astrocytes protects neurons from copper-catalyzed cysteine neurotoxicity. *J. Neurosci.* **2001,** 21, 3322-3331.

5 van Meurs, J. B. J.; Dhonukshe-Rutten, R. A. M.; Pluijm, S. M. F.; van der Klift, M.; de Jonge, R.; Lindemans, J.; de Groot, L. C. P. G. M.; Hofman, A.; Witteman, J. C. M.; van Leeuwen, J. P. T. M.; Breteler, M. M. B.; Lips, P.; Pols, H. A. P.; Uitterlinden, A. G. Homocysteine levels and the risk of osteoporotic fracture. *N. Engl. J. Med.* **2004,** 350, 2033-2041.

6 Seshadri, S.; Beiser, A.; Selhub, J.; Jacques, P. F.; Rosenberg, I. H.; D'Agostino, R. B.; Wilson, P. W. F.; Wolf, P. A. Plasma homocysteine as a risk factor for dementia and Alzheimer's disease. *N. Engl. J. Med.* **2002,** 346, 476-483.

7 Forman, H. J.; Zhang, H.; Rinna, A. Glutathione: Overview of its protective roles, measurement, and biosynthesis. *Mol. Aspects Med.* **2009,** 30, 1-12.

8 Kimura, H.; Nagai, Y.; Umemura, K.; Kimura, Y. Physiological roles of hydrogen sulfide: Synaptic modulation, neuroprotection, and smooth muscle relaxation. *Antioxid. Redox Signaling* **2005,** 7, 795-803.

9 Hortová-Kohoutková, M.; Lázničková, P.; Frič, J. How immune-cell fate and function are determined by metabolic pathway choice: The bioenergetics underlying the immune response. *Bioessays* **2021,** 43, e2000067.

10 Mathis, D.; Shoelson, S. E. Immunometabolism: an emerging frontier. *Nat. Rev. Immunol.* **2011,** 11, 81.

11 Wang, A.; Luan, H. H.; Medzhitov, R. An evolutionary perspective on immunometabolism. *Science* **2019,** 363, eaar3932.

12 Muri, J.; Kopf, M. Redox regulation of immunometabolism. *Nat. Rev. Immunol.* **2021,** 21, 363-381.

13 Singer, B. D.; Chandel, N. S. Immunometabolism of pro-repair cells. *J. Clin. Invest.* **2019,** 129, 2597-2607.

14 Yan, Z.; Garg, S. K.; Banerjee, R. Regulatory T cells interfere with glutathione metabolism in dendritic cells and T cells. *J. Biol. Chem.* **2010,** 285, 41525-41532.

15 Yan, Z.; Banerjee, R. Redox remodeling as an immunoregulatory strategy. *Biochemistry* **2010,** 49, 1059-1066.

16 Yan, Z.; Garg, S. K.; Kipnis, J.; Banerjee, R. Extracellular redox modulation by regulatory T cells. *Nat. Chem. Biol.* **2009,** 5, 721-723.

17 Dawson, H.; Collins, G.; Pyle, R.; Deep-Dixit, V.; Taub, D. D. The immunoregulatory effects of homocysteine and its intermediates on T-lymphocyte function. *Mech. Ageing Dev.* **2004,** 125, 107-110.

18 Yang, R.; Qu, C.; Zhou, Y.; Konkel, J. E.; Shi, S.; Liu, Y.; Chen, C.; Liu, S.; Liu, D.; Chen, Y.; Zandi, E.; Chen, W.; Zhou, Y.; Shi, S. Hydrogen sulfide promotes Tet1- and Tet2-mediated Foxp3 demethylation to drive regulatory T cell differentiation and maintain immune homeostasis. *Immunity* **2015,** 43, 251-263.

19 Oh, S. A.; Li, M. O. TETs link hydrogen sulfide to immune tolerance. *Immunity* **2015,** 43, 211-213.

20 Ghezzi, P.; Romines, B.; Fratelli, M.; Eberini, I.; Gianazza, E.; Casagrande, S.; Laragione, T.; Mengozzi, M.; Herzenberg, L. A.; Herzenberg, L. A. Protein glutathionylation: coupling and uncoupling of glutathione to protein thiol groups in lymphocytes under oxidative stress and HIV infection. *Mol. Immunol.* **2002,** 38, 773-780.

21. Droege, W.; Eck, H. P.; Gmuender, H.; Mihm, S. Modulation of lymphocyte functions and immune responses by cysteine and cysteine derivatives. *Am. J. Med.* **1991,** 91, 140S-4.

22 Kurniawan, H.; Franchina, D. G.; Guerra, L.; Bonetti, L.; Soriano-Baguet, L.; Grusdat, M.; Schlicker, L.; Hunewald, O.; Dostert, C.; Merz, M. P.; Binsfeld, C.; Duncan, G. S.; Farinelle, S.; Nonnenmacher, Y.; Haight, J.; Das Gupta, D.; Ewen, A.; Taskesen, R.; Halder, R.; Chen, Y.; Jager, C.; Ollert, M.; Wilmes, P.; Vasiliou, V.; Harris, I. S.; Knobbe-Thomsen, C. B.; Turner, J. D.; Mak, T. W.; Lohoff, M.; Meiser, J.; Hiller, K.; Brenner, D. Glutathione Restricts Serine Metabolism to Preserve Regulatory T Cell Function. *Cell Metab.* **2020,** 31, 920-936.e7.

23 Mak, T. W.; Grusdat, M.; Duncan, G. S.; Dostert, C.; Nonnenmacher, Y.; Cox, M.; Binsfeld, C.; Hao, Z.; Brustle, A.; Itsumi, M.; Jager, C.; Chen, Y.; Pinkenburg, O.; Camara, B.; Ollert, M.; Bindslev-Jensen, C.; Vasiliou, V.; Gorrini, C.; Lang, P. A.; Lohoff, M.; Harris, I. S.; Hiller, K.; Brenner, D. Glutathione Primes T Cell Metabolism for Inflammation. *Immunity* **2017,** 46, 675-689.

24. Dawson, H.; Collins, G.; Pyle, R.; Deep-Dixit, V.; Taub, D. D. The immunoregulatory effects of homocysteine and its intermediates on T-lymphocyte function. *Mech. Ageing Dev.* **2004,** 125, 107-10.

25 Dröge, W.; Eck, H. P.; Gmünder, H.; Mihm, S. Modulation of lymphocyte functions and immune responses by cysteine and cysteine derivatives. *Am. J. Med.* **1991,** 91, 140S-144S.

26 Peterson, J. D.; Herzenberg, L. A.; Vasquez, K.; Waltenbaugh, C. Glutathione levels in antigen-presenting cells modulate Th1 versus Th2 response patterns. *Proc. Natl. Acad. Sci. U S A* **1998,** 95, 3071-6.

27 Jung, H. S.; Chen, X.; Kim, J. S.; Yoon, J. Recent progress in luminescent and colorimetric chemosensors for detection of thiols. *Chem. Soc. Rev.* **2013,** 42, 6019-6031.

28 Yin, C.-X.; Xiong, K.-M.; Huo, F.-J.; Salamanca, J. C.; Strongin, R. M. Fluorescent probes with multiple binding sites for the discrimination of Cys, Hcy, and GSH. *Angew. Chem., Int. Ed.* **2017,** 56, 13188-13198.

29 Dai, J.; Ma, C.; Zhang, P.; Fu, Y.; Shen, B. Recent progress in the development of fluorescent probes for detection of biothiols. *Dyes Pigm.* **2020,** 177, 108321.

30 Niu, L.-Y.; Chen, Y.-Z.; Zheng, H.-R.; Wu, L.-Z.; Tung, C.-H.; Yang, Q.-Z. Design strategies of fluorescent probes for selective detection among biothiols. *Chem. Soc. Rev.* **2015,** 44, 6143-6160.

31 Wintner, E. A.; Deckwerth, T. L.; Langston, W.; Bengtsson, A.; Leviten, D.; Hill, P.; Insko, M. A.; Dumpit, R.; VandenEkart, E.; Toombs, C. F.; Szabo, C. A monobromobimane-

based assay to measure the pharmacokinetic profile of reactive sulphide species in blood. *Br. J. Pharmacol.* **2010,** 160, 941-957.

32 Martinez-Losa, M.; Cortijo, J.; Juan, G.; Ramón, M.; Sanz, M. J.; Morcillo, E. J. Modulatory effects of N-acetyl-L-cysteine on human eosinophil apoptosis. *Eur. Respir. J.* **2007,** 30, 436-42.

33 West, C. A.; He, C.; Su, M.; Swanson, S. J.; Mentzer, S. J. Aldehyde Fixation of Thiol-reactive Fluorescent Cytoplasmic Probes for Tracking Cell Migration. *J. Histochem. Cytochem.* **2001,** 49, 511-517.

34 Hedley, D. W.; Chow, S. Evaluation of methods for measuring cellular glutathione content using flow cytometry. *Cytometry* **1994,** 15, 349-58.

35. Thibon, A.; Pierre, V. C. Principles of responsive lanthanide-based luminescent probes for cellular imaging. *Anal. Bioanal. Chem.* **2009,** 394, 107-120.

36 Eliseeva, S. V.; Bunzli, J.-C. G. Lanthanide luminescence for functional materials and bio-sciences. *Chem. Soc. Rev.* **2010,** 39, 189-227.

37 Garcia-Fernandez, E.; Pernagallo, S.; González-Vera, J. A.; Ruedas-Rama, M. J.; Díaz-Mochón, J. J.; Orte, A. Time-Gated Luminescence Acquisition for Biochemical Sensing: miRNA Detection. In *Fluorescence in Industry*, Pedras, B., Ed. Springer International Publishing: Cham, 2019; pp 213-267.

38 Xie, F.; Tan, H.; Li, Z.; Yang, H. A europium-based fluorescence probe for detection of thiols in urine. *Anal. Methods* **2014,** 6, 6990-6996.

39 Dai, Z.; Tian, L.; Song, B.; Ye, Z.; Liu, X.; Yuan, J. Ratiometric Time-Gated Luminescence Probe for Hydrogen Sulfide Based on Lanthanide Complexes. *Anal. Chem.* **2014,** 86, 11883-11889.

40 Fueyo-González, F.; Garcia-Fernandez, E.; Martinez, D.; Infantes, L.; Orte, A.; González-Vera, J. A.; Herranz, R. Smart lanthanide antennas for sensing water. *Chem. Commun.* **2020,** 56, 5484-5487.

41 González-Vera, J. A.; Fueyo-González, F.; Alkorta, I.; Peyressatre, M.; Morris, M. C.; Herranz, R. Highly solvatochromic and tunable fluorophores based on a 4,5-quinolimide scaffold: novel CDK5 probes. *Chem. Commun.* **2016,** 52, 9652-9655.

42 Breslow, R. Antiaromaticity. *Accounts Chem. Res.* **1973,** 6, 393.

43 Minkin, V. I.; Glukhovtsev, M. N.; Simkin, B. Y. *Aromaticity and Antiaromaticity: Electronic and Structural Aspects*. Wiley: 1994; p 313 pp.

44 Minkin, V. I. Glossary of terms used in theoretical organic chemistry (IUPAC recommendations 1999). *Pure Appl. Chem.* **1999,** 71, 1919-1981.

45 Becke, A. D. Density-functional thermochemistry. III. The role of exact exchange. *J. Chem. Phys.* **1993,** 98, 5648-52.

46 Lee, C.; Yang, W.; Parr, R. G. Development of the Colle-Salvetti correlation-energy formula into a functional of the electron density. *Phys. Rev. B* **1988,** 37, 785-789.

47 Adamo, C.; Jacquemin, D. The calculations of excited-state properties with Time-Dependent Density Functional Theory. *Chem. Soc. Rev.* **2013,** 42, 845-856.

48 Hariharan, P. C.; Pople, J. A. Influence of polarization functions on MO hydrogenation energies. *Theor. Chim. Acta* **1973,** 28, 213-22.

49 Frisch, M. J.; Trucks, G. W.; Schlegel, H. B.; Scuseria, G. E.; Robb, M. A.; Cheeseman, J. R.; Scalmani, *Gaussian 16 Rev. C.01*, Wallingford, CT, 2016.

50 Krygowski, T. M.; Cyranski, M. K. Structural Aspects of Aromaticity. *Chem. Rev.* **2001,** 101, 1385-1419.

51 Dobrowolski, J. C. Three queries about the HOMA index. *ACS Omega* **2019,** 4, 18699-18710.

52 Frizzo, C. P.; Martins, M. A. P. Aromaticity in heterocycles: new HOMA index parametrization. *Struct. Chem.* **2012,** 23, 375-380.

53 Setiawan, D.; Kraka, E.; Cremer, D. Quantitative assessment of aromaticity and antiaromaticity utilizing vibrational spectroscopy. *J. Org. Chem.* **2016,** 81, 9669-9686.

54 Krygowski, T. M. Crystallographic studies of inter- and intramolecular interactions reflected in aromatic character of π-electron systems. *J. Chem. Inf. Comput. Sci.* **1993,** 33, 70-8.

55 Radenkovic, S.; Durdevic, J.; Bultinck, P. Local aromaticity of the five-membered rings in acenaphthylene derivatives. *Phys. Chem. Chem. Phys.* **2012,** 14, 14067-14078.

56 Haas, Y.; Stein, G. Pathways of radiative and radiationless transitions in europium(III) solutions. Role of solvents and anions. *J. Phys. Chem.* **1971,** 75, 3668-3677.

57 Haas, Y.; Stein, G. Pathways of radiative and radiationless transitions in europium(III) solutions. The role of high energy vibrations. *J. Phys. Chem.* **1971,** 75, 3677-3681.

58 Krezel, A.; Bal, W. Coordination chemistry of glutathione. *Acta Biochim. Pol.* **1999,** 46, 567-580.

59 Liu, J.; Liu, H.; Li, Y.; Wang, H. Probing the coordination properties of glutathione with transition metal ions (Cr2+,Mn2+,Fe2+,Co2+, Ni2+,Cu2+,Zn2+,Cd2+,Hg2+) by density functional theory. *J. Biol. Phys.* **2014,** 40, 313-323.

60 Zhang, J.; Sun, X.; Wu, J. Heavy metal ion detection platforms based on a glutathione probe: a mini review. *Appl. Sci.* **2019,** 9, 489.

61. Rocha, G. B.; Freire, R. O.; Simas, A. M.; Stewart, J. J. P. RM1: a reparameterization of AM1 for H, C, N, O, P, S, F, Cl, Br, and I. *J. Comput. Chem.* **2006,** 27, 1101-1111.

62 Filho, M. A. M.; Dutra, J. D. L.; Cavalcanti, H. L. B.; Rocha, G. B.; Simas, A. M.; Freire, R. O. RM1 Model for the Prediction of Geometries of Complexes of the Trications of Eu, Gd, and Tb. *J. Chem. Theory Comput.* **2014,** 10, 3031-3037.

63 Stewart, J. J. P. *MOPAC2016*, 21.329L; Stewart Computational Chemistry: Colorado Springs, CO, USA, 2016.

64 Yin, G.-x.; Niu, T.-t.; Gan, Y.-b.; Yu, T.; Yin, P.; Chen, H.-m.; Zhang, Y.-y.; Li, H.-t.; Yao, S.-z. A Multi-signal Fluorescent Probe with Multiple Binding Sites for Simultaneous Sensing of Cysteine, Homocysteine, and Glutathione. *Angew. Chem., Int. Ed.* **2018,** 57, 4991-4994.

65 Hwang, C.; Sinskey, A. J.; Lodish, H. F. Oxidized redox state of glutathione in the endoplasmic reticulum. *Science* **1992,** 257, 1496-502.

66 Yue, Y.; Huo, F.; Ning, P.; Zhang, Y.; Chao, J.; Meng, X.; Yin, C. Dual-Site Fluorescent Probe for Visualizing the Metabolism of Cys in Living Cells. *J. Am. Chem. Soc.* **2017,** 139, 3181-3185.

67 Kakkar, T.; Thomas, N.; Kumi-Barimah, E.; Jose, G.; Saha, S. Photoluminescence intensity ratio of Eu-conjugated lactates—A simple optical imaging technique for biomarker analysis for critical diseases. *J. Biophotonics* **2018,** 11, e201700199.

68 Liu, Z.; Zhou, X.; Miao, Y.; Hu, Y.; Kwon, N.; Wu, X.; Yoon, J. A Reversible Fluorescent Probe for Real-time Quantitative Monitoring of Cellular Glutathione. *Angew. Chem., Int. Ed.* **2017,** 56, 5812-5816.

69 Heng, S.; Zhang, X.; Pei, J.; Abell, A. D. A rationally designed reversible 'turn-off' sensor for glutathione. *Biosensors* **2017,** 7, 36/1-36/13.

70 Corthay, A. How do regulatory T cells work? *Scand. J. Immunol.* **2009,** 70, 326-336.

71 Sharabi, A.; Tsokos, M. G.; Ding, Y.; Malek, T. R.; Klatzmann, D.; Tsokos, G. C. Regulatory T cells in the treatment of disease. *Nat. Rev. Drug Discovery* **2018,** 17, 823-844.

72 Romano, M.; Fanelli, G.; Albany, C. J.; Giganti, G.; Lombardi, G. Past, present, and future of regulatory T cell therapy in transplantation and autoimmunity. *Front. Immunol.* **2019,** 10, 43.

73 Hang, S.; Paik, D.; Yao, L.; Kim, E.; Trinath, J.; Lu, J.; Ha, S.; Nelson, B. N.; Kelly, S. P.; Wu, L.; Zheng, Y.; Longman, R. S.; Rastinejad, F.; Devlin, A. S.; Krout, M. R.; Fischbach, M. A.; Littman, D. R.; Huh, J. R. Bile acid metabolites control T(H)17 and T(reg) cell differentiation. *Nature* **2019,** 576, 143-148.

74 Purroy, C.; Fairchild, R. L.; Tanaka, T.; Baldwin, W. M.; Manrique, J.; Madsen, J. C.; Colvin, R. B. Erythropoietin Receptor-Mediated Molecular Crosstalk Promotes T Cell Immunoregulation and Transplant Survival. *J. Am. Soc. Nephrol.* **2017,** 28, 2377-2392.

SUPPORTING INFORMATION

GENERAL METHODS

All reagents were of commercial quality. Solvents were dried and purified by standard methods. Analytical TLC was performed on aluminum sheets coated with a 0.2 mm layer of silica gel 60 F_{254}. Silica gel 60 (230-400 mesh) was used for flash chromatography. HPLC-MS was performed on a Sunfire C_{18} (4.6×50 mm, 3.5 µm) column at 30°C, with a flow rate of 1 mL/min and gradient of 0.1% of formic acid in CH_3CN (solvent A) in 0.1% of formic acid in H_2O (solvent B) was used as mobile phase. Electrospray in positive mode was used for ionization. NMR spectra were recorded using Varian Inova or Mercury 400, and Varian Unity 500 spectrometers. The NMR spectra assignments were based on COSY, HSQC, and HMBC spectra. High resolution mass spectra (HRMS) were recorded on an Agilent 6520 Q-TOF instrument with an ESI source. MW experiments were carried out in sealed vessels in a MW Emrys$^{\mathrm{TM}}$ Synthesizer (Biotage AB), with transversal IR sensor for reaction temperature monitoring. UV-visible spectroscopy measurements were made at 25 Cº on a Lambda 35, Perkin Elmer, UV-vis spectrophotometer. Steady-state fluorescence emission spectra were performed at 25 ºC on a JASCO FP-8300 spectrofluorometer equipped with a 450 W xenon lamp for excitation. Lifetime experiments were acquired in a Varian Cary Eclipse Spectrofluorometer. Starna and Hellma quartz cuvettes of 1 cm path length and several volumes were employed.

EXPERIMENTAL SYNTHETIC METHODS

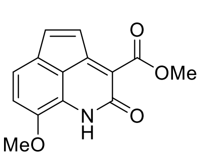

2a

Synthesis of methyl 8-methoxy-2-oxo-1,2-dihydrocyclopenta[*de*]quinoline-3-carboxylate (2a). 2,3-Dichloro-5,6-dicyano-1,4-benzoquinone (DDQ, 900 mg, 3.95 mmol) was added to a solution of methyl 8-methoxy-2-oxo-1,2,4,5-tetrahydrocyclopenta[*de*]quinoline-3-carboxylate (**1a**)[1] (810 mg, 3,30 mmol) in toluene (25 mL), and the mixture was stirred and heated to reflux for 4 h. Then, the reaction mixture was evaporated to dryness and the residue was purified by flash chromatography, using 0-5% gradient of MeOH in CH_2Cl_2 as eluent to give the oxidized compound **2a** as a red solid (350 mg, 42%). M.p. 203 ºC. HPLC-MS (30-95% gradient of 0.1 % solution of A in B, 10 min) t_R = 2.32 min. ^{1}H-RMN ($CDCl_3$, 400 MHz) δ: 3.89 (s, 3H), 3.91 (s, 3H), 6.62 (d, 1H, *J* = 7.5 Hz), 6.82 (d, 1H, *J* = 5.3 Hz), 6.96 (d, 1H, *J* = 7.5 Hz), 7.05 (d, 1H, *J* = 5.3 Hz), 9.79 (s, 1H). ^{13}C-RMN ($CDCl_3$, 100 MHz) δ: 52.5, 56.4, 110.8, 118.3, 119.9, 120.1, 125.5, 1264, 131.5, 141.0, 147.7, 152.8, 161.7, 164.8. HRMS (ESI) *m/z*: Calcd. for $C_{14}H_{11}NO_4$ ($[M+H]^+$): 258.0761, Found: 258.0757.

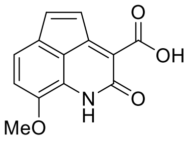

2b

Synthesis of 8-methoxy-2-oxo-1,2-dihydrocyclopenta[*de*]quinoline-3-carboxylic acid (2b). The methyl ester **2a** (200 mg, 0.77 mmol) was added to 2 N aqueous solution of NaOH (5 mL) and the mixture was heated to reflux for 30 min. Then, the solution was cooled and lyophilized, and the residue was purified by reverse flash chromatography using a KP-C18-HS cartridge and 0-10% gradient of CH_3CN in H_2O as eluent to give the free carboxylic acid **2b** as an orange-red solid (150 mg, 80 %). M.p. 274 ºC. HPLC-MS (5-95% gradient of 0.1 % solution of A in B, 10 min) t_R = 7.93 min. ^{1}H-RMN (D_2O, 400 MHz) δ: 3.91 (s, 3H), 6.74 (d, 1H, *J* = 5.5 Hz), 6.77 (d, 1H, *J* = 7.5 Hz), 7.12 (2d, 2H, *J* = 5.5 Hz and *J* = 7.5 Hz). ^{13}C-RMN (D_2O, 100 MHz) δ: 55.8, 109.6, 119.0, 119.1, 120.1, 124.4, 128.0, 130.8, 137.0, 144.2, 150.1, 166.3, 174.0. HRMS (ESI) *m/z*: Calcd. for $C_{13}H_9NO_4$ ($[M+H]^+$): 244.0604, Found: 244.0604.

COMPUTATIONAL METHODS

The geometry of the molecules in the singlet ground state (S_0) has been optimized with the B3LYP functional[2,3] and the 6-31+G(d,p) basis set[4]. Frequency calculations at the same computational level have been performed to confirm that the geometries obtained correspond to energetic minima. These geometries have been used as starting point for the optimization of the first excited single (S_1) and triplet (T_1) states. For the latter, TD-DFT[5] has been used. All the calculations have been performed with the Gaussian-16 program.

The aromaticity of the systems has been evaluated with the harmonic oscillator model of aromaticity (HOMA) parameter [6,7] as expressed in the following equation (S4.1).

$$HOMA = 1 - \frac{1}{n}\sum_1^n \propto_i (R_{opt} - R_i)^2 \qquad \text{(S4.1)}$$

The values used of R_{opt} and α were 1.388 and 257.7 for C-C bonds and 1.334 and 93.52 for C-N bonds, respectively.

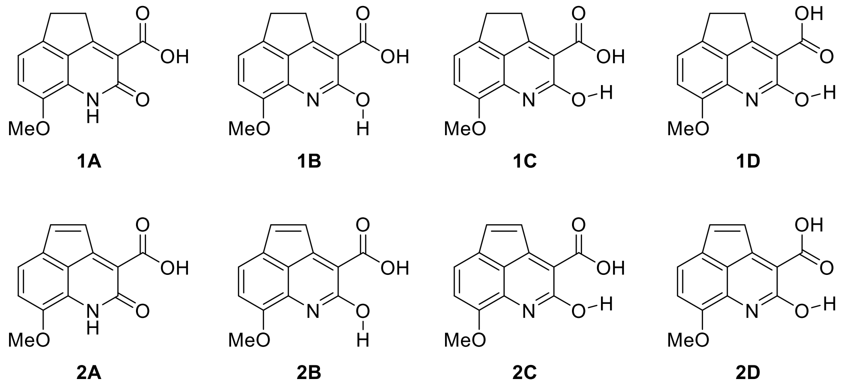

1A 1B 1C 1D

2A 2B 2C 2D

Figure S4.1. Tautomeric/rotameric structures considered in the calculations of the minimum energy structures of the S_0, S_1 and T_1 states for the free carboxylic acids **1b** and **2b**.

Table S4.1. Relative energies (E_{rel}, kJ mol^{-1}) of the **A**-**D** structures in the S_0, S_1 and T_1 states of **1b** and **2b**.

Compd	Energy state	**A**	**B**	**C**	**D**	
1b	S_0	0.0	29.3	30.0	16.2	
	S_1	0.0	28.8	6.7	-20.6	
	T_1	0.0	11.2	-0.9	-21.6	
2b	S_0	0.0	26.0	26.0	9.6	
	S_1	0.0	23.2	15.3	-1.6	
	T_1	0.0	27.0	22.8	7.0	

Table S4.2. Calculated HOMA values for periphery of the bicyclic quinolone ring of the **A**-**D** structures in the S_0, S_1 and T_1 energy states of **1b** and **2b.**

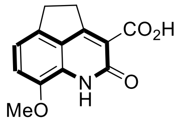

1b

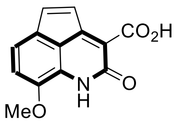

2b

Compd	Energy state	**A**	**B**	**C**	**D**
1b	S_0	0.	0.	0.	0.

		58	79	74	73
	S_1	0.56	0.71	0.66	0.62
	T_1	0.62	0.64	0.64	0.66
2b	S_0	0.50	0.72	0.67	0.66
	S_1	0.43	0.62	0.57	0.56
	T_1	0.43	0.62	0.57	0.55

Table S4.3. Calculated HOMA values for periphery of the tricyclic ring of the 1,2-dihydrocyclopenta[*de*]quinoline system of **2b** in the **A**-**D** structures in the S_0, S_1 and T_1 energy states.

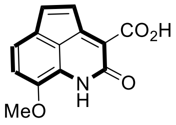

2b

Energy state	**A**	**B**	**C**	**D**
S_0	0.24	0.44	0.39	0.40
S_1	0.49	0.68	0.64	0.63
T_1	0.42	0.60	0.56	0.56

Table S4.4. ^{1}H NMR and ^{13}C NMR chemical shifts for **1b** and **2b**.

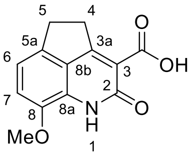

1b

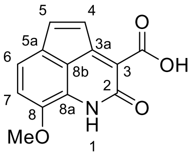

2b

Nucleus	**1b**^{a} δ(pm)	**2b**^{b} δ(pm)
4-H	3.51	6.74
5-H	3.15	7.12
6-H	6.93	7.12
7-H	6.98	6.77
2-C	169.4	174.0
C_2	167.6	166.3
C_3	116.4	119.0
C_{3a}	174.0	144.2
C_4	32.5	124.4
C_5	29.3	137.0
C_{5a}	137.8	130.8
C_6	114.7	120.1
C_7	112.0	109.6
C_8	149.6	150.1
C_{8a}	136.3	128.0
C_{8b}	130.9	119.1
OMe	55.5	55.8

^{a}In DMSO-d$_6$. ^{b}In H_2O

SPECTROSCOPY METHODS

a. Photophysical properties

Excitation and emission spectra of compounds were determined for 12 µM solutions in H_2O or CH_3CN. The spectra were recorded between 300 and 690 nm (0.5 nm increments and 0.1 s integration time) with excitation set at the appropriate excitation wavelength. Slit widths were set to 5 nm for excitation and to 5 nm for emission. All the spectra were corrected for background fluorescence by subtracting a blank scan of the solvent solution and spectrally corrected using certified fluorescence standards.

Fluorescence quantum yield determination. Fluorescence quantum yields (Φ_F) of quinolin-2(1*H*)-one derivatives **1b** and **2b** were determined in solvents of different polarity and calculated using quinine sulfate dihydrate (in 0.1M H_2SO_4) as reference[8]. Concentration of the sample and the reference was set to assure that the absorbance was less than 0.1 at identical excitation wavelengths. The following equation (S4.2) was used to calculate the quantum yield:

$$\Phi = \frac{I_x A_r n^2_x \Phi_r}{A_x I_r n^2_r} \tag{S4.2}$$

where *x* and *r* denote the sample and standard, respectively, *A* is the absorption at the excitation wavelength, *I* is the integrated fluorescence intensity, and *n* is the refractive index of the solvent.

Fluorescence lifetimes determination. Lifetime experiments of lanthanide complexes of the addition products of GSH, Hcy and Cys to **2b** (**2b**-GSH, **2b**-Hcy and **2b**-Cys) were acquired in a Varian Cary Eclipse Spectrofluorometer at room temperature using the following conditions: excitation wavelength 320 nm; emission wavelength 545 nm for terbium or 615 nm for europium; excitation slit width 5.0 nm, emission slit width 5.0 nm; total decay time 15.0 ms; delay time 0.1 ms; gate time 0.2 ms; number of cycles 20; PMT detector voltage 600 V.

b. Lanthanide luminescence sensitization and 2b reactivity studies

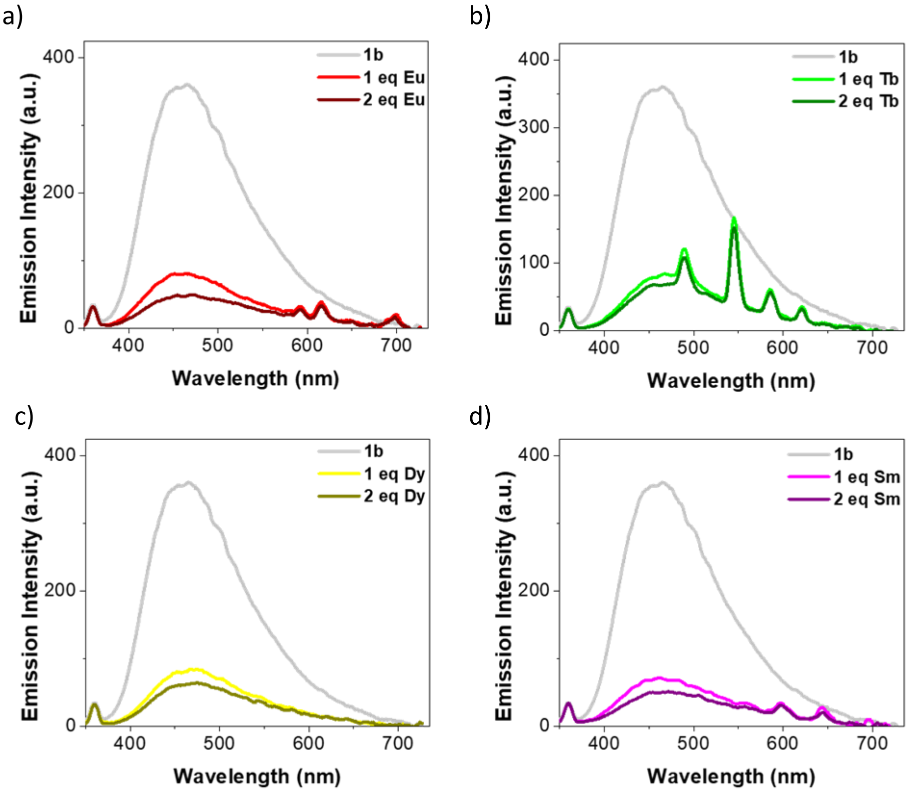

Figure S4.2. Emission spectra of **1b** (5 µM in Hepes buffer 50 mM, pH 7.4) and after addition of 1 and 2 equivalents of (a) $EuCl_3$, (b) $TbCl_3$, (c) $DyCl_3$ and (d) $SmCl_3$.

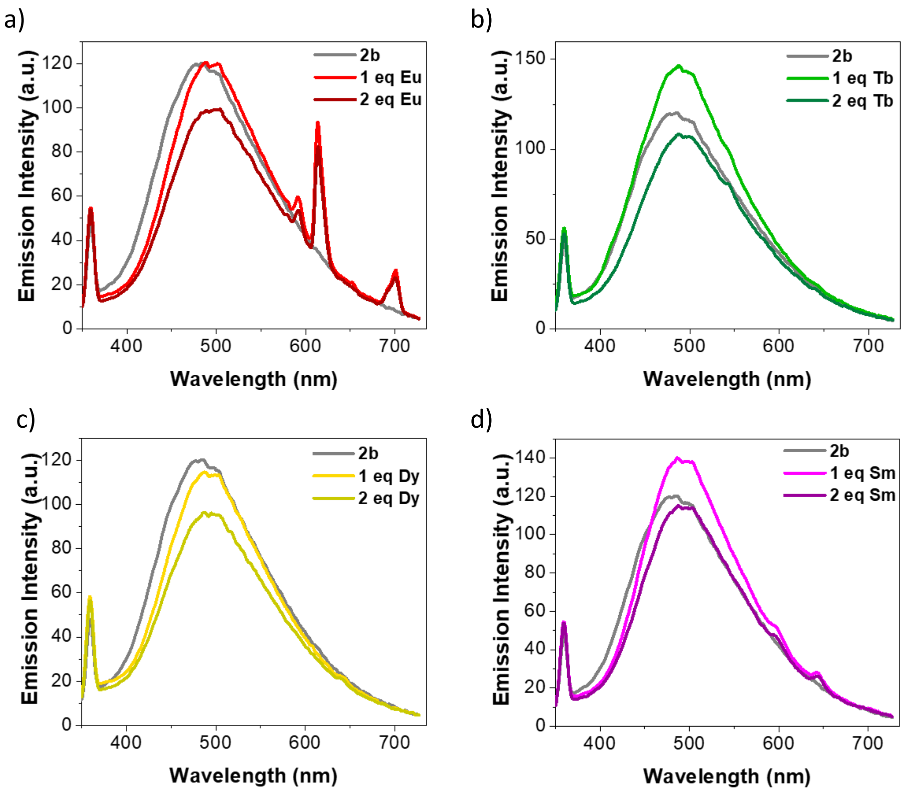

Figure S4.3. Emission spectra of **2b** (5 µM in Hepes buffer 50 mM, pH 7.4) and after addition of 1 and 2 equivalents of (a) $EuCl_3$, (b) $TbCl_3$, (c) $DyCl_3$ and (d) $SmCl_3$.

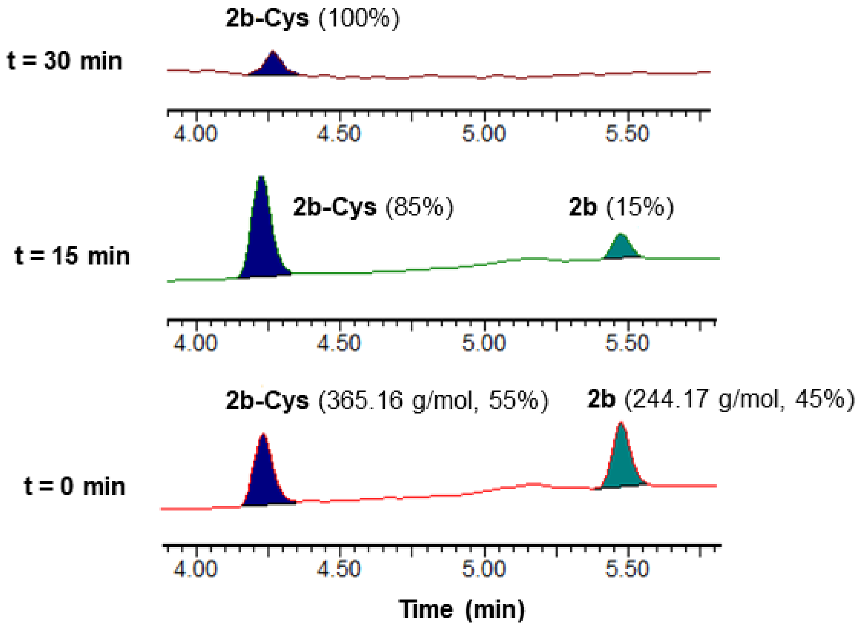

Figure S4.4. HPLC-MS analysis of **2b** (5 µM) after the addition of Cys (500 µM) in Hepes buffer pH 7.4.

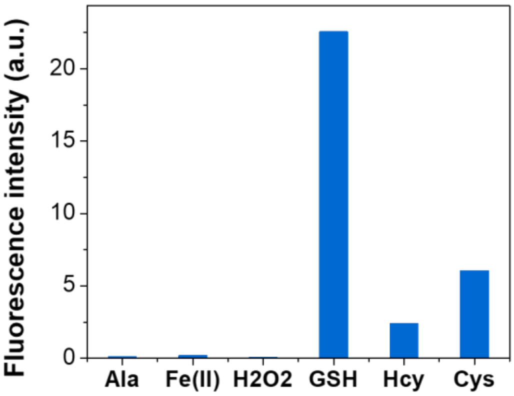

Figure S4.5. Fluorescence emission intensity of **2b** at 450 nm (5 µM in Hepes buffer 50 mM, pH 7.4) after addition of 100 equivalents of GSH and the possible interferents Ala, Fe^{2+}, H_2O_2.

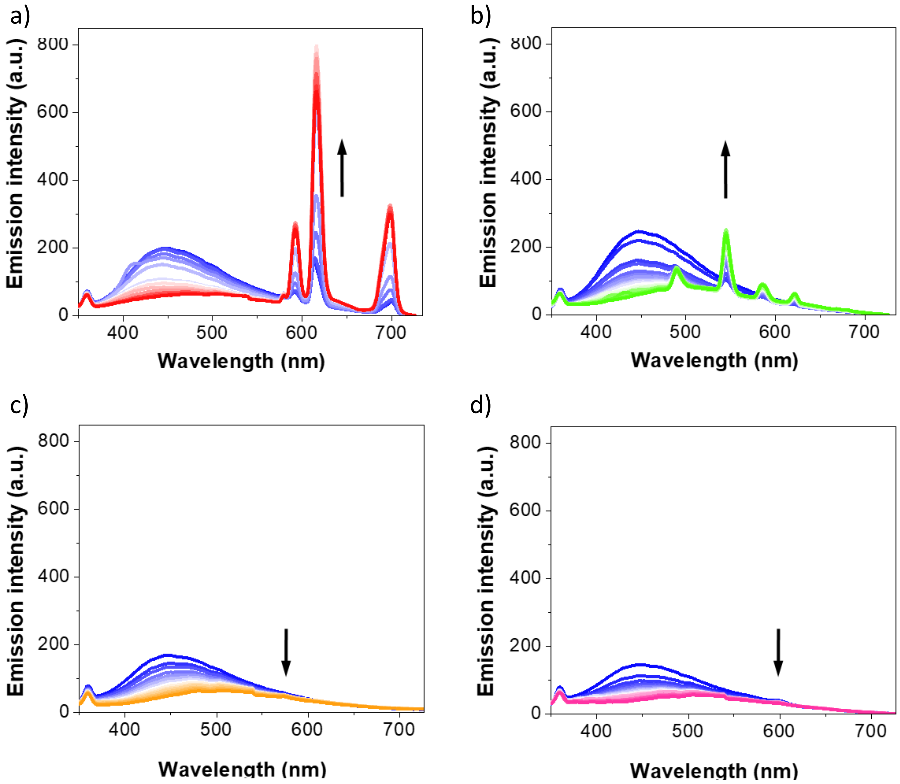

Figure S4.6. Titration spectra of **2b**-GSH (5 µM in Hepes buffer 50 mM, pH 7.4) with increasing equivalents (2–1000), indicated by arrows, of (a) $EuCl_3$, (b) $TbCl_3$, (c) $DyCl_3$ and (d) $SmCl_3$. Only with Eu^{3+} and Tb^{3+} the energy transfer was sufficiently effective to detect the lanthanide emission.

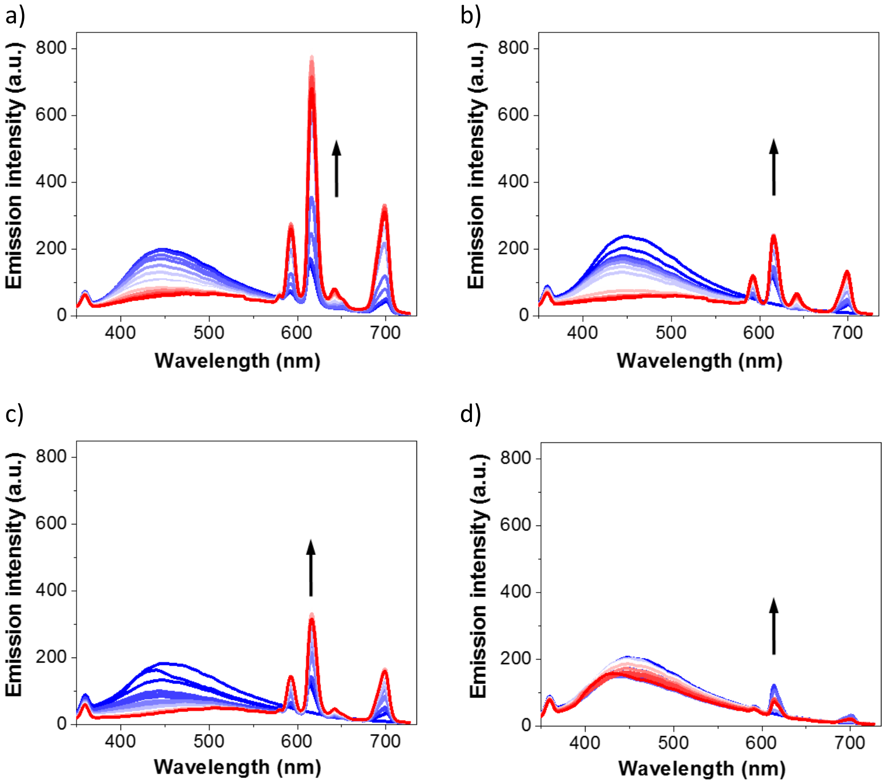

Figure S4.7. Titration spectra of (a) **2b**-GSH, (b) **2b**-Hcy, (c) **2b**-Cys and (d) **2b**-H_2S (5 µM, λ_{ex} = 320 nm) with increasing molar concentration of $EuCl_3$ (0.025-6.0 mM, increase indicated by arrows).

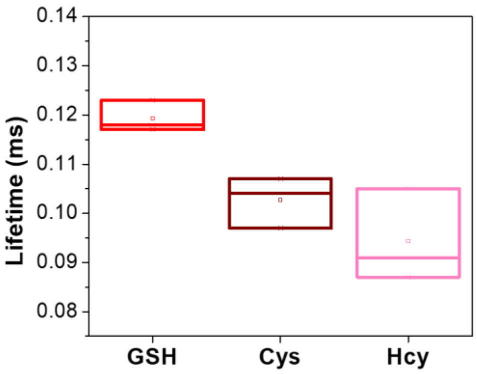

Figure S4.8. Luminescence lifetimes of lanthanide complexes **2b**-GSH, **2b**-Hcy and **2b**-Cys (5 µM in Hepes buffer 50 mM, pH 7.4) after addition of 100 equivalents of $EuCl_3$. Boxes correspond to the 25 and 75%, with a horizontal bar indicating the average value.

KINETIC STUDY

In the kinetic study, determined the rate law from the experimental was determined data using the differential method.

Since we worked with constant concentrations of the sensor, we can focus on the reaction order with respect to GSH, using the following logarithmic equation (S4.3):

$$\log v_0 = \log k_{obs} + n \log[GSH]_0$$

(S4.3)

One way to obtain the data is to plot the initial rate of the reaction (v_0) with different initial $[GSH]_0$. This technique is known as the initial-rate method. A plot of log v_0 against log $[GSH]_0$ would be a line with a slope equal to the reaction order with respect to GSH (Figure S4.9). The observed rate constant, which would include components depending on the concentration of the sensor, can be determined by the intercept. To obtain the data, we used different concentrations of GSH (5, 25, 50 and 500 μM) in the presence of $EuCl_3$ (1.5 mM), in Hepes buffer (50 mM, pH 7.4), keeping the **2b** concentration constant (5 μM). The analysis of the kinetics has been carried out using Origin 8.5, (OriginLab Corp., MA, USA).

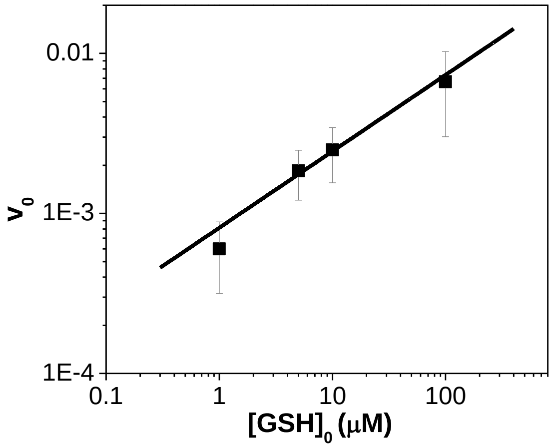

Figure S4.9. Representation of the logarithm of the initial slope of the kinetics versus the logarithm of the GSH concentration. The data show the average of three different kinetic curves. The error bars represent the standard deviation. The line represents the linear fitting to the following equation: $\log v_0 = -3.50 + 0.51 \log[GSH]_0$.

BINDING MODEL AND FITTING PARAMETERS

The titration curves of lanthanide complexes **2b**-GSH, **2b**-Hcy and **2b**-Cys with europium (Figure 4.3d) were satisfactorily fitted to a Hill binding model (equation S4.4):

$$F = F_{min} + (F_{max} - F_{min}) \frac{[Ln]^n}{K^n + [Ln]^n} \qquad (S4.4)$$

where F, F_{min} and F_{max} accounts, respectively, for current, minimum and maximum luminescence intensity at lanthanide emission wavelength; K, the apparent binding constant of the antenna-lanthanide complex; [Ln], the concentration of lanthanide; n, the Hill coefficient.

CELL VIABILITY

We incubated mouse splenocytes (Figures S4.10a and S4.10b) or human PBMCs (Figure S4.10c) with either compound **2b** (Figures S4.1a and S.41c) or $EuCl_3$ (Figure S4.10b) for 1 hour in PBS at 37 °C. We then washed the cells and stained them with fluorescent Fixable viability dye eFluor 780 (eBioscience, USA) as detailed in the manufacturer's protocol, and monitoring on a 3-laser Canto flow cytometer (BD bioscience) and analyzed the cells using FCS express software.

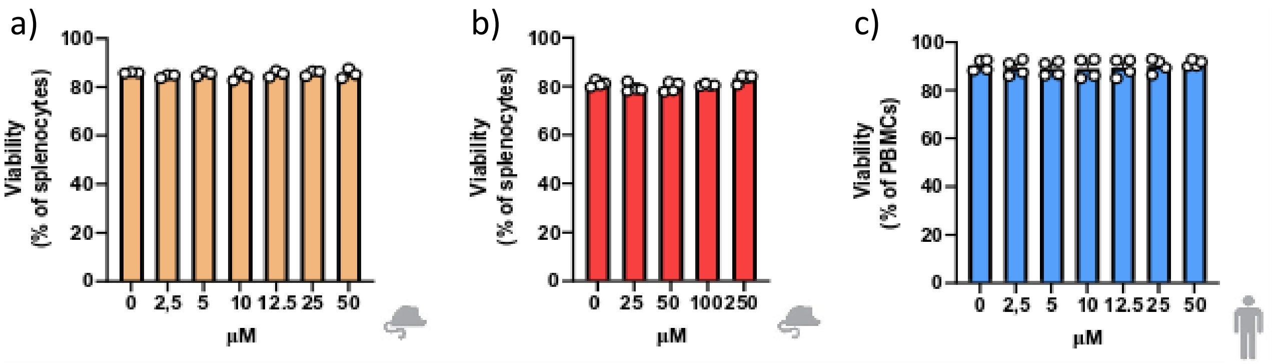

Figure S4.10. Flow cytometric quantification of the cell viability in mouse splenocytes (a, b) and human PBMCs (c). A. Mouse splenocytes incubated with **2b** at concentrations ranging from 0-50 µM; (B) Mouse splenocytes incubated with $EuCl_3$ at concentrations ranging from 0-250 µM; (C) Human PBMCs incubated with **2b** at concentrations ranging from 0-50 µM; (n=3 (a) or 4 (b) animals/group or n=4 (c) human samples/group from three independent experiments, ANOVA with Tukey HSD t-test, * $p<0.05$).

TIME-RESOLVED LUMINESCENCE ASSAYS

Luminescent assays were performed in 96 well plates in 200 µL 50 mM potassium phosphate (50 mM KH_2PO_4/K_2PO_4, pH 7.4) 150 mM NaCl, using a SpectraMax M2 spectrofluorimeter. Splenocytes were cultured in PBS with the sensor **2b** (25 µM) and $EuCl_3$ (250 µM) added at the same time, and then excited at 320 nm. The emission signal was acquired at 620 nm unless stated otherwise (measurement start 50 ms; measurement end 850 ms; 20 flashes per read). Data analysis was performed using Prism software. Experiments were performed in triplicate, and error bars indicate standard deviation from average.

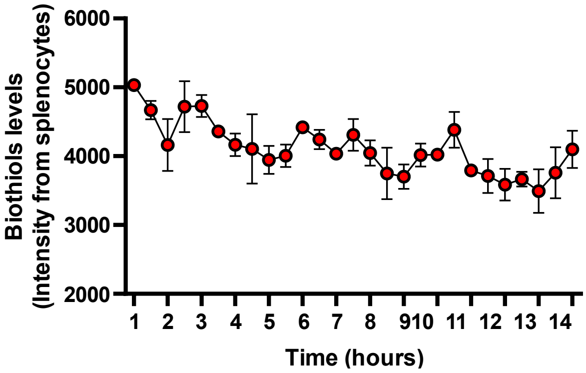

Figure S4.11. Time resolved-fluorescence kinetics of europium luminescence overtime (λ_{ex}= 320 nm, λ_{em}=620 nm, 14 h) in mouse splenocytes.

MICE AND HUMAN SAMPLES

Male and female C57BL/6-*Foxp3*-YFP and Wild type B6 mice were purchased from The Jackson Laboratory (stocks #016959 and #000651, respectively) and bred at mouse facilities of the Icahn School of Medicine at Mount Sinai. Mice were aged 8 weeks at the start of the experiment. Data depicted in the figures include male and female mice as we used both male and female mice for T_{REG} induction experiments. This study was carried out in strict accordance with the recommendations in the Guide for the Care and Use of Laboratory Animals and under the protocol (IACUC-2018-2) approved by the Institutional Animal Care and Use Committee of the Icahn School of Medicine at Mount Sinai of the USA. All animals were housed in the animal facilities at the Icahn School of Medicine at Mount Sinai. For experiments in human cells, we used peripheral blood mononuclear cells (PBMCs) from buffy coats obtained from Fully anonymous deidentified donors to the New York Blood Bank of the USA, and thus were determined by the institution not to constitute human subjects research.

LYMPHOCYTE ISOLATION FROM THE SPLEEN AND PBMCS

Spleens were harvested in PBS and mechanically disaggregated through a mesh strainer (70 μm) with the aid of the back of a syringe plunger. PBS was decanted after centrifugation and red blood cells lysed (ACK lysis buffer, 4 min at room temperature, Roche). Cells were then resuspended in PBS and filtered again through a 70 μm nylon mesh. The isolated single-cell suspension of enriched either spleen or PBMCs leukocytes was processed for different assays or used to isolate naïve CD4$^+$ T cells naïve T cells using magnetic separation (EasySep™ Mouse or Human Naïve CD4$^+$ T Cell Isolation Kit, STEMCELL Kit) for T$_{REG}$ induction cultures.

FLOW CYTOMETRY, SURFACE STAINING AND BIOTHIOL LEVELS

Cells were evaluated for surface antigen expression (CD4, PE-cyanine7 Anti-mouse CD4 (GK 1.5), TONBO biosciences, USA) and intracellular biothiol levels culturing the cells either with the sensor at 25 µM or the sensor with $EuCl_3$ (250 µM) at the same time in the incubator for 30 minutes, following washes in PBS or a buffer consisting of 2% rat serum 2 mM EDTA. Data were acquired on a 3-laser Canto flow cytometer (BD bioscience) and analyzed using FCS express software.

IN VITRO T$_{REG}$ INDUCTION

In vitro T$_{REG}$ induction either mouse naïve CD4$^+$ T cells or Human peripheral blood mononuclear cells (PBMCs) were isolated from spleens or buffy coats by Ficoll density gradient centrifugation (Histopaque, SigmaAldrich) at 490g. Naïve CD4$^+$ T cells were enriched from murine splenocytes (CD44loCD62hi) or human peripheral blood mononuclear cells (CD45RA+CD45RO-) (EasySep™ Mouse Naïve CD4$^+$ T Cell Isolation Kit, EasySep™ Human Naïve CD4$^+$ T Cell Isolation Kit, respectively, STEMCELL Technologies) and their purity checked by flow cytometry. Mouse cultures: 200,000 naïve CD4$^+$ T cells were incubated with IL-2 (2.75 ng/ml, Peprotech), TGFβ (0.7 ng/ml, Peprotech) and stimulated with either αCD3/αCD28 (15 µl/million cells, Gibco) (polyclonal). Human cultures: 200,000 naïve CD4$^+$ T cells were cultured with IL-2 (100 U/ml, BD Pharmingen), TGFβ (3 ng/ml, Peprotech) and stimulated with αCD3/αCD28 (15 µl/million cells, Gibco).

XIII. NMR SPECTRA (^{1}H-NMR AND ^{13}C-NMR) OF 2A AND 2B

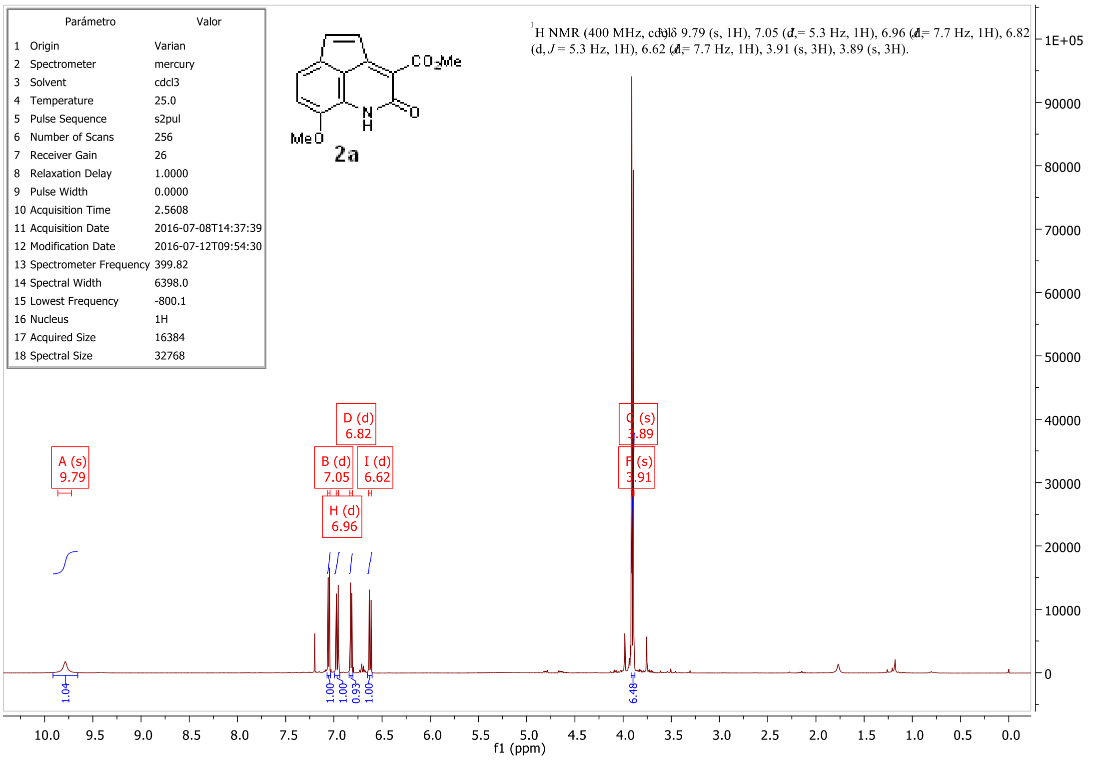

Parámetro		Valor
1	Origin	Varian
2	Spectrometer	mercury
3	Solvent	cdcl3
4	Temperature	25.0
5	Pulse Sequence	s2pul
6	Number of Scans	256
7	Receiver Gain	26
8	Relaxation Delay	1.0000
9	Pulse Width	0.0000
10	Acquisition Time	2.5608
11	Acquisition Date	2016-07-08T14:37:39
12	Modification Date	2016-07-12T09:54:30
13	Spectrometer Frequency	399.82
14	Spectral Width	6398.0
15	Lowest Frequency	-800.1
16	Nucleus	1H
17	Acquired Size	16384
18	Spectral Size	32768

^{1}H NMR (400 MHz, cdcl$_3$) δ 9.79 (s, 1H), 7.05 (d, J = 5.3 Hz, 1H), 6.96 (d, J = 7.7 Hz, 1H), 6.82 (d, J = 5.3 Hz, 1H), 6.62 (d, J = 7.7 Hz, 1H), 3.91 (s, 3H), 3.89 (s, 3H).

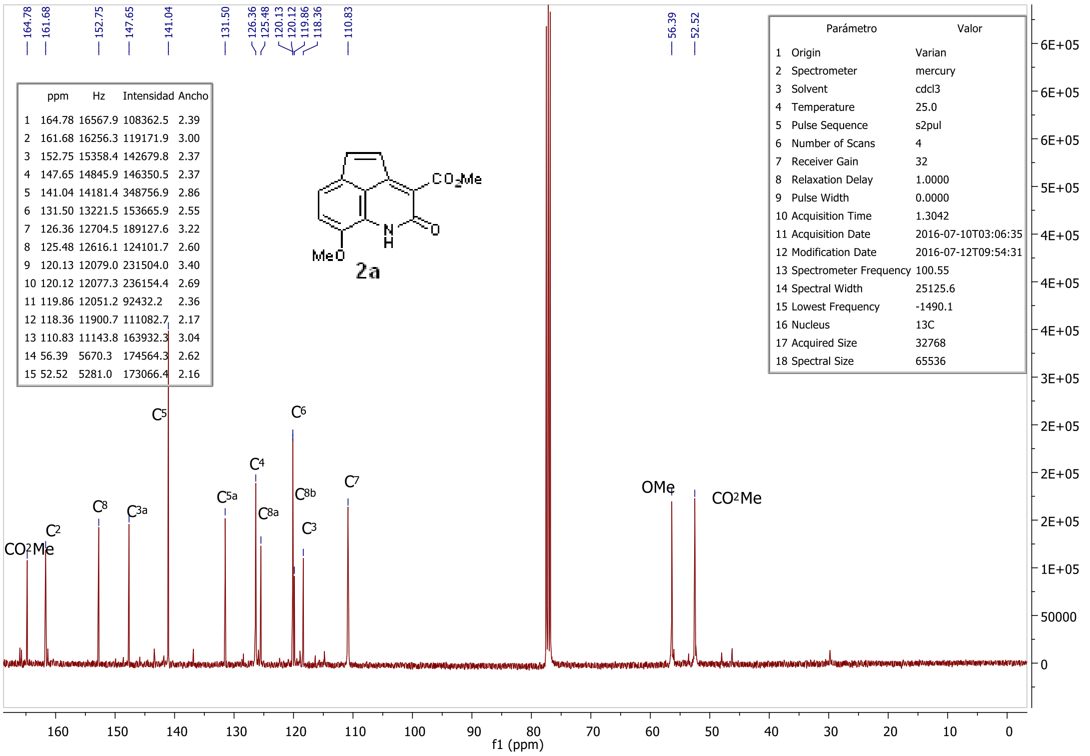

	ppm	Hz	Intensidad	Ancho
1	164.78	16567.9	108362.5	2.39
2	161.68	16256.3	119171.9	3.00
3	152.75	15358.4	142679.8	2.37
4	147.65	14845.9	146350.5	2.37
5	141.04	14181.4	348756.9	2.86
6	131.50	13221.5	153665.9	2.55
7	126.36	12704.5	189127.6	3.22
8	125.48	12616.1	124101.7	2.60
9	120.13	12079.0	231504.0	3.40
10	120.12	12077.3	236154.4	2.69
11	119.86	12051.2	92432.2	2.36
12	118.36	11900.7	111082.7	2.17
13	110.83	11143.8	163932.3	3.04
14	56.39	5670.3	174564.3	2.62
15	52.52	5281.0	173066.4	2.16

Parámetro		Valor
1	Origin	Varian
2	Spectrometer	mercury
3	Solvent	cdcl3
4	Temperature	25.0
5	Pulse Sequence	s2pul
6	Number of Scans	4
7	Receiver Gain	32
8	Relaxation Delay	1.0000
9	Pulse Width	0.0000
10	Acquisition Time	1.3042
11	Acquisition Date	2016-07-10T03:06:35
12	Modification Date	2016-07-12T09:54:31
13	Spectrometer Frequency	100.55
14	Spectral Width	25125.6
15	Lowest Frequency	-1490.1
16	Nucleus	13C
17	Acquired Size	32768
18	Spectral Size	65536

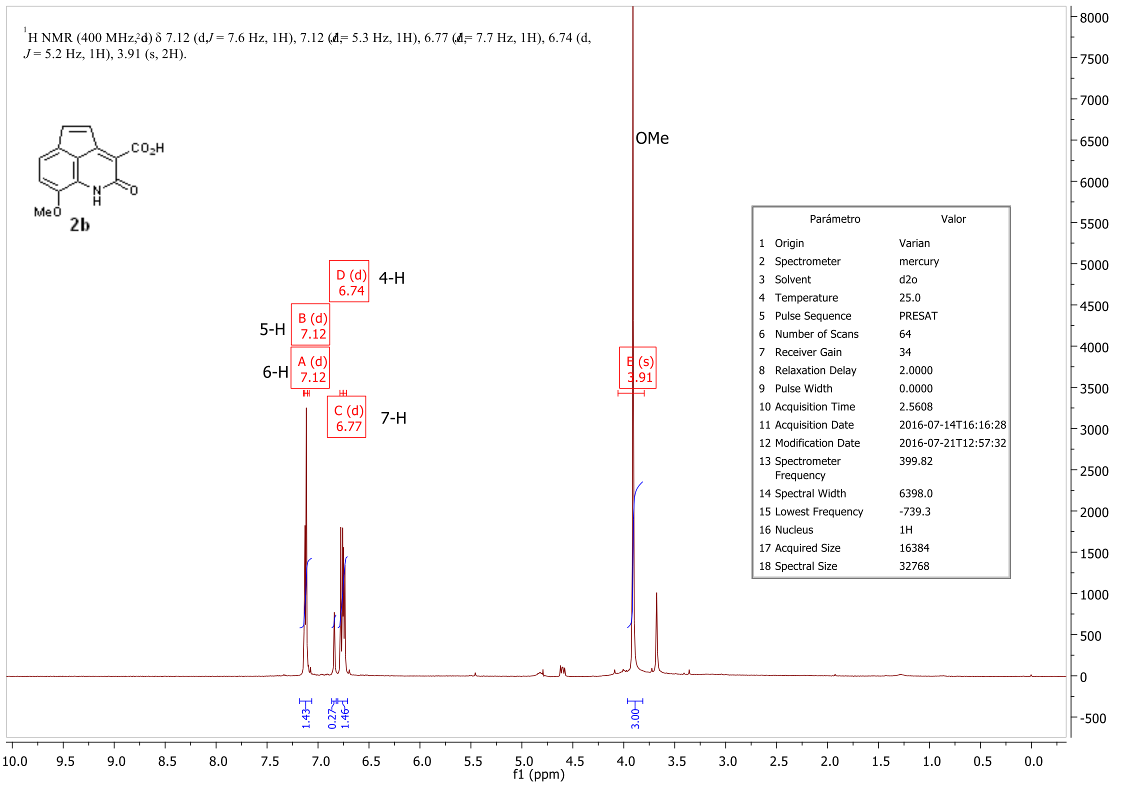

^{1}H NMR (400 MHz, ^{2}d) δ 7.12 (d, *J* = 7.6 Hz, 1H), 7.12 (d, *J* = 5.3 Hz, 1H), 6.77 (d, *J* = 7.7 Hz, 1H), 6.74 (d, *J* = 5.2 Hz, 1H), 3.91 (s, 2H).

	Parámetro	Valor
1	Origin	Varian
2	Spectrometer	mercury
3	Solvent	d2o
4	Temperature	25.0
5	Pulse Sequence	PRESAT
6	Number of Scans	64
7	Receiver Gain	34
8	Relaxation Delay	2.0000
9	Pulse Width	0.0000
10	Acquisition Time	2.5608
11	Acquisition Date	2016-07-14T16:16:28
12	Modification Date	2016-07-21T12:57:32
13	Spectrometer Frequency	399.82
14	Spectral Width	6398.0
15	Lowest Frequency	-739.3
16	Nucleus	1H
17	Acquired Size	16384
18	Spectral Size	32768

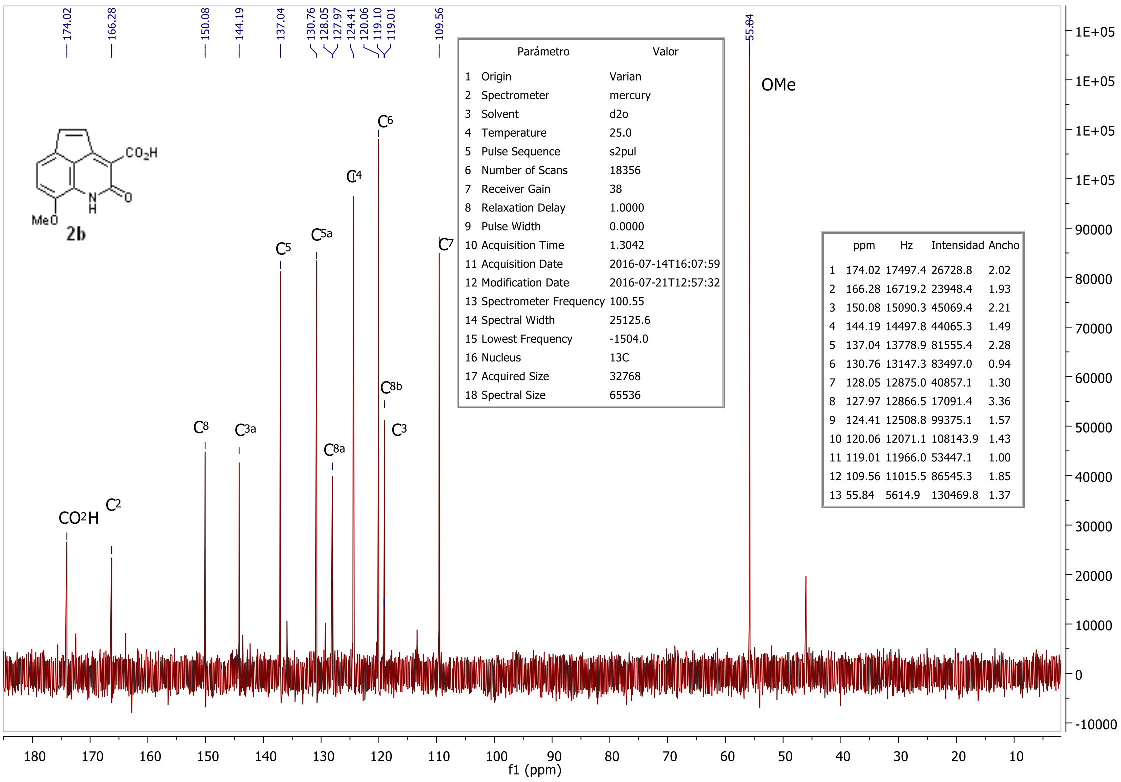

	Parámetro	Valor
1	Origin	Varian
2	Spectrometer	mercury
3	Solvent	d2o
4	Temperature	25.0
5	Pulse Sequence	s2pul
6	Number of Scans	18356
7	Receiver Gain	38
8	Relaxation Delay	1.0000
9	Pulse Width	0.0000
10	Acquisition Time	1.3042
11	Acquisition Date	2016-07-14T16:07:59
12	Modification Date	2016-07-21T12:57:32
13	Spectrometer Frequency	100.55
14	Spectral Width	25125.6
15	Lowest Frequency	-1504.0
16	Nucleus	13C
17	Acquired Size	32768
18	Spectral Size	65536

	ppm	Hz	Intensidad	Ancho
1	174.02	17497.4	26728.8	2.02
2	166.28	16719.2	23948.4	1.93
3	150.08	15090.3	45069.4	2.21
4	144.19	14497.8	44065.3	1.49
5	137.04	13778.9	81555.4	2.28
6	130.76	13147.3	83497.0	0.94
7	128.05	12875.0	40857.1	1.30
8	127.97	12866.5	17091.4	3.36
9	124.41	12508.8	99375.1	1.57
10	120.06	12071.1	108143.9	1.43
11	119.01	11966.0	53447.1	1.00
12	109.56	11015.5	86545.3	1.85
13	55.84	5614.9	130469.8	1.37

BIBLIOGRAPHY

1 J. A. González-Vera, F. Fueyo-González, I. Alkorta, M. Peyressatre, M. C. Morris and R. Herranz, *Chem. Commun.*, **2016**, 52, 9652-9655.

2 Becke, A. D. Density-functional thermochemistry. III. The role of exact exchange. *J. Chem. Phys.* **1993**, 98, 5648-52.

3 Lee, C.; Yang, W.; Parr, R. G. Development of the Colle-Salvetti correlation-energy formula into a functional of the electron density. *Phys. Rev. B* **1988**, 37, 785-789.

4 Hariharan, P. C.; Pople, J. A. Influence of polarization functions on MO hydrogenation energies. *Theor. Chim. Acta* **1973,** 28, 213-22.

5 Adamo, C.; Jacquemin, D. The calculations of excited-state properties with Time-Dependent Density Functional Theory. *Chem. Soc. Rev.* **2013**, 42, 845-856.

6 Krygowski, T. M.; Cyranski, M. K. Structural Aspects of Aromaticity. *Chem. Rev.* **2001**, 101, 1385-1419.

7 Krygowski, T. M. Crystallographic studies of inter- and intramolecular interactions reflected in aromatic character of π-electron systems. *J. Chem. Inf. Comput. Sci.* 1993, 33, 70-8.

8 (a) Wuerth, C.; Grabolle, M.; Pauli, J.; Spieles, M.; Resch-Genger, U. *Nat. Protoc.*, **2013**, *8*, 1535-1550 (b) Brouwer, A. M. *Pure Appl. Chem.*, **2011**, *83*, 2213-2228; (c) Rurack, K.; Spieles. M. *Anal. Chem.*, **2011**, *83*, 1232-1242.

CONCLUSIONS

CONCLUSIONS

SECTION 1

- The probe 2-Me-4-OMe-TM is suitable for detecting phosphate through a buffer-mediated ESPT reaction in aqueous solution.
- It has been demonstrated that 2-Me-4-Ome-TM presents high sensitivity to the solvent's acidity, forming specific hydrogen bonding interactions, and polarity, affecting the equilibrium of the prototropic species but also increasing the fluorescence lifetime of the anionic form.
- 2-Me-4-OMe-TM was able to detect differences in polarity between different regions of cells by FLIM microscopy allowing the isolation of some organelles where 2-Me-4-Ome-TM showed a specific pattern of intensity.

SECTION 2

- Through steady-state fluorescence and FLIM, we confirmed the use of the solvatofluorochromic dye 2-Me-4-OMe-TM as a fluorescent probe for the initial stages of Aβ42 amyloid aggregation.
- By establishing a polarity scale based on the ratiometric value of the average fluorescence lifetimes between two different emission bands, we were able to detect changes in the hydrophobicity of the aggregates and established a method for distinguishing between aggregates of different types.
- FLIM has proven to be an excellent approach for studying amyloidogenic aggregation supporting the use of the xanthenic derivative 2-Me-4OMe TM for noninvasive detection of preamyloid aggregates.

SECTION 3

- The AIE phenomenon of PEMC was confirmed through different approaches by using different solvent proportions, increasing the viscosity and forming micelles.
- The rate of spontaneous incorporation of PEMC into cells was studied and the intracellular pattern produced by AIE was observed.
- The strong differences in fluorescence intensity and fluorescence lifetime of different intracellular compartments allowed us to study these regions selectively.

- The use of this luminogen was demonstrated in bioimaging with a mitochondria biomarker to analyze these organelles through their fluorescence lifetimes.

SECTION 4

- The small, non-fluorescent, Michael acceptor **2b,** after its reaction with biothiols, becomes fluorescent and an efficient Eu^{3+} antenna, which self-assembles with the cation in water.
- This property makes **2b** a highly selective GSH biosensor, which can be monitored through either the increase of the fluorescence of the antenna or the luminescence of Eu^{3+}.
- The potential of **2b** as a GSH biosensor was demonstrated to study murine and human cells of the immune system through flow cytometry ($CD4^+$ T, $CD8^+$ T, and B cells), and to monitor changes in their metabolism as naïve $CD4^+$ T cells polarize to Treg, providing a proof-of-concept of the use of **2b** to monitor biothiols in immune cells.